CYTOSKELETON AND MOLECULAR MOTORS IN THE CAUSATION OF MOTOR NEURON DISEASES

Fabio Andre Amaral Lopes Simoes

A thesis submitted to the University of Brighton and the University of Sussex for a programme of study undertaken at the Brighton and Sussex Medical School for the degree of Doctor of Philosophy

February 2018

Abstract

Amyotrophic lateral sclerosis (ALS) and spinal muscular atrophy with lower extremity predominance (SMA-LED) are motor neuron diseases defined by the loss of motor neurons. RNA metabolism and molecular transport have both become increasingly implicated in the pathogenesis of motor neuron diseases. As such, this thesis explores the role of TAR-DNA binding protein 43 (TDP-43) in the regulation of peripherin expression in ALS, and the molecular consequences of mutations in *DYNC1H1*, a component of the cytoplasmic dynein motor complex, in SMA-LED.

TDP-43 is a DNA/RNA binding protein implicated in ALS pathogenesis. Recent evidence suggests that TDP-43 regulates peripherin, an ALS associated intermediate filament protein. Here, analysis of peripherin in the lumbar spinal cord of TDP-43$^{+/F210I}$ mice revealed a significant increase in the levels of Per-45, a shift towards an increase in Per-58 in the Triton X-100 soluble fraction that did not reach statistical significance, and an increase in an isoform of 50 kDa in the insoluble fraction. These changes in the expression of peripherin in TDP-43$^{+/F210I}$ mice may indicate a regulatory role for TDP-43 in peripherin expression, which could contribute to ALS pathology.

Furthermore, there is evidence that defects in neurodevelopment are present in SMA-LED. Analysis of paxillin, a key focal adhesion protein in mouse embryonic fibroblasts from the *Legs at odd* angles (Loa) model of SMA-LED was performed, which indicated a reduction in its expression which may underpin the previously reported migration phenotypes in these cells. This data provides further evidence that SMA-LED may be a neurodevelopmental disorder. Furthermore, analysis revealed that the Golgi apparatus in DYNC1H1$^{+/D338N}$ patient fibroblasts was significantly condensed, while in BICD2$^{+/I189F}$ fibroblasts there was a decrease in localisation of dynein to the Golgi. The lack of dynein at the Golgi in BICD2$^{+/I189F}$ fibroblasts indicates that BICD2 may be necessary for the recruitment of the molecular motor to the organelle. These Golgi phenotypes may also contribute to impaired migration in disease. Importantly, analysis of DYNC1H1$^{+/D338N}$ patient fibroblasts and mouse embryonic fibroblasts (MEFs) from the *Loa* mouse strain showed a significant decrease in α-tubulin acetylation, a phenotype previously seen in another DYNC1H1 substitution.

In conclusion, these data support previous data which suggested that peripherin expression is altered in the context of TDP-43 mutations, potentially contributing to ALS pathology. Additionally, Golgi phenotypes were found in both DYNC1H1$^{+/D338N}$ and BICD2$^{+/I189F}$ fibroblasts with potential consequences for cellular migration. Finally, decreased microtubule acetylation may be a common factor in SMA-LED linked with *DYNC1H1* mutations. The conserved nature of this phenotype could indicate a potential target for therapeutics.

List of Figures

List of Tables

Abbreviations

acrv1	Acrosomal vesicle protein 1
ADHD	Attention deficit hyperactivity disorder
AID	Auxin-inducible degron
ALS	Amyotrophic lateral sclerosis
AP	Alkaline phosphatase
ARD1	Arrest-defective-1
ARP2/3	Actin-related protein 2/3
ATG13	Autophagy-related 13
ATP	Adenosine triphosphate
Aux	Indol1-3-acetic-acid
BAC	Bacterial artificial chromosome
BCA	Bicinchoninic acid assay
BDNF	Brain derived neurotrophic factor
BICD	Bicaudal D
BICD2	Bicaudal d homolog 2
BICD2-N	N-terminus of BICD2
BICDR-1	Bicaudal D related protein 1
BICDR-2	Bicaudal D related protein 2
BSA	Bovine serum albumin
C9orf72	Chromosome 9 open reading frame 72 gene
CaMKIIα	Calcium/calmodulin-dependent protein kinase II α
CAMSAP2	Calmodulin-regulated spectrin-associated protein 2
CC	Coiled-coil
CCP	Cytosolic carboxypeptidase
CENP-F	Centromere protein F precursor
CFTR	Cystic fibrosis transmembrane conductance regulator
CGN	*cis* Golgi network
CHMP2B	Charged multivesicular protein 2B
CLIP170	CAP-Gly domain-containing linker protein 170
CMT2	Charcot-Marie-Tooth disease
CNS	Central nervous system

Abbreviations

COPII	Coat protein complex II
Cra1	Cramping-1
Cryo-EM	Cryo-electron microscopy
DBPS	Dulbecco's phosphate-buffered saline
DCTN1	Dynactin
DDB	Dynein/dynactin/BICD2
DENN	Differentially expressed in normal and neoplastic cells
Dox	Doxycycline
DRG	Dorsal Root Ganglion
DYNC1H1	Dynein cytoplasmic 1 heavy chain 1
EB1	End binding protein 1
ECM	Extracellular matrix
EGF	Epidermal growth factor
EGFR	Epidermal growth factor receptor
ELP3	Elongator complex protein 3
ENU	N-ethyl-N-nitrosourea
ER	Endoplasmic reticulum
ERES	ER exit sites
ERGIC	ER-Golgi intermediate compartment
EWS	Ewing RNA binding protein
FAs	Focal adhesions
FAK	Focal adhesion kinase
fALS	Familial amyotrophic lateral sclerosis
FDA	United States Food and Drug Administration
FIP200	FAK family kinase-interacting protein of 200 kDa
FMRP	Fragile X mental retardation protein
FRAP	Fluorescence recovery after photobleaching
FTD	Frontotemporal dementia
FUS	Fused in sarcoma
GCP	γ-tubulin complex proteins
GEF	Guanine exchange factor
GEF	Guanine nucleotide exchange factor
GFAP	Glial fibrillary acid protein

Abbreviations

Grb2	Growth factor receptor bound protein 2
Grn	Progranulin
GTP	Guanosine-5'-triphosphate
HC	Heavy chain
HDAC6	Histone deacetylase 6
HIV-1	Human immunodeficiency virus type 1
hnRNP	Heterogeneous ribonucleoprotein
HRP	Horse radish peroxidase
IC	Intermediate chain
IF	Intermediate filament
IFT	Intraflagellar transport
INM	Interkinetic nuclear migration
JIP1	C-Jun-amino-terminal kinase-interacting protein 1
KIFAP3	Kinesin-associated protein 3
LB	Lysogeny broth
LC	Light chain
LD	Leucine-rich domains
LIC	Light intermediate chain
Lis1	Lissencephaly 1
LMN	Lower motor neurons
lncRNA	Long non-coding RNA
Loa	Legs at odd angles
LSC	Lumbar spinal cords
MEK	Mitogen-activated protein kinase kinase
MLC	Myosin light chain
MMG	Myomegalin
MND	Motor neuron disease
mPrp	Mouse prion promoter
mRNP	Messenger ribonucleoprotein
MTBD	Microtubule binding domain
MTOC	Microtubule organisation centre
MYPT1	Myosin phosphatase targeting subunit
NAT1	N-acetyltransferase 1 complex
ncRNA	Non-coding RNA

Abbreviations

NES	Nuclear export signal
NFH	Neurofilament heavy
NFL	Neurofilament light
NFM	Neurofilament middle
NGF	Nerve growth factor
NLS	Nuclear localisation signal
Nude	Nuclear distribution protein E
Nudel	Nude like1
Nup133	Nucleoporin133
PAR	Poly-ADP-ribose
PCR	Polymerase chain reaction
PINK1	PTEN-induced putative kinase 1
PMA	Progressive muscular atrophy
PNS	Peripheral nervous system
pre-mRNA	Pre-messenger RNA
PTM	Post-translational modifications
PXN	Paxillin gene
RAF	RAF proto-oncogene serine/threonine-protein kinase
RAN	Repeat-associated non-ATG-dependent
RanBP2	Ran-binding protein 2
RGP	Radial glial progenitor
RNP	Ribonucleoprotein
Roadblock 1	Roadblock/LC7 encoded by *DYNLRB1*
Roadblock 2	Roadblock/LC7 encoded by *DYNLRB2*
ROCK	Rho kinase
ROS	Reactive oxygen species
RRM	RNA recognition motif
sALS	Sporadic amyotrophic lateral sclerosis
SCF	Skp1-Cullin-F-box
SDS-PAGE	SDS polyacrylamide gel electrophoresis
SIP30	SNAP25 interacting protein 30
SIRT2	Sirtuin 2
SMA	Spinal muscular atrophy

Abbreviations

SMA-LED	Spinal muscular atrophy, lower extremity predominance
SMCR8	Smith-Magenis Syndrome chromosome region candidate 8
SMN	Survival motor neuron
snRNP	Small nuclear ribonucleoprotein
SOC	Super optimal broth with catabolite repression
SOD1	Superoxide dismutase 1
SP-10	Serine protease 10
Src	Src proto-oncogene, non-receptor tyrosine kinase
Swl	Sprawling
TAF	TATA-Box binding protein associated factor 15
TANK	TRAF family member-associated NF-KB activator
TBK1	TANK-binding kinase 1
TDP-43	TAR DNA binding protein 43
TDPBR	TDP binging region
TEMED	Tetramethylethylenediamine
tet-OsTIR1	Tetracycline inducible Os-TIR1
TFIID	Transcription factor II D
TGN	*trans* Golgi network
TIR1	Transport inhibitor response 1
TLS	Translocated in liposarcoma
TrkB	Tropomyosin-related kinase B
TTL	Tubulin Tyr ligase
ULK1	Unc-51-like kinase 1
UMN	Upper motor neurons
VAPB	Vesicle-associated membrane protein
Vegfa	Vascular endothelial growth factor a
VTC	Vesicular tubular cluster
WDR41	WD-40 repeat 1
αTAT1	Alpha tubulin acetyltransferase 1
γ-TuRC	γ-tubulin ring complex

Acknowledgements

I would like to begin by thanking Dr Majid Hafezparast for the opportunity to complete my PhD in his lab and for the endless support he has given me during this time. I particularly want to thank him for the endless patience he has shown as I developed as a researcher under his tutorage. I have gained immensely from the knowledge and expertise that he imparts on all his students. I am also grateful for the support that I have received from my other supervisors, Professor Nigel Leigh and Professor Sarah Newbury. They have always been willing to help in any way they could.

I would also like to thank past and present members of the Hafezparast lab, especially Muruj Barri and Ryan Green who gave me a great deal of support throughout my entire PhD and from whom I learned a great deal. I would also like to thank Greig Joilin for his support, which he especially showed during my writing of this thesis.

I also want to express my gratitude towards my mum, Maria, and my Dad, Joaquim, for their unwavering support throughout my entire education. The support they have given me has allowed me to pursue what I want in life and this PhD would not be possible without them. I would also like to say thank you to my grandad, Jose and uncle, Jorge for helping to raise me and for their support. I would also like to extend a special thank you to my sisters, Patricia and Vanessa.

I also owe my gratitude to my girlfriend, Hannah, without whom this process would have been much more difficult. Her endless support has kept me motivated throughout.

Finally, I would also like to extend my gratitude to Brighton and Sussex Medical School and to Marion Brownridge for the funding for my PhD.

Declaration

I declare that the research contained in this thesis, unless otherwise formally indicated within the text, is the original work of the author. The thesis has not been previously submitted to this or any other university for a degree, and does not incorporate any material already submitted for a degree.

Signed

Dated

Chapter 1: Introduction

1. Organisation of the nervous system

The nervous system is anatomically divided in to the central nervous system (CNS) and the peripheral nervous system (PNS). The PNS consists of sensory neurons and receptors which provide the CNS with information regarding the external and internal environment, and motor nerves which innervate muscles (Purves et al., 2008). On the other hand, the CNS is most broadly described as being composed of the brain and the spinal cord. The brain itself comprises of the cerebrum (cerebral cortex, basal ganglia, hippocampus and the amygdaloid nuclei), diencephalon (thalamus and hypothalamus), brain stem (midbrain, pons and medulla oblongata) and the cerebellum (Kandel et al., 2013). Additionally, the spinal cord is divided into cervical, thoracic, lumbar, sacral and coccygeal regions (Purves et al., 2008; Kandel et al., 2013).

1.1 Motor system

The motor system is typically described has having a hierarchical architecture with four distinct but interactive systems (Purves et al., 2008). The first of these are the lower motor neurons (LMNs) which project from the brain stem and spinal cord (ventral roots) to innervate their peripheral skeletal muscle targets (within the head and body, respectively) to elicit voluntary movement (Figure 1.1).

Anatomically, the spinal cord is formed from a central grey matter region enclosed by surrounding white matter. In each side of the spinal cord the grey matter is subdivided into the dorsal horn and ventral horn, see Figure 1.1 (Purves et al., 2008). It is within the ventral horn that the cell bodies of LMNs reside, whilst projections of sensory neurons entering through the dorsal roots are found within the dorsal horn. The cell bodies of these sensory neurons are found within the dorsal root ganglion (DRG) alongside the spinal cord. A significant proportion of synaptic inputs to the LMNs are via interneurons of the local circuitry within the spinal cord grey matter. This local circuitry receives input from sensory neurons and higher centres and is important in the co-ordinated activity of muscle groups (Purves et al., 2008; Kandel et al., 2013).

Figure 1.1

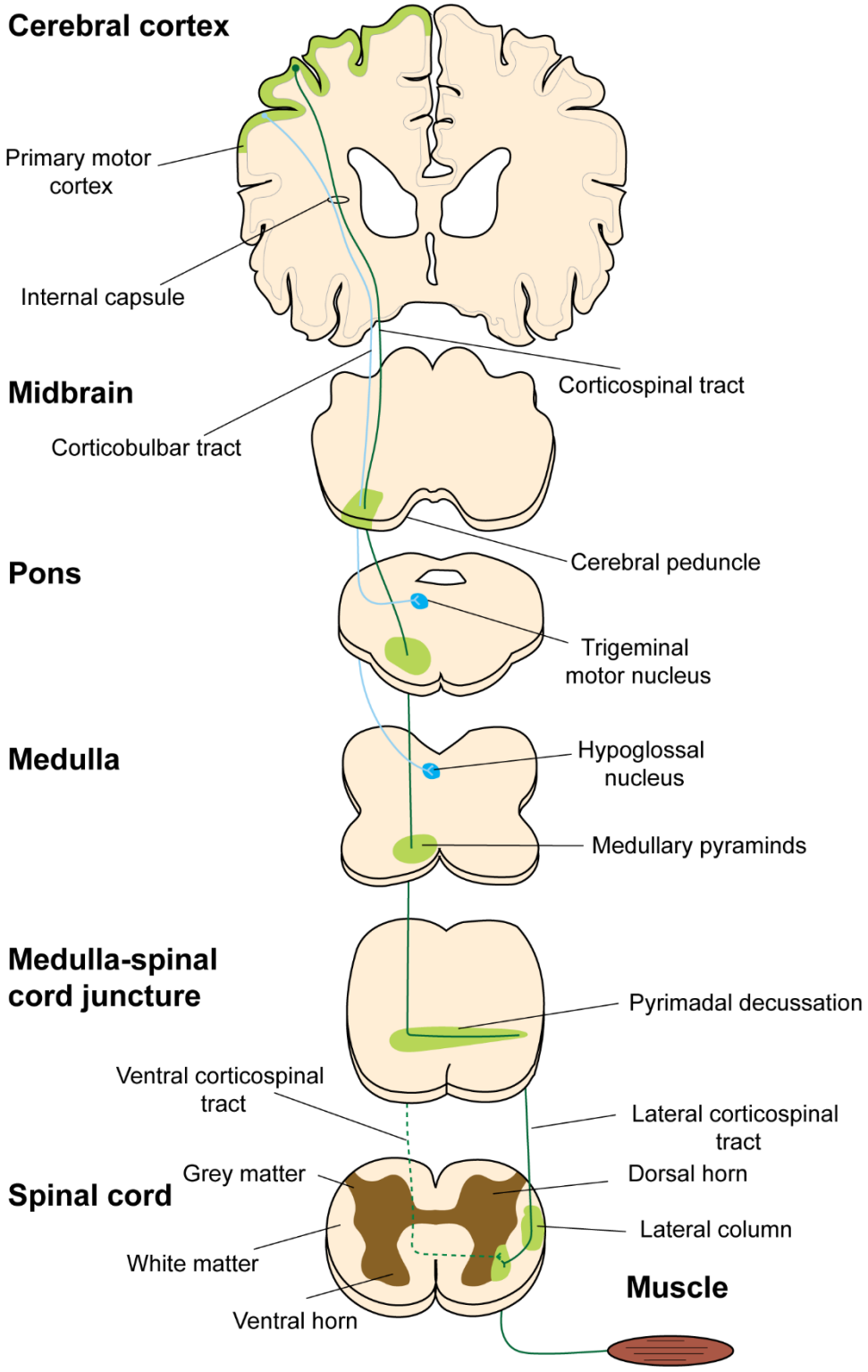

Figure 1.1 Schematic representation of the descending pathways of UMNs in the corticospinal (green line) and corticobulbar tracts (blue line) and their synapse with LMNs in the spinal cord. Adapted from Kandel et al. 2013 with added information from Purves et al. 2008.

The second system are the upper motor neurons (UMNs) which project from the brain stem or cerebral cortex to synapse with the LMNs either directly or via interneurons (Purves et al., 2008). Specifically, these connections form several white matter tracts down the spinal cord. These tracts are typically delineated into the pyramidal (corticospinal and corticobulbar tracts) and extrapyramidal (vestibulospinal, reticulospinal, colliculospinal and rubrospinal) tracts (Purves et al., 2008; Kandel et al., 2013).

The UMNs of the corticospinal and corticobulbar tracts (the direct pathways) originate in cortical layer V of the primary motor cortex, premotor cortex and supplementary motor areas (Purves et al., 2008; Kandel et al., 2013). The axons from the UMNs in these regions descend via the subcortical white matter and pass through the posterior limb of the internal capsule prior to entering the cerebral peduncle in the midbrain, see Figure 1.1. Subsequently, they travel through the base of the pons and form the medullary pyramids in the ventral surface of the medulla. The UMNs of the corticobulbar tract exit the tract at the appropriate level to innervate the corresponding LMNs of the cranial nerves. At the caudal region of the medulla most (~90 %) of the spinal UMNs of the corticospinal tract decussate across the midline (pyramidal decussation) and form the lateral corticospinal tract which mainly terminate in the lateral regions of the ventral horn and intermediate grey matter of the spinal cord. The remaining UMNs (~10 %) continue down the spinal cord and only cross the midline at their target level of the spinal cord, forming the ventral corticospinal tract. Some UMNs from the primary motor cortex which descend through lateral corticospinal tract form direct synapses with α-motor neurons (LMNs) which innervate the distal extremities (important for discrete movement of the fingers). The remaining UMNs from both the lateral and ventral corticospinal tracts act through the local spinal circuitry to affect LMNs. Note that there are also UMNs within the corticospinal and corticobulbar tract which originate from cortical layer V of the somatic sensory regions in the anterior parietal lobe. These neurons are not directly responsible for controlling LMNs but are thought to be important for proprioception.

Movements involving the proximal musculature of the limbs and axial musculature for posture and locomotion are regulated by nuclei within the brain stem (Purves et al., 2008; Kandel et al., 2013). These nuclei are the vestibular nuclei projecting via

the vestibulospinal tract, the reticular formation projecting via the reticulospinal tract, and the superior colliculus projecting via the colliculospinal tract. These pathways descend and regulate LMNs in the medial portion of the ventral horns of the spinal cord. On the other hand, the rubrospinal tract originating in the red nucleus, projects within the lateral column and terminates on the lateral regions of the ventral horn and the intermediate zone. In doing so, the red nucleus is involved in regulating the distal musculature of the upper extremities (arm and hand movement). These tracts form the indirect pathways by which the cortex regulates LMNs as the above nuclei receive inputs from cortical regions including the motor areas.

The final parts of the system are the cerebellum and basal ganglia which do not have direct connections to the LMNs or the local spinal circuitry, but use their connections to modulate UMN activity (Purves et al., 2008). The cerebellum is the larger of these two systems and it receives input from somatosensory neurons within the spinal cord and the descending axons of the corticospinal tract (Purves et al., 2008; Kandel et al., 2013). This enables it to act as an “error-correcting mechanism” by detecting the difference between intended movement and the actual movement that occurred. This happens in real time and is important for long term motor learning. On the other hand, the basal ganglia receive input from the motor and sensory areas of the cortex and from areas involved in motivation, cognition and emotion. It is thought to be important in the suppression of unwanted movements and to prime the UMN system for movement.

1.2 Motor neuron diseases

Motor neuron diseases (MNDs) are a heterogeneous group of disorders defined by the presence of motor neuron degeneration and classified in accordance to their differing clinical presentation, aetiological pathology and underlying genetics. One of the most common differentiators used to group these diseases is based on the specific type of motor neurons affected (UMN, LMN or both), see Table 1.1. This thesis primarily focusses on amyotrophic lateral sclerosis (ALS) and spinal muscular atrophy, lower extremity predominance (SMA-LED).

Table 1.1

Motor neurons affected	Disease	Features	Onset	Ref.
UMN	**Hereditary spastic paraplegia (HSP)**	Heterogeneous group of distal neuropathies affecting the longer corticospinal tract motor neurons, often with involvement of ascending fibres. Lower limb symptoms include weakness and spasticity.	Childhood to 70 years of age	(Lo Giudice et al., 2014)
	Primary lateral sclerosis (PLS)	Rare slowly progressive motor disorder which causes stiffness, poor co-ordination and reduced balance, and slight weakness. See section 1.2.1.2.1.	Slow progression with onset usually at usually at 20 years of age	(Statland et al., 2015)
LMN	**Monomelic amyotrophy (MMA) or Hirayama disease**	Mostly affects the upper limbs, and predominantly the distal muscles of the hand and forearm. No sensory involvement.	Late teens - early twenties	(Garg et al., 2016; Yoo et al., 2015)
	Multifocal motor neuropathy (MMN)	Rare neuropathy only affecting motor neurons and predominantly affecting upper limbs.	Mostly before 50 years of age	(Lawson and Arnold, 2014)
	Progressive bulbar palsy (PBP)	Primarily affects motor neurons in the brain stem causing symptoms such as dysphagia and dysarthria.	Fifth decade of life	(Zhang et al., 2017a)
	Charcot-Marie-Tooth (CMT) disease	Group of neuropathies with motor and sensory involvement. Insidious onset leading to muscle wasting and sensory loss.	First to second decade of life but can be variable	(Hoyle et al., 2015)
	Spinal Muscular atrophy (SMA)	Group of disorders affecting spinal and brain stem motor neurons. Characterised by muscle wasting in proximal muscles usually starting in the lower limbs. See section 1.2.2	Variable	(Juntas Morales et al., 2016)

Motor neurons affected	Disease	Features	Onset	Ref.
	Spinal muscular atrophy, lower extremity predominance (SMA-LED)	Muscle atrophy and weakness with predominance in the proximal lower limbs. Non-progressive or slowly progressive. Can be compounded with cognitive impairment. See section 1.2.2.1	Congenital or early childhood onset	(Harms et al., 2010, 2012).
LMN	**Spinobublar muscular atrophy (SBMA) or Kennedy's disease**	Degeneration of motor neurons within the spinal cord and brain stem causes atrophy of bulbar, facial and limb muscles. Commonly presents with cramps, leg weakness and tremor.	30 - 50 years	(Garg et al., 2016)
	Distal hereditary motor neuropathies (dHMN)	A collection of genetically heterogeneous disorders which primarily affect the distal limb muscles. Predominantly inherited in an autosomal dominant manner but recessive and X-linked inheritance patterns have been observed.	Commonly in childhood or in teenage years but adulthood onset does occur	(Garg et al., 2016)
	Progressive muscular atrophy (PMA)	Sporadic disorder causing bilateral muscle atrophy and weakness. See section 1.2.1.2.1.	Adulthood	(Bogucki et al., 2016)
UMN and LMN	**Amyotrophic lateral sclerosis (ALS)**	Rapidly progressive motor neuron disease affecting upper and lower motor neurons with either bulbar, spinal or respiratory onset. Causes muscle atrophy and weakness, fasciculations and spasticity. See section 1.2.1.	At around 60 years of age (juvenile cases also occur)	(Swinnen and Robberecht, 2014)

Table 1.1 Motor neurons diseases grouped according to the type of neurons they affect. UMN = upper motor neuron, LMN = lower motor neuron.

1.2.1 Amyotrophic lateral sclerosis (ALS)

ALS (OMIM: 105400) is an unremittingly progressive motor neuron disease associated with degeneration of both upper and lower motor neurons (Taylor et al., 2016). Despite earlier descriptions of ALS, Jean-Martin Charcot receives credit for defining the disease as it is recognised today and for being the first to use the term “amyotrophic lateral sclerosis” (Rowland, 2001; Al-Chalabi and Hardiman, 2013). The term “amyotrophy” is a reference to the atrophy of the muscles, and “lateral sclerosis” is a description of the hardening of the corticospinal tracts caused by motor neuron degeneration and subsequent gliosis (Wijesekera and Leigh, 2009).

1.2.1.1 Epidemiology

ALS has an incidence of 2.16 per 100,000 people per year within the European population, a number similar to previous epidemiological studies on the US population (Logroscino et al., 2010). Precise worldwide incidence rates are difficult to ascertain due to a difficulty in conducting epidemiological studies in other areas (Cronin et al., 2007). The lifetime risk of developing ALS are 1:350 and 1:400, for males and females respectively (Al-Chalabi and Hardiman, 2013). Additionally, the prevalence rate is approximately 5 per 100,000 people (Wijesekera and Leigh, 2009; Taylor et al., 2016). Age of onset is extremely variable but most commonly arising within the fifth or sixth decade of life (Swinnen and Robberecht, 2014). Occasional cases of juvenile ALS have been noted and this subset is usually characterised with an onset before the age of 25. However, only about 5 % of cases occur below the age of 30 (Wijesekera and Leigh, 2009).

1.2.1.2 Onset and clinical presentation

ALS is a clinically heterogeneous disease with no definitive test for diagnosis, instead clinicians undergo a process of elimination of ALS-like conditions (Wijesekera and Leigh, 2009). A common approach for clinical diagnosis is the use of the El Escorial criteria and its subsequent revisions (Airlie House criteria, Awaji-Shima criteria). However, these criteria were first established in 1994 to provide a standardized method of diagnosis for the inclusion of patients in clinical trials and not for use in clinical practice (Al-Chalabi et al., 2016).

ALS typically presents with a focal onset where a group of muscles is initially affected before eventually spreading to other regions of the motor system (McDermott and Shaw, 2008). Stratification of the disease is usually accomplished by delineating in accordance to the site of onset. As such, ALS is usually grouped as being of spinal onset, bulbar onset or respiratory onset (Figure 1.2).

Approximately 65 % of patients present with spinal onset, which begins with asymmetric weakness, either proximally or distally within upper and lower limbs (Figure 1.2) (Wijesekera and Leigh, 2009; Hardiman et al., 2011; Swinnen and Robberecht, 2014). Examination of the weakened muscles reveals muscle atrophy and pathological reflexes such as the presence of the Babinski reflex. Additionally, patients may notice fasciculations which are rapid involuntary contractions of muscles noticeable under the skin (Wijesekera and Leigh, 2009). Subsequently, spasticity (muscle stiffness or hypertonia) develops affecting gait and dexterity. In the latter stages patients may also develop hyperreflexia (Wijesekera and Leigh, 2009; Swinnen and Robberecht, 2014). The relentless progressive nature of the disease means that other limbs become affected and patients eventually develop bulbar and respiratory symptoms (Wijesekera and Leigh, 2009). In some instances the spread the of the disease is contiguous and some have hypothesised that this may reflect the cellular spread of the disease (Ravits and La Spada, 2009).

Bulbar onset occurs in approximately 30 % of patients where muscle weakness initially affects bulbar muscles causing dysarthria of speech, dysphagia and tongue fasciculations (Figure 1.2) (Hardiman et al., 2011; Swinnen and Robberecht, 2014). Most patients inevitably develop an increased difficulty in swallowing leading to sialorrhoea (excessive drooling) which is compounded by bilateral weakness in the lower region of the face (Wijesekera and Leigh, 2009). Concurrently, patients may exhibit “pseudobulbar” symptoms which include emotional lability, excessive yawning, and uncontrolled laughter or crying (Wijesekera and Leigh, 2009; Swinnen and Robberecht, 2014). Patients are liable to developing limb associated symptoms almost concomitantly and in the majority of cases within at least 2 years (Wijesekera and Leigh, 2009).

In comparison, a relatively small percentage (approximately 5 %) of patients present with respiratory onset (Figure 1.2) (Wijesekera and Leigh, 2009; Hardiman et al., 2011). Symptomatically, these patients may show symptoms associated with type 2 respiratory failure or nocturnal hypoventilation which include dyspnoea and orthopnoea (Wijesekera and Leigh, 2009; Swinnen and Robberecht, 2014). Additionally, symptoms such as dropped head, camptocormia, absent abdominal reflexes, frequent neck flexion or extension weakness are more common in respiratory onset ALS (Gautier et al., 2010; Ferguson and Elman, 2007). Importantly, patients have no significant spinal or bulbar symptoms.

The prognosis of ALS patients is varied as would be expected from such a heterogenous condition. Typically patients die within 3 years of diagnosis due to respiratory failure or other pulmonary complications (Swinnen and Robberecht, 2014; Wijesekera and Leigh, 2009). However, bulbar and respiratory onset appear to have a poorer prognosis in comparison to spinal onset (Swinnen and Robberecht, 2014). Typically, bulbar onset patients survive approximately 2 years and the percentage of patients which survive for 10 years or more is only 3 % (Chio et al., 2011). The prognosis for respiratory onset is even poorer with a reported mean survival of only 1.4 years.

Figure 1.2

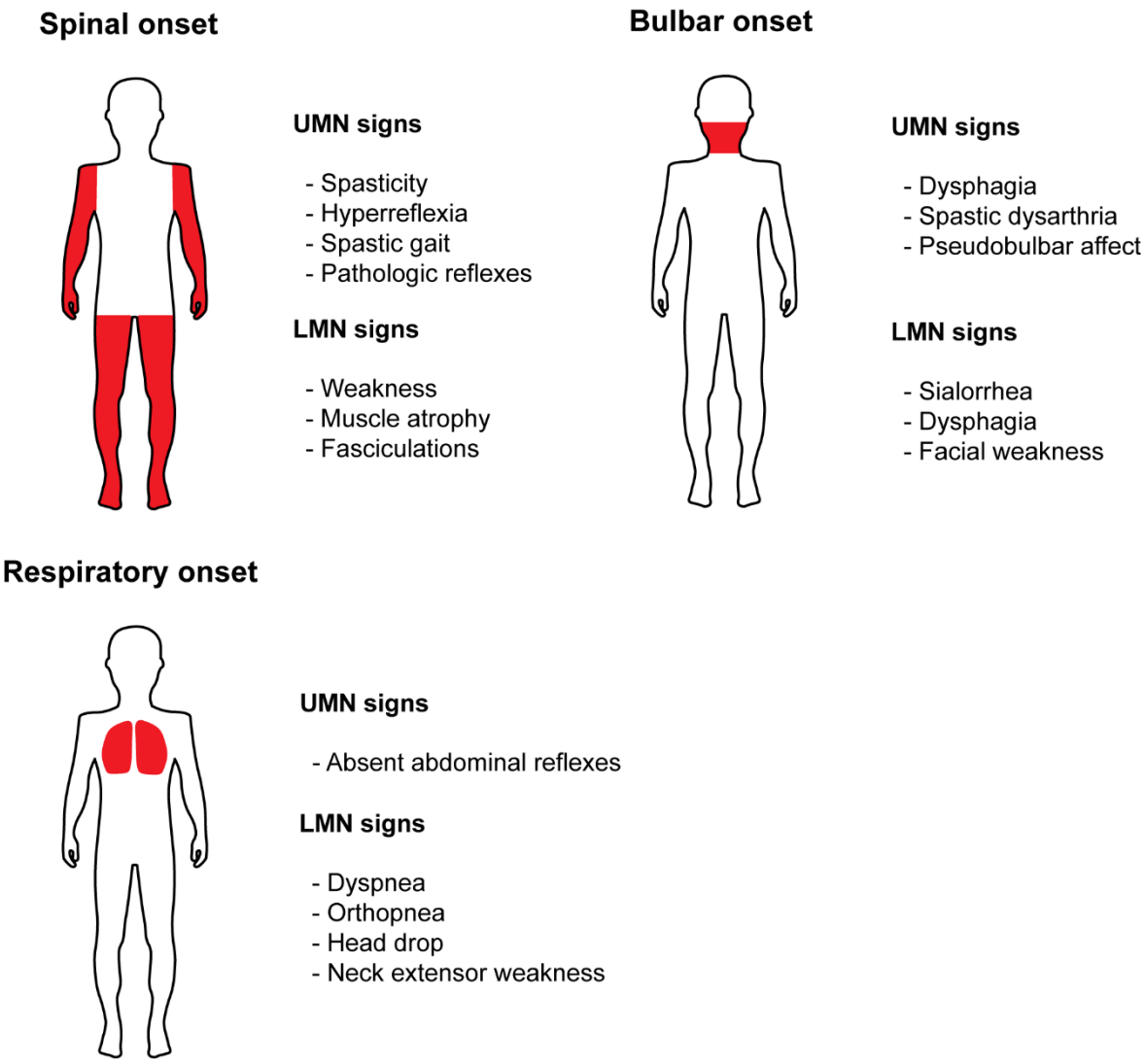

Figure 1.2 Illustrations showing the different onset types of ALS (spinal, bulbar and respiratory) and their associated upper and lower motor neuron signs. Adapted from Ferguson *et al.*, 2007; Swinnen *et al.*, 2014**.**

1.2.1.2.1 Restriction phenotypes of ALS

While ALS is only diagnosed if there is involvement of both UMNs and LMNs, there are several conditions for which degeneration of motor neurons is restricted to either the UMNs or LMNs (Swinnen and Robberecht, 2014). These syndromes are thought of as existing on a spectrum with ALS and most patients eventually developing classical ALS.

Progressive muscular atrophy (PMA) is an adult onset disease which affects LMNs (Swinnen and Robberecht, 2014). It is clinically discrete from adult-onset spinal muscular atrophy (SMA) (see Table 1.1) as it is most commonly asymmetric and may affect limbs distally and/or proximally. Additionally, its progression is markedly faster than adult-onset SMA. Evidence that it occurs in a pathological spectrum with ALS arises from the fact that UMN signs eventually present in up to 50 % of patients and these ultimately develop ALS (Wijesekera and Leigh, 2009; Rowland, 2010). This is compounded by the fact that in post-mortem analysis of PMA patients there is often pathology within the lateral corticospinal tract including the characteristic ubiquitin inclusions associated with ALS (Ince et al., 2003).

Flail arm syndrome reflects the fact that in some patients, the involvement of LMNs is restricted to the upper limbs for a minimum of a year (Swinnen and Robberecht, 2014). Typically, the muscle atrophy is symmetrical and localised to the proximal upper limb resulting in the limb hanging flaccidly and sometimes becoming non-functional (Wijesekera and Leigh, 2009). Invariably, all patients progress to develop the classic presentation of ALS including involvement of UMN signs (Swinnen and Robberecht, 2014). This syndrome is also known as Vulpian-Bernhardt syndrome, hanging arm syndrome, neurogenic man-in-a-barrel syndrome and brachial amyotrophic diplegia (Wijesekera et al., 2009). This is a rare condition but is significantly more common in men (400:1, male to female ratio) and has a better prognosis than classical ALS (Chio et al., 2011).

Conversely, flail leg syndrome is defined by the weakening of the distal lower limbs arising in a symmetrical manner (Wijesekera et al., 2009). This is due to the degeneration of LMNs in the lower limbs (Swinnen and Robberecht, 2014). Like flail arm syndrome, patients with flail leg syndrome eventually display signs of UMN and bulbar involvement but progression is very slow.

Primary lateral sclerosis (PLS) is defined as a progressive degenerative syndrome affecting only the UMNs for at least 4 years (Wijesekera and Leigh, 2009; Gordon et al., 2006). However, there is evidence that patients eventually develop LMN involvement, a progression also observed in a review of PLS autopsies (Gordon et al., 2006; D'amico et al., 2013).

1.2.1.3 Treatment of ALS

There is currently no treatment which cures ALS (Blasco et al., 2016). The heterogeneous nature of the disease and the lack of a precise aetiology has complicated the development of pharmaceutical drugs for treatment (Petrov et al., 2017). For 22 years, the only FDA (United States Food and Drug Administration) approved drug was riluzole which only modestly increases patient survival by 2-3 months. Originally thought to target the glutamate excitotoxicity present in ALS by acting on glutamate receptors, it is now thought that this is unlikely as it fails to reach the necessary concentrations in vivo to achieve this. However, it is now suggested that the effects of riluzole are via its widespread effects on neurotransmission such as its suppression of the persistent sodium current, enhancement of calcium dependent potassium currents and even reducing neurotransmitter release (Bellingham, 2011). In the time since riluzole's approval by the FDA in 1995, over 60 drugs have been researched as potential pharmacological therapies for ALS, see Table 1.2 for summary of those which underwent human clinical trials (Petrov et al., 2017). Finally, this year a new drug, Endaravone, was approved for use by the FDA, having already been approved in Japan and South Korea in 2015 (Martinez et al., 2017). Endaravone targets oxidative stress present in ALS by acting as a free radical scavenger. Additionally, in a recent phase 3 clinical trial masitinib slowed the progression of ALS when given as an add-on to riluzole in comparison to a placebo control group (Petrov et al., 2017). Masitinib is a tyrosine kinase inhibitor which is thought to benefit patients by controlling neuroinflammation.

Table 1.2

Type	Compound	Clinical trial phase/s reached	Outcome
Anti-glutamatergic	Ceftriaxone	1-3	Failure
	Memantine	2-3	Failure
	Riluzole	3	Mixed
	Talampanel	2	Failure
Anti-inflammatory	Celecoxib	2-3	Failure
	Erythropoietin	2-3	Failure
	Glatiramer acetate	2-3	Failure
	Minocylcine	1-3	Failure
	NP001	1-2	Failure
	Pioglitazone	2	Failure
	Valproic acid	3	Failure
Anti-oxidative	Coenzyme Q10	2	Failure
	Creatine	2-3	Failure
	Edaravone	2-3	Mixed
Neuroprotective	Dexpramipexole	2-3	Failure
	Olesoxime	2-3	Failure
	TCH346	2-3	Failure
	Xaliproden	2-3	Failure
Neurotrophic factors	BDNF	1-3	Failure
	CNTF	1-3	Failure
	IGF-1	3	Failure
Csf1r inhibition	Masitinib	2-3	Positive
Other	Lithium	2-3	Failure
	Tirasemtiv	2	Failure

Figure 1.2 Table summarising the drugs which have undergone human ALS clinical trials. Adapted from Petrov et al. 2017**.**

1.2.1.4 Genetics of ALS

ALS is primarily a sporadic disease (sporadic ALS; sALS), but approximately 10 % of cases are familial (familial ALS; fALS) and these cases have been associated with a plethora of genes (Renton et al., 2014). In fact, the genes responsible for approximately 70 % of fALS cases are currently known (Martin et al., 2017). fALS is mostly inherited in an autosomal dominant manner, but can also occur in a autosomal recessive or X-linked fashion (Chen et al., 2013; Taylor et al., 2016).

It is important that the distinction between sALS and fALS be understood. Often, sALS is incorrectly thought of as incidences of the disease without a genetic underpinning, when it should only infer a lack of familial history of the condition (Taylor et al., 2016). An increasing number of the genetic variants causing fALS are also found in sALS cases (Taylor et al., 2016). In support of this, studies reveal that the heritability of sALS is approximately 60 % (Al-Chalabi et al., 2010; Wingo et al., 2011). For example, approximately 7 % of sALS cases in white patients from Europe, the USA, Middle East and Australia are caused by the *chromosome 9 open reading frame 72* gene (*C9orf72)* repeat expansion (Majounie et al., 2012). Table 1.3 outlines the main genes implicated in ALS and lists their current contribution to both sALS and fALS. For a complete list please see ALSoD database (http://alsod.iop.kcl.ac.uk/index.aspx; (Abel et al., 2013)).

This thesis will elaborate on *SOD1*, *TARDBP*, *FUS* and *C9orf72* as these account for 60-80 % of fALS cases (Zufiría et al., 2016). In addition, focus will also be given to *PRPH* due to its relevance in this research.

Table 1.3

Gene	Protein	Location	Heredity	fALS explained	sALS explained
SOD1	Superoxide dismutase 1, soluble	21q22.11	AD/AR	12 %	1.5 %
ALS2/Alsin	Alsin	2q33.2	AR	<1 %	<1 %
ALS3	Unknown	18q21	AD	Unknown	Unknown
SETX	Senataxin	9q34.13	AD	<1 %	<1 %
SPG11	Spastic paraplegia 11	15q14	AR	<1 %	<1 %
FUS	Fused in sarcoma (FUS)	16p11.2	AD/AR	4 %	<1 %
ALS7	Unknown	20p13	AD/AR	Unknown	Unknown
VAPB	VAMP (Vesicle-associated membrane protein) associated protein B and C	20q13.33	AD	<1 %	<1 %
ANG	Angiogenin	14q11.1	AD	<1 %	<1 %
TARDBP	TAR DNA binding protein 43 (TDP-43)	1p36.22	AD	4 %	1%
FIG4	FIG4 phosphoinositide 5-phosphatase	6q21	AD/AR	<1 %	<1 %
OPTN	Optineurin	10p13	AD/AR	<1 %	<1 %
ATXN2	Ataxin 2	12q24.1	AD	<1 %	<1 %
VCP	Valosin containing protein	9p13.3	AD	1 %	1 %
UBQLN2	Ubiquilin 2	Xp11.21	XD	<1 %	<1 %
SIGMAR1	Sigma nonopioid intracellular receptor 1	9p13.3	AR	<1 %	<1 %
CHMP2B	Charged multivesicular body protein 2B	3p11.2	AD	<1 %	<1 %
PFN1	Profilin 1	17p13.3	AD	<1 %	<1 %
ERBB4	erb-b2 receptor tyrosine kinase 4	2q33.3-q34	AD	Unknown	Unknown
HNRNPA1	Heterogeneous nuclear ribonucleoprotein A1	12q13.1	AD	<1 %	<1 %
MATR3	Matrin 3	5q31.2	AD	<1 %	<1 %
C9orf72	Unknown	9p21.2	AD	40 %	7 %
CHCHD10	Coiled-coil-helix-coiled-coil-helix domain containing 10	22q11.23	AD	<1 %	<1 %
UNC13A	unc-13 homolog A (C. elegans)	19p13.11	Unknown	Unknown	Unknown

Gene	Protein	Location	Heredity	fALS explained	sALS explained
DAO	D-amino-acid oxidase	12q24	AD	<1%	<1%
DCTN1	Dynactin subunit 1	2p13	AD	<1%	<1%
NEFH	Neurofilament, heavy polypeptide	22q12.2	AD	<1%	<1%
PRPH	Peripherin	12q13.12	AD	<1%	<1%
SQSTM1	Sequestosome 1	5q35	AD	1%	<1%
TAF15	TATA-box binding protein associated factor 15	17q12	AR/AD	<1%	<1%
SPAST	Spastin	2p24-p21	AD	<1%	<1%
ELP3	Elongator acetyltransferase complex subunit 3	8p21.1	Allelic	<1%	<1%
LMNB1	Lamin B1	5q23.2	Unknown	Unknown	Unknown
GLE1	GLE1 RNA export mediator	9q34.11	AD	<1%	<1%
SS18L1	Calcium-responsive transactivator	20q13.33	AD	<1%	<1%
GRN	Granulin precursor	17q21.31	AD	<1%	<1%
EWSR1	EWS RNA binding protein 1	22q12.2	AD	<1%	<1%
HNRNPA2B1	Heterogeneous nuclear Ribonucleoprotein A2/B1	7p15.2	AD	<1%	<1%
TBK1	TANK binding kinase 1	12q14.1	AD	Unknown	Unknown
TUBA4A	Tubulin alpha 4a	2q35	AD	1%	<1%
CCNF	Cyclin F	16p13.3	Unknown	Unknown	Unknown
NEK1	NIMA related kinase 1	4q33	Unknown	Unknown	Unknown

Table 1.3 Table showing the principal genetic contributors to sALS and fALS. AD = autosomal dominant, AR = autosomal recessive, XR = X-linked. Adapted from Cirulli et al. 2015 with further information from White & Sreedharan 2016; Zufiría et al. 2016; Chen et al. 2013; Marangi & Traynor 2015.

1.2.1.4.1 Cu/Zn Superoxide dismutase 1 (SOD1)

Linkage analysis provided a significant milestone in the understanding of the genetic basis of ALS, allowing the first disease locus (ALS1) to be identified on chromosome 21 (Siddique et al., 1991). Subsequent, work showed this gene to be *SOD1* and identified 11 missense mutations in 13 fALS families (Rosen et al., 1993). Since this seminal discovery, over 180 mutations in *SOD1* have been reported in ALS (see ALSoD database; http://alsod.iop.kcl.ac.uk/index.aspx; (Abel et al., 2013)).

SOD1 mutations are now known to be one of the major causes of ALS and account for 12 % of fALS cases and 1.5 % of sALS cases (Cirulli et al., 2015). As is most common in ALS, most *SOD1* mutations responsible for fALS are inherited predominantly in an autosomal dominant manner with a high penetrance (Marangi and Traynor, 2015). However, it is not clear how many of the reported *SOD1* variants are pathogenic, as experimental evidence showing their pathogenicity is only available for some (Marangi and Traynor, 2015). Additionally, there is a poor correlation between the clinical phenotype and individual mutations (Picher-Martel et al., 2016). Moreover, patient phenotype is often inconsistent between affected members of the same family.

1.2.1.4.1.2 Structure and function of SOD1

Reactive oxygen species (ROS) are an inevitable product of normal cellular metabolism, such as in mitochondrial respiration (Che et al., 2016). ROS are crucial modulators of several cellular processes including signal transduction and stress responses. However, high levels of ROS lead to oxidative stress and cell toxicity through their interaction with several organic molecules such as proteins, lipids and DNA (Che et al., 2016; Valko et al., 2007). Therefore, the cellular homeostasis of ROS is established by balancing the ROS production with the activity of the antioxidant system (Che et al., 2016). In aerobic organisms, the principal line of protection against damage by oxygen radicals is performed by the SOD family of enzymes. This enzymatic function of SOD enzymes was originally discovered in 1969 (McCord and Fridovich, 1969). It is now known that mammals have three distinct SOD enzymes and all perform the key function of catalysing the disproportionation of superoxide (O_2^-) into oxygen (O_2) and hydrogen peroxide (H_2O_2) (Che et al., 2016; Rakhit and Chakrabartty, 2006). The hydrogen peroxide

is subsequently further converted to water in a reaction which is catalysed by both catalase and peroxiredoxin (Che et al., 2016).

Two SOD enzymes have Copper and Zinc as cofactors (SOD1 and SOD3) and the third uses manganese as a cofactor (SOD2). SOD2 is localised within the mitochondria, while SOD3 is only found extracellularly (Mondola et al., 2016). Conversely, SOD1 is primarily a cytosolic enzyme but there is evidence that it is also present in the nucleus, within in the mitochondrial intermembrane space, lysosomes and within the lumen of the endoplasmic reticulum (ER) and Golgi (Tsang et al., 2014; Sturtz et al., 2001; Crapo et al., 1992; Urushitani et al., 2008). Additionally, there is evidence from cell lines that SOD1 is secreted through the ER-Golgi network (Mondola et al., 2003; Turner, 2005).

SOD1 is made up of 153 amino acids and is encoded by a relatively small gene comprised of 5 exons interspaced with 4 introns (Kaur et al., 2016). It is ubiquitously expressed and forms about 0.5 % of the total protein content of the human brain and 1-2 % of the protein content of the entire CNS (Andersen, 2006; Pardo et al., 1995). SOD1 is an approximately 32 kDa homodimer with each monomer (15.8 kDa) consisting of an 8 stranded Greek-key β-barrel and several loops, including an electrostatic loop and a metal binding loop, as shown in Figure 1.3 (Shaw and Valentine, 2007). Importantly, each monomer can form an intramolecular disulphide bridge between cysteine 146 and cysteine 57. The homodimer is held together by strong hydrophobic interactions which make SOD1 a very stable protein (Rakhit and Chakrabartty, 2006).

Recent research suggests that SOD1 may have functions in other processes within the cell outside of its role in ROS homeostasis. These roles include its function as a transcription factor in the nucleus, acting as an RNA binding protein and as a signal modulator in glucose metabolism (Chung, 2017).

Figure 1.3

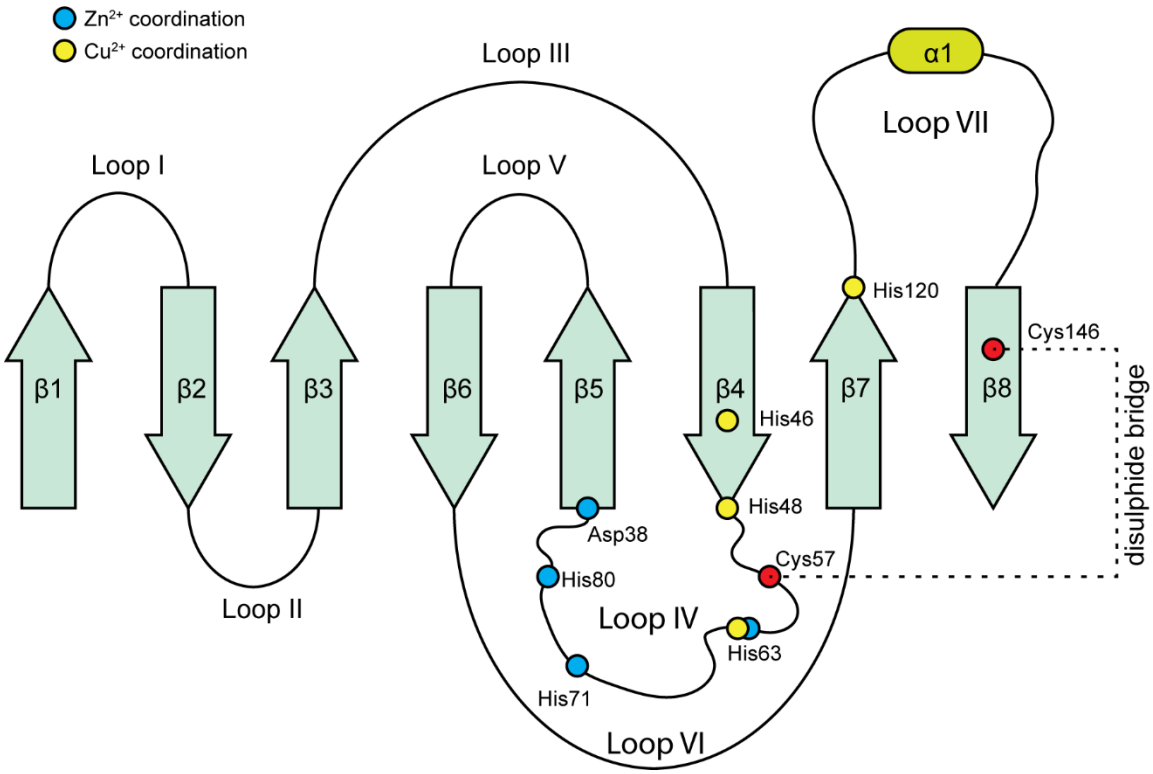

Figure 1.3 Schematic representing the structure of SOD1. This diagram shows the 8 β-sheets, the alpha helix (α1 shown in green) and the loops, which make up a SOD1 monomer. Additionally, residues which are important for the binding of Cu^{2+} and Zn^{2+} are shown in yellow and blue dots respectively. Red dots represent the residues which form the disulphide bridge in the tertiary structure of SOD1. Adapted from Tafuri et al. 2015.

1.2.1.4.1.3 SOD1 in ALS

It could be hypothesised that *SOD1* mutations are pathogenic as they may cause a loss of dismutase function. However, it has become apparent that this is unlikely as most mutant SOD1 proteins have been shown not to exhibit decreased enzymatic activity (Borchelt et al., 1994; Mondola et al., 2016). Additionally, the knockout of wild-type SOD1 does not cause ALS-like phenotypes in mice (Reaume et al., 1996). Therefore, it is now thought that SOD1 mutations cause a toxic gain of function leading to pathology (Dion et al., 2009).

A feature of SOD1 related ALS are TDP-43 negative, SOD1 positive proteinaceous inclusions (Kato et al., 2000; Mackenzie et al., 2007; Maekawa et al., 2009). These SOD1 positive aggregates are also a feature of many SOD1 mouse models (Wood et al., 2003). Therefore, it has been suggested that mutations in the SOD1 protein interfere with its tertiary structure increasing the protein's propensity to aggregate and form these potentially pathogenic inclusions (Sangwan and Eisenberg, 2016).

1.2.1.4.1.4 SOD1 mouse models

The discovery of *SOD1* as a causative gene in ALS allowed for the generation of the first mouse model of the disease. This was achieved in 1994, with the generation of transgenic mice harbouring either a wild-type human transgene or mutant transgene producing SOD1 with either a glycine to alanine substitution at position 93 (G93A) or an alanine to valine substitution at position 4 (A4V) (Gurney et al., 1994). However, only the G93A mouse line developed motor neuron disease like symptoms at 3 to 4 months. Specifically, these mice showed motor deficits at 80-90 days of age when tested on a rotarod or using a hangwire test (Picher-Martel et al., 2016). Furthermore, they developed motor neuron degeneration, muscle weakness, hind limb paralysis and died at 130 days. Subsequently, numerous SOD1 mouse models have been generated and they show variable phenotypes with differences in age of onset and survival (see Table 1.4 for summary of SOD1 mouse models reviewed in Picher-Martel et al. 2016; McGoldrick et al. 2013. The variation seen between SOD1 mouse models is likely due to the mutations, the levels of transgenic SOD1 being expressed, gender and the genetic background used for the mouse line.

Table 1.4

Mutation	Promoter	Age at onset (weeks)	Survival (weeks)	Phenotype				Ref.
				Paralysis	Cognitive symptoms	Neuropathological findings and particularities	Gliosis	
$hSOD1^{WT}$	Human *SOD1*	58-70	Normal	N	nd	Mitochondria vacuolisation and swelling, spinocerebellar axonal degeneration, 20-30% MN loss	Y	(Jaarsma et al., 2000)
$hSOD1^{WT}$	Human *SOD1*	36	52	Y	nd	SOD1 inclusions, vacuolisation, MN loss, Glial cell aggregates	Y	(Graffmo et al., 2013; Gurney et al., 1994; Epstein et al., 1987)
A4V	Human *SOD1*	>85	Normal	N	N	nd	N	(Deng et al., 2006)
$A4V/SOD1^{WT}$	Human *SOD1*	35	48	Y	nd	SOD1 inclusions, MN degeneration	Y	(Deng et al., 2006; Gurney et al., 1994; Epstein et al., 1987)
G37R	Human *SOD1*	15-17	25-29	Y	Learning deficit	MBV, LMN first affected, raised somatosensory thresholds	Y	(Wong et al., 1995; Filali et al., 2011)

Mutation	Promoter	Age at onset (weeks)	Survival (weeks)	Phenotype				Ref.
				Paralysis	Cognitive symptoms	Neuropathological findings and particularities	Gliosis	
H46R	Human *SOD1*	20	24	Y	nd	LBHI, ubiquitin, SOD1 inclusions	Y	(Chang-Hong et al., 2005)
H46R/H48Q	Human *SOD1*	17-26	nd	Y	nd	HI, ubiquitin	nd	(Wang et al., 2002)
H46R/H48Q/H63G/H120G	Human *SOD1*	35-52	nd	Y	nd	Fibrillary SOD1-ubiquitin inclusions	Y	(Wang et al., 2003)
D83G[a]	Mouse *Sod1*	15	70-84	N	nd	Sensory deficit, tremors, 20% LMN and UMN loss	Y	(Joyce et al., 2014)
L84V	Human *SOD1*	21-26	26-30	Y	nd	nd	nd	(Tobisawa et al., 2003)
G85R	Human *SOD1*	35-43	37-45	Y	nd	Rapid progression, SOD1-ubiquitin inclusions in neurons and astrocytes	Y	(Bruijn et al., 1997)
G85R/SOD1^{WT}	Human *SOD1*	16-21	23-30	Y	nd	SOD1 aggregates	Y	(Wang et al., 2009; Gurney et al., 1994; Epstein et al., 1987)
G86R[b]	Mouse *Sod1*	13-17	17	Y	nd	Rapid progression (5 days)	nd	(Ripps et al., 1995)

Mutation	Promoter	Age at onset (weeks)	Survival (weeks)	Phenotype				Ref.
				Paralysis	Cognitive symptoms	Neuropathological findings and particularities	Gliosis	
D90A	Human *SOD1*	52	61	Y	nd	Distended bladder, SOD1 inclusions, MN loss	Y	(Jonsson et al., 2006)
G93A	Human *SOD1*	13-17	17-26	Y	Y	MN loss, SOD1 aggregates, NMJ loss before onset	Y	(Gurney et al., 1994; Quarta et al., 2015)
G93A/SOD1^{WT}	Human *SOD1*	20-23	25-30	Y	nd	Vacoules, MN loss	Y	(Jaarsma et al., 2000; Gurney et al., 1994; Epstein et al., 1987)
Thy1.2-G93A^{C}	Thy1.2	54->104	62->104	N	nd	SOD1 aggregates	Y	(Jaarsma et al., 2008)
L126Z	Human *SOD1*	28-44	47	Y	nd	Eosinophilic inclusion, MN loss, ubiquitin inclusions	Y	(Wang et al., 2005; Deng et al., 2006; Karch and Borchelt, 2010)
G127X	Human *SOD1*	35	36	Y	nd	Rapid disease course, SOD1-ubiquitin inclusions	Y	(Jonsson et al., 2004)

Mutation	Promoter	Age at onset (weeks)	Survival (weeks)	Phenotype				Ref.
				Paralysis	Cognitive symptoms	Neuropathological findings and particularities	Gliosis	
G93A^{dl}	Human *SOD1*	24-26	40-50	Y	nd	Lower level of transgene expression, SOD1 aggregates, loss of MN	nd	(Acevedo-Arozena et al., 2011)
T116X	Human *SOD1*	41	43	Y (If crossed with hSOD1^{WT})	nd	Only homozygous mice develop ALS-like phenotype	nd	(Han-Xiang et al., 2008)
L126delTT	Human *SOD1*	17	18	Y	nd	ALS-like symptoms e.g. weakness, muscle atrophy, loss of MN	Y	(Watanabe et al., 2005)

Table 1.4 Table summarising the mouse models of SOD1. Y = yes, N = no, nd = not described, a = homozygous SOD1$^{D83G/D83G}$, b = Mouse *Sod1* mutation, c = homozygous SOD1^{G93A} Thy1.2 promoter, LBHI = lewy-body-like hyaline inclusion, HI = hyaline inclusion, MN = motor neuron, NMJ = neuromuscular junction. Adapted from Picher-Martel et al., 2016 with extra information from Joyce et al. 2011.

1.2.1.4.1.5 SOD1 and the dynein molecular motor

It has been reported that dynein exhibits an interaction with mutant SOD1 (A4V, G85R and G93A) but not with wild type SOD1 (Zhang et al., 2007). Additionally, dynein was found to localise with SOD1 to protein aggregates within spinal motor neurons of G93A and G85R mice. Importantly, the level of dynein co-localisation with SOD1 at protein aggregates correlated with the amount of aggregates present in different SOD1 mutants (Ström et al., 2008). This implies that dynein may contribute to the formation of these aggregates in SOD1 related ALS. In support of this, the disruption of the dynein complex by the overexpression of p50 resulted in the abolition of SOD1 mutant aggregates in cultured cells (Ström et al., 2008). Interestingly, co-localisation of kinesin with SOD1 mutant aggregates was not observed (Shi et al., 2010). Additionally, only dynein mediated retrograde transport appeared to be affected in a sciatic nerve ligation assay in SOD1 G93A mutant mice.

Unexpectedly, it has been shown that crossing SOD1 G93A mice with mice harbouring a heterozygous *dynein 1 heavy chain 1* (*Dync1h1*) mutation (*Loa; Legs at odd angles* mice) results in an increase in life span and a delayed onset of disease (Kieran et al., 2005). There was also a marked increase in muscle function in the offspring of these mice in comparison to SOD1 G93A mice. Surprisingly, this was attributed to a measurable rescue of impaired axonal transport. It was hypothesised that the *Loa* mutation restored balance between retrograde and anterograde transport. This was also observed in a subsequent study in which SOD1 G93A mice were crossed with mice carrying another dynein mutation (*Cra1*; *Cramping*) (Teuchert et al., 2006). However, later studies suggested that the *Loa* mutation was beneficial in SOD1 mutant mice due to its ability to reduce the accumulation of mutant SOD1 in mitochondria which normally causes mitochondrial dysfunction (El-Kadi et al., 2010).

Furthermore, in spinal motor neurons of SOD1 G93A mice there is a lysosomal impairment at an early asymptomatic stage which was found to be caused by a reduction in late endosomal transport which is mediated by dynein (Xie et al., 2015). This was attributed to the competitive binding of SOD1 G93A to the intermediate chain of dynein.

1.2.1.4.2 TAR DNA binding protein 43 (TDP-43)

A significant milestone in ALS research was the identification of TDP-43 as the major constituent of ubiquitinated inclusions which are a hallmark of the disease (Neumann et al., 2006; Arai et al., 2006). This implicated TDP-43 as a pivotal protein in the aetiology of ALS as this pathology is present in over 95 % of sALS patients (Ling et al., 2013). The central role of TDP-43 in ALS pathogenesis was further substantiated by the identification of missense mutations within the gene encoding TDP-43 (*TARDBP*) which caused autosomal dominant ALS (Kabashi et al., 2008; Sreedharan et al., 2008). Mutations in *TARDBP* are now known to account for 4 % of fALS cases and 1 % of sALS cases with at least 52 missense mutations, 1 truncation and 1 insertion deletion (Cirulli et al., 2015; Buratti, 2015).

1.2.1.4.2.1 Structure and function of TDP-43

TARDBP consists of 6 exons, 5 of which encode TDP-43, which is a highly conserved and ubiquitously expressed RNA binding protein of 414 amino acids (43kDa) (Ayala et al., 2005; Buratti and Baralle, 2008; Wang et al., 2004). It was originally identified as the regulatory factor capable of binding to the TAR element of the human immunodeficiency virus type 1 (HIV-1) (Ou et al., 1995). TDP-43 can shuttle between the nuclear and cytoplasmic compartments but is predominantly localised within the nucleus (Winton et al., 2008; Ayala et al., 2008).

TDP-43 shares a high degree of structural homology with the heterogeneous ribonucleoprotein (hnRNP) group of proteins, indicating that it could belong to the same family (Ou et al., 1995; Buratti and Baralle, 2001; Ayala et al., 2005). TDP-43 is made up of 5 functional domains; two RNA recognition motifs (RRM1 and RRM2), a nuclear export signal (NES), a nuclear localisation signal (NLS) and a C-terminal glycine rich domain, as shown in Figure 1.4 (Buratti and Baralle, 2001; Kuo et al., 2009; Warraich et al., 2010; Ayala et al., 2008; Winton et al., 2008). Each RRM contains an octameric ribonucleoprotein 1 (RNP1) and a hexameric ribonucleoprotein 2 (RNP2) segment which are important for RNA binding. These segments exhibit a particularly high level of conservation between species (Buratti and Baralle, 2001). Specifically, they confer TDP-43's ability to preferentially bind to long UG repeats with a minimum length of 6 bp (Kuo et al., 2009; Buratti and Baralle, 2001). Conversely, both the N-terminus and C-terminus are important in mediating protein-protein interactions (Ratti and Buratti, 2016).

Figure 1.4

(a)

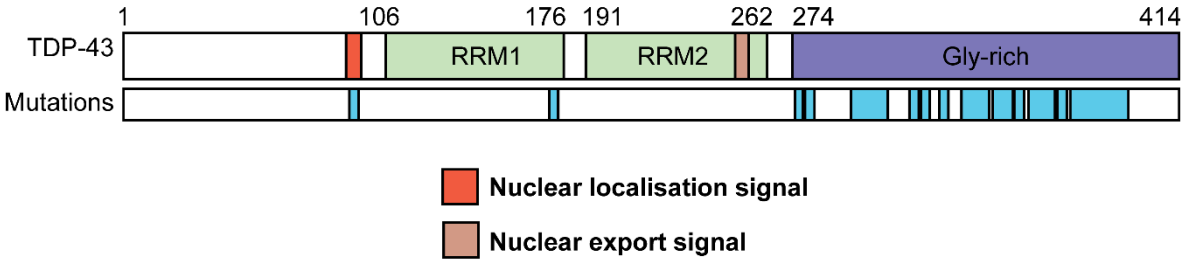

(b)

Mutations			
A90V	G298S	N345K	G376D
D169G	M311V	G348C/V/R	N378D/S
K263E	A315T/E	N352S/T	S379P/C
N267S	A321V/G	G357S/R	A382P/T
G287S	Q331K	M359V	I383T/V
G290A/V	S332N	R361S/T	G384R
S292N	G335D	P363A	W385G
G294A/V	M337V	G368S	N390D/S
G295R/S/C	Q343R	Y374X	S393L

Figure 1.4 (a) Diagram of TDP-43 protein structure showing the nuclear localisation signal, RNA recognition motif 1 (RRM1), RNA recognition motif 2 (RRM2), nuclear export signal and the Glycine rich domain. The sites affected by mutations are also shown. **(b)** List of all known *TARDBP* missense mutations which alter the amino acid sequence. Adapted from Kapeli et al. 2017; Harrison & Shorter 2017.

1.2.1.4.2.1.1 TDP-43 and transcription

As previously noted, TDP-43 acts as transcriptional repressor for HIV-1 (Ou et al., 1995). Other examples of its ability to act in transcription include its ability to bind to the acrosomal vesicle protein 1 (acrv1) promoter to repress the expression of acrv1 in spermatocytes (Lalmansingh et al., 2011). Additionally, TDP-43 was shown to be a putative regulatory factor in the expression of serine protease 10 (SP-10) by interacting with TG repeats on the complementary strand of the SP-10 promoter (Acharya et al., 2006; Abhyankar et al., 2007). Further supporting a role of TDP-43 in transcription was the analysis of TDP-43 localisation within the nucleus of rat neurons (Casafont et al., 2009). TDP-43 was found concentrated in perichromatin fibrils which are known active sites of transcription and was absent from transcriptionally silent regions. Furthermore, TDP-43 co-purified with transcriptional regulators including TATA-Box binding protein associated factor 15 (TAF15), which is also associated with ALS (Ling et al., 2010).

1.2.1.4.2.1.2 TDP-43 and regulation of splicing

The first indication that TDP-43 was involved in the splicing of pre-mRNA arose in 2001. TDP-43 was shown to act as splicing regulator by binding to UG repeats proximal to the 3' splice site of exon 9 of the cystic fibrosis transmembrane conductance regulator (*CFTR*) transcript and causing the skipping of this exon and thus the production of a non-functional CFTR protein (Buratti et al., 2001; Buratti and Baralle, 2001). Important for this function of TDP-43 is its association with heterogeneous nuclear ribonucleoprotein A/B (Buratti et al., 2005). Further associations between TDP-43 and proteins which are part of the splicing machinery have also be observed (Freibaum and Chitta, 2010). Subsequently, high-throughput approaches were used to try and identify further target transcripts for TDP-43 (Tollervey et al., 2011; Xiao et al., 2011; Polymenidou et al., 2011; Sephton et al., 2010). For example, the use of cross-linking and immunoprecipitation in conjunction with high-throughput sequencing showed that TDP-43 binds to more than 6000 brain RNA targets which constitutes approximately 30 % of the total transcriptome of the brain (Polymenidou et al., 2011). Furthermore, this study showed that the knockdown of TDP-43 using antisense oligonucleotides altered the splicing of 965 transcripts and changed the levels of 601 mRNAs. Additionally, it was shown that binding of TDP-43 both near

exon-intron junctions and at some distance from the closest exon could influence the selection of splice sites. Interestingly, one of the targets identified in this report was TDP-43's own transcript where it was seen to enhance splicing of an intron via its interaction to its 3' UTR and in doing so triggering nonsense-mediated decay to reduce its levels. However, subsequently it was revealed that this was not the primary method of TDP-43 autoregulation and only true for a specific isoform. Instead, it was shown that TDP-43 binds to a TDP binding region (TDPBR) which initiates a complex interplay between transcription, splicing and 3' end processing which ultimately results in decreased TDP-43 levels (Eréndira Avendaño-Vázquez et al., 2012; Ayala et al., 2011). Furthermore, caution should be taken when interpreting the results from such studies as the high-throughput method can mask changes caused by secondary effects of TDP-43 loss (Buratti et al., 2013). However, other targets of TDP-43 have been experimentally verified as reviewed in Ratti & Buratti 2016. Finally, TDP-43 has also been implicated in the suppression of non-conserved cryptic exons which typically result in frameshifts or premature stop codons and subsequent degradation of transcripts via nonsense-mediated decay (Tan et al., 2016; Ling et al., 2015).

1.2.1.4.2.1.3 TDP-43 regulates miRNA biogenesis

MicroRNAs (miRNAs) are non-coding RNAs responsible for post-transcriptional regulation of a large proportion of the transcriptome (Hawley et al., 2017; Rinchetti et al., 2017). TDP-43 has been implicated in the regulation of miRNA biogenesis due to its association with both Drosha and Dicer complexes through its C-terminal region (Gregory et al., 2004; Kawahara and Mieda-Sato, 2012). Significantly, TDP-43 was later shown to be able to regulate the stability of Drosha in vitro and thus possibly have a wide-ranging impact on the production of miRNAs (Di Carlo et al., 2013). Similarly, TDP-43 was also shown to regulate Dicer mRNA and protein levels in the human neuronal SK-N-BE cell line, again suggesting it has a far reaching impact on miRNA biogenesis (Colombrita et al., 2015). In support of this, several miRNA species have been shown to become dysregulated in TDP-43 depletion such as let7b, miR206 and miR132 (Ratti and Buratti, 2016). Additionally, through TDP-43's direct interaction with either pri-miRNAs and pre-miRNAs, combined with its association with the Drosha and Dicer complexes, it

was able to promote their processing into mature miRNAs (Kawahara and Mieda-Sato, 2012).

1.2.1.4.2.1.4 TDP-43 and non-coding RNAs (ncRNAs)

In contrast to miRNAs which are only approximately 22 nucleotides, long non-coding RNAs (lncRNAs) are more than 200 nucleotides in length (Ederle and Dormann, 2017). However, the precise function of these lncRNAs is not yet fully elucidated, but are thought to affect cellular processes at a transcriptional and post-transcriptional level (Ratti and Buratti, 2016). For example, lncRNAs are involved in the recruitment of chromatin modifiers to sites of transcription (Batista and Chang, 2013). TDP-43 is known to interact with a wide range of lncRNAs including metastasis associated lung adenocarcinoma transcript 1 (MALAT1) which is linked with nuclear splicing speckles and nuclear enriched abundant transcript 1 (NEAT1) which is important in the formation of paraspeckles (Ederle and Dormann, 2017). In line with this, TDP-43 is also found to be enriched in paraspeckles (Nishimoto et al., 2013). However, the precise role of TDP-43 in relation to lncRNA is not yet known (Ratti and Buratti, 2016). Additionally, bioinformatic predictions have suggested that TDP-43 can also interact with certain ncRNAs (Cirillo et al., 2013).

1.2.1.4.2.1.5 TDP-43 and mRNA stability

TDP-43 was first implicated in regulating mRNA stability through its interaction with the 3' UTR of neurofilament light (NFL) mRNA and in doing so, stabilising the transcript (Strong et al., 2007). Similarly, TDP-43 also binds to and stabilises the coding region of histone deacetylase 6 (HDAC6) (Fiesel et al., 2010). Conversely, the binding of TDP-43 to the 3' UTRs of vascular endothelial growth factor a (*Vegfa*) and progranulin (*Grn*) mRNA results in reduced stability of the transcripts (Colombrita et al., 2009). Indeed, since mRNA stability is often inferred by the binding of RNA binding proteins to the 3' UTRs of mRNAs, and given the abundance of TDP-43 binding sites within this region, it is not surprising that an increasing number of transcripts are being identified has being stabilised or destabilised by TDP-43 (Ratti and Buratti, 2016).

1.2.1.4.2.1.6 TDP-43 and mRNA trafficking

The transport of mRNAs is particularly pivotal in polarized cells such as neurons for the maintenance of neuronal activity and plasticity (Ratti and Buratti, 2016). This transport of mRNAs within messenger ribonucleoprotein (mRNP) granules allows for the local translation of proteins (Ederle and Dormann, 2017). In this context, it is interesting that TDP-43 has been shown to undergo active transport along axons and exhibits co-localisation within mRNP granules with other RNA transport associated proteins such as survival motor neuron (SMN), fragile X mental retardation protein (FMRP) and Staufen 1 (Fallini et al., 2012; Wang et al., 2008). Interestingly, these TDP-43 positive mRNP granules were seen to increase in axons and dendrites following neuronal stimulation. The localisation of TDP-43 bound to RNA at presynaptic membranes of axon terminals in the neuromuscular junction of adult mice provides further evidence of a role in mRNA trafficking for TDP-43 (Narayanan et al., 2013). Subsequently, similar findings were reported in axons of iPSC-derived motor neurons, where TDP-43 mRNP granules were bidirectionally transported (Alami et al., 2014). This report also identified the NFL transcript as a transcript whose transport is mediated by TDP-43 mRNP granules.

1.2.1.4.2.1.7 TDP-43 and translation

Staufen and FMRP are both known regulators of local translation, therefore implicating TDP-43 in a similar role (Wang et al., 2008). Relevantly, this study also showed that TDP-43 acts as a translational repressor in an in vitro environment using a luciferase reporter. Additionally, TDP-43 associated with both β-actin and calcium/calmodulin-dependent protein kinase II α (CaMKIIα) mRNAs in response to depolarisation has been shown to increase local protein synthesis from these transcripts. Interestingly, proteomics have shown that TDP-43 interacts with several proteins involved in the regulation of translation and so many other instances of translational regulation by TDP-43 may yet be identified (Freibaum and Chitta, 2010). TDP-43 is also thought to play a role in the formation of stress granules, which are important for the stalling of translation in response to cellular stress (Bäumer et al., 2014).

1.2.1.4.2.2 TDP-43 in ALS

As previously mentioned, TDP-43 was identified as the major component of ubiquitinated inclusions found in most cases of ALS (Neumann et al., 2006; Arai et

al., 2006; Ling et al., 2013). In these inclusions, it is abnormally phosphorylated and present as C-terminal truncated fragments of 25 kDa and 35 kDa (Ling et al., 2013; Lee et al., 2012). Additionally, it has been shown that in ALS an alternate start codon can be used to generate a TDP-35 splice variant which causes aggregation and motor neuron death (Xiao et al., 2015b). The consequential loss of TDP-43 within the nucleus potentially results in a loss of function in relation to the roles it performs in transcription, splicing, miRNA biogenesis and its regulation of ncRNAs (Ederle and Dormann, 2017). Conversely, the aggregates of TDP-43 within the cytoplasm and mutations of TDP-43 may infer a toxic gain of function which could also contribute to the pathogenesis of disease.

In support of this, several genes have been found to be differentially spliced in the lumbar spinal cord of ALS patients and are also seen in transgenic mice which express low levels of mutant TDP-43 (Xiao et al., 2011; Yang et al., 2014; Arnold et al., 2013). Additionally, cryptic exons which are normally excluded from transcripts via TDP-43 repression are found in transcripts within ALS-FTD (frontotemporal dementia) brains (Ling et al., 2015; Tan et al., 2016). Similarly, cytoplasmic inclusions may result in the sequestering of TDP-43 which compromises TDP-43's cytosolic functions such as mRNA stability, mRNA trafficking and translation (Ederle and Dormann, 2017). Evidence shows that A315T and M337V substitutions of TDP-43 cause abnormal axonal transport of NFL mRNA (Alami et al., 2014). Mouse models also provide evidence for both a loss and gain of function mechanism of TDP-43 (Scotter et al., 2015). Conditional or partial knockout of TDP-43 results in ALS-like motor phenotype and motor neuron defects (Kraemer et al., 2010; Wu et al., 2012; Iguchi et al., 2013). Similarly, the overexpression of wild-type TDP-43 also recapitulates disease phenotypes (Wils et al., 2010).

1.2.1.4.2.3 TDP-43 mouse models

Several TDP-43 ALS mouse models have been developed since it became apparent that TDP-43 could be a pivotal protein in the diseases aetiology (Table 1.5). Since TDP-43 levels in neurons of patients are high (usually between 1.5 - 2.5 fold higher), the first mouse model attempted to replicate this observation (Picher-Martel et al., 2016). To achieve this, transgenic mice were made to overexpress human wild-type TDP-43 to similar levels using the mouse prion

promoter (mPrp) or the Thy1.2 promoter. The phenotype of these mice varied in accordance to level of TDP-43 expression. Hemizygous mice did not exhibit the age dependent motor neuron degeneration that defines ALS (Stallings et al., 2010). Furthermore, homozygous mice exhibited a rapid onset and fast deterioration which caused death within approximately 2 months but mostly failed to recapitulate motor neuron degeneration and the TDP-43 inclusions seen in ALS (Xu et al., 2010). More success was achieved using the Thy1.2 promoter, these mice also had an early onset fast progressing phenotype but did show motor neuron loss (Picher-Martel et al., 2016). An attempt to obtain more faithful models was made using the human endogenous promoter to express both wild-type and mutant (A315T and G348C) human TDP-43 at moderate levels (Swarup et al., 2011). These mice show a progressive motor phenotype (without paralysis) and showed signs of cognitive impairment. Significantly, the mutant mice also developed both nuclear and cytoplasmic inclusions positive for TDP-43 and ubiquitin. It appears that mouse models with low TDP-43 expression exhibit the motor symptoms of ALS and TDP-43 inclusions but lack paralysis, whilst high expression of TDP-43 results in a fast disease progression mostly without motor neuron loss and TDP-43 inclusions (Picher-Martel et al., 2016). Recently, a more successful TDP-43 model was generated by crossing TDP-43^{WT} and TDP-43^{Q331K} mice to generate a double transgenic which better capture the ALS phenotype (Mitchell et al., 2015). Not only did these mice exhibit substantial motor neuron loss in the anterior horn of the spinal cord but also had proteinaceous inclusions positive for TDP-43, p62 and ubiquitin. The disease progression in these mice was rapid with an early onset and the mice died by 8-10 weeks.

1.2.1.4.2.3.1 TDP-43^{F210I} mice

In addition to the transgenic TDP-43 models discussed above, *N-ethyl-N-nitrosourea* (ENU) mutagenesis has also been used to generate TDP-43 mutant mice. A product of this approach was the TDP-43^{F210I} mouse line where the amino acid substitution is on RRM2 of the TDP-43 protein (Ricketts, 2012). TDP-43^{F210I} homozygous mice exhibit embryonic lethality but survive at least until embryonic day 14.5 (E14.5). At this stage, the homozygous mice show signs of underdevelopment such as reduced organ size. Conversely, heterozygous mice develop normally when compared to wild type mice. Despite maintaining normal

nuclear localisation in these mice, TDP-43 was shown to have a lower binding affinity to UG repeats. Consequently, it was unable to rescue exon skipping in the CFTR gene in vitro and in ex vivo. It was also shown that both heterozygous and homozygous mice show altered auto-regulation of TDP-43 and splicing patterns of other transcripts.

Table 1.5

Variant	Promoter (fold expression)	Age at onset (weeks)	Survival (weeks)	Phenotype				Ref.
				Paralysis	Cognitive symptoms	Neuropathological findings and particularities	Gliosis	
hTDP-43^{WT}	mPrp (3-4)	None	Normal	N	nd	Diffuse ubiquitin staining, no NCI	Mild	(Stallings et al., 2010)
	mPrp (2.5)[a]	3	4-8	Y	nd	pTDP-43 NCI, cytosolic ubiquitination, axonal degeneration, no MN loss	Y	(Xu et al., 2010)
	mThy1.2 (3.8-5.1)	2-8	4-27	Y	nd	Rapid disease progression, rare pTDP-43 NCI, MN loss, phenotype correlates with protein level	Y	(Wils et al., 2010)
	mThy1.2 (1.3-3.6	Males: 2/Females:3	nd	nd	nd	Mitochondrial aggregation, no TDP-43 NCI, decreased axon calibre, no MN loss	nd	(Shan et al., 2010)
	mCaMKII[b] (0.4-1.7)	4	nd	nd	nd	Brain atrophy, neuron loss, mosaic expression, rare pTDP-43 NCI	Y	(Igaz et al., 2011)
	CAG	None	Normal	N	nd	No motor impairment, neuron loss in frontal cortex, no NCI	nd	(Tian et al., 2011)
	hEP (3)	42	Normal	N	Y	No TDP-43/ubiquitin NCI, motor dysfunction without paralysis	Y	(Swarup et al., 2011)
	CaMKIIα (TRE) (induced from p21)	nd	correlate with time dose of TDP-43	nd	nd	Early induction: pTDP-43, ubiquitin positive NCI, mitochondrial abnormalities.	Y	(Cannon et al., 2012)

Variant	Promoter (fold expression)	Age at onset (weeks)	Survival (weeks)	Phenotype				Ref.
				Paralysis	Cognitive symptoms	Neuropathological findings and particularities	Gliosis	
mTDP-43^{WT}	maMKII (2)[a]	8	71	N	Y	Learning/memory deficit, TDP-43ubiquitin positive NCI, progressive motor deficits	Y	(Tsai et al., 2010b)
A315T	mPrp (4)	4	10.7	Y	nd	Rare pTDP-43 NCI, no GCI, MA	Y	(Stallings et al., 2010)
	mPrp (3)	12-16	22 ± 2.7	Y	nd	Ubiquitin positive/TDP-43 negative NCI, UMN/LMN loss	Y	(Wegorzewska et al., 2009)
	hEP (3)	38	Normal	N	Y	TDP-43/ubiquitin positive NCI at 10months, peripherin inclusions, decrease axonal calibre, motor dysfunction without paralysis	Y	(Swarup et al., 2011)
	mEP (2.5)[c]	nd	nd	nd	N	TDP-43 NCI, 10 % MN loss	nd	(Stribl et al., 2014)
Q331K	mPrp (1.5)	12	Normal	N	nd	Decreased motor performance at 10 months, muscle fibrillations at EMG, No NCI	Y	(Arnold et al., 2013)
WT/Q331K	mPrP (3.3)	3	8-10	Y	nd	TDP-43/ubiquitin/p62 positive NCI, 70 % MN loss in spinal cord anterior horn	Y	(Mitchell et al., 2015)

Variant	Promoter (fold expression)	Age at onset (weeks)	Survival (weeks)	Phenotype				Ref.
				Paralysis	Cognitive symptoms	Neuropathological findings and particularities	Gliosis	
M337V	mPrp (2.7)[a]	3	4	Y	nd	Tremors, pTDP-43 NCI, cytosolic ubiquitination, no MN loss, MA	Y	(Xu et al., 2011)
	mPrp (1.5)	40	Normal	N	nd	Decreased motor performance at 10 months, no NCI	nd	(Arnold et al., 2013)
	Thy1.2 (1.7)[a]	<2	25	Y	nd	Ubiquitin/TDP-43 NCI, worse phenotype than TPD-43^{WT} mouse	Y	(Janssens et al., 2013)
	CaMKIIa(TRE): line 14A	<1	Normal	nd	nd	Neuronal cell death at P5, No TDP-43 or ubiquitin aggregates, TDP-43 framents	nd	(D'Alton et al., 2014)
	CaMKIIa(TRE) line 8A	40	Normal	nd	nd	Ubiquitin positive aggregates	nd	
G348C	hEP (3)	36	36	N	Y	TDP-43/ubiquitin positive NCI at 10 months, peripherin inclusions, decreased axonal calibre, motor dysfunction without paralysis	Y	(Swarup et al., 2011)
Knockout	HB9-Cre	13	40	nd	nd	Targeted loss of TDP-43 in spinal cords motor neurons, 60 % loss of MN and motor phenotype, accumulation of ubiquitinated proteins	Y	(Wu et al., 2012)
	Vacht-Cre	50	Normal	nd	nd	MA, motor dysfunction in homozygous KO, atrophy of MNs, neurofilament positive accumulations	Y	(Iguchi et al., 2013)

Variant	Promoter (fold expression)	Age at onset (weeks)	Survival (weeks)	Phenotype				Ref.
				Paralysis	Cognitive symptoms	Neuropathological findings and particularities	Gliosis	
TDP-43-25 (25kDa fragment)	Thy 1.2 (4.7)	24	nd	N	nd	No neurodegeneration, no TDP-43 NCI	Y	(Caccamo et al., 2012)

Table 1.5 Table summarising the mouse models of TDP-43. Y = yes, N = no, nd = not described, a = homozygotes, b = TRE induction after birth, C = knock-in mice, NCI = neuron cytoplasmic inclusion, GCI = glial cytoplasmic inclusion, KO = knockout, MA = muscle atrophy, hEP = human endogenous promoter, mEP = mouse endogenous promoter, MN = motor neuron. Adapted from Picher-Martel et al. 2016 with more information from McGoldrick et al. 2013; Philips & Rothstein 2015.

1.2.1.4.3 Fused in Sarcoma (FUS)

Two concurrent reports in 2009 reported that ALS cases linked to chromosome 16 were caused by mutations in the fused in sarcoma (*FUS*) gene (Kwiatkowski et al., 2009; Vance et al., 2009). The *FUS* gene consists of 15 exons which encode the 526 amino acid FUS protein, which is also known as translocated in liposarcoma (TLS) (Aman et al., 1996; Dormann and Haass, 2011). Mutations in *FUS* are mostly dominant and are understood to explain approximately 4 % of fALS cases and <1 % of sALS cases (Cirulli et al., 2015; Robberecht and Philips, 2013). Interestingly, FUS exhibits a significant functional overlap with TDP-43, which further implicated RNA metabolism as a central pathology in ALS (Renton et al., 2014).

1.2.1.4.3.1 Structure and function of FUS

FUS is a highly conserved, ubiquitously expressed protein belonging to the FET (**F**us, **E**WSR1 and **T**AF15) family which also includes TAF15 and Ewing RNA binding protein (EWS) (Deng et al., 2014). Structurally, FUS consists of an N-terminal transcriptional activation domain (QGSY rich region), a glycine rich region, an RRM domain (with nuclear export signal), a arginine-glycine-glycine repeat (RGG) region, a C2/C2 zinc finger motif, a second RGG region and a C-terminal proline-tyrosine (PY) nuclear localisation signal (Figure 1.5) (Guerrero et al., 2016; Svetoni et al., 2016). Interestingly, two prion-like domains were identified within the FUS protein which span the initial 126 N-terminal residues of the QGSY rich region and residues 391 to 405 of the second RGG region (Gitler and Shorter, 2011; Cushman et al., 2010). Most ALS associated FUS mutations are found within exons 12-15 of the *FUS* gene which encode for the C-terminal portion of the protein, specifically the C2/C2 zinc finger motif, the third RGG region and the nuclear localisation signal (Svetoni et al., 2016). The rest of the mutations are within exons 3 - 6 which encode the QGSY rich region and the first RGG region. Similar to TDP-43, FUS shuttles between cytoplasmic and nuclear compartments despite being a predominantly nuclear protein (Zinszner et al., 1997).

Figure 1.5

(a)

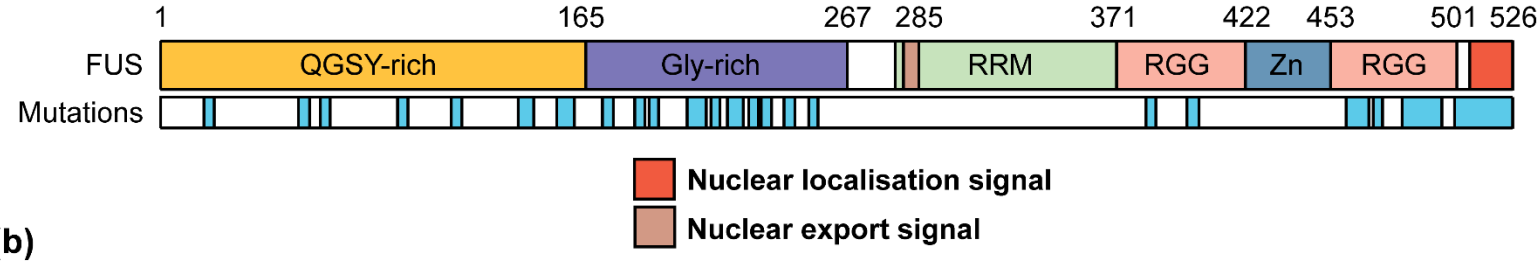

(b)

Mutations

P18S	G174-G175del	G228-G229insG	M464I	R502WfsX15	E516V
S57del	G187S	G230delG	G466VfsX14	G503WfsX12	H517D/P/Q
N63S	G191S	G230C	G472VfsX57	G504WfsX12	R518G/K/del
S96del	G206S	R234C/L	R487C	G507D	Q519X
S115N	Q210H	R244C	R491C	G509D	R521S/G/C/H/L
S142N	R216C	G245V	G492EfsX527	K510WfsX517	R522G
G144-Y149del	G222-G223insG	M254V	R495X	K510E/R	R524R/S/T/W
G156E	G223del	R383C	R495EfsX527	S513P	P525L
N159Y	G225V	G399V	R495QfsX527	R514G/S	X527YextX
G173-G174del	G226S	S462F	G497AfsX527	G515C	

Figure 1.5 (a) Diagram of FUS protein structure showing the QGSY-rich region, Glycine rich domain, RNA recognition motif, nuclear export signal, two glycine-arginine-arginine (RGG) rich domains, a Zinc finger motif (Zn) and the nuclear localisation signal. The sites affected by mutations are also shown. **(b)** List of all known *FUS* mutations which alter the amino acid sequence. Adapted from Kapeli et al. 2017; Harrison & Shorter 2017.

Originally, FUS was thought to preferentially bind to RNA sequences which harboured a GGUG motif (Lerga et al., 2001; Lagier-Tourenne et al., 2012). However, several studies failed to reproduce this finding and it is becoming increasingly clear that the secondary and tertiary structure of RNA is more important for FUS binding (Colombrita et al., 2012; Hoell et al., 2011; Ishigaki et al., 2012; Rogelj et al., 2012). Like TDP-43, FUS is implicated at multiple levels of RNA metabolism.

Several lines of evidence indicate that FUS has a role in the regulation of transcription. For example, FUS can directly bind to the C-terminal region of RNA polymerase II, and in doing so regulates the phosphorylation of serine 2 of the enzyme and in turn its activity, and FUS can also interact with its general transcription factor, transcription factor II D (TFIID) (Schwartz et al., 2012; Bertolotti et al., 1996). Additionally, FUS has a well-documented role in regulating the splicing of many transcripts as it can interact with various components of the spliceosome which are required for its assembly, including SMN, U1 small nuclear ribonucleoprotein (snRNP) and SM-snRNPs (Gerbino et al., 2013; Yamazaki et al., 2012). As with TDP-43, FUS has also been implicated in the regulation of miRNA biogenesis. It was shown to not only interact with Drosha but also recruit it to sites of active transcription to promote the processing of pri-miRNAs (Gregory et al., 2004; Morlando et al., 2012). FUS has also been shown to interact with a large proportion (30 %) of all known lnRNAs (Lagier-Tourenne et al., 2012; Lourenco et al., 2015). FUS is also involved in the translocation of mRNA for local translation in neurons. For example, in hippocampal neurons, FUS is seen localised to mRNP granules in dendrites and within axon terminals (Fujii et al., 2005; Schoen et al., 2016).

FUS has also been shown to be involved in DNA repair mechanisms following DNA damage. It is able to promote the formation of D-loops and homologous recombination in response to DNA double strand breaks (Baechtold et al., 1999). Additionally, FUS was shown to be recruited to the site of DNA damage through its interaction with Poly-ADP-ribose (PAR) polymerase (Rulten et al., 2014).

1.2.1.4.3.2 FUS in ALS

Similar to TDP-43, FUS is a component of ubiquitinated inclusions in neurons and glial cells within the motor cortex, basal ganglia and spinal cord (Nolan et al., 2016). However, it is important to note that the two proteins are mutually exclusive in relation to their presence in these inclusions, with no TDP-43 in ALS-FUS cases. Significantly, most FUS mutations are localised within the C-terminal NLS domain which may be the primary cause of FUS mislocalisation (Dormann et al., 2010). FUS related fALS is predominantly a LMN disease which typically presents at a younger age and exhibits a more severe progression. The toxicity of these aggregates is yet to be fully understood (Ratti and Buratti, 2016). However, it is thought that they may act as protein sinks which reduce the availability of active proteins in the cells.

As with TDP-43, the loss of FUS function within the nucleus has been suggested to result in altered mRNA processing (Ederle and Dormann, 2017). For example, FUS harbouring pathogenic mutations caused the relocation of snRNPs to the cytoplasm and consequently altered alternative splicing (Gerbino et al., 2013). Similarly, mice made to express FUS which mislocalises to the cytoplasm due to a lack of its NLS, showed aberrant splicing. The same phenotype was also observed in FUS knockout mice (Scekic-Zahirovic et al., 2016). Alterations in splicing were also observed in patient fibroblasts harbouring FUS mutations which cause a loss of FUS activity (Sun et al., 2015). However, FUS knockout mice do not show motor symptoms, suggesting that a loss of FUS function is not enough to cause motor neuron death (Gerbino et al., 2013). Conversely, the overexpression of wild-type FUS has been shown to cause motor symptoms in mice suggesting a toxic gain of function (Mitchell et al., 2013). Therefore, evidence exists for both loss and gain of function mechanisms in the pathogenesis of FUS.

1.2.1.4.3.3 FUS mouse models

As discussed above, *FUS* knockout mice were originally generated to investigate the role of FUS in DNA damage (Hicks et al., 2000). These mice were sterile and died within 24 hours of birth. More recently, another line of *FUS* knockout mice did generate mice which grew to adulthood (Kino et al., 2015). These mice did not show ALS-like phenotypes until almost two years but did show behavioural abnormalities including hyperactivity and a reduction in anxiety-like behaviour.

Mice overexpressing human wild-type FUS were also generated and exhibited motor neuron degeneration and consequently paralysis from 8 weeks of age. However, despite a cytoplasmic increase in FUS there were no ubiquitinated FUS inclusions (Mitchell et al., 2013). An additional mouse line was also generated using the ubiquitously expressed CAG promoter to drive FUS^{WT} or FUS^{R521G} expression. These mice lacked degeneration of both lateral spinal column and ventral horns, and did not have FUS inclusions but did show motor impairment and gliosis (Sephton et al., 2014). Table 1.6 summarises these FUS mouse models.

Table 1.6

Variant	Promoter	Age at onset (weeks)	Survival (weeks)	Phenotype				Ref.
				Paralysis	Cognitive symptoms	Neuropathological findings and particularities	Gliosis	
KO	n/a	nd	nd	nd	nd	24 h death, chromosomal abnormality, sterility	nd	(Hicks et al., 2000)
	n/a	nd	nd	nd	Y	No motor phenotypes, hyperactive behaviour	nd	(Kino et al., 2015)
$hFUS^{WT}$	mPrp	4 weeks	10-13 weeks	Y	N	Tremors, weight loss, deficit in rotarod, increased cytoplasmic FUS, spinal MN loss and NMJ loss	Y	(Mitchell et al., 2013)
$hFUS^{WT}$, $hFUS^{R521G}$	CAG	10	30	N	Y	More lethality in FUS^{wt}, no MN loss in lateral column, MA, NMJ loss, reduced social interaction and motor performance	Y	(Sephton et al., 2014)
$hFUS^{WT}$	SBT-rAAV	nd	nd	nd	nd	Normal FUS localisation in nucleus,	nd	(Verbeeck et al., 2012)
$hFUS^{R521C}$	SBT-rAAV	nd	nd	nd	nd	FUS redistributed to cytoplasm, no inclusions	nd	
$hFUS^{\Delta 14}$	SBT-rAAV	nd	nd	nd	nd	Most redistribution of FUS to nucleus, NCIs positive for FUS, ubiquitin, p62, α-internexin	nd	

Table 1.6 Table summarising the mouse models of FUS. Y = yes, N = no, nd = not described, NMJ = neuromuscular junction, MN = motor neuron, NCI = neuronal cytosolic inclusion. Adapted from Picher-Martel et al. 2016 with extra information from McGoldrick et al. 2013.

1.2.1.4.4 *C9orf72* hexanucleotide repeat expansion

Linkage analysis and genome-wide association studies indicated the existence of an important genetic locus on chromosome 9p21 for ALS, FTD and ALS-FTD (see section 1.2.1.7) (Renton et al., 2011). Subsequently, a GGGGCC $(G_4C_2)_n$ hexanucleotide repeat expansion within the non-coding region of the *chromosome 9 open reading frame 72* gene (*C9orf72)* was identified as the cause of chromosome 9p21 related ALS, FTD and ALS-FTD (Renton et al., 2011; DeJesus-Hernandez et al., 2011). This repeat expansion is now known to be the most common cause of both fALS (40% of cases) and sALS (7% of cases) (Cirulli et al., 2015).

C9orf72 is a highly-conserved gene consisting of 11 exons where the repeat expansion is within the intronic region flanked by the non-coding exons 1a and 1b, as shown in Figure 1.6 (Wen et al., 2017; Todd and Petrucelli, 2016). The pre-messenger RNA (pre-mRNA) expressed by *C9orf72* is alternatively spliced to generate 3 different transcript variants (Todd and Petrucelli, 2016). Transcript variants 1 and 3 retain exon 1a and therefore the hexanucleotide repeat is localised within the intron between 1a and 1b. On the other hand, transcript variant 2 retains exon 1b and this means the repeat is within its promoter region. The size of the repeat within healthy individuals is varied with some reported as high as 23 but most have 2 to 8 repeats (Freibaum and Taylor, 2017). Conversely, affected individuals have 30 or more G_4C_2 repeats but commonly can harbour expansions of this repeat numbering in the thousands.

1.2.1.4.4.1 Structure and function of C9orf72

Unfortunately, to date the protein encoded by the *C9orf72* gene is still poorly characterised. The aforementioned transcript variants lead to the translation of two isoforms of the protein, a 481 amino acid isoform a (from transcript variants 2 and 3) and a 222 amino acid isoform b (from transcript variant 1) (Todd and Petrucelli, 2016; Tang, 2016). Intracellularly, C9orf72 is localised in both the cytoplasmic and the nuclear compartments and is seen on some intracellular membranes (Farg et al., 2014). Additionally, there is evidence that it can be secreted into the extracellular environment (Tang, 2016).

Figure 1.6

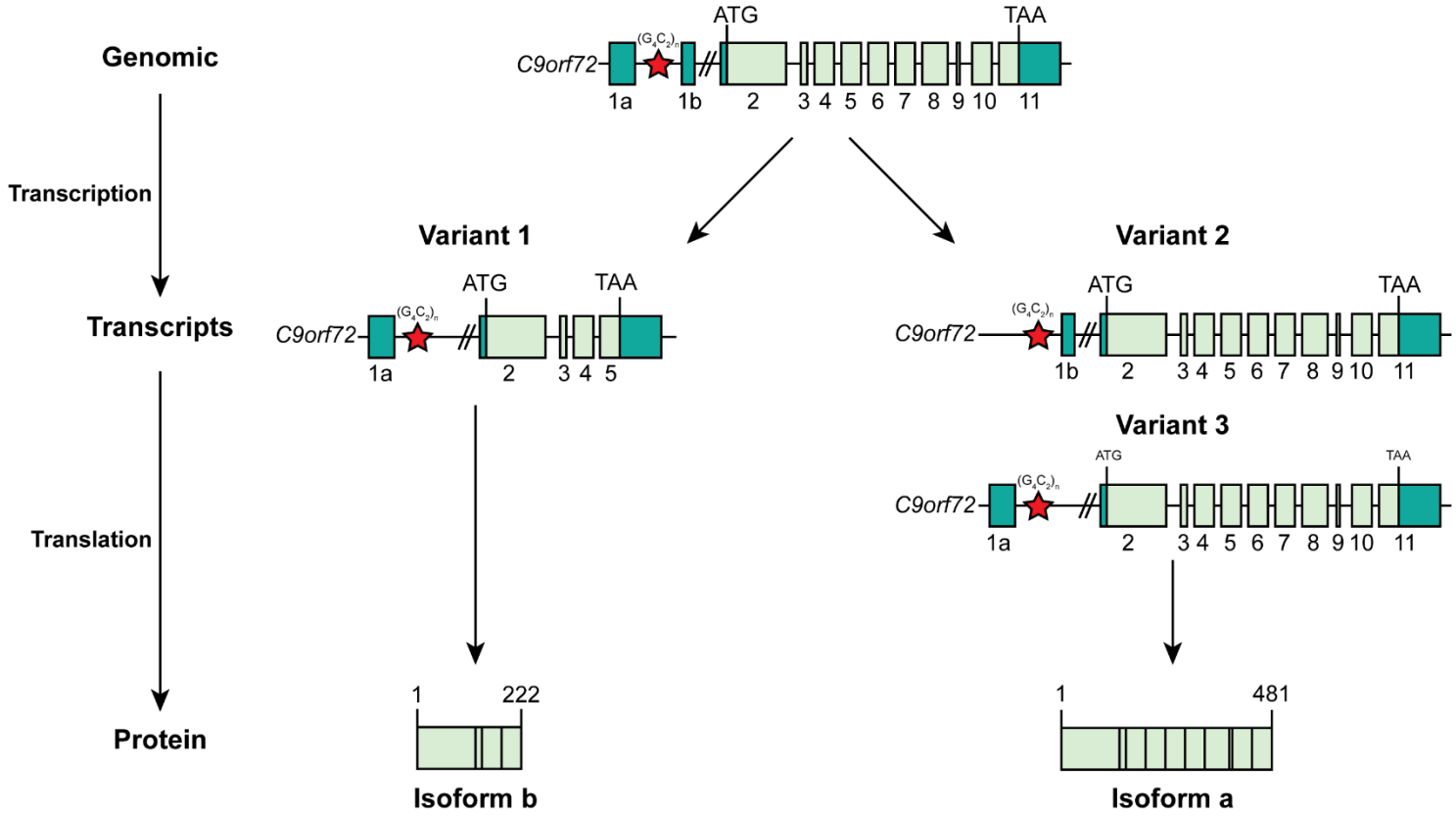

Figure 1.6 Diagram depicting the generation of the two isoforms of the protein encoded by *C9orf72*. The red star depicts the position of the $(G_4C_2)_n$ expansion. Three different transcripts are produced leading to the production of an a and b isoform. Adapted from Todd & Petrucelli 2016.

Structurally, the defining feature of C9orf72 is the presence of a “differentially expressed in normal and neoplastic cells” (DENN) domain (Zhang et al., 2012; Levine et al., 2013). This DENN domain is flanked at the N-terminus by a longin domain (u-DENN domain) and at the C-terminus by alpha domain (d-DENN domain) (Zhang et al., 2012).

The presence of a DENN domain indicates that C9orf72 is a modulator of Rab GTPase activity by acting as a Rab Guanine exchange factor (GEF) (Tang, 2016). Supporting this notion is the fact that C9orf72 was seen to co-localise and immunoprecipitate with Rabs 1, 5, 7 and 11 in neuronal cell lines and primary motor neurons (Farg et al., 2014). Similar co-localisation was also seen between C9orf72 and Rab11 and 7 in human spinal motor neurons (Farg et al., 2014). Rab GTPases are responsible for regulating membrane trafficking throughout the cell by interacting with molecular motors, vesicular coat proteins and SNARE proteins. Therefore, the implication is that C9orf72 is able to modulate membrane trafficking through its regulation of Rab proteins (Tang, 2016).

Additionally, C9orf72 forms a tripartite complex with two other proteins. The first is another DENN protein called Smith-Magenis Syndrome chromosome region candidate 8 (SMCR8) and the second is WD-40 repeat 1 (WDR41) which has an unknown function (Zhang et al., 2012; Sullivan et al., 2016). The C9orf72-SMRC8-WDR41 tripartite complex interacts with Rabs including Rab8A and Rab39B which are important for regulating neuronal trafficking and dendritic transport of receptors (Tang, 2016). Furthermore, this tripartite complex also interacts with FAK family kinase-interacting protein of 200 kDa (FIP200), autophagy-related 13 (ATG13) and Unc-51-like kinase 1 (ULK1) which are involved in the initiation of autophagy (Sullivan et al., 2016; Webster et al., 2016). Evidence suggests that C9orf72 regulates autophagy initiation by interacting with both Rab1a and ULK1 complex (FIP200, ATG13, ULK1) (Webster et al., 2016). In doing so, it mediates the interaction between the complex and Rab1a, thereby regulating the trafficking of the complex to the phagophore for the initiation of autophagy. Further implicating C9orf72 in autophagy is evidence that it localises to autophagosome-like structures which are positive for the autophagosome marker microtubule-associated protein 1A/1B-light chain (LC3) (Farg et al., 2014). Additionally, there is evidence that C9orf72 has a further role in directing aggregated protein clearance

via Rab39B and p62 (Tang, 2016). Interestingly, while this complex does not interact with the ALS associated TRAF family member-associated NF-KB activator (TANK)-binding kinase 1 (TBK1), it does interact with TBK1 adaptors such as TANK, and TBK1 is a substrate for SMRC8 (important for autophagy regulation) (Tang, 2016). Mutations in TBK1 are known to be associated with ALS (Cirulli et al., 2015).

Overall, there is mounting evidence that through its interactions with Rab GTPases, C9orf72 is deeply involved in the regulation of membrane trafficking and autophagy (Tang, 2016).

1.2.1.4.4.2 C9orf72 in ALS

The pathological mechanisms underlying how the $(G_4C_2)_n$ repeat expansion causes disease is still not fully understood. The reduction in mRNA of the three transcripts of C9orf72 in patients potentially indicates that this is mediated by a loss of function (Haeusler et al., 2016). A similar decrease was observed using antibodies directed at the C9orf72 protein in patient fibroblasts (Renton et al., 2011). However, another study showed a specific decrease in the protein levels of the long isoform and a concomitant increase in the short isoform (Xiao et al., 2015a). Further evidence against a loss of function arose from the comparison of heterozygous and homozygous patients. In the event of a loss of function mechanism you would expect the homozygous patients to show a more severe phenotype in comparison to heterozygous patients but this was not the case (Fratta et al., 2013). Furthermore, reducing C9orf72 expression in mice either by knockout, conditional knockout or using antisense oligonucleotides failed to produce ALS-like phenotypes (Haeusler et al., 2016). Therefore, the consensus is that the pathology of C9orf72 is caused by a toxic gain of function at both the RNA level and protein level.

The $(G_4C_2)_n$ repeat expansion leads to the formation of predominantly nuclear RNA aggregates (RNA foci) within the CNS of patients (Moens et al., 2017; Haeusler et al., 2016). RNA foci are also formed by the bidirectional transcription of the repeat expansion producing aggregates formed of transcripts with a $(G_4C_2)_n$ expansion. Additionally, the $(G_4C_2)_n$ expansion causes the formation of both G-quadroplex and R-Loop structures (Wen et al., 2017). The RNA foci are known to

sequester several RNA binding proteins which inevitably results in them being unavailable for normal RNA metabolism (Moens et al., 2017). Furthermore, the G-quadruplex and R-loop structures have been observed to cause nucleolar stress including a disruption of polymerase activity (Haeusler et al., 2014). Significantly, a correlation between the increased number of RNA foci in the frontal cortex and the age of onset of FTD has been reported (Mizielinska et al., 2013). The final gain of function mechanism arises when RNA transcripts containing the $(G_4C_2)_n$ repeat expansion enter the cytoplasm and are subsequently translated into dipeptide repeats through repeat-associated non-ATG-dependent (RAN) translation (Haeusler et al., 2016). This translation results in the production of glycine-proline (GP), glycine-alanine (GA) and glycine-arginine (GR) dipeptide repeats from the sense transcript of the $(G_4C_2)_n$ repeat expansion. Conversely, the antisense transcript generates proline-glycine (PG), proline-arginine (PR) and proline-alanine (PA) dipeptides. These dipeptide repeat proteins are found to be part of p62 positive, TDP-43 negative inclusions in both neurons and glial cells in patients (Wen et al., 2017). However, they are rarely seen in spinal cord motor neurons (Haeusler et al., 2016). It remains unclear how significant the contribution of these products of RAN translation are to the pathogenesis of disease.

1.2.1.4.4.3 Mouse models of the *C9orf72* hexanucleotide repeat expansion

The first report of a mouse model for the C9orf72 $(G_4C_2)_n$ hexanucleotide repeat expansion was published in 2014 (Hukema et al., 2014). However, the paper describing this model was subsequently retracted (Hukema et al., 2016). Nevertheless, a mouse model was finally generated using an AAV vector injected into the CNS of P0 mice (postnatal day 0) which caused the expression of 2 or 66 repeats of G_4C_2 (Chew et al., 2015). Subsequently, further mouse models using a bacterial artificial chromosome (BAC) were reported in 2015 (O'Rourke et al., 2015; Peters et al., 2015). Table 1.7 summarises mouse models reviewed in Picher-Martel et al., 2016.

Table 1.7

Number of repeats	Promoter	Age at onset (weeks)	Survival (weeks)	Phenotype				Ref.
				Paralysis	Cognitive symptoms	Neuropathological findings and particularities	Gliosis	
66	nd	24	Nd	nd	Y	Nuclear RNA foci, phosphoTDP-43 inclusions, cytosolic and nuclear DPR, anxiety and social abnormalities, motor impairment	Y	(Chew et al., 2015)
100-1000	BAC	None	Normal	N	N	RNA foci, DPR, no NCI	N	(O'Rourke et al., 2015)
500	BAC	None	Normal	N	N	RNA foci, DPR, no NCI	N	(Peters et al., 2015)
450	BAC[b]	52	Normal	N	Y	RNA foci, DPR, age-dependent protein accumulation, no motor deficits or MN loss, age dependant cognitive deficit, no TDP-43 mislocalisation	N	(Jiang et al., 2016)
500	BAC[b]	16	20-40[c]	Y	Y	NMJ loss, reduced axonal size, MN loss, RNA foci, DPR, TDP-43 NCI	Y	(Liu et al., 2016a)

Table 1.7 Table summarising the mouse models of C9orf72. Y = yes, N = no, nd = not described, MN = motor neuron, MNJ = neuromuscular junction, DPR = dipeptide repeat, [b]BAC clone had sequence for human C9orf72 exons and promoter, [c]34% of female mice died within this period, majority of other mice developed cognitive symptoms at older age. Adapted from Picher-Martel et al. 2016.

1.2.1.4.5 Peripherin

Peripherin is a class III intermediate filament that in adults is predominantly expressed in the PNS and at low levels in select neuronal populations of the CNS including spinal motor neurons (Troy et al., 1990a; Goldstein et al., 1991, 1996; Troy et al., 1990b; Brody et al., 1989; Parysek and Goldman, 1988; Leonard et al., 1988). Peripherin expression is at its highest levels late in embryological development and in the early postnatal brain (Kost et al., 1992). Specifically, peripherin is highly expressed during the initial stages of neuritic outgrowth and axonogenesis, and subsequently diminishes (Szaro and Strong, 2010; Lariviere and Julien, 2004).

1.2.1.4.5.1 Structure and function of peripherin

Intermediate filaments (IFs) are defined by a diameter of approximately 10 nm and thus are “intermediate” to the diameter of the other two main components of the cytoskeleton, actin and microtubules (Lépinoux-Chambaud and Eyer, 2013). In humans, there are 70 different genes encoding IFs which are classified into 6 distinct classes: class I and II (acidic and basicic keratins respectively), class III (vimentin, desmin, peripherin and glial fibrillary acid protein (GFAP), Class IV (neurofilament light (NFL), neurofilament heavy (NFH), neurofilament middle (NFM) and α-internexin), class V (nuclear lamins), and class VI (nestin) (Yuan et al., 2017; Szeverenyi et al., 2008). IFs were originally thought to only confer structural and mechanical integrity to cells. However, they are now known to be involved in physiological functions including regulating the distribution of organelles, signal transduction and gene regulation (Kornreich et al., 2015).

All IFs, including peripherin, share a common tripartite structure which consists of a predominantly α-helical central rod domain that is flanked by the non α-helical “head” (N-terminal) and “tail” domains (C-terminus), as shown in Figure 1.7 (McLean et al., 2008). The rod domain is subdivided in to 3 coiled domains (1a, 1b and 2a/b) which are interspaced by non α-helical linkers (L1 and L12). Unlike the conserved central rod domain, both the head and tail domains exhibit variability between IFs. For example, peripherin has a relatively short tail domain, harbouring a single site of tyrosine phosphorylation (Yuan et al., 2017; Chernyatina et al., 2015). The rod domain is thought to confer the ability for IFs to assemble into filamentous networks (McLean et al., 2008).

Figure 1.7

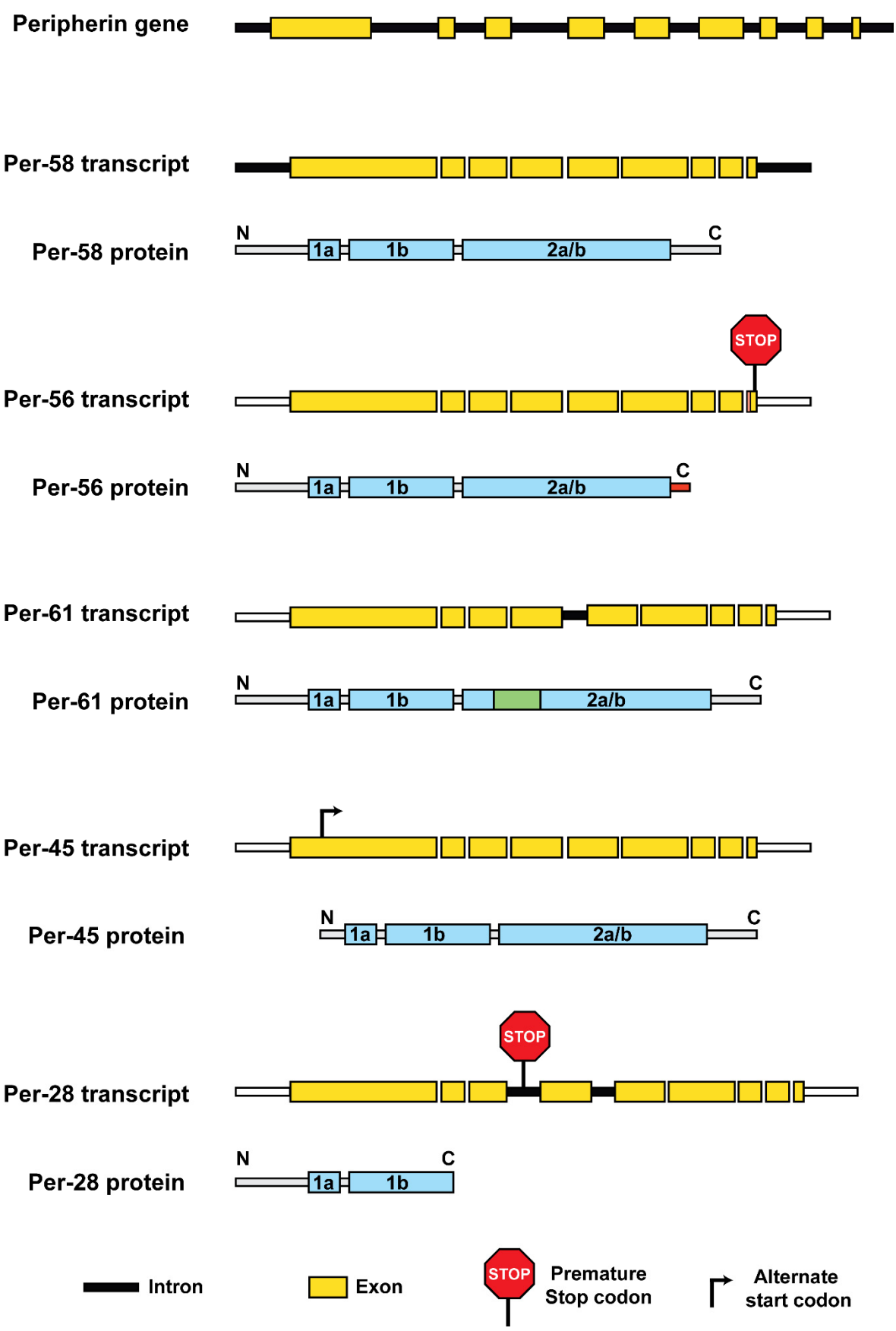
Peripherin gene
Per-58 transcript
Per-58 protein
N
1a
1b
2a/b
C
Per-56 transcript
STOP
Per-56 protein
Per-61 transcript
Per-61 protein
Per-45 transcript
Per-45 protein
Per-28 transcript
Per-28 protein
Intron
Exon
Premature
Stop codon
Alternate
start codon

Figure 1.7 Diagram showing the genomic structure of the peripherin gene, resulting mRNA transcripts and protein isoforms. Per-58 is the canonical isoform and uses all 9 exons. Per-56 is generated by the use of a cryptic acceptor site on exon 9 which results in the deletion of 62 base pairs which causes a frameshift. This means the C-terminal 21 amino acids are replaced with 8 new amino acids (shown in orange on the Per-56 transcript) and a premature stop to translation, which overall creates a new C-terminus (shown in red in the Per-58 transcript). Per-61 is formed by the retention of intron 4 (shown in green on the Per-61 protein). Per-45 is generated by the use of an alternate start codon during translation, resulting in a shorter N-terminus. Per-28 is generated due to the retention of introns 3 and 4 which leads to a premature stop codon. Adapted from Suter 2008 with added information from Zhao & Ronald K.H. Liem 2016

Peripherin has been shown to be able to assemble into both homopolymeric and heteropolymeric filaments by co-assembling with the neurofilament subunits (NFH, NFL and NFM) (Beaulieu et al., 1999; Athlan and Mushynski, 1997; Parysek et al., 1991; Cui et al., 1995; Ho et al., 1995). As such, it had long been hypothesised that peripherin may be a subunit of neurofilaments due to its expression also being limited to neurons and being particularly enriched in axons (Portier et al., 1983). However, only recently has this been confirmed by the application of the criteria that define the subunits of neurofilaments to peripherin (Yuan et al., 2012).

The precise biological function of peripherin remains to be elucidated. However, it has been implicated in neurite growth and stability, primarily because there is an increase in peripherin expression during the initiation of axonal outgrowth (Zhao and Liem, 2016). However, blocking peripherin synthesis using antisense oligonucleotides in PC12 cells suggested that peripherin is involved in stability but not the initiation of neurite outgrowth (Troy et al., 1992). Conversely, siRNA knockdown of peripherin also in PC12 cells impeded the initiation, extension and subsequent maintenance of neurites (Helfand et al., 2003). In peripherin null mice there is no discernible decrease in viability or the presence of any observable phenotype (Larivière et al., 2002). Additionally, there were no abnormalities in the ventral and dorsal roots or other regions of the spinal cord. However, the there

was an increase in α-internexin which may have compensated for the loss of peripherin. However, a subset of sensory neurons did show defects. Recently, peripherin has also been implicated in vesicle trafficking through its association with SNAP25 interacting protein 30 (SIP30) (Gentil et al., 2014). Additionally, peripherin may be involved in the transport of TDP-43 to the neurite terminals (Muresan and Muresan, 2016).

1.2.1.4.5.1.1 Peripherin isoforms

Rat cDNA encoding peripherin was originally isolated from PC12 cells in 1988 (Leonard et al., 1988). Subsequently, three peripherin isoforms were identified at both mRNA and protein level by the screening of a mouse neuroblastoma cell line (Landon et al., 1989, 2000). These alternatively spliced isoforms were named Per-58 (the canonical isoform which corresponds to the cDNA isolated in 1988 by Leonard et al), Per-56 and Per-61, as a reference to their molecular weight (kDa). Per-58 (457 amino acids) is produced by a transcript consisting of all 9 exons of the *PRPH* gene (Figure 1.7). One the other hand, Per-56 (461 amino acids) arises by the use of a cryptic acceptor site at the beginning of exon 9 which results in a deletion of 62 nucleotides. Consequently, the deletion of these base pairs results in a frameshift which substitutes the C-terminal 21 amino acids with 8 new amino acids (LLRPQPEL), forming a unique C-terminus. Per-61 (507 amino acids) is formed by the retention of intron 4, which encodes for a further 32 amino acids at the beginning of the third coiled domain of peripherin (2a). Per-61 is only produced in mice due to the difference in the sequence of intron 4 between the two species (Xiao et al., 2008). Intron 4 in mice is 96 bp in length, while in humans it is 91 bp and its retention would cause a frameshift resulting in a premature stop codon yielding a 32 kDa C-terminally truncated protein, thus precluding the existence of Per-61 in humans. Subsequently, a 45 kDa peripherin isoform (Per-45) was identified, which is generated by the use of a downstream in frame alternate start codon (McLean et al., 2008). Specifically, in the mouse peripherin gene, the third ATG start codon ($mATG^3$) of the transcript is used as the translational start site instead of the canonical second ATG ($mATG^2$). In the human gene, the second ATG start codon ($hATG^2$) is used instead of the canonical first ATG codon ($hATG^1$). Finally, a human specific 28 kDa isoform (Per-28) was identified, which is generated by the retention of introns 3 and 4 (Xiao et al., 2008). This results in the

use of a premature stop codon 30 bp into intron 3, yielding the C-terminally truncated 28 kDa protein. In summary, Per-58, Per-56, Per-45 and Per-61 exist in mice, and Per-58, Per-56, Per-45 and Per-28 exist in humans, see Figure 1.7 for summary.

1.2.1.4.5.1.2 Peripherin in ALS

Peripherin is a major constituent of the ubiquitinated proteinaceous inclusions in ALS including in “Lewy-body like” inclusions, hyaline conglomerate inclusions, axonal spheroids and Bunina bodies (Corbo and Hays, 1992; He and Hays, 2004; Migheli et al., 1993; Wong et al., 2000; Mizuno et al., 2011). Additionally, there is an upregulation of peripherin expression in ALS lumbar spinal cord tissue (Robertson et al., 2003; McLean et al., 2010). Also, a similar increase was also observed at the mRNA level in ALS cervical and lumbar spinal cord tissue (Strong et al., 2004). There is also a specific increase in the Per-28 isoform of peripherin at both the mRNA and protein level in ALS spinal cord (Xiao et al., 2008). Interestingly, it was shown that alteration of the stoichiometry of Per-28 expression relative to the other peripherin isoforms induced aggregation formation in SW13vim(-) cells (a human adrenal cortex carcinoma-derived cell line lacking expression of intermediate filaments) (Xiao et al., 2008; Hedberg and Chen, 1986). Similar results were obtained by the expression of the isoform in motor neurons. Furthermore, Per-28 was seen to be a component of the aggregates seen in ALS spinal cords. These findings indicate that the alternative splicing of peripherin is altered in ALS tissue resulting in increased Per-28 and its presence within aggregates.

Interestingly, increases in peripherin expression are typically associated with neuronal injury and regeneration (Xiao et al., 2006). This may suggest an attempt of injured neurons to recover following injury. However, transgenic mice overexpressing peripherin exhibit age dependent motor neuron degeneration with a late onset (approximately 2 years) which occurs much sooner if compounded with a lack of NFL (a reduction of NFL has been reported in ALS) (Beaulieu et al., 1999). A similar result occurs when peripherin is overexpressed in cultured motor neurons (Robertson et al., 2001). Recently, peripherin was identified as part of a protein signature that characterises vulnerable neurons in ALS (Hedlund et al., 2010; Comley et al., 2015).

Peripherin was also detected in aggregates present in SOD1^{G93A} transgenic mice (Tu et al., 1996). Similar peripherin pathology was also observed in SOD1^{G37R} transgenic mice with peripherin localised to aggregates in both symptomatic and pre-symptomatic mice, indicating peripherin pathology occurs at an early stage of the disease (Beaulieu et al., 1999). Additionally, the expression of the assembly incompetent Per-61 isoform in motor neurons is toxic and leads to neuronal death (Robertson et al., 2003). Per-61 was also detected in both SOD1^{G37R} and SOD1^{G93A} transgenic mice but not in wild-type or peripherin transgenic mice (McLean et al., 2010; Robertson et al., 2003). These data indicate that Per-61 may be a neurotoxic splice variant of peripherin which contributes to ALS. Additionally, Per-56 was found to aggregate in small diameter sensory dorsal root ganglion neurons and is detrimental to the assembly of NFL and NFM (Sassone et al., 2016).

Finally, 2 *PRPH* missense mutations and a deletion have been associated with ALS, see Table 1.8 for details. Additionally, 2 missense mutations, c.706-13C>T and C.870+12G>A, in introns 3 and 4 respectively, may affect the protein sequence of Per-28 or Per-61 (Corrado et al., 2011).

1.2.1.4.5.1.2.1 Peripherin isoform expression in TDP-43^{A315T} transgenic mice

Alterations in the expression of peripherin isoforms in TDP-43^{A315T} mice were previously reported (Barri, 2015). Analysis of the lumbar spinal cord of these mice showed alterations in the levels of Per-45, Per-56 and an unidentified isoform at 50 kDa. It was suggested that the changes in Per-45 represented a potential role for TDP-43 in regulating the alternative translation of this isoform. Furthermore, significantly increased expression of Per-61 was also detected in the same TDP-43^{A315T} model and in TDP-43^{G348C} mice which also had significant peripherin pathology (Swarup et al., 2011).

Table 1.8

Base pair change	Type of mutation	Amino acid substitution	Details	Ref.
c.420G<T	Substitution	p.D141Y	Prone to form aggregates in comparison to wild-type peripherin in transfected cells.	(Leung et al., 2004; Corrado et al., 2011)
c.398G>C	Substitution	p.R133P	Affects a highly conserved residue and is predicted to have a detrimental effect on protein structure and function.	(Corrado et al., 2011)
c.228delC	Deletion	-	Results in a predicted truncated peripherin isoform of 85 amino acid residues (8.8kDa) with the C-terminal 9 amino acids being unique to the isoform. This isoform was assembly incompetent and disrupted filament formation of the other isoforms with NFL.	(Gros-Louis et al., 2004)

Table 1.8 Table showing the *PRPH* mutations associated with ALS.

1.2.1.5 Autophagy

As discussed, intracellular inclusions are a neuropathological hallmark of ALS and other neurodegenerative diseases (Webster et al., 2017; Blokhuis et al., 2013; Ross and Poirier, 2004). In ALS, these inclusions are found in affected neurons and glial cells within the brain stem, spinal cord, cerebellum, hippocampus and frontal and temporal lobes (Webster et al., 2017). As previously mentioned, ubiquitinated inclusions are most commonly positive for TDP-43 with the exception being SOD1 and FUS related fALS in which SOD1 and FUS positive inclusions are seen, respectively (Webster et al., 2017). Several other proteins in ALS also demonstrate a propensity to aggregate which include VCP, DCTN1, OPTN, UBQLN2 and dipeptide repeats generated from the repeat expansion in C9orf72. These proteinaceous inclusions in ALS are thought to be a result of the failure of clearance mechanisms including the autophagy-lysosome pathway.

Macroautophagy (hereafter referred to as autophagy), the most prevalent form of autophagy, is a highly conserved catabolic process responsible for the degradation of cellular contents including misfolded proteins and organelles (Deng et al., 2017b; Gao et al., 2017). The precise mechanism of autophagy is beyond the scope of this thesis but is reviewed here Bento et al., 2016.

Importantly, several proteins encoded by ALS linked genes are involved autophagy, see Table 1.9. Clearance mechanisms such as autophagy are particularly important in neurons as they are post-mitotic and so are unable to clear protein aggregates through asymmetric distribution (Lee et al., 2015). Additionally, the morphology of neurons presents further unique problems for the autophagy process (Ramesh and Pandey, 2017). Autophagosomes are able to form within any region of neurons where toxic substrates form that require disposal (Maday, 2016). However, the principal location of lysosomes, with which autophagosomes fuse to form autolysosomes to facilitate the degradation of its contents, is within the soma. Therefore, these autophagosomes are actively transported by dynein/dynactin from the periphery towards the soma (Maday, 2016). Interestingly, autophagosomes simultaneously bind both dynein and kinesin-1 motors which allows for bidirectional motility (Maday et al., 2012). However, this bidirectional movement is only exhibited in the initial stages, soon after the activity of the bound kinesin-1 motors is attenuated resulting in primarily retrograde movement which is driven by dynein. As the autophagosomes become more acidified the movement once again becomes more bidirectional. This transport is regulated by huntingtin and JIP1 through their interactions with dynein and kinesin-1 (Wong and Holzbaur, 2014; Fu et al., 2014).

Interestingly, the knockdown of the neuron specific intermediate chain, DYNC1I1, caused an impairment in the arborisation of cultured hippocampal neurons (Liu et al., 2016b). It was found that this could be rescued by stimulating the RAS-RAF-MEK signalling pathway which stimulates MEK-dependent autophagy.

Table 1.9

Gene Symbol	Protein	Autophagy involvement	Ref.
C9orf72	C9orf72	Regulates the initiation of autophagy.	(Sullivan et al., 2016; Yang et al., 2016)
TBK1	TBK1	Phosphorylates autophagy receptors (p62 and OPTN) and it also regulates selective autophagy.	(Wild et al., 2011; Richter et al., 2016; Pilli et al., 2012; Matsumoto et al., 2015)
OPTN	Optineurin	A substrate of TBK1 and autophagy receptor protein and is also involved in selective autophagy.	(Deng et al., 2017a; Wild et al., 2011; Richter et al., 2016)
SQSTM1	P62	A substrate of TBK1 and ULK1, is an autophagy receptor and is involved in selective autophagy.	(Deng et al., 2017a; Pilli et al., 2012; Lim et al., 2015)
UBQLN2	Ubiquilin-2	A potential autophagy receptor.	(Rothenberg et al., 2010; N'Diaye et al., 2009)
TARDBP	TDP-43	Regulates autophagy initiation and autophagosome-lysosome fusion.	(Xia et al., 2016)
FUS	FUS	ALS-linked mutations (P525L and R522G) impair autophagy.	(Soo et al., 2015)
VCP	Vasolin-containing protein	Regulates the clearance of lysosomes.	(Papadopoulos et al., 2017)
SOD1	Superoxide dismutase 1	Mutant SOD1 disrupts autophagy.	(Xie et al., 2015; Nassif et al., 2014; Chen et al., 2015; Bandyopadhyay et al., 2014; Morimoto et al., 2007)
ALS2	Alsin	Pathogenic mutations in *ALS2* disrupt the formation of amphisomes	(Otomo et al., 2011)
VAPB	Vesicle associated membrane protein -associated B/C	Regulates ER-mitochondrial contact	(Gomez-Suaga et al., 2017)
SigR1	Sigma receptor-1	Regulates autophagosome-lysosome	(Dreser et al., 2017; Vollrath et al., 2014)

Table 1.9 Table showing the ALS linked genes which are implicated in the autophagy-lysosome pathway. Adapted from Deng, Sheehan, *et al.*, 2017.

1.2.1.6 Mitochondria and mitochondrial stress

Mitochondrial pathology is often seen in neurodegenerative diseases (Bonafede and Mariotti, 2017). These organelles are pivotal in several cellular functions including the production of energy through cellular respiration, calcium homeostasis and apoptosis. Importantly, mitochondria are also the main source of ROS within the cell (Islam, 2017). Mitochondrial defects have been observed in spinal cords and muscle biopsies of fALS and sALS patients (Bonafede and Mariotti, 2017). These defects included disorganized cristae and membranes, swelling and vacuolation. Similar observations have also been made in the $SOD1^{G93A}$ mouse model of ALS. In addition to these morphological changes, altered production of both ATP and ROS, energy and calcium homeostasis, abnormal initiation of apoptosis, and altered mitochondrial transport have also been observed (Pasinelli et al., 2000; Menzies et al., 2002; Damiano et al., 2006; Mattiazzi et al., 2002). Importantly, several SOD1 mutations (G93A, A4V, G85R and G37R) were found to cause impaired anterograde transport both in vivo and in vitro (De vos et al., 2007). Consequently, studies found mitochondria positioning to be affected in these mice (Vande Velde et al., 2011; Magrané et al., 2014). Similarly, the overexpression of wild type and mutant TDP-43 has been shown to reduce mitochondrial transport and affect the localisation of mitochondria in primary motor neurons (Wang et al., 2013). Furthermore, similar results have also been obtained in association with both *FUS* and *C9orf72* mutations (De Vos and Hafezparast, 2017).

The unique morphology of neurons requires that mitochondria be transported and positioned to allow for localized ATP production (Maday et al., 2014). Mitochondrial motility is bidirectional and therefore is mediated by both kinesin-1 and dynein motors (Maday et al., 2014). The transport of mitochondria is partly regulated by neuronal activity through locally released calcium which serves to immobilise mitochondrial transport (Sajic et al., 2013). Interestingly, it has been found that mitochondrial motility is important for the maintenance of axonal mitochondrial quality by allowing the removal of stressed damaged mitochondria and the provision of healthy replacements (Lin et al., 2017).

Damaged mitochondria are disposed via the PINK1/Parkin pathway which regulates the autophagy of mitochondria (mitophagy) (Narendra et al., 2008).

However, recently it has been suggested that this process mainly occurs in the soma of neurons (Sung et al., 2016; Devireddy et al., 2015). This raises the question of how damaged mitochondria are cleared from axons. It was found that syntaphilin acts to immobilise mitochondria to microtubules (Chen and Sheng, 2013; Kang et al., 2008). Furthermore, in chronic mitochondrial stress conditions, the levels of syntaphilin are reduced to allow for greater dynein mediated retrograde transport of mitochondria to facilitate the clearing of the damaged organelles (Lin et al., 2017). Note that it was also shown that dynein mediated retrograde transport also plays a role in the degradation of syntaphilin following its release from mitochondria. Additionally, analysis of ventral root axon bundles in hSOD1^{G93A} mice indicated that this pathway is activated at an asymptomatic stage to facilitate the removal of damaged mitochondria (Lin et al., 2017). However, despite depletion of syntaphilin occurring by disease onset at P120 there remains an accumulation of damaged mitochondria within axons, suggesting that the transport machinery itself is defective.

1.2.1.7 The ALS-FTD spectrum

Over time it has become clear that ALS should not be viewed as a disease which only affects motor neurons. In fact, ALS is known to affect brain areas outside of the motor system, including the frontotemporal region (Al-Chalabi et al., 2016). Consequently, behavioural and cognitive impairment is often reported in ALS cases (Wheaton et al., 2007; Ringholz et al., 2005). Strikingly, up to 15 % of ALS patients also develop symptoms which are consistent with FTD. FTD is characterised by the progressive loss of neurons in the frontal and temporal cortex which causes alterations in behaviour and personality and progressive impairment of language skills (Van Langenhove et al., 2012). This is the first indicator that ALS and FTD could be overlapping diseases. The discovery of TDP-43 positive inclusions not only in ALS, but that it is also the most common pathology associated with FTD (in more than 50% of cases), further emphasised this link (Arai et al., 2006; Neumann et al., 2006; Vanden Broeck et al., 2014). Subsequently, the discovery that TDP-43 mutations not only account for approximately 4 % of sALS cases but are also seen in some cases of FTD provided the first genetic link between the conditions (Cirulli et al., 2015; Borroni et al., 2009; Kovacs et al., 2009). Similarly, FUS mutations were also found in FTD

cases, as well as FUS positive inclusions (Ling et al., 2013). Subsequently, further genetic overlap was found with mutations occurring in *C9orf72*, *VCP*, *VAPB, SQSTM1*, *OPTN* and *CHMP2B* in cases of ALS, FTD and ALS-FTD. Therefore, the current consensus is that ALS and FTD are linked genetically, pathologically and are thought to comprise a disease spectrum.

1.2.2 Spinal muscular atrophy

Spinal muscular atrophy is a term given to a group of disorders that characteristically exhibit degeneration of the motor neurons within the spinal cord and brainstem (Faravelli et al., 2015). However, it is most typically used to describe the form of the disease which is caused by mutations within survival motor neuron 1 (*SMN1*) on chromosome 5q11.2-13.3, accounting for approximately 95 % of cases (Lefebvre et al., 1995; Brzustowicz et al., 1990; Arnold et al., 2015). Often referred to as “5q-SMA” or “proximal spinal muscular atrophy”, it is inherited in an autosomal recessive manner (Arnold et al., 2015). It is characterised by muscle wasting in proximal muscles usually starting in the lower limbs (Faravelli et al., 2015). This form of SMA has an incidence of approximately 1 in 10,000 live births (Ogino et al., 2002). Additionally, about 1:40 to 1:60 are carriers of mutations in *SMN1*, but this frequency varies greatly between different ethnic groups (Hendrickson et al., 2009; Sugarman et al., 2012; Faravelli et al., 2015). Overall, it is the most common cause of infant mortality due to a genetic abnormality (Faravelli et al., 2015).

The human genome harbours 2 highly homologous *SMN* genes on the same chromosome, the telomeric *SMN1* and the centromeric *SMN2* (Lefebvre et al., 1995). These differ only by 5 base pairs, but the most crucial difference is a C>T substitution within exon 7 in *SMN2* (Lorson et al., 1999; Monani et al., 1999). Although this does not produce an amino acid change, it alters the alternative splicing of exon 7 causing its exclusion in the *SMN2* transcript resulting in the production of a truncated version of the SMN protein which is rapidly degraded (Lorson et al., 1999; Monani et al., 1999; Burnett et al., 2009). However, in approximately 10 % of instances exon 7 is retained within the *SMN2* transcript allowing for the production of the full-length SMN protein (Faravelli et al., 2015). Therefore, in patients which lack *SMN1* due to homozygous deletions, gene conversion (*SMN1* converts to *SMN2*) or compound heterozygosity, *SMN2 derived*

full-length SMN protein acts to compensate. Interestingly, there is variation in the gene copy number of *SMN2* which consequently determines the severity of the phenotype based on the total amount of SMN protein produced (Feldkötter et al., 2002; Elsheikh et al., 2009). Accordingly, SMA exists on a spectrum where patients are delineated into 5 types in accordance to the severity of the phenotype (see Table 1.10) (Faravelli et al., 2015). How the lack of SMN protein underlies the selective loss of motor neurons is still not fully understood, but it is suggested that its loss affects the formation of snRNPs which are important for pre-mRNA splicing. Therefore, RNA metabolism may underlie the pathogenesis of SMA but further evidence is required.

Table 1.10

Type	Age of onset	Function	Natural age at death	*SMN2* copy number
0	Prenatal	Respiratory failure at birth	Weeks	1
1	0-6 months	Never sit	<1 year	2-3
2	<18 months	Sit	>25 years	3
3	>18 months	Stand or ambulatory	Adult	3-4
4	>21 years	Ambulatory	Adult	4 or more

Table 1.10 Table showing the 5 types of SMA which are delineated in accordance to the severity of the phenotype. Adapted from Arnold et al. 2015.

1.2.2.1 Spinal muscular atrophy, lower extremity predominance (SMA-LED)

SMA-LED was coined to describe patients suffering from an autosomal dominant SMA, which predominantly affected the proximal muscles of the lower limbs (Harms et al., 2010). Descriptions of similar phenotypes with the same inheritance pattern exist as far back as 1917 (Timme, 1917).

The clinical spectrum of SMA-LED has expanded over time with the identification of further patients. In addition to the weakness and atrophy of distal but mainly proximal muscles of the lower limbs, it is understood to be of congenital or early onset with little or no progression (Harms et al., 2010, 2012). There is also an absence of sensory involvement but the phenotype is often compounded with cognitive impairment (Harms et al., 2012; Scoto et al., 2015). Other common symptoms include joint contractures, foot deformities and abnormal gait.

1.2.2.1.1 Genetics of SMA-LED

The first genetic locus associated with SMA-LED was identified as a 6.1 Mb region of chromosome 14q32 using linkage analysis (Harms et al., 2010). This region contained 73 annotated genes which were subsequently sequenced to identify the causative mutation (Harms et al., 2012). A heterozygous c.1750A>C mutation within exon 8 of the *DYNC1H1 (dynein cytoplasmic 1 heavy chain 1)* gene was found to be responsible for the disease. This mutation causes a p.I584L substitution on the DYNC1H1 protein which is a subunit of the cytoplasmic dynein motor complex. Additionally, a c.2011A>G mutation in exon 8 and a c.3170A>G mutation in exon 11 were identified in two separate kindreds causing p.K671E and p.Y970C amino acid substitutions respectively. Subsequently, several other SMA-LED causative mutations in *DYNC1H1* were discovered, see Table 1.11 for a comprehensive list. SMA-LED caused by *DYNC1H1* mutations is designated SMA-LED1 (OMIM #158600). Later, three concurrent studies reported a second disease locus at chromosome 9q22.31 using genome-wide linkage analysis and identified *BICD2* (*Bicaudal d homolog 2*) as the causative gene using exome sequencing (Neveling et al., 2013; Oates et al., 2013; Peeters et al., 2013). Interestingly, BICD2 is an adaptor protein of the cytoplasmic dynein motor complex. A comprehensive list of SMA-LED *BICD2* mutations is found in Table 1.12. SMA-LED caused by mutations on BICD2 is designated SMA-LED2 (OMIM #615290).

Table 1.11

Gene	Mutation	Protein domain	Ref.
DYNC1H1	p.I584L	Tail domain (DIC binding region)	(Harms et al., 2012)
	p.K671E	Tail domain (DIC binding region)	
	p.Y970C	Tail domain (DLIC binding region)	
	p.H306R	Tail domain	(Tsurusaki et al., 2012)
	p.Q1194R	Tail domain	(Fiorillo et al., 2014)
	p.E3048K	Motor domain (AAA4)	
	pR598C	Tail domain (DIC binding region)	(Punetha et al., 2015; Peeters et al., 2015)
	p.R264L	Tail domain	(Peeters et al., 2015)
	p.E2616K	Motor domain (AAA2)	(Scoto et al., 2015)
	p.R1603T	Motor domain (linker)	
	p.W673C	Tail domain (DIC binding region)	
	p.V612M	Tail domain (DIC binding region)	
	p.E603V	Tail domain (DIC binding region)	
	p.R598C	Tail domain (DIC binding region)	
	p.R598L	Tail domain (DIC binding region)	
	p.M581L	Tail domain (DIC binding region)	
	p.R399G	**Tail domain**	
	p.D338N	**Tail domain**	
	p.R264G	Tail domain	
	p.S3360G	Motor domain (stalk)	(Strickland et al., 2015)
	p.G807S	Tail domain (DLIC binding region)	(Niu et al., 2015)
	p.P776L	Tail domain	(Ding et al., 2016)
	p.R3384G	Motor domain (MTBD on stalk)	(Chen et al., 2017)
	p.G1132E	Tail domain	

Table 1.11 Summary of all *DYNC1H1* mutations associated with SMA-LED and the domain in which they are located. Those shown in bold are investigated in this thesis. Dynein structures from Carter et al. 2016; Kon et al. 2012.

Table 1.12

Gene	Mutation	Protein domain	Ref.
BICD2	p.S107L	CC1	(Neveling et al., 2013; Oates et al., 2013; Peeters et al., 2013)
	p.T703M	CC3	(Neveling et al., 2013)
	p.N188T	CC1	
	p.I189F	**CC1**	(Oates et al., 2013)
	p.R501P	CC2	
	p.E774G	CC3	(Peeters et al., 2013)
	p.R747C	CC3	(Synofzik et al., 2014)
	p.A535V	CC2	(Rossor et al., 2015)
	p.K508T	CC2	
	p.G839R	-	(Rudnik-Schöneborn et al., 2016)
	p.K734N	CC3	
	p.L683R	CC3	(Fiorillo et al., 2016)

Table 1.12 Summary of all *BICD2* mutations associated with SMA-LED and the domain in which they are located. Those shown in bold are investigated in this thesis.

1.2.2.1.1.1 DYNC1H1^{D338N}

The p.D338N *DYNC1H1* de novo heterozygous mutation was identified in a patient which presented with symptoms at birth such as talipes (club foot) and arthrogryposis (joint contractures in two or more areas of the body) (Scoto et al., 2015). Upon examination at 3 years of age, the maximum motor milestone displayed by the patient was the ability to sit independently. Contractures were present in the hips and knees and the patient also exhibited adducted thumbs and a tremor. Muscle atrophy was evident in both upper limbs and distally in the lower limbs causing weakness in these muscles. However, weakness was also evident in bulbar muscles and consequently the patient required ventilation and a percutaneous endoscopic procedure was performed at 1 years of age needing Nissen fundoplication. The patient was not tested for cognitive symptoms but did display a speech delay. An MRI proved to be normal, as did a nerve conduction study. On the other hand, a muscle biopsy indicated excessive connective tissue. Fibroblasts from this patient were biopsied and were used for the research presented here.

1.2.2.1.1.2 DYNC1H1^{R399G}

The p.R399G *DYNC1H1* mutation was identified in a kindred (Scoto et al., 2015). The father harboured the heterozygous p.R339G mutation (as did the mother) and displayed lower limb denervation, muscle atrophy and weakness of the lower limbs. Interestingly, the onset occurred in adulthood but at birth the patient was hypotonic and had proximal contractures. However, the patient could walk independently. The patient was not tested for cognitive impairment but had a positive family history. The homozygous offspring harboured the codominant homozygous p.R399G DYNC1H1 substitution and showed a much more severe phenotype. The onset in the child was at birth at which point the patient exhibited arthrogryposis in both lower and upper limbs and axial hypotonia. Upon examination at 9.5 years of age, the patient showed contractures in the hips, knees and had iliotibial band syndrome. The patient also had distal lower limb muscle atrophy and proximal weakness. However, he could sit independently, stand with support and crawled but was incapable of independent ambulation. Additionally, cognitive tests showed mental retardation in association with attention deficit hyperactivity disorder (ADHD). In both patients, deep tendon reflexes were present but were weak. Fibroblasts from this patient were biopsied and were used for the research presented here.

1.2.2.1.1.3 BICD2^{I189F}

The de novo p.I189F heterozygous mutation was identified in a patient which presented at birth and exhibited joint contractures (knee, hips and Achilles tendon) and a calcaneovalgus foot (Oates et al., 2013). Additionally, the patient had both proximal and distal muscle weakness but predominantly distal muscle wasting. Consequently, the patient had delayed motor milestones, an abnormal gait and required the use of a wheelchair. Deep tendon reflexes were reduced in the lower limbs and had an abnormal plantar response. Interestingly, the patient also exhibited mild weakness in the elbow and increased upper limb deep tendon reflexes but also had upper motor neuron involvement. Fibroblasts isolated from this patient were used for the research presented.

1.2.2.1.1.4 Mutations of dynein components and other diseases

In addition to SMA-LED, mutations in *DYNC1H1* have also been reported in Charcot-Marie-Tooth disease (CMT2) which is a peripheral neuropathy affecting

motor and sensory neurons (Lipka et al., 2013). Furthermore, several *DYNC1H1* mutations are also associated with malformation of cortical development and learning disability (Scoto et al., 2015). Mutations in the p150^{Glued} (*DCTN1*) subunit of dynactin are also associated with ALS and Perry syndrome (a late onset neurodegenerative disease associated with parkinsonism) (Farrer et al., 2009; Munch et al., 2004). Interestingly, recently a mutation in *BICD2* has also been found associated with juvenile ALS (Huang and Fan, 2017).

1.2.2.2 Dynein family

The dynein family is one of three cytoskeletal motor protein families and is broadly divided into axonemal and cytoplasmic dynein (Roberts et al., 2013; Bhabha et al., 2016). Axonemal dynein was the first microtubule molecular motor to be identified and was named after the unit of force, dyne (Gibbons, 1963; Gibbons and Rowe, 1965). Today it is understood to mediate microtubule sliding within the microtubule-based core (axoneme) of cilia and flagella in eukaryotes (Roberts et al., 2013; Bhabha et al., 2016). Subsequently, cytoplasmic dynein 1 was isolated in calf brain tissue and was found to mediate microtubule based intracellular transport in the retrograde direction (towards microtubule minus ends) (Paschal et al., 1987; Paschal and Vallee, 1987; Schroer et al., 1989). A second cytoplasmic dynein was later isolated, which exclusively mediates retrograde intraflagellar transport (IFT) (cytoplasmic dynein 2 or IFT dynein) (Ishikawa and Marshall, 2011). Cytoplasmic dynein 1 (referred to from this point as dynein) is the member of the family relevant to SMA-LED and so will be the focus of further discussion.

1.2.2.2.1 Cytoplasmic dynein 1 (dynein)

1.2.2.2.1.1 Structure of the dynein complex

The size and complexity of the approximately 1.5 MDa dynein multisubunit complex has made it difficult to determine its precise structure (Carter et al., 2016). However, significant progress has been made within the last few years using X-ray crystallography and high resolution cryo-electron microscopy (Cryo-EM).

The core of the complex around which the other subunits assemble is formed by a homodimer of DYNC1H1 (hereafter referred to as heavy chain (HC)), see Figure 1.8a, b (Schiavo et al., 2013). Each HC is approximately 500 kDa and is divided into two functional domains, the tail domain which is implicated in cargo binding

and binding to regulators of dynein and the motor domain responsible for the generation of movement (Chowdhury et al., 2015; Cianfrocco et al., 2015). Previously, the dimerization domain of the HC was reported as being between residues 300 and 1140 in the tail domain (Tynan et al., 2000). However, recent studies using high resolution Cryo-EM have demonstrated that the dimerization domain lies approximately within the N-terminal 200 amino acid residues (Figure 1.8b) (Urnavicius et al., 2015; Chowdhury et al., 2015; Carter et al., 2016). After this region each tail forms an elongated rod that harbours the binding site for an intermediate chain (IC) (encoded by either by *DYNC1I1* or *DYNC1I2*) and a light intermediate chain (LIC) (encoded by *DYNC1LI1* or *DYNC1LI2*) (Chowdhury et al., 2015; Pfister et al., 2006; Carter et al., 2016). The LIC binding region is estimated to be between amino acid residues 900 and 990, adjusted from the previously reported position (residues 649-800) (Carter et al., 2016; Chowdhury et al., 2015; Tynan et al., 2000). On the other hand, the IC binding region is estimated to be between amino acid residues 560 and 770 based on Cryo-EM (Carter et al., 2016).

The N-terminus of the two ICs present in the complex form an extended region to which the light chain dimers bind, see Figure 1.8a, b (Carter et al., 2016). These dimers maintain the ICs together and consequently restrict the movement of the HCs, keeping them almost parallel to each other. Each intermediate chain binds to three different types of light chain (LC) (Chowdhury et al., 2015; Pfister et al., 2006). The first type is either Tctex1 encoded by *DYNLT1*, or rp3 encoded by *DYNLT3*, the second is Roadblock/LC7 encoded by either *DYNLRB1* (Roadblock 1) or *DYNLRB2* (Roadblock 2) and the third is LC8 encoded by either *DYNLL1* (LC8a) or *DYNLL2* (LC8b).

X-ray crystallography also began to allow for a better understanding of the structure of the 380 kDa HC motor domain in 2011, see Figure 1.8a, b (Carter et al., 2011; Kon et al., 2011). These and later higher definition studies showed that the motor domain consists of six AAA+ (ATPases Associated with various Activities) domains which are linked together and arranged in a ring formation (Bhabha et al., 2016; Carter et al., 2016). AAA1-4 are able to bind adenosine triphosphate (ATP) but only AAA1, AAA3 and AAA4 are capable of hydrolysis. However, it is AAA1 that is the primary site of ATP hydrolysis and is pivotal for

dynein motility (Bhabha et al., 2016). Conversely, the lack of hydrolysis on AAA2 means that it is thought to act as a stable site for nucleotide binding and contributes to the formation of the AAA1 nucleotide binding site (Roberts et al., 2013). The function of hydrolysis of ATP on AAA3 and AAA4 is not fully understood, but it is thought to play a regulatory role in dynein motility (Bhabha et al., 2016). AAA5 and AAA6 lack the nucleotide binding domains and as such are thought to facilitate the transmission of conformational changes throughout the AAA+ ring (Cianfrocco et al., 2015). The motor domain also contains three other structures, the stalk, buttress/strut and the linker (Bhabha et al., 2016). The coiled-coil stalk emanates from AAA4 and at the tip of its 15 nm length resides the microtubule binding domain (MTBD). The buttress is a shorter coiled-coil which extends from AAA5 and makes contact with the stalk. The linker is composed of 4 bundled α-helices which stretch across the N-terminal portion of the AAA+ ring.

1.2.2.2.1.1.2 Summary of the mechanochemical cycle of dynein

The first step in the mechanochemical cycle of dynein to generate force is the binding of ATP to the nucleotide free AAA1 (going from state 1 to state 2) (Carter et al., 2016; Cianfrocco et al., 2015). This binding alters the AAA1 and causers the buttress to move, which in turn causes the sliding of one of the helices within the coiled coil of the stalk and consequently alters the conformation of the MTBD. Additionally, the binding of ATP to AAA1 causes the linker to clash with AAA4, resulting in its bending, followed by ATP hydrolysis. The motor then diffuses to a new site towards the microtubule minus end and binds. Upon completion of ATP hydrolysis and the release of ADP from the AAA1 site, the tension that keeps the linker bent is released, allowing it to straighten (power-stroke) which moves the other motor domain, the tail and attached cargo forward.

Figure 1.8

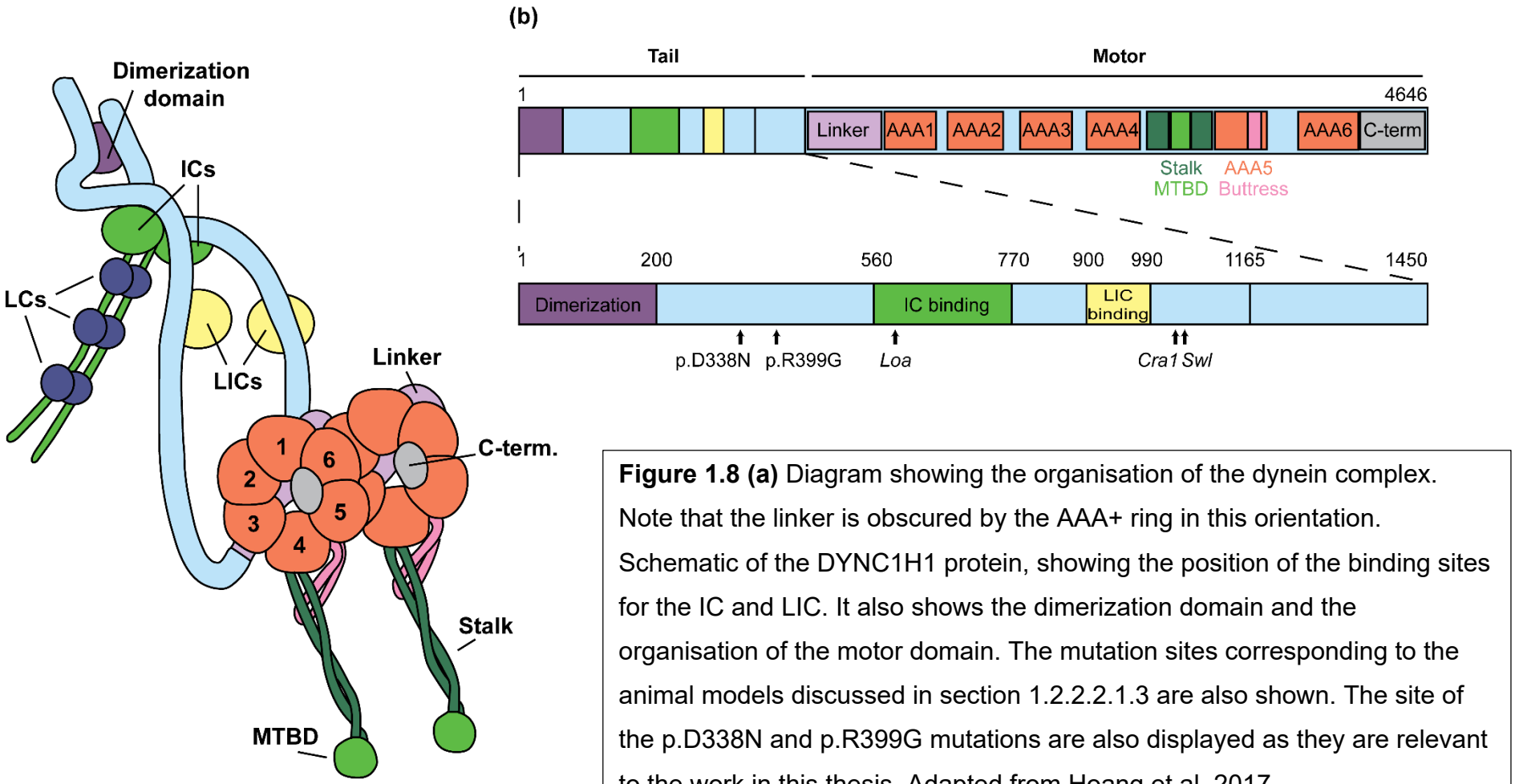

Figure 1.8 (a) Diagram showing the organisation of the dynein complex. Note that the linker is obscured by the AAA+ ring in this orientation. Schematic of the DYNC1H1 protein, showing the position of the binding sites for the IC and LIC. It also shows the dimerization domain and the organisation of the motor domain. The mutation sites corresponding to the animal models discussed in section 1.2.2.2.1.3 are also shown. The site of the p.D338N and p.R399G mutations are also displayed as they are relevant to the work in this thesis. Adapted from Hoang et al. 2017.

1.2.2.2.1.2 Functions of dynein

Dynein is the only molecular motor which moves in the retrograde direction on microtubules over long distances, and therefore is involved in a large variety of cellular processes (Cianfrocco et al., 2015). For example, it is involved in the endocytic pathway, where it is the principal mediator of early endosome transport away from the cell's cortical region as they mature into late endosomes and eventually fuse with lysosomes (Huotari and Helenius, 2011; Granger et al., 2014). Importantly, endosomes transported by dynein are also used as signalling compartments, allowing the transmission of signals from different areas of the cell (Roberts et al., 2013). Neurons are particularly dependent on this process due to the large distance between the site of receptor activation and the site of effector function (Sorkin and von Zastrow, 2009). The dynein-dependent transport of receptor-ligand complexes within endosomes from nerve termini to the cell body includes brain derived neurotrophic factor (BNDF) activated tropomyosin-related kinase B (TrkB) and epidermal growth factor (EGF) activated epidermal growth factor receptor (EGFR) (Garrett et al., 2014). Additionally, dynein is important in the transport of autophagosomes towards their fusion with lysosomes (Kimura et al., 2008). It is also responsible for the transport of several other membrane bound organelles such as mitochondria, lipid droplets and peroxisomes, as well as the transport of stress granules, processing bodies, cytoskeletal filaments and other proteins (Cianfrocco et al., 2015; Roberts et al., 2013).

Outside of its transport function, dynein is also important for several other processes through its ability to generate force and tension (Roossien et al., 2015). For example, it is important in the assembly of microtubules which make up the mitotic spindle and in the segregation of chromosomes (Roberts et al., 2013). However, of relevance to the work presented in this thesis is dynein's role in neuronal and cellular migration, which is explored further below.

1.2.2.2.1.2.1 Impaired axonal transport in motor neuron diseases

Due to the extreme morphology of neurons, they rely on the efficiency of the intracellular transport machinery. Deficits in both retrograde and anterograde axonal transport have been observed in neurons from $SOD1^{G93A}$ mice (Bilsland et al., 2010; De vos et al., 2007). Additionally, mutations in components of the transport machinery have been identified in ALS. Specifically, a base pair change

was found in the gene encoding the p150 subunit of dynactin (*DCTN1*) (Puls et al., 2003). Subsequent mutations were found in this gene associated with both fALS and sALS (Munch et al., 2004). The expression of mutant p150 in mice caused motor neuron disease phenotypes and impaired vesicular transport within the cell bodies of motor neurons (Laird et al., 2008). Impaired axonal transport was also noted in SOD1 transgenic mouse models of ALS (Wijesekera and Leigh, 2009). Subsequently, a mutation which caused a reduction in the expression of kinesin-associated protein 3 (KIFAP3) was found to result in the extension of the lifespan of sALS patients (Landers et al., 2009). Finally, mutations in vesicle-associated membrane protein (VAPB) and charged multivesicular protein 2B (CHMP2B) have also been found in ALS cases. Both of these proteins are important in vesicle trafficking (Nishimura et al., 2004; Cox et al., 2010).

The p.H306, p.I584L and Y970C *DYNC1H1* mutations, which cause SMA-LED, have also been shown to impair the run length of the dynein-dynactin-BICD2 complex (Hoang et al., 2017). Furthermore, several *DYNC1H1* mutations associated with malformation of cortical development were also seen to have the same effect. Some of these (p.K3336N, R3344Q, R3384Q and K129I) also affected the amount of processive dynein-dynactin-BICD2 complexes and the velocity of their travel. A p.H3822P substitution appeared to have the most severe effect as it also impacted microtubule gliding. Additionally, axonal transport deficits are also seen in the *Loa* mouse model of SMA-LED, see section 1.2.2.2.1.3.1 for details (Hafezparast et al., 2003).

1.2.2.2.1.2.2 Dynein in migration and neurodevelopment

Dynein is implicated in neuronal migration during neurodevelopment due to the discovery of developmental brain diseases associated with mutations in *DYNC1H1* and genes encoding dynein adaptors (Vallee et al., 2009). Multiple, mutations in *DYNC1H1* have been reported to cause malformation of cortical development associated with intellectual disability, including the p.R399G mutation (Scoto et al., 2015). Lissencephaly 1 (Lis1) is a dynein adaptor which is named after the term which describes the smooth surface of the cortex caused by defects in neuronal migration, a phenotype which occurs in patients with *Lis1* mutations (Wynshaw-Boris and Gambello, 2001). Furthermore, analysis of brains from the *Loa* animal model of SMA-LED also showed neuronal migration defects (see section

1.2.2.2.1.3.1) (Ori-McKenney and Vallee, 2011; Hafezparast et al., 2003). More recently, Dr Muruj Barri in the Hafezparast lab, identified a decrease in paxillin phosphorylated at Tyr118 (pPax^{Y118}) in *Loa* mouse embryonic fibroblasts (MEFs) (Barri, 2015). Paxillin is a key focal adhesion (FA) protein important for cell migration. Similarly, she also identified a decrease in pPax^{Y118} in DYNC1H1^{R399G} patient fibroblasts. Furthermore, she observed that FAs were smaller and that *Loa* MEFs migrated more slowly in a wound healing assay. Interestingly, it has been previously reported that the IC interacts with paxillin (Rosse et al., 2012). However, this was not replicated in the Hafezparast lab by Dr Muruj Barri (Barri, 2015).

1.2.2.2.1.2.2.1 Cell migration and focal adhesions

A key part of cellular migration is the ability for cells to apply force to their extracellular environment in order to gain traction to facilitate their movement (Case and Waterman, 2015). The internal force that needs to be transmitted to their environment is principally generated by the actin cytoskeleton. In fact, it is the polymerization of actin filaments which drives cellular migration (Pollard and Cooper, 2009). The transmission of force to the extracellular environment occurs at the site of integrin attachment to the extracellular matrix (ECM), commonly known as FAs (Case and Waterman, 2015). Integrins are transmembrane proteins, which form α and β subunit heterodimers and directly attach to components of the ECM (Krause and Gautreau, 2014).

However, for cells to be able to undergo directional migration they need to become polarized (Huttenlocher, 2005). Polarized cells have a leading edge, which points in the direction of travel and a trailing a trailing edge (Figure 1.9). Cell polarisation requires complex signalling, mainly regulated by the Rho family (Mayor and Etienne-Manneville, 2016). At the leading edge, Rac and Cdc42 cause the protrusion of the membrane, forming both filopodia and lamellipodia, while inducing the interaction between integrins and the ECM (Mayor and Etienne-Manneville, 2016). Simultaneously, at the trailing edge, a signalling pathway induces the contraction of cell. Lamellipodia are a flat thin extension of the membrane at the leading edge, while filopodia are “finger-like” protrusions at the edge of the lamellipodia (Krause and Gautreau, 2014). Filopodia are formed of bundled actin filaments and are used by the cell to detect cues for the migration

from their environment and are particularly important in neuronal guidance (Leijnse et al., 2015). However, the focus here will be on lamellipodia as this is the site of FA formation.

Within the lamellipodia, there is rapid actin polymerization which is mainly driven by the actin nucleator actin-related protein 2/3 (ARP2/3) (Krause and Gautreau, 2014). ARP2/3 forms new actin filaments branching from existing filaments. Additionally, proteins such as ENA/VASP and formins stop the capping of the nascent actin filaments and speed up elongation. This polymerization of actin creates a pushing force on the leading edge of the membrane (Case and Waterman, 2015). However, at the edge of the lamellipodia and lamella (region behind the lamellipodia) most of the lamellipodial actin networks undergoes depolymerization. This means the lamellipodial actin network is undergoing treadmilling with new actin monomers added at the tip of the lamellipodia and depolymerization occurring at the base (Case and Waterman, 2015; Krause and Gautreau, 2014). The actin treadmilling and the counter-force of the actin filaments pushing against the membrane drive the retrograde flow of actin at the lamellipodia (Case and Waterman, 2015). Additionally, at the lamella the molecular motor myosin II exerts a pulling force on the actin bundles which reorganises and disassembles them, which forms the basis of actin retrograde flow within the lamella. Interestingly, in neuronal growth cones, the separation between the lamella and lamellipodia is less well defined, and it has been shown that myosin II also contributes to lamellipodial retrograde flow (Forscher and Smith, 1988; Case and Waterman, 2015).

The crucial function of FAs is to link the ECM to the actin network, allowing them to act as anchor points which slow retrograde flow (Case and Waterman, 2015). Talin and vinculin are thought to be the main constituents of this molecular clutch thanks to their interaction with actin (Jansen et al., 2017). This changes the balance between retrograde flow and actin polymerization and consequently allows actin polymerization to push against the membrane forming protrusions. Furthermore, the force applied against the FAs by the retrograde flow of the actin network drives the propulsion of the cell forward (Case and Waterman, 2015; Mayor and Etienne-Manneville, 2016). The trailing edge is also important in the disassembly of FAs and the contraction of the cell body (Mayor and Etienne-

Manneville, 2016). Similar mechanisms underlie the extension of axons towards their targets guided by the growth cone. In fact, growth cone advance was seen to be inversely proportional to the speed of the actin retrograde flow (Lin and Forscher, 1995).

FAs are highly dynamic structures which consist of an extensive repertoire of proteins including scaffolding proteins, kinases, phosphatases and structural proteins (Case and Waterman, 2015). FAs initially form within the lamellipodial protrusion as nascent FAs which are small and punctate in morphology (Zaidel-Bar et al., 2003; Choi et al., 2008; Lawson et al., 2012), as shown in Figure 1.9. These have a short half-life and most disassemble, while the remainder are stabilised and undergo maturation into fully formed FAs (Case and Waterman, 2015). Linkage to F-actin and myosin II activity is required for the maturation of FAs (Sun et al., 2014). Finally, they continue to elongate due to the retrograde flow of actin, becoming fibrillar adhesions and are eventually disassembled at the rear of the cell (Zaidel-Bar et al., 2003; Case and Waterman, 2015).

Figure 1.9

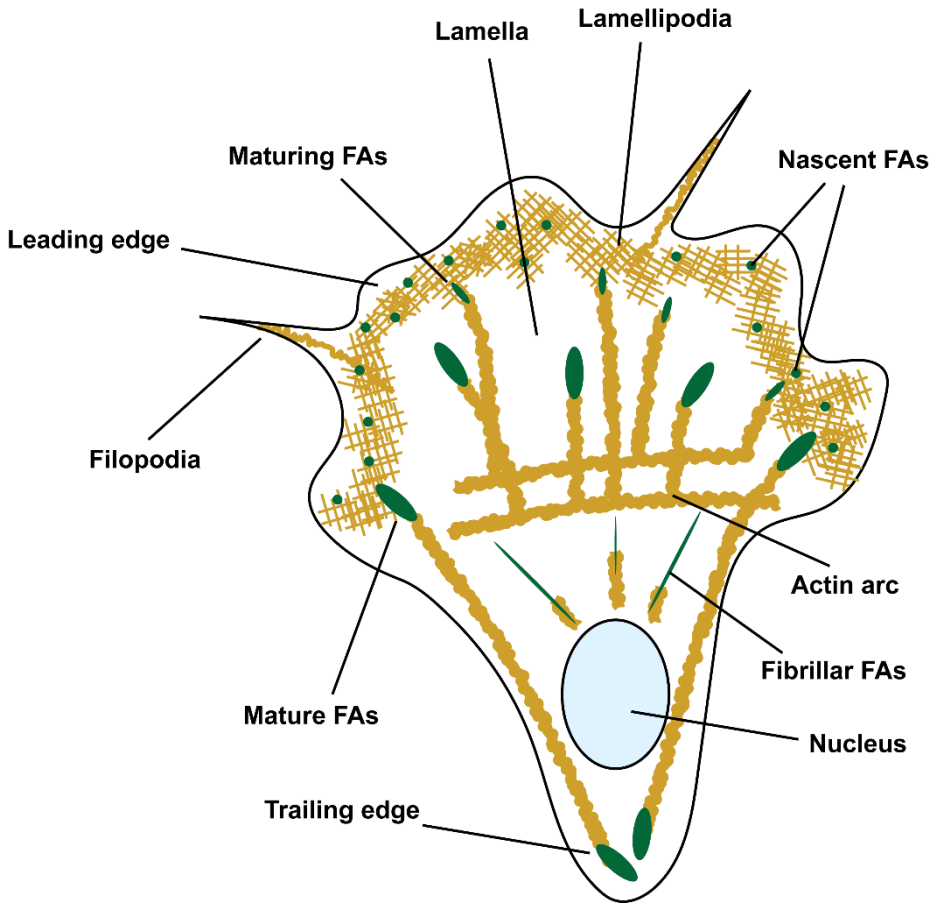

Figure 1.9 Illustration of a polarized cell undergoing migration. At the leading edge, nascent focal adhesions (FAs) are forming and begin to mature due to the contractility of acto-myosin. At the lamella, large mature FAs can be seen which eventually become fibrillar FAs. FAs are disassembled at the trailing edge. Adapted from Clainche & Carlier 2008.

1.2.2.2.1.2.2.2 Paxillin

Paxillin is one of the central proteins within FAs, where it acts as a scaffolding protein for the recruitment of other structural and signalling molecules (López-colomé et al., 2017). The paxillin gene (*PXN*) on chromosome 12q24 is highly conserved and expressed in most tissues, with the nervous system exhibiting the lowest expression. There are four known alternatively spliced isoforms of paxillin with different expression patterns (Schaller, 2001; Tumbarello et al., 2005). Isoform α is the canonical isoform and is the most widely expressed (López-colomé et al., 2017). Isoform β is formed by the insertion of exon 15 and exhibits a more restricted expression pattern than α (López-colomé et al., 2017). Isoform γ is formed when an alternative 5' donor site of exon 16 is used, and appears to be involved in cell differentiation. Finally, isoform δ has a shorter N-terminal domain in comparison to isoform α and is only expressed in epithelial cells. While all four isoforms are found in humans, in mice only the α, β and δ isoforms are detected (Mazaki et al., 1998; Tumbarello et al., 2005).

Structurally, paxillin consists of a proline rich region at the N-terminus followed by a series of 5 leucine-rich domains (LD1-5) (Figure 1.10) (López-colomé et al., 2017). The proline rich region forms the site for the binding of SH3 containing proteins, and the LD domains mediate interactions with signalling and structural proteins containing SH2 domains. Table 1.13 summarises the binding partners known for paxillin LD domains. Importantly these include members of the Src proto-oncogene, non-receptor tyrosine kinase (Src) family and focal adhesion kinase (FAK). Through its association with FAK, paxillin is also known to indirectly interact with p130cas, growth factor receptor bound protein 2 (Grb2) and talin (Turner, 2000). The C-terminal portion of the protein is formed of four cysteine-histidine-enriched LIM domains.

Figure 1.10

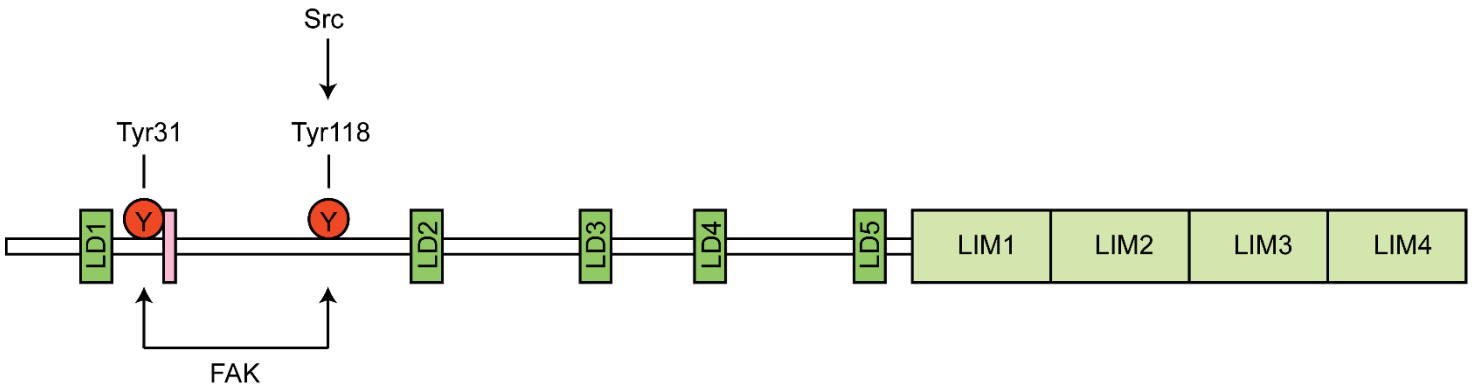

Figure 1.10 Schematic representation of the structure of paxillin, showing leucine-rich domains 1-5 (LD1-5) and 4 LIM domains. The SH3 binding site is shown in pink, while the Tyr31 and Tyr118 sites are also indicated. FAK phosphorylates both Tyr31 and Tyr118, and Src phosphorylates Tyr118. Adapted from López-Colomé et al. 2017.

Paxillin is one of the first proteins recruited to nascent FAs, which is an indicator of its importance in their assembly (Deakin and Turner, 2008). Paxillin is recruited to FAs primarily via its LIM3 domain with some involvement of LIM2, a process facilitated by the phosphorylation of S457/481 on LIM3 and T403 on LIM2 (Brown et al., 1996, 1998). Of note is the fact that FAK assembles at nascent FAs earlier than paxillin (Hu et al., 2014). The activation of integrin results in the autophosphorylation of FAK at Tyr397 which creates a binding site for the SH2 domain of the Src kinases (López-colomé et al., 2017). Subsequently, the active FAK/Src complex phosphorylates paxillin (Src phosphorylates Tyr118 and Tyr88, while FAK phosphorylates Tyr31 and Tyr118. The phosphorylation at these sites and various others regulate various signalling pathways and the recruitment of various binding partners, which coordinate to remodel the cytoskeleton to facilitate migration (López-colomé et al., 2017). Additionally, paxillin phosphorylation by upstream pathways regulates the expression, turnover and the localisation of paxillin. However, of particular relevance to this thesis is the phosphorylation at the Tyr118 site (which is functionally coupled to Tyr31 phosphorylation) and so this will be explored further.

Table 1.13

Paxillin LD motif	Direct interactions	Indirect interactions
LD1 - LDALLADL	Actopaxin, Vinculin/metavinculin, Papillomavirus E6 protein.	Actin (via actopaxin and vinculin).
LD2 - LDRLLLEL	Vinculin/metavinculin, Focal adhesion kinase (FAK). (likely to mediate interaction with PYK2, a FAK family member)	Not determined.
LD4 - LDELMASL	Vinculin (weak), FAK1, Paxillin kinase linker (PKL), Clathrin. (likely to mediate interaction with PYK2, a FAK family member)	PIX (via PKL), PAK (via PIX), Nck (via PAK).

Table 1.13 Summary of paxillin binding partners at LD domains. Adapted from Turner 2000.

1.2.2.2.1.2.2.3 Paxillin phosphorylation at Tyr118 and Tyr31

As discussed above, paxillin phosphorylation at Tyr118 is mediated by both Src and FAK, while FAK is solely responsible for Tyr31 phosphorylation (López-colomé et al., 2017). The phosphorylation of paxillin at these sites is associated with both the assembly and the turnover of FAs (Zaidel-Bar et al., 2007). In cells lacking either FAK or Src, which consequently decreases paxillin phosphorylation at Tyr118 and Tyr31, FAs are more stable and appear larger (Ilić et al., 1995; Volberg et al., 2001). Additionally, in the absence of FAK there is a slower turnover of FAs (Webb et al., 2004). This is contrast to faster turnover in cells lacking tyrosine phosphatase Shp2 (Von Wichert et al., 2003). Additionally, phosphorylation of paxillin at Tyr118 and Tyr31 is higher in nascent adhesions in comparison to mature FA, and completely absent in fibrillar adhesions (Zaidel-Bar et al., 2007). These differences in the phosphorylation state of paxillin at these sites correlates with the level of turnover at each of those adhesion types. Highest turnover is found at nascent adhesions, followed by FAs, while fibrillar adhesions exhibit the slowest turnover. Interestingly, the expression of non-phosphorylatable paxillin at Tyr118 and Tyr31 caused a reduction in nascent adhesions, mature FAs, and increased fibrillar adhesions, while also causing a reduction in the adhesion turnover. Conversely, the expression of phosphomimetic paxillin increased the number of nascent adhesions and reduced the number of fibrillar adhesions, while dramatically increasing the turnover of both nascent and mature FAs. These experiments confirmed that Tyr118 and Tyr31 are crucial for regulating the turnover of adhesions which was shown to be mediated by an increased recruitment of FAK. The turnover of adhesions is critical for migration as they can counteract the forward propulsion of cells (Stehbens and Wittmann, 2014). In line with this, disrupting FAK-paxillin interactions has been shown to negatively influence cell migration (Deramaudt et al., 2014).

Interestingly, the phosphorylation at these sites has been shown to impact the turnover of paxillin at adhesion sites. The inhibition of Src family members kinases by treatment with PP2 causes a reduction in the turnover rate of paxillin at previously formed adhesion sites (Qin et al., 2015).

In addition to the regulation of FA dynamics, the phosphorylation of paxillin at Tyr118 and Tyr31 and association with FAK allows for the binding of several

proteins. For example, it creates a binding site for the SH2 domain of Crk and p120RasGAP which either lead to the activation of Rac or inhibition of Rho respectively (López-colomé et al., 2017).

A mechanism which regulates paxillin phosphorylation is the activity of myosin II (Pasapera et al., 2010). Myosin II activity increases the FAK-Src mediated phosphorylation of Tyr118 and Tyr31. In fact, inhibition of myosin II by treatment with blebbistatin causes a drastic reduction in the phosphorylation of Tyr118 and Tyr31. Similar results were obtained by the use of a Rho kinase (ROCK) inhibitor which is upstream of myosin II and regulates its activity by regulating the phosphorylation of the myosin light chain (MLC) (Ridley, 2003; Kaneko-Kawano et al., 2012). ROCK acts in a twofold fashion, it not only directly phosphorylates MLC but also dephosphorylates myosin phosphatase targeting subunit (MYPT1) which inactivates myosin phosphatase activity (Kaneko-Kawano et al., 2012). Upstream of ROCK is RhoA, which has previously been reported to stimulate FA formation by triggering acto-myosin contractility (Chrzanowska-Wodnicka and Burridge, 1996).

1.2.2.2.1.3 Mouse models of *Dync1h1* mutations

1.2.2.2.1.3.1 *Loa* mouse model

The Legs at odd angles (*Loa*) model of dynein dysfunction originated from mutagenesis programme in which mice were treated with the ENU chemical mutagen (Schiavo et al., 2013). The name given to these mice alludes to the fact that the mutants exhibited hind limb grasping when suspended by the tail. This abnormal grasping reflex is a sign of deficits in the neuromuscular system. Subsequently, the causative mutation was mapped to chromosome 12 and further analysis revealed a T to A transversion in the *Dync1h1* gene causing phenylamine at position 580 to be substitute by tyrosine (p.F580Y) (Witherden et al., 2002; Hafezparast et al., 2003). Behavioural assessment revealed that heterozygous *Loa* mice have a reduced grip strength and limb tone and performed worse in the wire manoeuvre compared to wild-type mice (Rogers et al., 2001). Reduced rota-rod testing scores also suggested progressive deficits in motor function, balance and co-ordination in the *Loa* mice. Subsequent analysis confirmed that heterozygous *Loa* mice have an age-dependent progressive muscle atrophy and reduced locomotor ability (Hafezparast et al., 2003). Histopathological analysis

revealed a loss of motor neurons in the anterior horn of the spinal cord. Homozygous *Loa* mice have a more severe phenotype which results in death within 24 hours of birth, whilst heterozygotes have a normal lifespan. Homozygous *Loa* mice also had a 50% reduction in the number of anterior horn cells in the spinal cord. In these mice, the migration and pathfinding of facial motor neurons to their destination within the hindbrain was also defective (Hafezparast et al., 2003). Similarly, they also exhibit defective neuronal migration causing abnormalities in neocortical lamination (Ori-McKenney and Vallee, 2011). It has also been shown that *Loa* heterozygous mice can develop early-onset proprioceptive sensory defect as indicated by the loss of lumbar DRG neurons and the lack of the Hoffman's reflex (Chen et al., 2007; Ilieva et al., 2008). Furthermore, nerves innervating the limbs in *Loa* heterozygous mice showed reduced branching (Hafezparast et al., 2003). Similarly, there was also an altered morphology of dendrites from trigeminal motor neurons in heterozygous mice (Wiggins et al., 2012).

Importantly, in motor neuron cultures derived from *Loa* homozygous mice there was a significant impairment of dynein mediated fast retrograde axonal transport (Hafezparast et al., 2003). Furthermore, live cell analysis of lysosomes in wild-type and *Loa* mutant axons further confirmed that the *Loa* mutation impairs retrograde axonal transport (Ori-McKenney et al., 2010; Hafezparast et al., 2003). Defective axonal transport caused by the *Loa* mutation could be the underlying cause of the neurodevelopmental phenotypes observed in these mice (Hafezparast et al., 2003; Ori-McKenney et al., 2010). As a consequence of altered transport, in *Loa* mice there is abnormal transport of signalling endosomes which causes aberrant ERK1/2 and c-FOS activation (Garrett et al., 2014).

Interestingly, single molecule analysis by the use of quantum dot and optical-trap experiments on purified wild-type and mutant dynein underlined reduced processivity, early run termination and diminished motor coordination as the underlying cause of the observed impaired retrograde transport (Ori-McKenney et al., 2010). However, these studies do not explain how the *Loa* mutation directly impairs the dynein complex.

The *Loa* mutation resides within the IC binding region of the HC and in an area which had previously been thought to constitute the dimerization domain

(Hafezparast et al., 2003; Tynan et al., 2000; Carter et al., 2016; Urnavicius et al., 2015; Chowdhury et al., 2015). Interestingly, it has been shown that this mutation alters the affinity of the HC to several other components of the dynein complex and the stability of the complex (Deng et al., 2010; Ori-McKenney et al., 2010). Immunoprecipitation experiments have shown that there is an increased affinity between the IC and *Loa*/*Loa* HC in comparison to wild-type (Deng et al., 2010). A similar effect was also seen between *Loa/Loa* mutant HC and the LIC. Consequently, Tctex-1 was also seen to associate more tightly with the IC, whilst the interaction of the complex with dynactin (a dynein adaptor which regulates some cargo binding and processivity) is reduced.

1.2.2.2.1.3.2 *Cra1* mouse model

As with the *Loa* model, the Cramping-1 (*Cra1*) model arose from an ENU mutagenesis program (Hafezparast et al., 2003). This model has a tyrosine to cysteine substitution at position 1055 (p.Y1055C). Heterozygous mice with this mutation also exhibit progressive locomotor deficits and the same grasping reflex as the *Loa* model. Furthermore, *Cra1* homozygous mice also die within 24 hours of birth, are unable to feed or move within that time and have a severe loss of anterior horn cells embryonically. On the other hand, heterozygous mice have a normal life span but were reported to have a progressive loss of spinal motor neurons within the anterior horn as observed at 3 and 16 months of age. However, in the years after the first description of these mice conflicting reports have arisen. For example, a study found that there was no loss of either upper or lower motor neurons in the *Cra1* mice but reported degeneration of sensory neurons (Dupuis et al., 2009). Furthermore, they also found no abnormalities at the neuromuscular junctions (NMJs). However, a later study showed that *Cra1* mice exhibit early onset but non progressive neuronal dysfunction (as measured by grip strength) without a loss of sensory neurons and abnormalities at NMJs were detected (Courchesne et al., 2011). It is not clear what underlies the variation seen in reports concerning these mice.

1.2.2.2.1.3.3 *Swl* mouse model

The sprawling (*Swl*) mouse model was first described in 1967, but the mutation was only later identified as a X-radiation induced 9 bp deletion within exon 12 of the *Dync1h1* gene (Chen et al., 2007). The deletion corresponds to residues 1040-

1043, which causes the substitution of four amino acid residues (glycine, isoleucine, valine and threonine) to a single alanine residue. Like the other mouse models described, homozygosity for *Swl* was embryonically lethal and heterozygous mice display a hind limb grasping phenotype when suspended by the tail. Heterozygous mice exhibit a normal lifespan but have proprioceptive sensory neuropathy with an early onset, which was underlined by the loss of lumbar proprioceptive DRG neurons and muscle spindles. Importantly, α-motor neurons were spared, even in mice which had been aged. Retrograde axonal transport of nerve growth factor (NGF) is also impaired in *Swl* heterozygous mice. Interestingly, this study also revealed that neither *Swl*, *Loa* or *Cra1* mutations impair the homodimerization of the HC in the dynein complex (Zhao et al., 2016). As indicated previously, the dimerization domain is no longer thought to be between residues 300 and 1140 which encompasses the site of these mutations, but within the N-terminal 200 residues (Urnavicius et al., 2015; Chowdhury et al., 2015; Carter et al., 2016; Tynan et al., 2000).

1.2.2.2.1.4 Dynein adaptors

Since a single type of dynein is responsible for nearly all retrograde transport in eukaryotic cells, an added layer of complexity is required to regulate dynein's selective interaction with a myriad of different cargoes (Roberts et al., 2013; Vallee et al., 2012). This is achieved via interactions with adaptor proteins, which in some cases also regulate the cellular localisation of dynein and its processivity, see Table 1.14 for summary (Vallee et al., 2012). One of these adaptors, dynactin is an essential co-actor without which dynein is largely non-processive (McKenney et al., 2014). However, it has become increasingly clear that for a stable dynein-dynactin complex to form a second adaptor protein is required such as BICD2 (Carter et al., 2016).

1.2.2.2.1.4.1 Dynactin

Like dynein, dynactin is itself a 1 MDa multisubunit complex formed from 23 subunits assembled around an actin-like filament which is made up of Actin related protein-1 (Arp1) (Carter et al., 2016). The core filament is formed from 2 protofilaments which wrap around each other (Urnavicius et al., 2015). The top protofilament consists of 5 Arp1 subunits and the bottom protofilament consist of 3 Arp1 subunits and a β-actin subunit (Figure 1.11). As with actin filaments, the

dynactin filament has a barbed and a pointed end which are capped. The barbed end is capped by a CapZαβ heterodimer and the pointed end is capped by Arp11, both capping proteins bind the top and bottom protofilaments. However, at the pointed end, Arp11 then binds to p25, p27 and p67 which may be involved in cargo attachment. On top of this filament there is a shoulder domain consisting of a bundle of α-helices which contains 4 copies of p50/dynamitin, 2 copies of p24 and 2 copies of the largest subunit of dynactin, $p150^{Glued}$. The $p150^{Glued}$ subunits form a long projection, where its C-terminus resides within the shoulder and the N-terminus contains the CAP-Gly domain which interacts with microtubules. However, the shorter p135 isoform of $p150^{Glued}$ may instead be present which lacks this microtubule binding domain.

Table 1.14

Adaptor	Function	Ref.
Lissencephaly 1 (LIS1)	Interacts with the motor domain of the HC. Important for dynein recruitment and regulation particularly in the initiation of axonal transport and in cell migration.	(Jaarsma and Hoogenraad, 2015)
Nuclear distribution protein E/Nude like1(NudE/Nudel)	Interact with the IC and Lis1 and so modulates Lis1 interaction with dynein and therefore affects several dynein functions. Can also regulate interactions with cargo.	(Cianfrocco et al., 2015; Jaarsma and Hoogenraad, 2015)
Dynactin	Acts as a cargo adaptor but is important for the full activation of dynein (see sections 1.2.2.2.1.4.1 and 1.2.2.2.1.5)	(Cianfrocco et al., 2015)
Bicaudal D homog 2 (BICD2)	Cargo adaptor and allows for a stable dynein/dynactin complex (see sections 1.2.2.2.1.4.2 and 1.2.2.2.1.5)	
Spindly	Important for the recruitment of dynein to the kinetochores.	
Hook family	Act as cargo adaptors and can also stabilise dynein/dynactin complex	

Table 1.14 Summary dynein adaptors and their function.

Figure 1.11

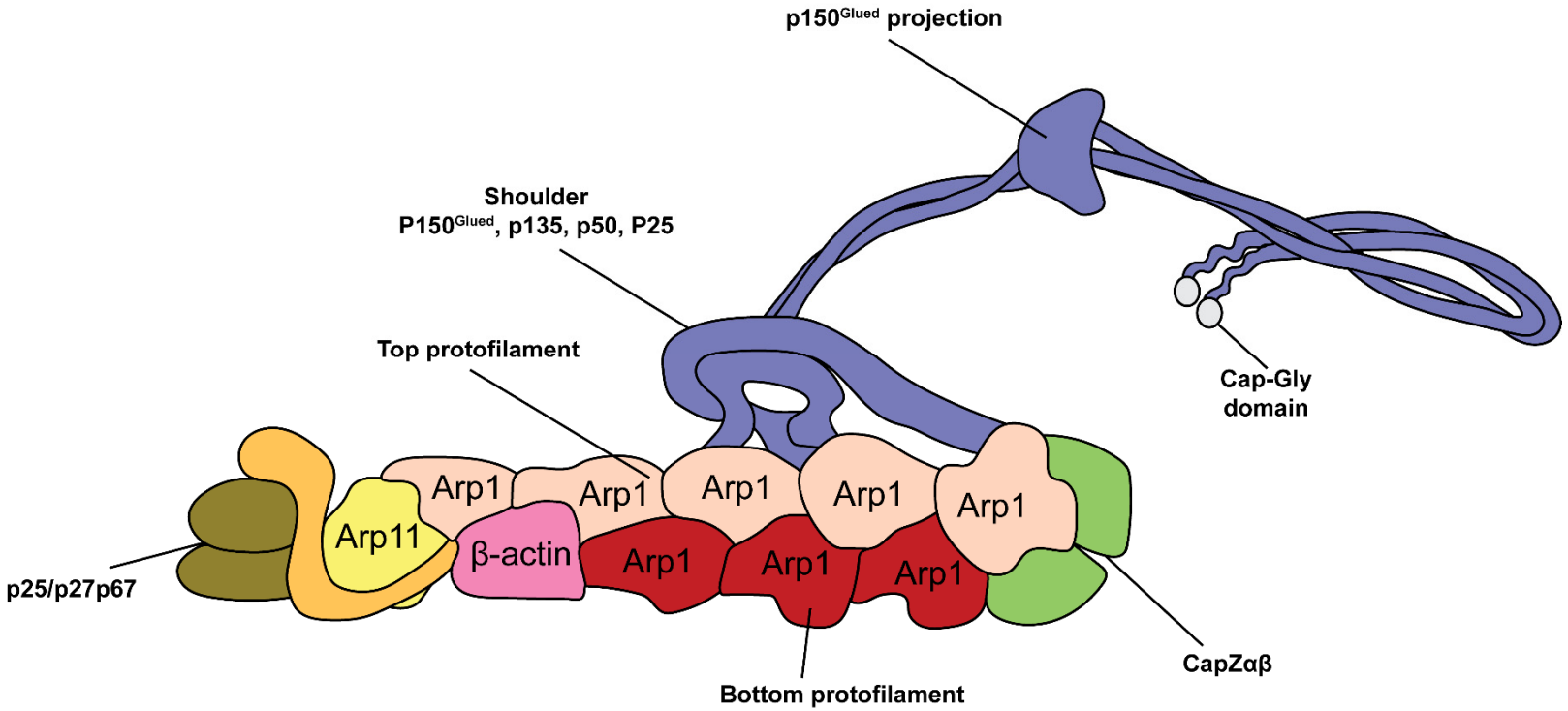

Figure 1.11 Figure showing the structure of dynactin. Dynactin consists of two protofilaments (top and bottom), the top consists of 5 Arp1 subunits, the bottom consists of 3 Arp1 subunits and a β-actin subunit. The barbed end is capped by a CapZαβ heterodimer and the pointed end is capped by Arp11, which in turn binds to p25, p27 and p67. The shoulder is formed of 4 copies of p50/dynamitin, 2 copies of p24 and 2 copies of $p150^{Glued}$. The $p150^{Glued}$ subunits form a long projection which ends with a Cap-Gly domain. Adapted from Linas Urnavicius et al. 2015; Carter et al. 2016.

1.2.2.2.1.4.2 Bicaudal D homolog 2 (BICD2)

Bicaudal D (BICD) was originally identified in Drosophila where mutations in its gene (*BicD*) produced two-tailed (bicaudal) embryos as a result of altered mRNA transport (Mohler and Wieschaus, 1986; Wharton and Struhl, 1989; Suter et al., 1989; Swan and Suter, 1996; Swan et al., 1999; Suter and Steward, 1991; Mach and Lehmann, 1997). Mammals possess two BICD orthologs, BICD1 and BICD2 and two distantly related proteins, Bicaudal D related protein 1 (BICDR-1) and Bicaudal D related protein 2 (BCDR-2). BICD1, BICD2 and BICDR-1 have been shown to interact with the dynein complex, but this section will focus on BICD2 as it is better documented and is mutated in SMA-LED (Schlager et al., 2010; Hoogenraad et al., 2001; Matanis et al., 2002; Neveling et al., 2013).

BICD2 consists of three coiled-coil (CC) domains. The N-terminal CC1 domain and the central CC2 domain mediate the proteins interaction with the dynein complex and dynactin (Hoogenraad and Akhmanova, 2016). On the other hand, the C-terminal CC3 domain mediates cargo binding via its association with cargo-associated proteins (Hoogenraad and Akhmanova, 2016; Hoogenraad et al., 2001). Interestingly, CC2 also mediates BICD2's interaction with the kinesin-1 family (KIF5) (Grigoriev et al., 2007).

The CC domains of BICD2 allow the protein to homodimerize. Additionally, a model has been suggested in which the interaction of the N-terminal CC1/CC2 domain with the C-terminal CC3 domain maintains BICD2 in a diffuse inhibited state (Hoogenraad et al., 2001, 2003; Splinter et al., 2012; Liu et al., 2013). Upon interaction of the C-terminal portion with a cargo-associated protein, the inhibitory interaction is broken and BICD2 is able to bind to the dynein complex.

Interestingly, BICD2 has been implicated in the recruitment of the dynein/dynactin complex to nuclear pore complexes. A study in 2010 used pull-down assays which utilised a tagged C-terminal fragment of BICD2 as bait followed by mass spectrometry and found that Ran-binding protein 2 (RanBP2), a nuclear pore complex protein, was a potential BICD2 binding partner (Splinter et al., 2010). This interaction was further verified using co-immunoprecipitation of endogenous RanBP2 with endogenous BICD2. Subsequently, evidence confirmed that the C-terminal portion of BICD2 specifically interacts with a region of RanBP2 previously

known to interact with kinesin-1 isoforms. Furthermore, experiments suggested that RanBP2 is required for the recruitment of BICD2 to nuclear pore complexes during the G2 phase of the cell cycle. Specifically, it was shown that during G2, BICD2 switches from binding Rab6-bound membranes to binding at nuclear pore complexes at the nuclear envelope and cytoplasmic annulate lamellae (stacks of cytoplasmic nuclear pore complexes). Importantly, evidence showed that BICD2 is required for the recruitment of the dynein/dynactin complex to nuclear pore complexes. Therefore, a mechanism emerges whereby RanBP2 recruits BICD2 to nuclear pore complexes and BICD2 in turn recruits dynein/dynactin to these same complexes. This recruitment of dynein/dynactin/BICD2 to the nuclear envelope by RanBP2 was shown to be important for the relative positioning of the centrosome and nuclear envelope during prophase. Interestingly, it was also suggested that BICD2 regulates the activity of kinesin-1, which was found to be antagonistic to the activity of dynein/dynactin during prophase. In summary, BICD2 is important for proper localisation of the centrosome and nucleus during mitotic entry via its ability to bind RanBP2, dynein/dynactin and kinesin-1. A later study showed that LIS1 is required for the targeted recruitment of dynein/dynactin to nuclear pore complexes by BICD2 (Splinter et al., 2012).

Interestingly, this function of BICD1 and dynein/dynactin has been linked to the interkinetic nuclear migration (INM) exhibited by radial glial progenitor (RGP) cells, which are precursors for neurons and glial cells within the vertebrate neocortex (Hu et al., 2013). INM describes the oscillation of the nucleus during mitotic division of RGP cells. During G1 the nucleus ascends basally along the elongated RGPs to undergo S phase, and then descends to the ventricular surface during G2. This behaviour of the nucleus had previously been linked to microtubule motor proteins (Tsai et al., 2010a). It was found that microtubules were orientated with their minus ends pointed towards the apical surface, whilst the plus ends were faced towards the basal surface. Interestingly, knockdown of DYNC1H1 or LIS1 resulted in the inhibition of nuclear migration towards the apical surface. Conversely, RNAi directed at KIF1A impaired nuclear migration towards the basal surface. Similar results were seen after the inhibition of dynactin (Del Bene et al., 2008). It was found that RanBP2 recruitment of dynein/dynactin was important for early apical movement of the nucleus in these cells during G2 (Hu et al., 2013).

Late apical migration was mediated by a different dynein recruitment mechanism to the nuclear pores, in which nucleoporin 133 (Nup133) recruits centromere protein F precursor (CENP-F), which in turn recruits NudE and NudEL and consequently dynein. Interference with these processes resulted in impaired neurogenesis and migration. Additionally, RanBP2 phosphorylation by Cdk1 was shown to facilitate the recruitment of BICD2 and consequently dynein/dynactin and microtubules to nuclear pore complexes during apical nuclear migration (Baffet et al., 2015).

Figure 1.12

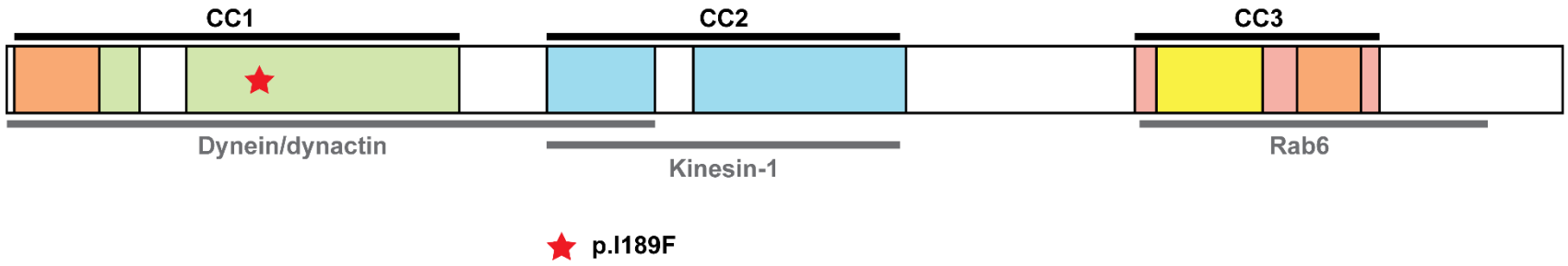

Figure 1.12 Schematic of BICD2 structure, showing the location of the p.I189F substitution. BICD2 consists of three coiled-coil (CC) domains. CC1 mediates interactions with dynein/dynactin (green), CC2 mediates interactions with kinesin-1 (blue) and CC3 mediates cargo binding through cargo-associated proteins like Rab6 (red). Within CC3 there is a conserved BICD domain. The orange boxes represent other highly conserved regions within CC1 and CC3. Adapted from Hoogenraad & Akhmanova 2016

1.2.2.2.1.5 Activation of dynein by the dynein/dynactin/BICD2 complex

Recent studies have shown that purified dynein is not able to engage in long distance processive motion which is characteristically seen *in vivo* (McKenney et al., 2014; Schlager et al., 2014). Instead, it has been shown that for full processsivity to be achieved both dynactin and a cargo adaptor such as BICD2 or Hook3 are required (McKenney et al., 2014; Schlager et al., 2014; Schroeder and Vale, 2016; Olenick et al., 2016). This implies that dynein is present in an inhibited state which requires activation (Dodding, 2014).

Interestingly, dynein exists in two structural configurations. In the first, the two motor heads are apart (open dynein) and in other the motor heads appear to be positioned together (known as the phi-particle) (Amos, 1989). It has been suggested that dynein in its phi-particle conformation represents the inhibited state due to the self-dimerisation of the motor domains (Torisawa et al., 2014).

Cryo-EM has recently elucidated how dynein is autoinhibited and how this is inhibition is released by the binding of dynactin and a cargo adaptor like BICD2 (Zhang et al., 2017b). The purification of dynein from insect cells yielded a large proportion of dynein in the phi-particle configuration (>85 %). EM revealed that in the phi-particle a novel direct interaction between the HCs near the LIC binding domain is present, while it was not found in the open dynein configuration, indicating that it may serve to stabilise the motor domain dimerization in the phi-particle. The motor domain in the phi-particle configuration is held together by interactions at the linker, AAA4, AAA5 and stalk domain. In this configuration, the stalks (containing the MTBD) are locked in the low microtubule affinity conformation. This phi-particle configuration represents autoinhibited dynein with lower microtubule binding affinity and lower affinity for dynactin/BICD2. However, the switch between the phi-particle state to an open state is not sufficient to induce long distance processive movement. Dynein in the open state is predominantly represented by a configuration in which the stalks are inverted (pointed towards each other) and therefore non-processive. However, the binding of dynactin/BICD2 causes a twist in the HC, changing the alignment of the motor domain meaning that the stalks are then predominantly found in a parallel arrangement and constrains them in this position. This parallel arrangement of the stalk is thought to be more conducive to microtubule binding.

The structure of the dynein/dynactin/BICD2 (DDB) complex has also been elucidated using Cryo-EM (Urnavicius et al., 2015), see Figure 1.13. The dynein HC tail interacts with the Arp1 filament of dynactin and occupies the length from the β-actin subunit to the barbed end of the filament. An approximately 270 amino acid coiled coil at the N-terminus of BICD2 stretches the length of the dynactin filament (its C-terminus is at the pointed end and N-terminus at the barbed end) and stabilises this interaction. Specifically, this occurs in the clefts of Arp1-D and Arp1-F, and Arp1-F and β-actin. BICD2 also resides between one of the HCs and dynactin.

In summary, the processes described above explain the necessity of both dynactin and a cargo adaptor such as BICD2 for the activation and sustained processivity of dynein (McKenney et al., 2014; Schlager et al., 2014; Zhang et al., 2017b).

Figure 1.13

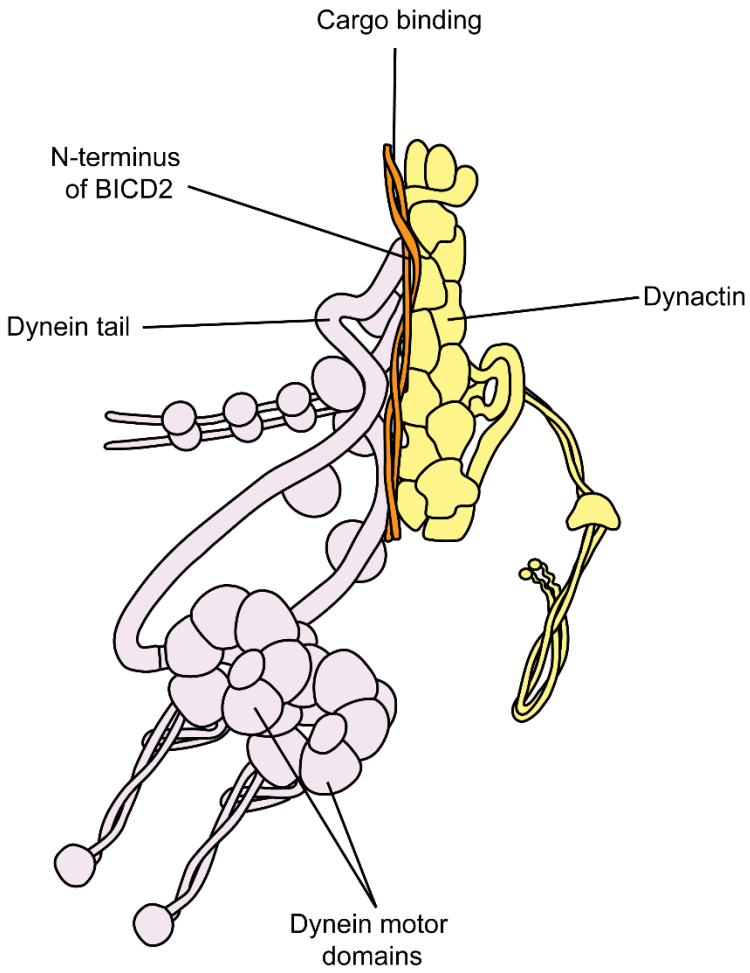

Figure 1.13 Schematic of the interaction between dynein-dynactin and the N-terminus of BICD2. The tail of the HCs interacts with the Arp1 filament of dynactin and occupies the entire length of the filament. BICD2 stretches along the length of the dynactin filament with its C-terminus towards dynactin's pointed end. BICD2 stabilises the interaction between dynein and dynactin. Adapted from Carter et al. 2016.

1.2.2.3 Golgi apparatus

The Golgi apparatus (hereafter referred to as the Golgi) is a pivotal organelle in the cellular secretory pathway (Wei and Seemann, 2017). It is composed of flattened membrane disks known as cisternae which are stacked on top of each other forming the Golgi stack (Witkos and Lowe, 2017; Lowe, 2011). Each stack is functionally and structurally divided into three compartments, through which cargo is transported (Nakamura et al., 2012; Witkos and Lowe, 2017; Sundaramoorthy et al., 2015; Brandizzi and Barlowe, 2013). Firstly, cargo exists the ER at ER exit sites (ERES) in coat protein complex II (COPII) vesicles which are then clustered into a membranous ER-Golgi intermediate compartment (ERGIC). Cargo subsequently proceeds to the *cis* Golgi network (CGN) on the *cis* face of the Golgi before progressing through the medial Golgi where it undergoes modification. Finally, it is sorted and packaged within the *trans* Golgi network (TGN) on the *trans* face of the Golgi and is subsequently delivered to their specific cellular compartment such as the plasma membrane, endosomes and secretory vesicles. The method through which cargo is transported from the *cis* to the *trans* face of the Golgi remains under debate (Witkos and Lowe, 2017). However, a model where cargo is retained within cisternae which mature as they move through the stack is currently the best recognised for most cargoes. It has also been shown that the TGN also receives cargo from outside the stack, which mostly arrives from the endosomal compartment, while the CGN is also capable of returning cargo, such as misfolded proteins, to the ER. Therefore, there is bidirectional transport at both the *cis* and *trans* face of the Golgi. This structure of the Golgi is highly conserved amongst eukaryotes (Lowe, 2011).

However, whereas most lower eukaryotes simply have multiple dispersed stacks, in vertebrates the Golgi stacks are laterally interconnected by tubular reticular structures forming a continuous structure referred to as the Golgi ribbon (Nakamura et al., 2012; Lowe, 2011). Importantly, in vertebrates this singular Golgi is found located in close proximity to the microtubule organisation centre (MTOC) at the centrosome (Yadav and Linstedt, 2011). The accurate positioning of the Golgi is crucial for several cellular processes including neuronal arborisation and cell migration (Figure 1.14a) (Yadav et al., 2012). Interestingly, in neurons Golgi stacks are found in dendrites (known as “Golgi outposts”) which are thought to be

involved in the local delivery of receptors and dendritic arborisation (Wei and Seemann, 2017; Jeyifous et al., 2009). Important for the formation of the Golgi ribbon, its maintenance and positioning are microtubules and dynein (Lowe, 2011).

Figure 1.14

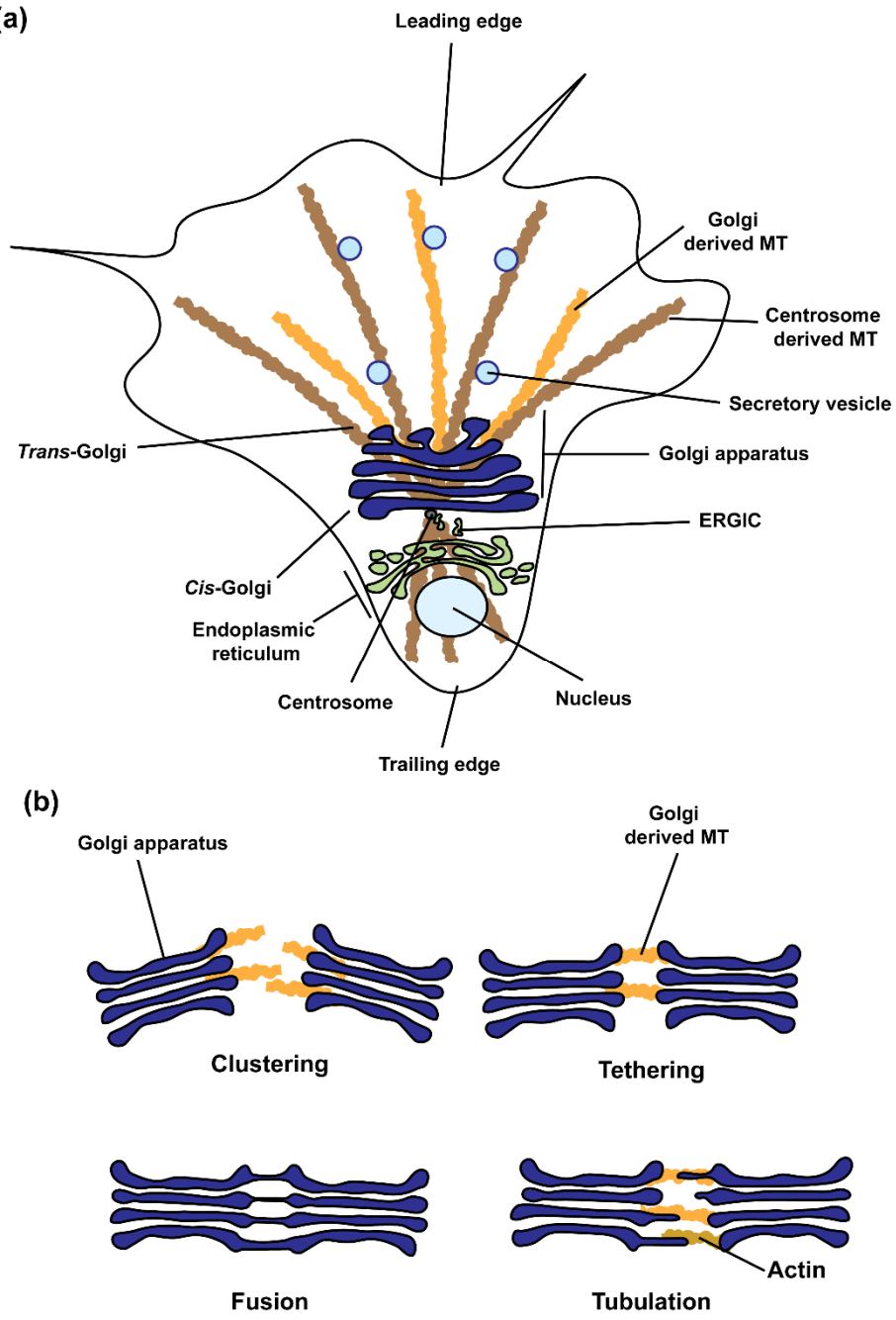

Figure 1.14 (a) Golgi positioning during cell migration allows for the directed secretion towards the cell edge along microtubules. **(b)** Schematic of the steps in Golgi assembly. Golgi stacks undergo clustering using Golgi-derived microtubules and are transported towards the centrosome. Tethering proteins further connect the Golgi stacks before undergoing tabulation and fusion to form the Golgi ribbon. Adapted from: Yadav & Linstedt 2011; Nakamura et al. 2012; Wilson et al. 2011.

1.2.2.2.3.1 Microtubules at the Golgi

In most cells, the primary microtubule organising and nucleation centre is the centrosome (Rios, 2014). The centrosome consists of a pair of centrioles surrounded by the pericentriolar matrix containing the components which are necessary for microtubule nucleation. Specifically, the γ-tubulin ring complex (γ-TuRC) which consist of γ-tubulin and γ-tubulin complex proteins (GCPs). However, in some differentiated cells including neurons most microtubules are nucleated at acentrosomal sites. Interestingly, the Golgi can act as a site of microtubule nucleation including in neurons (Chabin-Brion et al., 2001; Ori-McKenney et al., 2012; Efimov et al., 2007). This nucleation is dependent on γ-TuRC like the nucleation seen at the centrosome (Efimov et al., 2007).

Golgi-derived microtubules are thought to be important for the formation of the Golgi ribbon, whilst centrosome derived microtubules are important for the localisation of the Golgi (Miller et al., 2009; Hurtado et al., 2011). Depolymerisation of microtubules through treatment with nocodazole or colchecine results in the Golgi fragmenting and the dispersal of the Golgi stacks (mini-stacks) (Haase and Rabouille, 2015). Simply inhibiting Golgi microtubule nucleation does not disperse the Golgi but causes the fragmentation of the Golgi ribbon (Rios, 2014). The current model stipulates that Golgi-derived microtubules cluster Golgi stacks in the periphery (G-stage) and these are then transported on centrosome derived microtubules to the pericentrosomal position (C-stage) (Miller et al., 2009; Nakamura et al., 2012; Lowe, 2011). Subsequently, these clustered Golgi stacks undergo tubulation and fusion to form the Golgi ribbon for which Golgi-derived microtubules are essential (Figure 1.14b). Therefore, the formation of an intact Golgi ribbon requires the cooperation of both Golgi-derived and centrosome derived microtubules.

Additionally, the asymmetric nature of Golgi-derived microtubules is important for the polarization of the cell and therefore for cell migration (Miller et al., 2009). The inhibition of Golgi microtubule nucleation results in aberrant directed cell migration (Miller et al., 2009; Hurtado et al., 2011). Overall, cells require an intact polarised Golgi located at the centrosome to enable the polarized secretion which sustains directional migration (Rios, 2014).

1.2.2.2.3.1.1 Post-translational modification of microtubules

Microtubules consist of cylindrical polymers of α-tubulin and β-tubulin heterodimers and are important for a variety of cellular functions including intracellular transport and organelle positioning (Janke and Chloë Bulinski, 2011). The post-translational modifications (PTMs) of microtubules allows for their specialisation (Howes et al., 2014). Interestingly, microtubules associated with the Golgi are highly enriched in acetylated and detyrosinated microtubules (Thyberg and Moskalewski, 1993; Skoufias et al., 1990). Additionally, the rate of acetylation on Golgi-derived microtubules is especially rapid indicating that they are stabilised immediately after formation (Sanders and Kaverina, 2015; Chabin-Brion et al., 2001).

Many of the PTMs of microtubules occur on the C-terminus of tubulin which extend perpendicularly from the microtubule surface (Howes et al., 2014). One such modification is the reversible enzymatic removal of the C-terminal tyrosine residue (detyrosination) present on most α-tubulin isotypes (Song and Brady, 2015). This process occurs preferentially once tubulin is polymerised into microtubules but the responsible cytosolic carboxypeptidase (CCP) is yet to be identified (Kumar and Flavin, 1981; Song and Brady, 2015; Gundersen et al., 1987). However, this modification is reversible in soluble tubulin dimers by the tubulin Tyr ligase (TTL) enzyme (Janke and Chloë Bulinski, 2011). Whilst detyrosination is often associated with stable long live microtubules this does not mean that the modification imparts stability (Song and Brady, 2015). It merely reflects the fact that detyrosination preferentially occurs on polymerised tubulin dimers into microtubules as oppose to soluble tubulin. This generates microtubules in which the “older” minus end are detyrosinated (detyr-microtubules) and the “newer” plus end is tyrosinated (tyr-microtubules). It is thought that detyrosination and tyrosination are used to differentially regulate the interactions of microtubules with other proteins. Interestingly, CAP-Gly domain-containing linker protein 170 (CLIP170) which is a +TIP binding protein is preferentially recruited to end binding protein 1 (EB1) bound tyr-microtubules (Peris et al., 2006; Bieling et al., 2008). CLIP170 is then able to recruit dynactin through its interaction of the $p150^{Glued}$ subunit. Interestingly, the $p150^{Glued}$ subunit of dynactin also preferentially binds to tyr-microtubules (Peris et al., 2006; Nirschl et al., 2016; McKenney et al., 2016).

EB1, CLIP170 and p150^{Glued} are responsible for the recruitment of dynein to microtubule plus ends. Therefore, the tyrosination state of microtubules regulates the recruitment of these proteins to the plus end of microtubules and consequently of dynein and thus impact the initiation of dynein mediated transport (McKenney et al., 2016; Nirschl et al., 2016). Additionally, the tyrosination state of microtubules has been implicated in the regulation of various members of the kinesin family (Song and Brady, 2015).

In contrast to detyrosination, acetylation occurs within the lumen of microtubules on lysine 40 (Lys40) of α-tubulin (Song and Brady, 2015). Several enzymes have been identified which are capable of acetylating Lys40 such as elongator complex protein 3 (ELP3), arrest-defective-1 (ARD1) - N-acetyltransferase 1 complex (NAT1) complex, histone acetyltransferase GCN5, and alpha tubulin acetyltransferase 1 (αTAT1). However, abolishing αTAT1 activity results in an almost complete loss of microtubule acetylation indicating that it is the enzyme primarily responsible for the acetylation of microtubules (Kalebic et al., 2013; Shida et al., 2010; Akella et al., 2010). Conversely, deacetylation preferentially occurs on soluble tubulin dimers once released from microtubules (Song and Brady, 2015). Histone deacetylase 6 (HDAC6) and sirtuin 2 (SIRT2) are the deacetylases responsible for the deacetylation of Lys40 of α-tubulin. However, mice lacking HDAC6 show hyperacetylation of microtubules (Zhang et al., 2008). Additionally, only the knockdown of HDAC6 had a significant effect on the acetylation of microtubules in MDA-MB-231 cells (Deakin and Turner, 2014). Therefore, HDAC6 is considered to be the primary deacetylase for Lys40 (Sadoul and Khochbin, 2016). Acetylation of microtubules is predominantly associated with stable, long-lived microtubules. Therefore, there is on-going debate as to whether the modification imparts stability or is simply a marker that accumulates on microtubules which survive long enough to undergo this modification: currently, consensus sides with the latter. However, two recent studies have shown that acetylation of microtubules is not simply a marker of stability but actually infers resistance to mechanical breakage by altering the flexibility and compliance of microtubules (Portran et al., 2017; Xu et al., 2017). Interestingly, dynein has been shown to have a higher affinity to acetylated microtubules in vitro (Dompierre et al., 2007; Bhuwania et al., 2014). Furthermore, it has also been shown that the

acetylation state of microtubules affects the velocity of axonemal dynein (Alper et al., 2014). Therefore, it is suggested that the acetylation state of microtubules could regulate dynein activity (Sadoul and Khochbin, 2016). Similarly, kinesin is also thought to be regulated by the microtubule acetylation. Recently, it was shown that the inhibition of dynein using Ciliobrevin D which inhibits the ATPase activity of the motor domain of the HC caused a decrease in acetylation and tyrosination of microtubules in neuronal cultures (Sainath and Gallo, 2014). Also, it has been reported that HDAC6 interacts with the $p150^{Glued}$ subunit of dynactin in the context of aggresome formation (Kawaguchi et al., 2003). It is unknown whether this interaction may allow dynein to modulate the levels of microtubule acetylation.

1.2.2.2.3.2 Dynein at the Golgi

Dynein is responsible for transport from post-Golgi compartments such as endosomes and lysosomes back to the TGN. It also mediates the transport of cargo from the ER to the CGN but the precise sequence of events is still unclear (Jaarsma and Hoogenraad, 2015). Currently there are two models which attempt to explain how cargo from the ER is transported to the Golgi via the ERGIC (Brandizzi and Barlowe, 2013). Both models begin with the COPII vesicles exiting the ER and moving in a microtubule and dynein-independent manner (Appenzeller-Herzog, 2006). Subsequently, in the transport complex model, COPII vesicles fuse to form the ERGIC (also known as the vesicular tubular cluster (VTC) or the transport complex (TC)) (Appenzeller-Herzog, 2006). The ERGIC itself is then transported in a microtubule and dynein-dependent manner and either undergoes fusion with other ERGIC to form new *cis*-Golgi cisternae or fuses with the first cisternae of the *cis*-Golgi. A more recent model (the stable compartment model) stipulates that the ERGIC is not a transient structure but a stable organelle which exists between ER and the Golgi (Appenzeller-Herzog, 2006). In this model, COPII vesicles are transported from the ER and fuse with the ERGIC. This is followed by a dynein and microtubule dependent transport from the ERGIC to the *cis*-Golgi.

The transport of cargo from the ER to the Golgi by dynein is suggested to maintain the Golgi at the centrosome (Allan et al., 2002). Further evidence that dynein is important for localisation of the Golgi to a pericentrosomal position was obtained

using purified Golgi complexes applied to “semi-intact” cells (Corthésy-Theulaz et al., 1992). Additionally, the importance of dynein to the integrity of the Golgi is illustrated by various knockdown and inhibition studies. The disruption of the dynactin complex and therefore inhibition of dynein function via the overexpression of p50/dynamitin causes Golgi fragmentation (Burkhardt et al., 1997). The Golgi is also fragmented in cells cultured from HC knockout mice (Harada et al., 1998). More recently, siRNA was used to knockdown individual components of the dynein complex (Palmer et al., 2009). For several of these subunits (HC, IC2, LIC1, Tctex-1 and Roadblock1) knockdown resulted in the fragmentation of the Golgi. Interestingly, the concomitant knockdown of the dynein adaptor proteins NudE and Nudel or depletion of LIS1 also causes Golgi fragmentation (Lam et al., 2010).

A study also using the overexpression of p50/dynamitin or the CC1 domain of $p150^{Glued}$ to inhibit dynein, was able to show which steps of Golgi reassembly following nocodazole washout are dependent on dynein (Miller et al., 2009). The inhibition of dynein halted both the clustering of the Golgi stacks (G-stage) at the periphery and the centripetal movement of these stacks towards the centrosome (C-stage).

Recently, progress was made with the identification of golgin160 as the protein responsible for recruiting dynein to the Golgi membranes (Yadav et al., 2012). Golgin160 binds to the IC of the dynein complex through one of its coiled-coil domains (CC7) and attaches to the Golgi membranes via its N-terminal interaction with Arf1. Interestingly, the knockdown of golgin160, preventing the recruitment of dynein, stopped the transport of membranes at the C-stage, thus stopping the peri-centrosomal localisation of the Golgi. Therefore, it is suggested that Golgin160 recruitment of dynein is important for the localisation and maintenance of Golgi positioning at the centrosome.

Interestingly, dynactin is proposed to be capable of binding to Golgi membranes directly via the interaction of its Arp1 subunit and βIII-spectrin on Golgi membranes (Jaarsma and Hoogenraad, 2015). Furthermore, the knockdown of βIII-spectrin also causes Golgi fragmentation and impaired recovery following microtubule depolymerisation with nocodazole (Salcedo-Sicilia et al., 2013).

Dynein is also crucial for the nucleation of microtubules at the Golgi which as discussed are important in ribbon formation (Rivero et al., 2009). Additionally, in Drosophila, dynein is also important for the transport of Golgi outposts to distal dendrites through its interaction with lava lamp which binds α-spectrin on Golgi membranes (Zheng et al., 2008; Papoulas et al., 2005). However, a mammalian homolog of lava lamp is yet to be identified.

1.2.2.2.3.3 BICD2 at the Golgi

The best understood function of BICD2 at the Golgi is its role in Ras-related protein Rab-6A dependent retrograde transport from the Golgi to the ER. RAB proteins are small Ras-Like GTPases which act as regulators of intracellular vesicular transport (Hutagalung and Novick, 2011). RAB proteins are active when bound to guanosine-5'-triphosphate (GTP) and are associated with membranes at which point they recruit specific proteins to facilitate transport. RAB6A is involved in intra-Golgi transport, where it specifically coordinates COPI-independent retrograde transport from the Golgi to the ER (Martinez-Carrera and Wirth, 2015). Importantly, active RAB6A on the TGN recruits and binds to the C-terminus of BICD2 which in turn recruits the dynein-dynactin complex to facilitate the retrograde transport towards the ER. Furthermore, the importance of BICD2 to the Golgi is illustrated by the fact that a double knockdown of BICD1/2 and over expression of the N-terminus of BICD2 (BICD2-N) both cause Golgi fragmentation (Fumoto et al., 2006; Teuling et al., 2008).

Due to its coiled-coil structure, its localisation to the TGN of the Golgi and its interaction of a RAB family member (RAB6A), BICD2 is considered to be a Golgin (Martinez-Carrera and Wirth, 2015; Matanis et al., 2002). Golgins are part of a matrix surrounding the Golgi which helps maintain the integrity of the Golgi and mediate Golgi functions including vesicular transport (Witkos and Lowe, 2016).

1.2.2.2.3.4 Golgi fragmentation in SMA-LED

Two dynein mutations are associated with delayed recovery of the Golgi following fragmentation by treatment of nocodazole (Fiorillo et al., 2014). A similar phenotype was also observed in mouse embryonic fibroblasts from *Loa* homozygous mice (Hafezparast et al., 2003).

Several BICD2 mutations which cause SMA-LED are associated with Golgi phenotypes. Patient fibroblasts with either p.T703M or p.N188T have decreased BICD2 levels and Golgi fragmentation. The level of Golgi fragmentation in these patients correlated with severity of patient phenotype (Neveling et al., 2013). Additionally, the transfection of BICD2 with the p.S107L disease causing mutation into SH-SY5Y cells caused Golgi fragmentation (Peeters et al., 2013). The same study also showed that the p.S107L mutation increased the affinity of BICD2 for the dynein IC. Furthermore, it showed that the p.E774G mutation decreased the interaction between BICD2 and RAB6A. Another study found Golgi fragmentation in myocytes of patients harbouring either p.S107L or p.T703M mutant BICD2 (Unger et al., 2016). Interestingly, muscle fibres from the same patients exhibited BICD2 aggregates within the nuclei or within the perinuclear region. Similar alterations were observed when staining for RAB6. Transfecting SH-SY5Y with mutant BICD2 harbouring the p.R501P mutation produced similar perinuclear aggregation in the form of ring structures positive for RAB6A (Oates et al., 2013). The same study also showed that p.S107L and p.R501P mutant BICD2 interacts more tightly with the IC and $p150^{Glued}$.

Interestingly, Golgi fragmentation is also a feature of other neurodegenerative diseases including Alzheimer's disease, Parkinson's disease and ALS (Wei and Seemann, 2017).

1.3 Research aims

This thesis focusses on elucidating the cellular and molecular aetiology which underpins the degeneration of motor neurons in amyotrophic lateral sclerosis (ALS and in spinal muscular atrophy, lower extremity predominant (SMA-LED).

Dysfunctional RNA metabolism has increasingly become implicated in ALS, with the discovery of mutations in several RNA binding proteins (Strong, 2010). Of importance is the RNA binding protein TDP-43, which was first implicated in ALS upon the discovery that it is the principal component of the ubiquitin positive inclusions that characterise the disease (Neumann et al., 2006; Arai et al., 2006) (Cirulli et al., 2015; Buratti, 2015). Subsequently, causative mutations were identified in its gene (*TARDBP*) and to date up to 52 mutations have been identified and are known to account for up 4 % of fALS cases and 1 % of sALS

cases (Kabashi et al., 2008; Sreedharan et al., 2008). TDP-43 is involved in several steps of RNA metabolism including transcription, translation and mRNA stability (Lee et al., 2012). Recently, data from a transgenic mouse model of ALS from within the Hafezparast lab, implicated TDP-43 in the regulation of Peripherin expression, specifically the alternative translation of Per-45 (Barri, 2015). Peripherin is another ALS associated protein which is also found in inclusions in ALS and mutation to its gene (*PRPH*) are also linked with ALS. The aim here is to further elucidate TDP-43's role in the regulation of peripherin expression and specifically attempt to ascertain TDP-43's involvement in the alternative translation of Per-45. This was performed in a mouse line where endogenous mutagenized TDP-43 is expressed at isogenic levels, allowing for the elimination of overexpression artefacts from previous data.

SMA-LED is caused by mutations in *DYNC1H1* and *BICD2*. *DYNC1H1* encodes the heavy chain (HC) which forms the core of the dynein molecular motor, while *BICD2* encodes an adaptor of dynein (Neveling et al., 2013; Oates et al., 2013; Peeters et al., 2013; Harms et al., 2010). Several mutations in *DYNC1H1* associated with SMA-LED also cause malformation of cortical development (Scoto et al., 2015). Similarly, mutations in *Lis1* which encodes lissencephaly 1 causes a neuronal migration disorder (lissencephaly). The *Loa* mouse model of the disease also exhibits neuronal migration deficits (Hafezparast et al., 2003; Ori-McKenney and Vallee, 2011). Recently, data from the Hafezparast lab has shown that focal adhesions, which are crucial for normal cellular migration, have an abnormal morphology and consequently *Loa* MEFs exhibit slower migration (Barri, 2015). It is also suggested that this is caused by a decrease in the phosphorylation of the focal adhesion protein paxillin at Tyr118, which was observed to be reduced in *Loa* mouse embryonic fibroblasts. Here, the aim is to determine how mutations in the HC of dynein can alter the phosphorylation of paxillin and further investigate the effects of reduced Tyr118 phosphorylation on adhesion dynamics. To achieve this microscopy and various drug treatments were used to dissect a potential pathway linking dynein and paxillin.

Golgi pathology is associated with several *DYNC1H1* and *BICD2* mutations. Recently in the Hafezparast lab, Golgi fragmentation was observed in patient fibroblasts with a *DYNC1H1* mutation in association with reduced microtubule

acetylation. The aim here was to further investigate the involvement of dynein and BICD2 in Golgi pathology and to try and understand the underlying molecular mechanisms. To achieve these goals, DYNC1H1$^{+/D338N}$ patient fibroblasts and BICD2$^{+/I189F}$ patient fibroblasts were used to investigate Golgi morphology and dynein localisation at the Golgi. These cells and *Loa* mouse embryonic fibroblasts were also used to investigate the role of post-translational modifications Golgi integrity and pathology.

Chapter 2: Methods

2.1 Genotyping

2.1.1 DNA preparation

Tissue for DNA preparation was obtained in the form of an ear punch using a sterilised ear puncher, which yields approximately 0.2-0.3 cm^2 of tissue. When fibroblasts were used, they were grown to confluency in a T25 flask (Corning, Cat: 430639), trypsinized, and then centrifuged at 390 x g for 5 minutes and the pellet washed with Dulbecco's phosphate-buffered saline (DBPS). Subsequently, 200 µL of lysis buffer (100 mM Tris-HCL at pH 8.0, 5 mM EDTA, 0.2 % SDS and 200 mM NaCl) and 2 µL Proteinase K (20 mg/mL) were added and the sample incubated in a 55 ^oC water bath overnight. The samples were then centrifuged for 15 minutes at 16,100 x g, following which the supernatant containing the DNA was decanted into a new Eppendorf tube and a 1:20 dilution performed. For each polymerase chain reaction (PCR) reaction 1 µL of the diluted DNA was used.

2.1.2 Genotyping TDP-43^{F210I} mice

To enable the genotyping of the T>A substitution at position 628 (c.628T>A), a multiplex PCR was performed through two independent duplex reactions, each using 3 primers designed by PhD student Charlotte Chapman (see Table 2.1 for primer sequences). One set of primers (outer primers) amplified a 225 bp fragment encompassing the region with the mutation regardless of the presence of the mutation. These annealed at the area highlighted in blue and yellow for the forward and reverse primer respectively in Figure 2.1. The second set of primers (inner reverse primers) were designed to target the site of the mutation specifically (targeting the area highlighted in green in Figure 2.1). The first primer in this set, (inner wild type) contained the complementary base to the wild type 628 base at the 3’ end (T), whereas the second primer of this set (inner mutant) contained the complementary base to the mutant base (A). Additionally, in both the inner wild type and inner mutant primer, a second mismatch was introduced at the third base from the 3’ end of the primer (base highlighted in purple in Figure 2.1) to increase specificity. Each inner reverse primer was designed to work in conjunction with the outer forward primer to generate a 143 bp fragment.

Table 2.1

Primer	Sequence (5'-3')
Outer forward primer	GTGTTTACCATCTCCTGTTCTCTCTT
Outer reserve primer	GACAAATGACCAACAAATATACCTTATC
Inner reverse wild type	TACCACTTCTCCATACTGACAGAATAA
Inner reverse mutant	TACCACTTCTCCATACTGACAGAATAT

Table 2.1 Sequence of primers for the genotyping of TDP-43^{F210I} mice. The additional mismatch introduced in the inner primers to increase specificity is highlighted in purple. The site of the mutation is underlined with the base complementary to the wild type base shown in black and the base complementary to the mutant base in red.

Figure 2.1

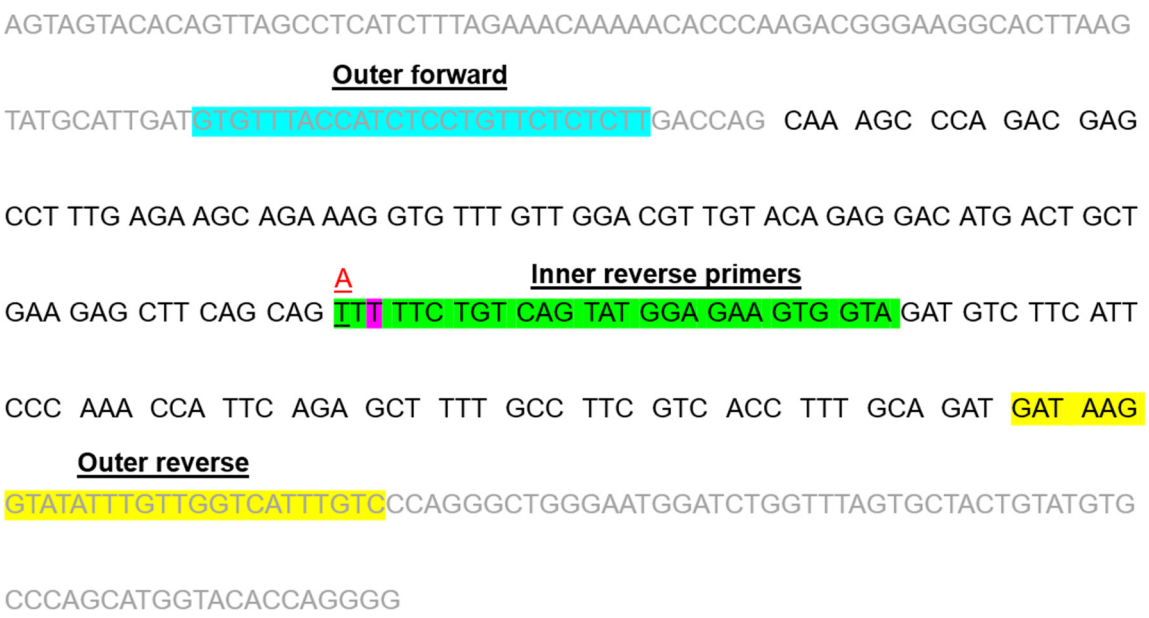

Figure 2.1 Sequence of *Tardbp* at the region surrounding the site of the F210I (c.628T>A) mutation. The site of the mutation is underlined, and the mutant base is shown in red above the site. The bases of the exon are in black and those of the surrounding introns are in grey. The outer primers are highlighted in blue and yellow for the forward and reverse primer respectively. The site complementary to the inner primers is highlighted in green with the purple base corresponding to the added mismatch in these primers for improved specificity.

Reaction 1 and 2 both contained the outer primers, but only one of the variants of the inner reverse primers, inner reverse wild type and inner reverse mutant respectively. Therefore, since the outer primers generate a 225 bp fragment in both reactions, the presence or absence of the inner 143 bp fragment demonstrated the genotype. The amplification of the 143 bp fragment would only occur in reaction 1 if the animal has a wild type allele, due to the two mismatches which would otherwise occur between the wild type inner reverse primer and the template (see Figure 2.2). Similarly, reaction 2 would only generate a 143 bp fragment if the animal has a mutant allele due to the mismatches which occur if this was not the case (see Figure 2.2).

The result would be that wild type mice would have the 2 bands in reaction 1 and only the 225 bp band in reaction 2 due to the lack of a mutant allele. Heterozygous mice would have 2 bands in reaction 1 and reaction 2 due to the presence of both a wild type and a mutant allele. Homozygous mutant mice would only have the 225 bp band in reaction 1 due to the lack of a wild type allele, and 2 bands in reaction 2. Figure 2.3a demonstrates these possible outcomes and a sample result can be seen in Figure 2.3b.

Each reaction consisted of 5 µL of HotStarTaq Master Mix (Qiagen, Cat:203443), 0.1 µM of each primer, 1 µL of template (from 1:20 dilution specified in section 2.1.1), with the volume made up to 10 µL with double distilled water. The samples were run using the PCR program detailed in Table 2.2 and subsequently on a 2 % agarose gel.

Figure 2.2

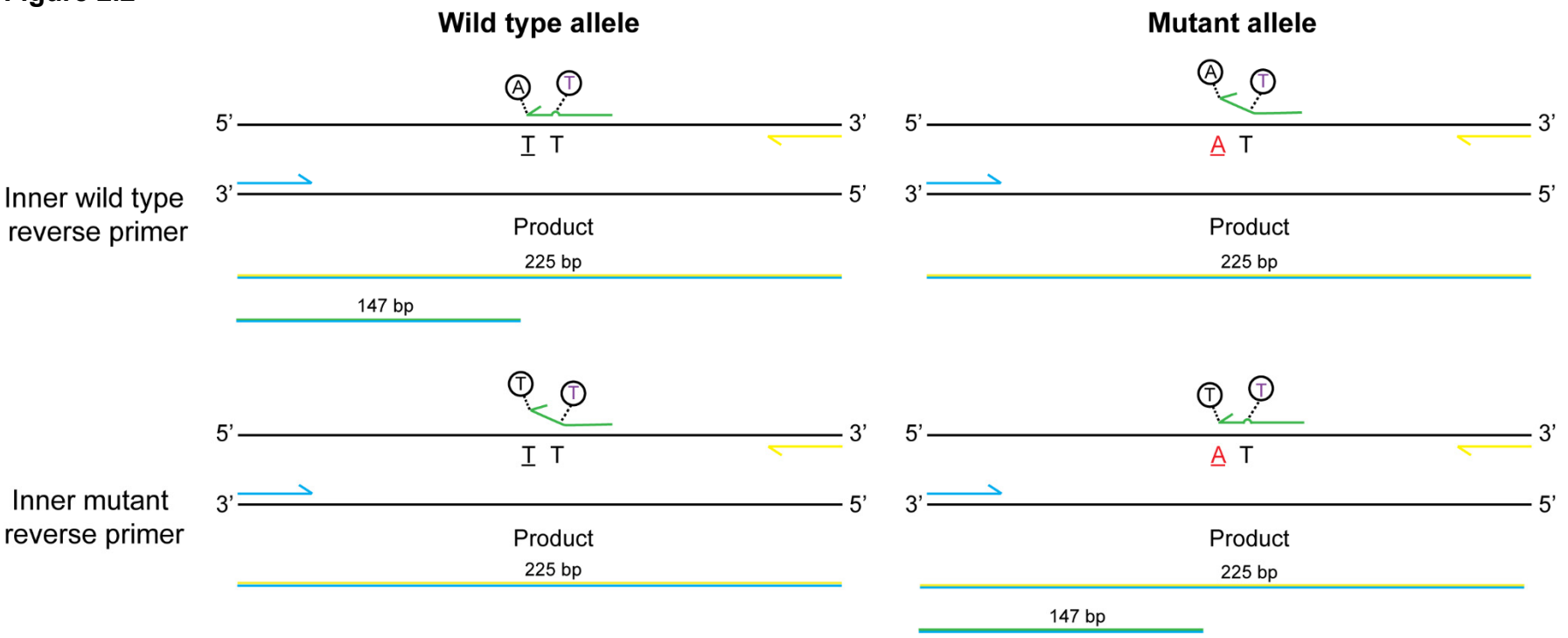

Figure 2.2 Schematic illustrating the principal of primer annealing for the TDP-43^{F210I} genotyping. For each sample two reactions were performed, and each reaction contains three primers. A set of outer primers (blue and yellow for the forward and reverse respectively) and an inner reverse primer which exists in two variations, one in which the 3' end is able to anneal to the wild type allele and with the other being able to anneal to the mutant allele. The site of the mutation is underlined, and the last base of the inner reverse primers are shown in black within a circle. Additionally, the inner reverse primers contain an additional mismatch shown in purple within a circle for added specificity.

Figure 2.3

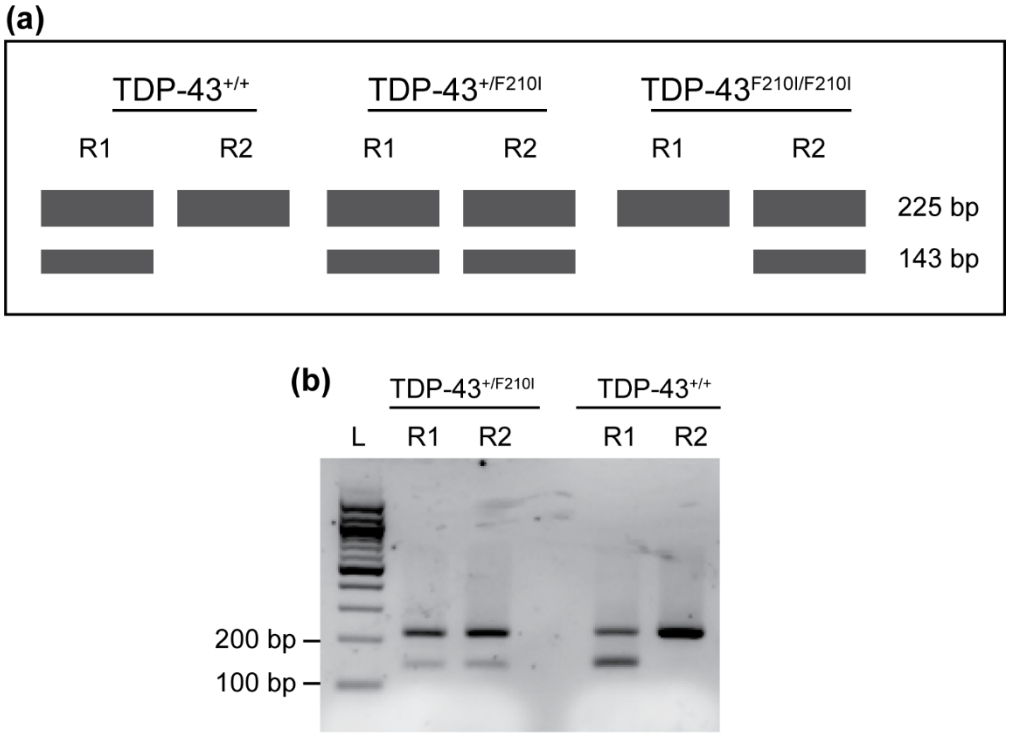

Figure 2.3 (a) Schematic representation of the expected band pattern for each potential outcome TDP-43^{F210I} genotyping. **(b)** A Sample result from TDP-43^{F210I} genotyping showing the outcome for a TDP-43$^{+/+}$ and TDP-43$^{+/F210I}$ mouse. The PCR products were run on a 2 % agarose gel for 20 minutes. R1: reaction 1, R2: reaction 2, L= 100 bp ladder (NEB, Cat: N3231).

Table 2.2

Number of cycles	Temperature	Time
1	95 ºC	15 minutes
35	94 ºC	30 seconds
	X ºC	30 seconds
	72 ºC	1 minute
1	72 ºC	10 minutes

Table 2.2 PCR program for TDP-43^{F210I} (X = 60 ºC), *Loa* (X = 62 ºC), DYNC1H1^{D338N} (X = 60.5 ºC) and BICD2^{I189F} genotyping (X = 60.5 ºC).

2.1.3 Genotyping *Loa* mice and fibroblasts

Tissue from both mice and fibroblasts were prepared as described in section 2.1.1. The genotyping of the *Loa* mutation was performed using PCR and a subsequent restriction digest. The PCR was used to amplify the region surrounding the c.1739T>A mutation using the primers described in Table 2.3, which anneal at the sites shown in Figure 2.4. The mutation generated a secondary *RsaI* restriction site (GT^{v}AC), shown highlighted in green in Figure 2.4. Therefore, the 696 bp product was digested with the restriction enzyme *RsaI*. When the mutation was present the enzyme would cut at the primary restriction site and the new secondary site, generating fragments of 24 bp (not visible on gels after electrophoresis), 135 bp and 537 bp. When the mutation was not present then two fragments would be produced, a 24bp (not visible on gels after electrophoresis) and a 672 bp fragment (see Figure 2.5a and b).

The PCR reactions consisted of 5 µL of HotStarTaq Master Mix (Qiagen, Cat:203443), 0.1 µM of each primer, 1 µL of template (from 1:20 dilution specified in section 2.1.1), with the volume made up to 10 µL with double distilled water. The samples were amplified using the PCR program detailed in Table 2.2, and subsequently restricted with 5 U of *RsaI* (NEB, Cat: R0167S) for 1.5 hours, being run on a 2 % agarose gel.

Table 2.3

Primer	Sequence (5'-3')
Forward primer	TGCTGTGTGCTCTCCTGTTT
Reverse primer	TTTTACAAGCTTGGCTTTGC

Table 2.3 Sequence of primers for the genotyping of the *Loa* mutation.

Figure 2.4

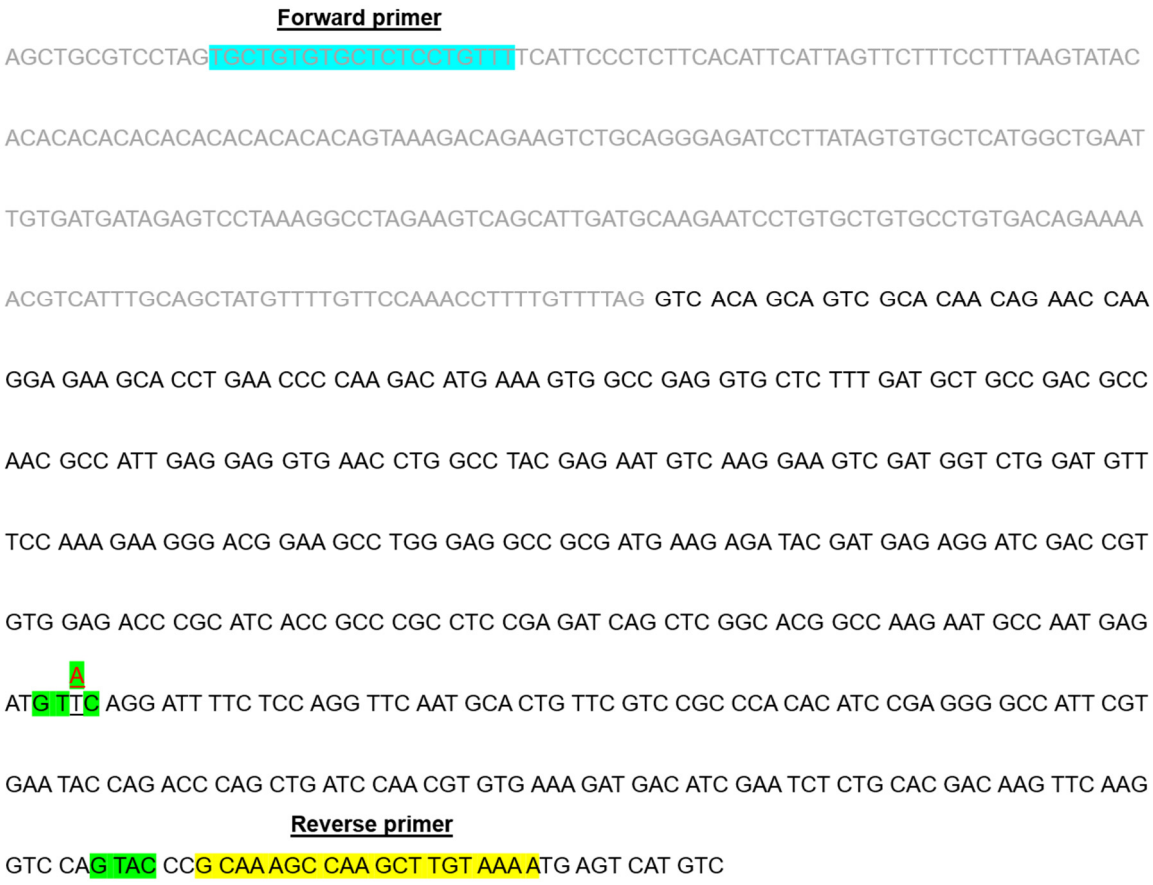

Figure 2.4 Sequence of the *Dync1h1* gene surrounding the *Loa* mutation site (underlined and mutant variant shown in red). The sites for the forward primer (highlighted in blue) and the reverse primer (highlighted in yellow) are also shown. Additionally, the primary *RsaI* restriction site and the secondary site formed by the mutation are highlighted in green. Introns are shown in grey and exons in black.

Figure 2.5

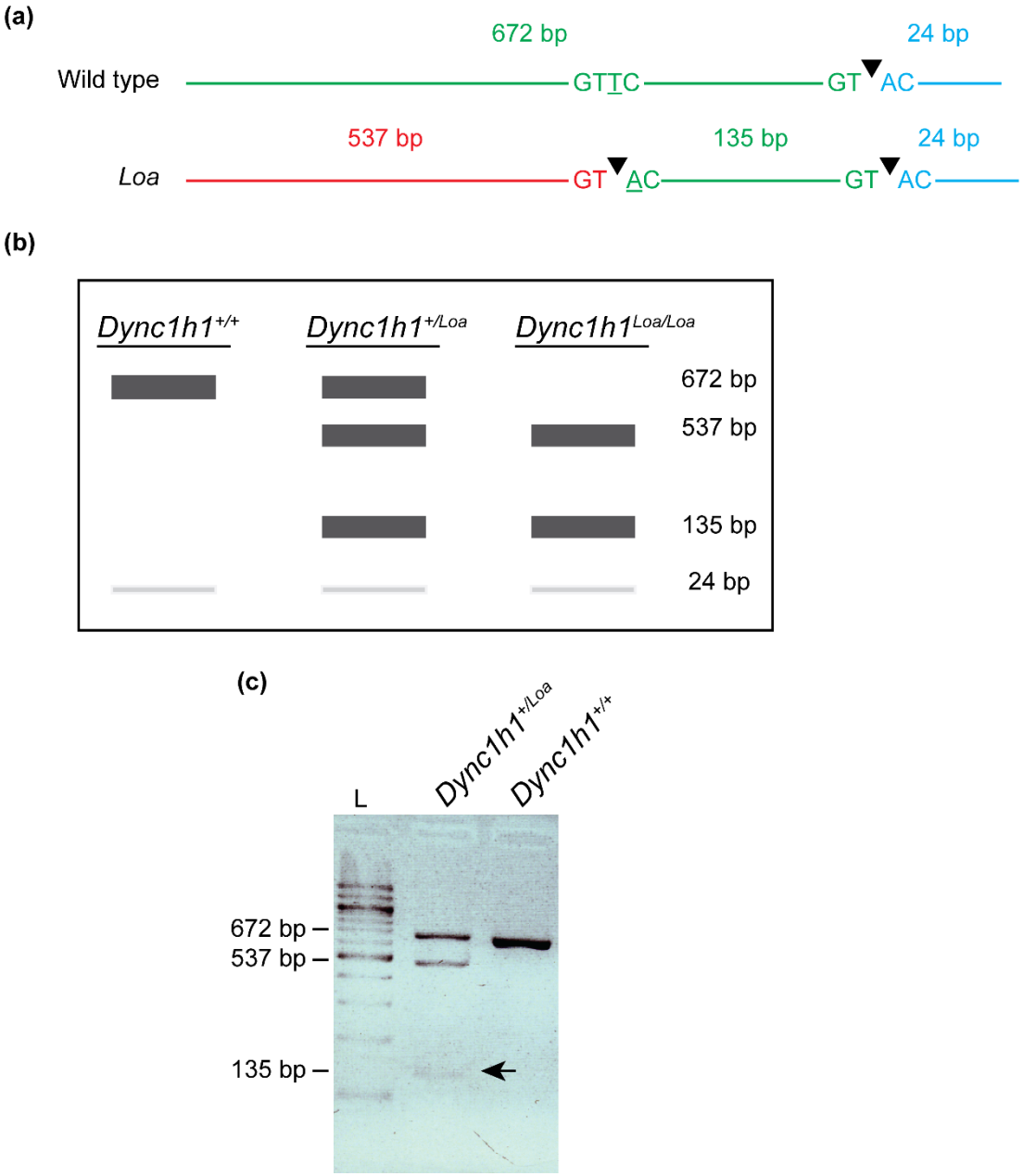

Figure 2.5 (a) Representation of the restriction digest following the PCR for *Loa* genotyping. A wild type allele produced two fragments (637 bp and 24 bp), whereas the *Loa* allele produced 3 fragments (537 bp, 135 bp and 24 bp). ▼ denotes the site of restriction. **(b)** Schematic representation of the bands expected from the resulting gel electrophoresis for a *Dync1h1*$^{+/+}$, *Dync1h1*$^{+/Loa}$, *Dync1h1*$^{Loa/Loa}$ genotype. **(c)** Sample gel electrophoresis of *Loa* genotyping showing the expected bands for *Dync1h1*$^{+/+}$ and *Dync1h1*$^{+/Loa}$. The PCR products were run on a 2 % agarose gel for 20 minutes. L= 100 bp ladder. (NEB, Cat: N3231).

2.1.4 Genotyping DYNC1H1^{D338N} fibroblasts

DNA for genotyping was obtained from human fibroblasts as described in section 2.1.1. Subsequently, 1 µL of DNA was used in a multiplex PCR to determine the presence of the c.1012G>A mutation, using the primers detailed in Table 2.4. For each sample two duplex reactions were performed, each reaction containing three primers. Two outer primers (annealing to the regions highlighted in blue and yellow for the outer forward and reverse primer in Figure 2.6) which would produce a band of 537 bp irrespective of the presence of the mutation; and an inner wild type forward or an inner mutant forward primer which anneal to the mutation site (area highlighted in green in Figure 2.6). The inner primers specifically targeted the mutation with the last base of the 3' end, with the inner wild type only fully annealing to the wild type allele and the inner mutant only fully annealing to the mutant allele (see Figure 2.7). The inner primers worked in conjunction with the outer reverse primer to produce a 413 bp band if fully annealed.

Each reaction had a total volume of 10 µL containing 5 µL of HotStarTaq Master Mix (Qiagen, Cat:203443), 0.1 µM of each primer and 1 µL of template (from 1:20 dilution specified in section 2.1.1). The volume was then made up to 10 µL with double distilled water. The PCR program used is shown on Table 2.2, following which the samples were run on 2 % agarose gel. The expected pattern of the results for the genotypes is shown in Figure 2.8a and a sample result is shown in Figure 2.8b.

Table 2.4

Primer	Sequence (5'-3')
Outer forward primer	GCAACATCAAAATGTTCC
Outer reverse primer	CGATGTCTCTCAACAATACC
Inner wild type forward	GACTACAATCCTCTGATGAAAG
Inner mutant forward	GACTACAATCCTCTGATGAAAA

Table 2.4 Sequence of primers for genotyping DYNC1H1^{D338N} fibroblasts. 3' end base pair which targets the mutation is underlined, with the mutant variant shown in red.

Figure 2.6

Figure 2.6 Sequence of the *DYNC1H1* gene surrounding the mutation site (underlined and mutant variant shown in red). The sites for the forward primer (highlighted in blue) and the reverse primer (highlighted in yellow) are also shown. Additionally, the site to which the inner forward primers anneal is shown highlighted in green. Introns are shown in grey and exons in black.

Figure 2.7

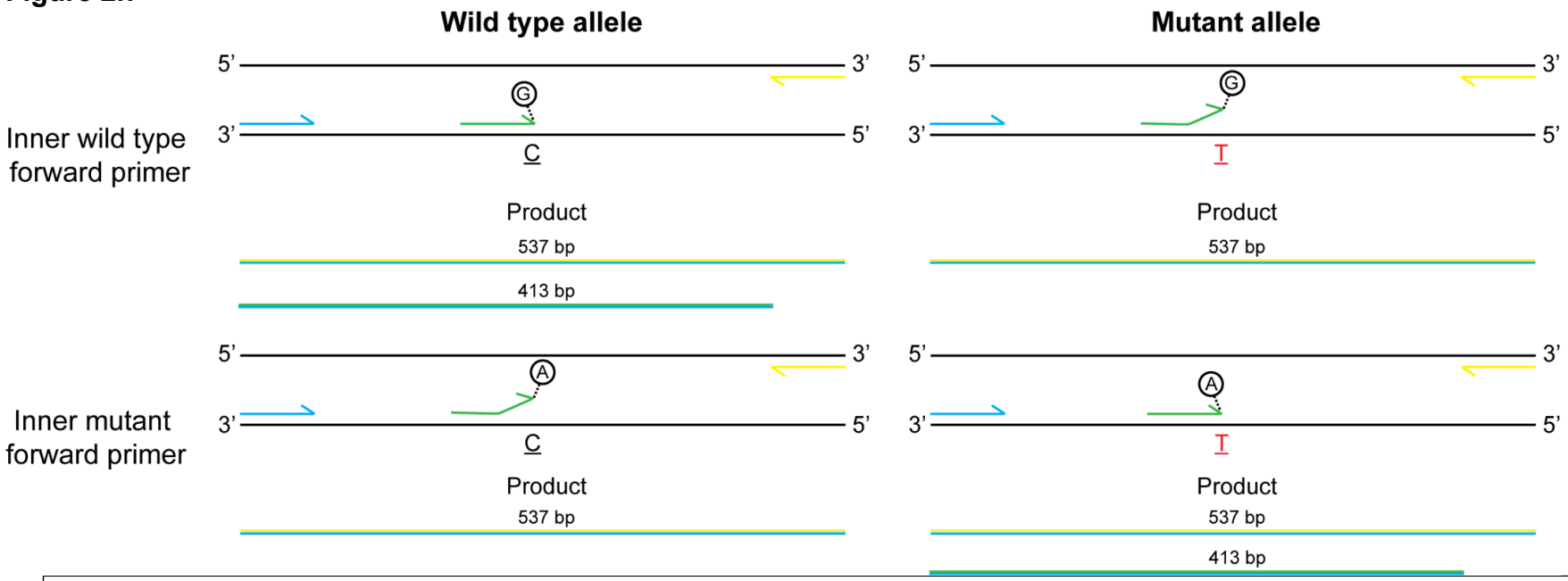

Figure 2.7 Schematic illustrating the principal of the primer annealing for the DYNC1H1^{D338N} genotyping. For each sample two reactions were carried out, each with three primers, the two outer primers (forward and reverse primer, shown in blue and yellow) respectively) and either an inner wild type forward or inner mutant forward primer (shown in green). The 3' end base of the inner forward primers are shown in a circle and the base affected by the mutation is shown underlined and in red for the mutant variant. Only at a wild type allele, would the inner wild type forward 3' end fully anneal and therefore produce a 413 bp fragment in conjunction with the outer reverse primer. Conversely, the inner mutant forward primer 3' end would only fully anneal at a mutant allele and cause the production of the 413 bp fragment. The outer primers produce a 537 bp fragment irrespective of the presence of the mutation.

Figure 2.8

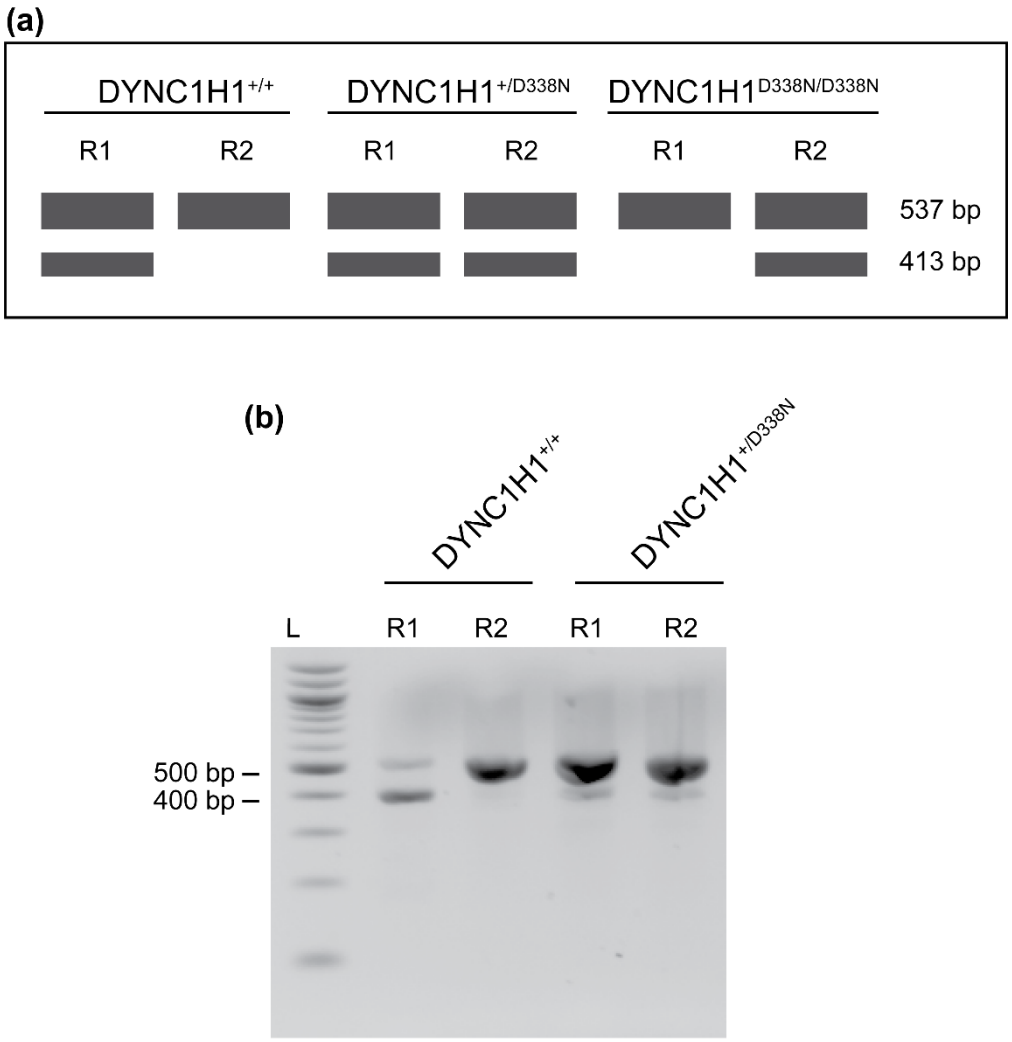

Figure 2.8 (a) Schematic representation of the expected band pattern for each potential outcome of the DYNC1H1^{D338N} genotyping. **(b)** A sample result showing the outcome for DYNC1H1$^{+/+}$ and DYNC1H1$^{+/D338N}$ fibroblasts. The PCR products were run on a 2 % agarose gel for 20 minutes. R1: reaction 1, R2: reaction 2, and L= 100 bp ladder (NEB, Cat: N3231).

2.1.5 Genotyping BICD2^{I189F} fibroblasts

DNA for genotyping the c.565A>T mutation causing the I189F substitution in BICD2 was prepared as described in section 2.1.1. The genotyping was performed in the form of a multiplex PCR reaction, with each sample requiring two duplex reactions, each with 3 primers (primers detailed in Table 2.5). Each reaction had two outer primers (outer forward and outer reverse, highlighted in blue and yellow in Figure 2.9) which produced a band of 629 bp irrespective of the presence of the mutation, as shown in Figure 2.10. Two inner forward primers specifically targeted the site of the mutation with the 3' end base pair (shown in green in Figure 2.9 and in Figure 2.10). The inner wild type would anneal to the wild type sequence and produce a fragment of 202 bp with the outer reverse primer, as shown in Figure 2.10. Conversely, the inner mutant forward fully annealed to the mutant sequence, producing the 202 bp fragment with the outer reverse primer, shown in Figure 2.10. The expected band pattern for each genotype is shown in Figure 2.11a and a sample result is shown in Figure 2.11b.

For each sample two 10 µL reactions were performed, with each consisting of 5 µL of HotStarTaq Master Mix (Qiagen, Cat:203443), 0.1 µM of each primer (the outer primers and 1 inner forward primer) and 1 µL of template (from 1:20 dilution specified in section 2.1.1). The volume was made up to 10 µL with double distilled water. The PCR program used is shown in Table 2.2 and the samples were then run on a 2 % agarose gel.

Table 2.5

Primer	Sequence (5'-3')
Outer forward primer	GCGCACTACTGTGTACATGC
Outer reverse primer	ACAGTGGTAAAGCTGGCCC
Inner wild type forward	GGAACTGGAGGAGGAGAACA
Inner mutant forward	GGAACTGGAGGAGGAGAACT

Table 2.5 Sequence of primers for the genotyping BICD2^{I189F} fibroblasts. 3' end base pair which targets the mutation is underlined, with the mutant variant shown in red.

Figure 2.9

Figure 2.9 Sequence of the *BICD2* gene surrounding the mutation site (underlined and mutant variant shown in red). The sites for the forward primer (highlighted in blue) and the reverse primer (highlighted in yellow) are also shown. Additionally, the site to which the inner forward primers anneal is shown highlighted in green. Introns are shown in grey and exons in black.

Figure 2.10

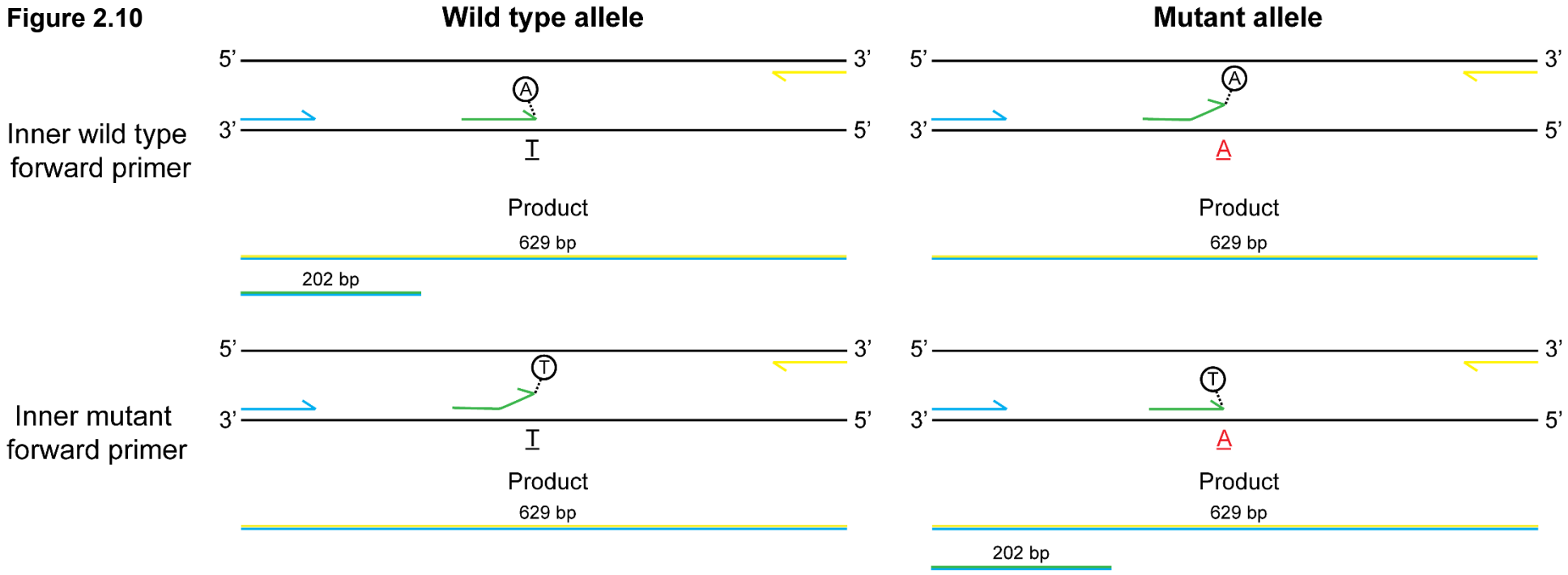

Figure 2.10 Schematic illustrating the principal of the primer annealing for the BICD2^{I189F} genotyping. Each of the reactions for genotyping contains three primers, the outer forward and outer reverse primer (shown in blue and yellow respectively) and an inner forward primer (shown in green). In each reaction, there was either the inner wild type forward which has the 3' end base (shown in the circle) complementary to the wild type sequence, or the inner mutant forward which has the 3' end base (shown in the circle) complementary to the mutant sequence. The outer primers generated a fragment of 629 bp irrespective of the presence of the mutation. The inner forward primers worked in conjunction with the outer reverse primer to produce a 202 bp fragment.

Figure 2.11

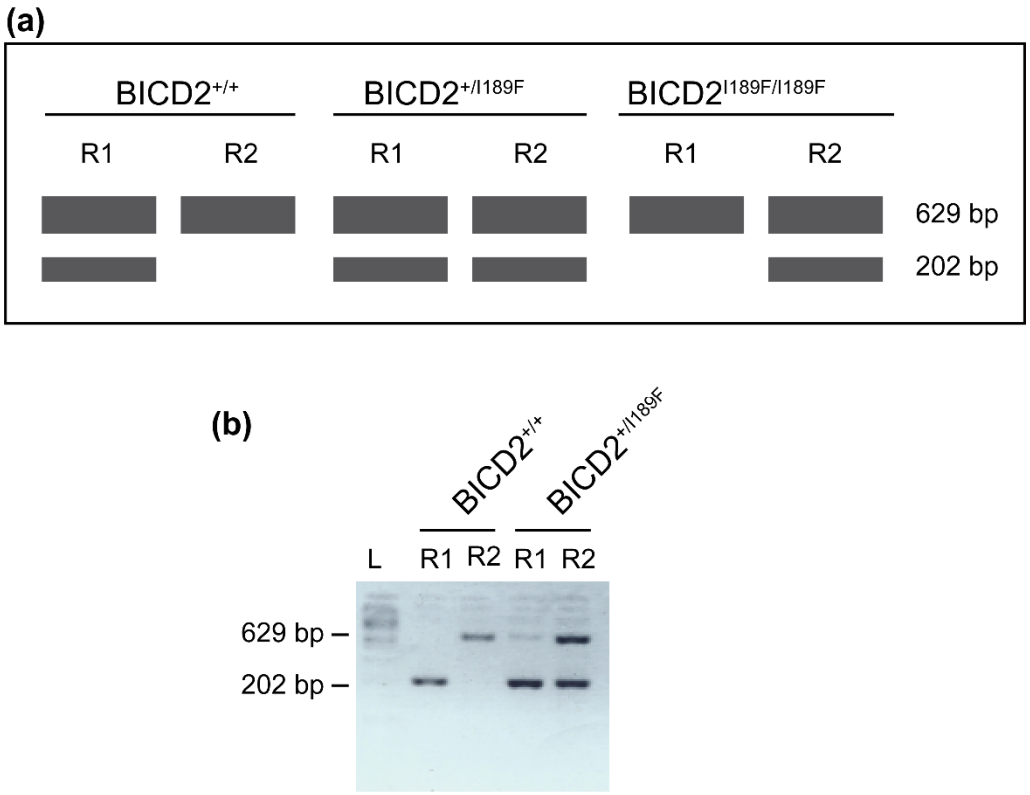

Figure 2.11 (a) Schematic representation of the expected band pattern for each potential outcome of the BICD2^{I189F} genotyping. **(b)** A sample result showing the outcome for BICD2$^{+/+}$ and BICD2$^{+/I189F}$ fibroblasts. The PCR products were run on a 2 % agarose gel for 20 minutes. R1: reaction 1, R2: reaction 2, NT = no template control and L= 100 bp ladder (NEB, Cat: N3231).

2.2 Dissection and tissue culture

2.2.1 Dissection of lumbar spinal cords (LSCs)

Mice were sacrificed using a CO_2 rodent euthanasia chamber and confirmation was performed by cervical dislocation. Mice were pinned ventral side down to a dissection board to allow access to the dorsal side. The dorsal side of the mouse was wiped with 70 % ethanol. Sterile surgical equipment was used for all subsequent steps. Tweezers were used to raise the skin on the back of the neck and surgical scissors created an opening in the skin centrally above the neck. Using the same scissors, the opening was widened laterally to stretch from shoulder to shoulder. After, the skin was cut in a caudal direction on both sides of

the mouse until reaching the hind limbs, allowing the peeling back of the skin to expose spinal column. A similar cut was then performed to remove the spinal column, where surgical scissors were used to separate the column from the mouse by cutting from the cranial region to the caudal region on both sides, ensuring not to remove any organs. The spinal column was subsequently placed on an ice pack and the removal of the spinal cord performed. Fine surgical scissors were used to open the spinal canal to expose the spinal cord, then either the lumbar portion of the cord was extracted using a scalpel or the entire spinal cord was extracted and placed in a cryogenic vial and snap frozen in liquid nitrogen.

2.2.2 Dissection of the brain for cofilin IPs

As for the dissection of the LSC, mice were sacrificed using a CO_2 rodent euthanasia chamber and confirmation was performed by cervical dislocation. The mouse was then pinned on a dissection board, ventral side down and wiped with 70% ethanol. An incision was made at the back of the neck and expanded to allow the removal of the skin from the head. Subsequently, three incisions were made at the base of the skull and tweezers were used to snap away the skull to allow the removal of the brain (care was taken not to damage the tissue). The brains were then placed in cryogenic vials and snap frozen in liquid nitrogen.

2.2.3 Culture media

Table 2.6 describes the culture media used for the various cell lines used in this work.

Table 2.6

Cell line	Culture reagent	Concentration
Neuro2a cells	DMEM (Gibco, Cat: 21969035)	-
	L-Glutamine (Gibco, Cat: 11500626)	1 %
	Penicillin/Streptomycin (Gibco, Cat:11528876)	1 %
	Foetal Bovine Serum (FBS) (Gibco, Cat:10270106)	10 %
Mouse embryonic fibroblasts (MEFs), human fibroblasts, HEK293 cells	DMEM (Gibco, Cat: 21969035)	-
	L-Glutamine (Gibco, Cat: 11500626)	1 %
	Penicillin/Streptomycin (Gibco, Cat:11528876)	1 %
	Bovine growth serum (GE Healthcare Hyclone SH30541.03)	10 %

Table 2.6 Table showing the constituents of cell culture media for the cell lines used in this work.

2.3 Biochemistry

2.3.1 Lysis and sample preparation from tissue

2.3.1.1 Neurofilament extraction from LSCs

Snap frozen LSCs from mice aged between 6 and 9 months or whole spinal cords from 5 month old mice underwent sequential homogenisation to enrich neurofilaments, based on protocols by Xiao et al. 2008. The sequential homogenisation involved three separate homogenisation steps (shown in Figure 2.12) with three different lysis buffers (see Table 2.7 for buffer details). Firstly, LSCs were weighed and 1 mL of Lysis buffer 1 (L1) was added per 100 mg of tissue in a glass Dounce homogeniser, which was used to break down the tissue (given 30 twists). Subsequently, a 21-gauge needle was used to further disrupt the tissue (6 times). The lysate was then centrifuged at 16,100 x g for 10 minutes at 4

°C, following which the supernatant (S1) was separated, and the pellet (P1) underwent a subsequent homogenisation step. Lysis buffer 2 (L2) was used to homogenise P1 with a 21-gauge needle, as was performed for the first homogenisation step. Again, the lysate was centrifuged at 16,100 x g for 10 minutes at 4 °C, the supernatant (S2) separated, and the pellet (P2) was used in the next homogenisation step. P2 was homogenised in lysis buffer 3 (L3) using a 21-gauge needle and the lysate centrifuged as in previous steps. The sucrose within L3 allowed for the separation and removal of lipids. The supernatant (S3) was collected and DPBS was added to the pellet (P3) to wash off any S3, before it was then again pelleted by centrifugation at 16,100 x g for 10 minutes at 4 °C. Lysis buffer 4 (L4) was then used to disrupt the filaments in P3 with a 21-gauge needle as described for previous steps. S1, S2, S3 and P3 were subsequently used in SDS-PAGE and immunoblotting. However, only S1, S2 and P3 underwent analysis as S3 was the product of a wash to remove lipids.

Table 2.7

Lysis Buffer	Constituents	Concentration
L1 - DPBS	DPBS without Ca^{2+} and Mg^{2+} (Sigma, Cat: D8537)	-
	Phosphatase inhibitor cocktail 2 (Sigma, Cat: P5726)	1X
	Phosphatase inhibitor cocktail 3 (Sigma, Cat: P0044)	1X
	Protease inhibitor (Roche, Cat: 11836170001)	1X
L2 - HSB with Triton X-100	NaCl	750 mM
	EDTA	5 mM
	Tris at pH 7.5	50 mM
	Triton X-100 (Sigma, Cat: X100)	1 %
	Phosphatase inhibitor cocktail 2 (Sigma, Cat: P5726)	1X
	Phosphatase inhibitor cocktail 3 (Sigma, Cat: P0044)	1X
	Protease inhibitor (Roche, Cat: 11836170001)	1X
L3 – HSB with sucrose	NaCl	750 mM
	EDTA	5 mM
	Tris at pH 7.5	50 mM
	Sucrose	1M
	Phosphatase inhibitor cocktail 2 (Sigma, Cat: P5726)	1X
	Phosphatase inhibitor cocktail 3 (Sigma, Cat: P0044)	1X
	Protease inhibitor (Roche, Cat: 11836170001)	1X
L4 – DPBS and SDS	DPBS without Ca^{2+} and Mg^{2+} (Sigma, Cat: D8537)	-
	Sodium dodecyl sulfate (SDS)	2 %

Table 2.7 Table showing the constituents of four lysis buffers used in the sequential homogenisation of lumbar spinal cords to enrich the neurofilaments. HSB = high salt buffer, DPBS = Dulbecco's Phosphate-Buffered Saline

Figure 2.12

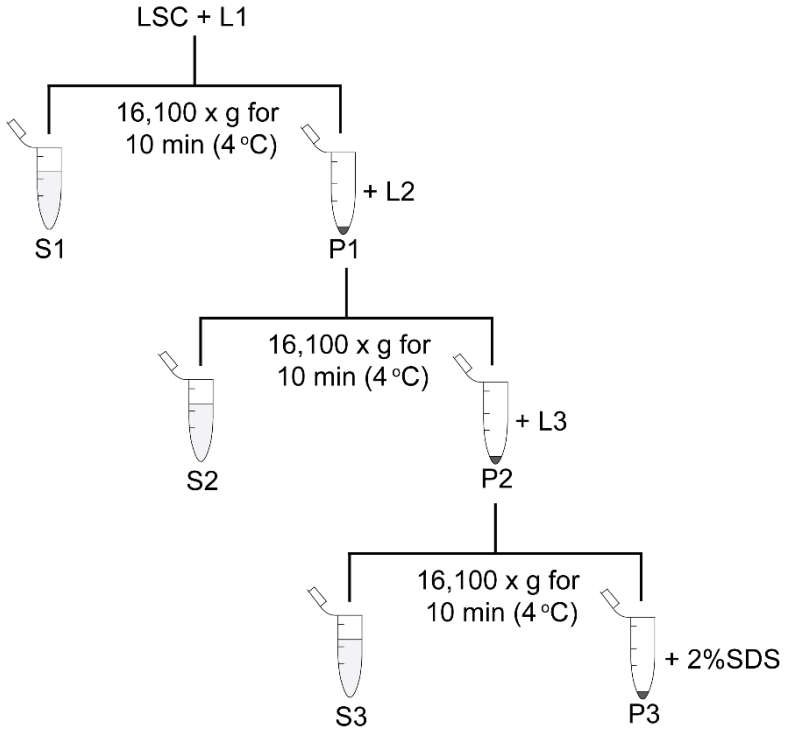

Figure 2.12 Schematic of sequential homogenisation of lumbar spinal cord (LSC) tissue using lysis buffer 1, 2 and 3 from Table 2.7. S1 = supernatant 1, S2 = supernatant 2, S3 = supernatant 3, P1 = pellet 1, P2 = pellet 2 and P3 = pellet 3.

2.3.1.2 Brain homogenisation for cofilin immunoprecipitation

Snap frozen brains were weighed and per 100 mg of tissue, 1 mL of lysis buffer (DPBS without Ca^{2+} and Mg^{2+} (Sigma, Cat: D8537), 1X Phosphatase inhibitor cocktail 2 (Sigma, Cat: P5726), 1X Phosphatase inhibitor cocktail 3 (Sigma, Cat: P0044), 1X Protease inhibitor (Roche, Cat: 11836170001)) were used to homogenise the tissue in a glass Dounce homogeniser. The lysate was then centrifuged at 16,100 x g for 15 minutes at 4 °C and the supernatant collected into a separate 1.5 mL Eppendorf tube.

2.3.2 Lysis and sample preparation from cells

2.3.2.1 Cell homogenisation for SDS-PAGE

Cells used for western blot analysis were grown in 6 well tissue culture plates (VWR, Cat: 734-1599), where they underwent any required drug treatments. For

homogenisation, the cells were first washed in DPBS (without Ca^{2+} and Mg^{2+}) and were then lysed using RIPA lysis buffer (1X RIPA (Merck Millipore, Cat: 20-188)) with 1X Phosphatase inhibitor cocktail 2 (Sigma, Cat: P5726), 1X Phosphatase inhibitor cocktail 3 (Sigma, Cat: P0044), and 1X Protease inhibitor (Roche, Cat: 11836170001)). Briefly, an adequate volume of lysis buffer was added (depending on the confluency of the cells) to each well and the plate swayed to ensure the spread of the buffer. Subsequently, a cell scrapper was used to remove the cells from the surface and the lysate collected into an Eppendorf tube. The lysate was then centrifuged at 1000 x g for 5 minutes at 4 ^{o}C and the supernatant collected (the pellet was stored at 4 ^{o}C). The protein concentration was then measured prior to loading on SDS-PAGE (SDS polyacrylamide gel electrophoresis) gels.

The exception to the protocol described above being the homogenisation of neuro2a cells for the experiment in section 3.2.3. Here, cells were plated in a T25 flask (Corning, Cat: 430639) following transfection. The cells were subsequently, trypsinized and centrifuged at 390 x g for 5 minutes. The supernatant was discarded and the pellet washed in DPBS (without Ca^{2+} and Mg^{2+}). RIPA lysis buffer (constitution described above) was added to the cell pellet, followed by vortexing and incubation on ice for 20 minutes with further intermittent vortexing (once every 5 minutes). The lysate was then centrifuged at 1000 x g for 5 minutes at 4 ^{o}C and the supernatant collected (the pellet was stored at 4 ^{o}C). The protein concentration was the measured prior to loading on SDS-PAGE gels using the bicinchoninic acid assay (BCA assay).

2.3.2.2 Cell homogenisation for immunoprecipitation

To determine the protein concentration of both cell and tissue lysates following homogenisation a bicinchoninic acid assay (BCA) (ThermoFisher scientific, Cat: 23227) was used. The standard curve and samples were prepared as per the manufacturer's protocol but scaled down to a total volume of 200 µL, and 1 µL of this was measured on a NanoDrop 2000 spectrophotometer.

2.3.5 Immunoprecipitation

50 µL of protein A sepharose beads (Life Technologies, Cat: 101041) were washed with DBPS (without Ca^{2} and Mg^{2+}) three times. All washes consisted of 1 mL of DPBS (without Ca^{2} and Mg^{2+}) added to the beads, incubation on a rotator at

4 °C for 10 minutes and centrifugation at 400 x g for 2 minutes at 4 °C. Subsequently, the beads were incubated on a rotator at 4 °C overnight with DPBS (without Ca^2 and Mg^{2+}) containing 3 % bovine serum albumin (BSA) (Sigma, Cat: A9056). The next day the beads were centrifuged as done previously and the blocking solution removed. One set of blocked beads was then conjugated to an antibody against the protein of interest and another set to the corresponding IgG control for 2 hours on a rotator at 4 °C (see Table 2.8 for antibody details). Simultaneously, the lysate was pre-cleared with washed beads to avoid non-specific interactions between proteins within the lysate and beads. Pre-clearing took place on a rotator at 4 °C for 1 hour. Both the beads conjugated to the antibody targeting the protein of interest and those conjugated to the IgG control underwent three further washes with DPBS (without Ca^2 and Mg^{2+}) as previously described. Subsequently, the pre-cleared homogenate was added to the conjugated beads and incubated overnight on a rotator at 4 °C. The next day the beads were centrifuged at 400 x g for 2 minutes and the homogenate removed (post-IP lysate). The beads underwent 6 washes with DPBS (without Ca^2 and Mg^{2+}) as described previously and a further similar wash but substituting DBPS for sterile double distilled water. 1X SDS sample buffer was then added to the beads, which were subsequently boiled at 95 °C for 5 minutes and then centrifuged at 16,100 x g for 5 minutes. The supernatant was removed and kept at -20 °C until analysed using SDS-PAGE and immunoblotting.

Table 2.8

Target of Immunoprecipitation	Antibody	IgG control	Amount conjugated to beads
Dynein IC	Mouse anti-Dynein intermediate chain 1 antibody 74.1 (Abcam, Cat: ab23905)	IgG Mouse (Merk Millipore, Cat: PP54)	2.5 µg
Cofilin	Rabbit anti-Cofilin antibody (Abcam, Cat: ab11062)	IgG Rabbit (Merk Millipore, Cat: PP64)	2.5 µg
Lfc/GEF-H1	Rabbit anti-GEF-H1 (Genetex, Cat: GTX125893	IgG Rabbit (Merk Millipore, Cat: PP64)	2.5 µg

Table 2.8 Antibodies used for immunoprecipitations and the concentrations of these antibodies conjugated to the beads.

2.3.6 SDS-PAGE

For experiments in sections 3.2.1, 3.2.2, 3.2.3 and 4.2.3, lab made 10 % Tris-glycine SDS-PAGE gels were run using SDS running buffer (0.31 M of Tris base, and 2.4 M Glycine in double distilled water). To make up these gels, a resolving gel was made consisting of 10 % acrylamide, 375 mM Tris-Cl at pH 8.8, 0.1% SDS, 0.5% ammonium persulfate and 0.05 % tetramethylethylenediamine (TEMED). Once set, a stacking gel was added, consisting of 1 % acrylamide, 125 mM Tris-Cl at pH 6.8, 0.1 % SDS, 0.5 % ammonium persulfate and 0.05 %

tetramethylethylenediamine (TEMED). The experiment in section 5.2.6 used 4-12 % Bis-Tris NuPAGE precast protein gel (Invitrogen, Cat: NP0323) with 1X NuPAGE MOPS SDS running buffer. All other experiments were run on 12 % Bis-Tris NuPAGE precast protein gel (Invitrogen, Cat: NP0343) with 1X NuPAGE MOPS SDS running buffer. Furthermore, 20 µg of protein for each sample was loaded for all experiments unless the homogenate concentration did not allow for this. In that instance, the maximum allowed for by the lowest concentrated sample was loaded, with an amount equal to this used for the rest of the samples. SeeBlue Plus2 Pre-stained protein standard (Thermofisher, Cat: LC5925) was used for all experiments and all SDS-PAGE gels were run for approximately 90 minutes at 140 V and subsequently transferred to PVDF membranes (Amersham, Cat: 10600021) at 100 V for 75 minutes at 4 ^{o}C.

2.3.7 Immunoblotting and analysis

The PVDF membrane was blocked on a rocker for 1 hour or overnight at 4^{o}C in 5 % skimmed milk in PBS-T (PBS and 0.05 % Tween-20 (Sigma, P9416)) (see Table 2.9). Subsequently, the membranes were rinsed with PBS-T and incubated with the primary antibody on a rocker, either overnight at 4 ^{o}C or for 1 hour at room temperature (see Table 2.9 for antibody details, dilutions, length of incubation and constituents of the antibody solution). After the primary antibody incubation, the membrane was washed in PBS-T. The washes consisted of one 15 minute incubation on a rocker and three 5 minute incubations. Next, the membrane was incubated with the secondary antibody, see Table 2.9 for details. The incubation with the secondary antibody was performed for 45 minutes on a rocker at room temperature and followed by a second round of washes (one 15 minute wash and three 5 minute washes in PBS-T). The relevant substrate for the secondary antibody (either horse radish peroxidase (HRP) or alkaline phosphatase (AP) was then evenly applied to the protein covered face of the membrane for 1 minute. The membrane was then placed between two transparency sheets and within a film cassette and the films (Thermofisher, Cat: 34089) developed in an X-ray developer. Note that when probing for a phosphoprotein, all solutions including blocking solution, wash solutions and antibody solutions consisted of TBS-T instead of PBS-T.

Table 2.9

Protein	Antibody	Blocking	Dilution	Incubation time	Secondary antibody
Acetylated tubulin	Mouse anti-acetylated tubulin (Sigma-Aldrich, Cat: T7451)	5 % Milk in PBS-T	1:2000 in PBS-T	Overnight at 4 ºC	Goat anti-mouse IgG AP (Sigma-Aldrich, Cat: A3562) at 1:10000
β-actin	Mouse anti-β-actin (Sigma-Aldrich, Cat: A5316)	5 % Milk in PBS-T or 5 % BSA in TBS-T if also probing for phosphoproteins	1:5000 in PBS-T	Overnight at 4 ºC	Goat anti-mouse IgG AP (Sigma-Aldrich, Cat: A3562) at 1:10000
Detyrosinated tubulin	Rabbit anti-detyrosinated tubulin (Abcam, Cat: ab48389)	5 % Milk in PBS-T	1:500 in PBS-T	Overnight at 4 ºC	Goat anti-rabbit IgG AP (Sigma-Aldrich, Cat: A3812) at 1:10000
pPaxillin^{Y118}	Rabbit anti-Phospho-Paxillin (Tyr118) (ThermoFisher Scientific, Cat: 44-722G)	5 % BSA in TBS-T	1:1000 in TBS-T	Overnight at 4 ºC	Goat anti-rabbit IgG AP (Sigma-Aldrich, Cat: A3812) at 1:10000

Protein	Antibody	Blocking	Dilution	Incubation time	Secondary antibody
Dynein HC	Rabbit anti-dynein HC (Santa Cruz, Cat: sc-9115)	5 % Milk in PBS-T	1:200 in PBS-T	Overnight at 4 ºC	Goat anti-rabbit IgG AP (Sigma-Aldrich, Cat: A3812) at 1:10000
Peripherin	Rabbit anti-Peripherin polyclonal (Merk Millipore, Cat: AB1530)	5 % Milk in PBS-T	1:1000 in PBS-T	Overnight at 4 ºC	Goat anti-rabbit IgG AP (Sigma-Aldrich, Cat: A3812) at 1:10000
α-tubulin	Mouse anti-α-tubulin (Merk Millipore, Cat: 05-829)	5 % Milk in PBS-T	1:1000 in PBS-T	Overnight at 4 ºC	Goat anti-mouse IgG AP (Sigma-Aldrich, Cat: A3562) at 1:10000*
V5	Mouse anti-V5 (ThermoFisher Scientific, Cat: R960-25)	5 % Milk in PBS-T	1:5000 in PBS-T	1 hour	Goat anti-mouse IgG AP (Sigma-Aldrich, Cat: A3562) at 1:10000
Cofilin	Rabbit anti-cofilin (Abcam, Cat: ab11062)	5 % Milk in PBS-T or 5 % BSA in TBS-T if also probing for phosphoproteins	1:10000 in PBS-T	Overnight at 4 ºC	Goat anti-rabbit IgG AP (Sigma-Aldrich, Cat: A3812) at 1:10000

Protein	Antibody	Blocking	Dilution	Incubation time	Secondary antibody
Paxillin	Mouse anti-Paxillin (Merk Millipore, Cat: 05-417)	5 % Milk in PBS-T	1:500 in PBS-T	Overnight at 4 ºC	Goat anti-mouse IgG AP (Sigma-Aldrich, Cat: A3562) at 1:10000
Myc	Mouse anti-C-Myc tag (Genscript, Cat: A00704)	5 % Milk in PBS-T	1:1000 in PBS-T	Overnight at 4 ºC	Goat anti-mouse IgG AP (Sigma-Aldrich, Cat: A3562) at 1:10000
Dynein LC (RP3)	Mouse anti-RP3 (a kind gift from Kevin Pfister)	5 % Milk in PBS-T	1:200 in PBS-T	Overnight at 4 ºC	Goat anti-mouse IgG AP (Sigma-Aldrich, Cat: A3562) at 1:10000
GEF-H1	Rabbit anti-GEF-H1 (Genetex, Cat: GTX125893	5 % Milk in PBS-T	1:1000 in PBS-T	Overnight at 4 ºC	Goat anti-rabbit IgG AP (Sigma-Aldrich, Cat: A3812) at 1:10000
Dynein IC	Mouse anti-Dynein intermediate chain 1 antibody 74.1 (Abcam, Cat: ab23905)	5 % Milk in PBS-T	1:1000 in PBS-T	Overnight at 4 ºC	Goat anti-mouse IgG AP (Sigma-Aldrich, Cat: A3562) at 1:10000

Protein	Antibody	Blocking	Dilution	Incubation time	Secondary antibody
Phospho-ERK1/2	Rabbit Anti-Phospho-p44/42 MAPK (Erk1/2) (Thr202/Tyr204)	5 % BSA in TBS-T	1:1000 in PBS-T	Overnight at 4 ºC	Goat anti-rabbit IgG AP (Sigma-Aldrich, Cat: A3812) at 1:10000

Table 2.9 Primary antibodies used for immunoblotting, the type of blocking performed, antibody dilution used and the length of the incubation. * For experiments in sections 3.2.1 and 3.2.3 Rabbit anti-mouse HRP was used at 1:10000 instead.

2.3.7.1 Analysis and quantification of immunoblots

For the quantification of western blots, the films were scanned on an Epson Perfection 4990 photo scanner and were quantified using one of two software packages. TotalLab TL100 image analysis software was used to quantify peripherin expression in the LSC, while all other western blots were quantified using the FIJI distribution of ImageJ.

2.3.8 Immunocytochemistry

For immunocytochemistry, cells were seeded onto sterile 13 mm round glass coverslips (Fisher Scientific, Cat: 12392128) in 24 well plates (VWR, Cat: 734-1605). Depending on the requirements of the experiment the coverslips were either left uncoated (experiments in sections 5.2.1 and 5.2.2) or coated with 10 µg/mL of collagen type 1 (BD biosciences, Cat: 354236) (experiments in section 4.2.1). The coating was performed by adding 200 µL at the correct concentration and leaving in a laminar flow tissue culture hood overnight to dry. The next day the coated cover slips were washed three times with double distilled water. Subsequently, cells were seeded at an appropriate density and left overnight to reach an adequate confluency.

After the removal of the culture media and a DPBS wash (adding and aspirating 1 mL of PBS for each wash), fixation was performed with 4% formaldehyde (Thermofisher, Cat: 28906) for 5 minutes at room temperature. After this incubation, the formaldehyde was aspirated and 3 washes with DPBS were performed. The fixed cells were then permeabilised by incubating with 1 mL PBS containing 0.2 % Triton X-100 for 2 minutes on a rocker. Subsequently, the permeabilised cells were blocked with PBS containing 5 % BSA for 30 minutes on a rocker at room temperature. Following the removal of the blocking solution the cells were then incubated on a rocker overnight at 4 ^{o}C in a humidified box with the primary antibody which was made up in PBS containing 1 % BSA (see Table 2.10 for antibody dilutions). The next day the antibody solution was removed and a 5 minute wash on a rocker was performed with PBSTS (1 mL PBS containing 0.1 % tween 20 and 0.02 % SDS). The solution was then removed and the fluorescent secondary antibody solution applied (made up in 1 mL PBS containing 1 % BSA), see Table 2.11 for antibody details. Note that this step and all subsequent steps were performed in near darkness due to the sensitivity of the fluorescent antibody

to light. After the 1 hour secondary antibody incubation, 3 further PBSTS washes were performed as described previously. The cover slips were then removed from the 24 well plate and mounted onto a droplet of ProLong Gold Antifade Mountant with DAPI (Invitrogen, Cat: P36931) on glass microscope slides. Quick dry nail varnish was used to seal the coverslip.

Table 2.10

Protein	Antibody	Dilution	Incubation time
Giantin	Rabbit anti-giantin (Biolegend, Cat: 924302)	1:200	Overnight
Dynein IC	Mouse Anti-Dynein intermediate chain 1 antibody [74.1] (Abcam, Cat: ab23905)	1:200	overnight

Table 2.10 Primary antibodies used for immunocytochemistry and the dilution used.

Table 2.11

Antibody	Dilution	Incubation time
Goat Anti-rabbit Alexa fluor 546 conjugate (ThermoFisher Scientific, A11035)	1:200	1 hour
Goat Anti-Mouse Alexa fluor488 conjugate (ThermoFisher Scientific, A11029)	1:200	1 hour

Table 2.11 Secondary antibodies used for immunocytochemistry and the dilution used.

2.4 Cell assays

2.4.1 Measuring paxillin turnover at focal adhesions

Loa homozygous and wild type MEFs were transfected with pEGFP-Paxillin (Rosse et al., 2012) using Lipofectamine LTX (ThermoFisher Scientific, Cat: 15338030) as detailed in section 2.7.2. The transfected MEFs were divided between 5 wells in 24 well plates for 48 hours. Subsequently, a cell spreading assay was performed where the cells were trypsinized and centrifuged at 390 x g for 5 minutes and then resuspended in 1 mL of live cell imaging media (ThermoFisher Scientific, Cat: A14291DJ). The cells were subsequently recentrifuged at 390 x g for 5 minutes and again resuspended in 1 mL of live cell imaging media and added to one well of a two well live cell imaging chamber (ThermoFisher, Cat: 155382) which had previously been coated with 10 µg/mL of Collagen type 1. For the coating, 1 mL of collagen was added to each well and allowed to dry overnight in a laminar flow tissue culture hood and washed three times with double distilled water. 3.5 hours after plating the cells in the live cell imaging chamber the cells underwent fluorescence recovery after photobleaching (FRAP) as described in section 2.5.1.

2.4.2 Treating MEFs with blebbistatin, ciliobrevin D, laminin or U0126 ERK1/2 inhibitor

For each genotype (wild type and *Loa* homozygous) 300,000 MEFs were seeded on 6 well plates (VWR, Cat: 734-1599) and incubated overnight. Subsequently, the cells were incubated with complete growth media (see Table 2.6 for media details) mixed with the required drug or equivalent volume of the vehicle control and incubated (see Table 2.12 for drug concentrations, controls and incubation times). After the treatment, the cells were lysed as described in section 2.3.2.1.

2.4.3 Synchronisation of the cell cycle with thymidine

Wild type and *Loa* homozygous MEFs were grown until 20-30 % confluent, at which point the media was swapped with new complete media containing 2 mM of thymidine (Sigma, Cat: T1895). After an 18 hour incubation the cells were washed 3 times in DPBS and incubated in thymidine free media for 9 hours. Subsequently, the media was once again swapped with new complete media containing 2 mM of thymidine, and the cells incubated for 17 hours. Finally, the cells were washed 3 times with DPBS and the cells lysed as per section 2.3.2.1.

Table 2.12

Drug	Concentration used	Vehicle control	Incubation time
(-) Blebbistatin (Sigma, Cat: B0560)	20 μM	DMSO	1 hour
Ciliobrevin D (Merk Millipore, Cat: 250401)	50 μM	DMSO	1 hour
U0126 (ERK1/2 inhibitor)	10 μM	DMSO	2 hours
Laminin (Sigma, Cat: L2020)	25 μg/mL	-	4 hours

Table 2.12 Table showing the working concentration, vehicle control and incubation time of drugs used to treat MEFs,

2.4.4 HC knockdown using auxin inducible degron system in HCT116 cells

HCT116 cells were plated in 6 well tissue culture plates (150,000) and left overnight to gain confluency. For each individual experiment, wells were treated with both 500 μM of indol1-3-acetic-acid (Aux) and 2 μg/mL of doxycycline (Dox) for either 4 hours, 8 hours or 24 hours. For the controls, a well was left untreated, a well was treated with 500 μM of indol1-3-acetic-acid only and another with 2 μg/mL of doxycycline only. After each time point elapsed, the cells were lysed as per the protocol in section 2.3.2.1. Note that the control wells were lysed at the 24-hour time point.

2.5 Microscopy

2.5.1 Fluorescence recovery after photobleaching (FRAP)

FRAP was performed using an Olympus 3I spinning disc microscope with an EMCCD Evolve camera (confocal) which operates using the 3i Slidebook software. The settings used for the imaging were: 100x magnification, 488nm filter (FITC), gain of 2, intensification of 200 and laser power of 300. FRAP was

performed by drawing a squared selection area which was set to be targeted with the 488 nm laser at full power for 1 ms at the 10 second timepoint of a time point series where an image was taken every 5 seconds. Quantification was performed using the inbuilt tools in Slidebook reader. Briefly, for each time point a fluorescence intensity reading was taken at the area bleached. Additionally, two control intensities were also measured: one for a control region which was not photobleached and second for a background region from outside of the cell. Both the region of interest intensity and the control region intensity were normalised to the background reading. Then, the region of interest intensity was normalised to the control region and the intensity presented as a percentage of the normalised intensity of the 0 second timepoint (first image taken).

2.5.2 Imaging and quantification of Golgi fragmentation and IC-Golgi co-localisation

Imaging of the Golgi to quantify the fragmentation of the organelle was performed on an Olympus-3I microscope with a 63 X oil objective mounted with an EMCCD Evolve camera. A Z-stack of 4 slices at a step size of 0.5 μM was used. The stack was max projected and the area surrounding the Golgi cropped and used for quantification. To ascertain the localisation of the IC at the Golgi images were taken on a Leica TSC SP8 confocal microscope (Leica Microsystems) at 63x magnification. To obtain Z-stacks for qualitative assessment of IC at Golgi the same settings were used with a slices taken every 0.32 μm.

Golgi fragmentation and IC-Golgi localisation quantification were performed by Dr. Carlos Reyes-Aldasoro Constantino (City, University of London) using in-house algorithms developed in Matlab ® (Natick, MA, USA). For Golgi fragmentation analysis, Golgi fragments were automatically counted to avoid bias using an intensity-based segmentation based on Otsu's algorithm for optimal thresholds (Otsu, 1979). An initial Otsu level was calculated for the entire region of interest and was reduced to 50 % of the value to segment what was assumed to be the entire cell. Subsequently, another threshold was calculated for the pixels previously segmented (those within were assumed to be the cell). As a consequence of discarding a large portion of the background, the second threshold was higher than the first, this meant that the first threshold removed the background and the second distinguished between the Golgi and the rest of the

cell. Detected Golgi fragments were then labelled (each region of connected pixels given a label) and regions with less than 10 pixels were excluded as noise. The Golgi fragments were counted and morphological measures obtained such as total area and convex area (space between Golgi membranes).

To quantify the IC (green channel) localisation at the Golgi (red channel), the green channel underwent segmentation to allow the identification of a general foreground and background which had red and green signal. This was achieved by thresholding and morphological closing with a circular structural element of 8-pixel radius. The overlap of the foreground region with the red channel allowed for the calculation of an Otsu threshold which was used to segmented the red channel. Each region in the green channel within the segment red region were labelled and the area occupied by these regions and their intensities calculated.

2.6 Cloning and plasmid preparation

2.6.1 Transformation of DH5-α E.Coli

For the propagation of plasmids, chemically competent DH5-α E.Coli (ThermoFisher, Cat: 18265017) were used. 50 µL aliquots of this bacterial strain were thawed on ice and once thawed 2 µL of plasmid DNA was added immediately. The bacterial cells were incubated with the plasmid with occasional agitation on ice for 30 minutes. After this time elapsed, the bacteria/DNA mixture was heat shocked in a water bath at precisely 42 ^{o}C for 40 seconds and put back on ice for a further 2 minutes. Subsequently, 200 µL of Super optimal broth with catabolite repression (SOC) medium or lysogeny broth (LB) was added to the cells which were then incubated at 37 ^{o}C for 1 hour in a shaker at 220 rpm. After this incubation, the mixture was plated onto LB agar plates which contained the appropriate selection antibiotic (see Table 2.13 for concentration). After being allowed to absorb onto the agar for 15 minutes, the plates were incubated at 37 ^{o}C overnight.

Table 2.13

Antibiotic	High copy plasmid (relaxed)	Low copy plasmid (strigent)
Ampicillin	50 µg/mL	20 µg/mL
Kanamycin	40 µg/mL	10 µg/mL

Table 2.13 Antibiotic concentrations used for selection in transformed cells and in cultures for plasmid purification.

2.6.2 Plasmid propagation and purification

2.6.2.1 Miniprep

Minipreps were performed using the QIAprep spin miniprep kit (Qiagen, Cat: 27104) as per the manufacturer's instructions. Briefly, 5 mL of LB containing the selective antibiotic (see Table 2.12 for concentrations) was inoculated with DH5-α E.Coli, which had been transformed with the relevant plasmid. This 5 mL culture was incubated overnight at 37 ^{o}C in a shaker at 220 rpm. The next day, the culture was centrifuged in a microcentrifuge tube at 8,000 rpm for 3 minutes at room temperature and the supernatant removed. The resulting pellet was resuspended in 250 µL of buffer P1 (with RNAse A) and the subsequent lysis and neutralisation steps followed in accordance to the manufacturer's instructions. After centrifuging the resulting solution for 10 minutes at 13,000 rpm, the supernatant was transferred to a QIAprep 2.0 spin column which was then centrifuged for 1 minute at 13,000 rpm and flow-through discarded. The subsequent series of washes was performed as per the manufacturer's instructions including the optional wash step with PB buffer. Finally, 50 µL of double distilled water was added directly to the membrane of the spin column which was left to stand for 1 minute and then centrifuged one final time at 13,000 rpm for 1 minute and the flow through containing the purified plasmid collected in a new microcentrifuge tube. The DNA concentration was then measured using a NanoDrop 2000 spectrophotometer.

2.6.2.2 Midiprep

For this procedure 100 mL of LB containing the appropriate selection antibiotic (see Table 2.12 for concentrations) was inoculated and incubated overnight at 37 ^{o}C on a shaker at 220 rpm. 25 mL of this culture was used for purification of plasmid DNA using the Purelink HiPure Plasmid Filter Midiprep Kit (Invitrogen, Cat: K2100-04). The procedure was followed in accordance to the manufacturer's protocol aside from variations at certain centrifugation steps. Briefly, the 25 mL of the overnight culture was centrifuged at 3760 x g for 15 minutes and the supernatant discarded. Subsequently, the pellet underwent resuspension, lysis and precipitation as per the manufacturer's protocol. The resulting solution was then centrifuged at 3760 x g for 32 minutes at room temperature. The supernatant was loaded into the equilibrated HiPure Midi columns and a series of washes and

an elution step was performed in accordance to the manufacturer's instructions. Then, 3.5 mL isopropanol was added to the eluted DNA and mixed prior to centrifugation at 3760 xg for 2 hours at 4 ^{o}C. The resultant pellet was then washed in 3 mL of 70 % ethanol and centrifuged a final time at 3760 x g for 20 minutes at 4 ^{o}C. The DNA pellet was then air dried for 10 minutes and resuspended in 200 µL of double distilled water. The concentration of the DNA was then measured using a NanoDrop 2000 spectrophotometer.

2.6.2.3 Maxiprep

The maxiprep purification of plasmid DNA was performed using the PureLink HiPure Plasmid Maxiprep Kit (Invitrogen, Cat: K2100-06) in accordance to the manufacturer's protocol, aside from variations in centrifugation speeds and times. Briefly, 100 mL of LB was inoculated and incubated overnight at 37 ^{o}C on a shaker at 220 rpm. Subsequently, the 100 mL culture was centrifuged at 3760 x g for 15 minutes, the supernatant discarded and the resuspension, lysis and precipitation steps performed in accordance to the manufacturer's instructions. The supernatant was then loaded onto the equilibrated HiPure Maxi column which underwent a series of washes prior to the elution as per the manufacturer's instructions. 10.5 mL of isopropanol was then added to the eluate and was mixed prior to centrifugation at 3760 x g for 2 hours at 4 ^{o}C. The resulting pellet was then washed in 5 mL 70 % ethanol and centrifuged at 3760 x g for 20 minutes at 4 ^{o}C. The pellet was then air dried for 10 minutes and resuspended in 200-500 µL of double distilled water and the DNA concentration measured with a NanoDrop 2000 spectrophotometer.

2.7 Transfections

2.7.1 Transfection of cells with electroporation

Electroporation of neuro2a cells was performed using the Neon transfection system (Invitrogen. Cat: MPK10025) in accordance to the manufacturer's instructions. Cells were trypsinzed and washed in warm DBPS (without Ca^{2+} and Mg^{2+}) and were then resuspended at a density of $5x10^{6}$ per mL in the provided R buffer. Prior to the electroporation 6.11 µg of pcDNA3.1-V5-His-WT-TDP-43 was added to the cells and mixed. The mixture was taken up with 100 µL neon tip using the neon pipette. The pipette containing the DNA-cell mixture was then placed in the electroporation module in a Neon tube containing 3 mL of Buffer E,

ensuring that no bubbles are present in the neon tip to avoid arcing. The cells then received a single pulse at 1,410 V with a width of 1 ms. The cells were then placed in complete media without antibiotic and incubated for 24 hours. For each sample 1,500,000 cells were electroporated and pooled.

2.7.2 Transfection of cells with lipofection

Transfections performed with lipofection were either performed using Lipofectamine 2000 (ThermoFisher Scientific, Cat: 11668027) or Lipofectamine LTX (ThermoFisher Scientific, Cat: 15338100) in accordance to the manufacturer's instructions. Briefly, cells were seeded on either a 24 or 6 well plate (see Table 2.14 for corresponding reagent volumes) an allowed to reach approximately 50-80 % confluency. The next day complete medium was replaced with medium lacking antibiotic.

For lipofectamine LTX the plasmid DNA was diluted in Opti-MEM I reduced serum media (ThermoFisher Scientific, Cat: 31985062) and Plus reagent added. This mixture was incubated at room temperature for 15 minutes. Then, the lipofectamine LTX reagent was added to the DNA-plus reagent mixture and incubated for a further 30 minutes at room temperature. Subsequently, the DNA-lipofectamine LTX reagent complexes were added to each well with gentle mixing prior to incubation.

For lipofectamine 2000, the lipofectamine reagent was mixed with Opti-MEM I reduced serum media and incubated at room temperature for 5 minutes. Concurrently, the plasmid DNA was also diluted into opti-MEM and also incubated for 5 minutes. The DNA mixture was then mixed with the lipofectamine 2000 mixture in a 1:1 ratio and incubated at room temperature for 20 minutes prior to being added to the cells and mixed.

Table 2.14

	Lipofectamine LTX		Lipofectamine 2000
	24 well	**6 well**	**24 well**
Volume of Opti-MEM to dilute DNA	100 µL	500 µL	250 µL
Volume of plus reagent	0.5 µL	2.5 µL	-
Volume of reagent used	1.75 µL	8.75 µL	5 µL
Volume of Opti-MEM used to dilute reagent	-	-	50 µL
Volume added to cells	100 µL	500 µL	50 µL

Table 2.14 Volumes used for the transfection of cells using lipofectamine LTX and Lipofectamine 2000 in both 24 and 6 well plates.

2.8 Generation of HEK293 cells stably expressing Myc-peripherin

A kill curve was generated by exposing HEK293 cells to G418 antibiotic at various concentrations ranging from 0.1 mg/mL to 2 mg/mL. The cells were maintained in antibiotic for a period of 2 weeks, with the media changed every 3 days to new media containing the corresponding antibiotic concentration. After the 2 weeks elapsed, the cells were counted using trypan blue (Sigma, Cat: T8154) to distinguish between live and dead cells. The kill curve suggested a concentration of 0.8 mg/mL to be adequate to kill most cells within 2 weeks. However, as this was a high concentration, 0.5 and 0.65 mg/mL were also used to generate the stably transfected cells.

Subsequently, HEK293 cells were transfected using Lipofectamine 2000 (see section 2.7.2) with either 2.5 µg or 5 µg of a plasmid which expresses c-terminally Myc tagged peripherin under the control of a CMV promoter and concomitantly expresses turboGFP under the control of a SV40 promoter (Origene, Cat: PS100001). 24 hours after the transfection the cells were incubated with either 0.5, 0.65 or 8 mg/mL of the G418 antibiotic for which the plasmid provides resistance to due to the presence of the neomycin resistance gene. The cells were maintained in antibiotic containing media for 7 weeks, after which they were tested for Myc-peripherin expression.

2.9 Statistical analysis

Statistical analysis was performed using either GraphPad Prism or SPSS statistics software. Firstly, when data contained more than 3 repeats, the ROUT method on GraphPad Prism was used to remove outliers with the Q value set at the recommended 1%. All data was then tested with the Shapiro-Wilk test to determine if it was normally distributed. Assuming that this assumption was met, all immunoblot data expressed as relative to a fixed value (1 or 100%) was compared using a one sample t-test and all other data was tested using unpaired t-tests. However, for data with more than two levels within a single independent variable a one-way ANOVA with Tukey's multiple comparison test was performed if the normality and homogeneity of the variance requirements were met. If the data failed the normal distribution test, Log^{10} transformation was used and the normality retested, if it passed a one-way ANOVA was used if the homogeneity of the variance requirements were met. If transformation was insufficient to meet the normality requirement but data met the homogeneity of the variance requirement a Kruskal-Wallis test was performed, and Dunn's multiple comparisons test used for post-hoc analysis. If data was normally distributed prior to or after transformation but the homogeneity of the variance requirement was not met a Welch's ANOVA was performed with Games-Howell multiple comparisons test for post-hoc analysis. For experiments where there were two independent variables (drug treatment and genotype), two-way ANOVAs were performed if the normality and homogeneity of the variance requirements were met. For both one-way and two-way ANOVAs, homogeneity of the variance was tested using the Brown–Forsythe test within GraphPad Prism. While data for Figures 4.5b, 4.7c and 4.8c failed the Shapiro-Wilk test for normality, given the small sample number (N = 3) and other similar data passing the test with larger sample numbers, two-way ANOVAs were deemed appropriate. Especially as two-way ANOVAs only require approximately normally distributed data. Finally, for the analysis of data with multiple time points across two genotypes multiple t-tests were performed and Holm-Sidak correction for multiple comparisons was used to adjust the *P* values to mitigate type 1 errors. For all statistical tests a confidence level of 95% was used, therefore p values of <0.05 were deemed significance.

Chapter 3: Increased Peripherin expression in the lumbar spinal cord of TDP-43^{F210I} mice

3.1 Introduction

Peripherin is a type III intermediate filament which has been implicated in the pathogenesis of ALS (McLean et al., 2010). There is evidence that the overall expression levels and the ratio of peripherin isoform expression is altered in ALS (McLean et al., 2010). Additionally, toxic disease associated splice variants of peripherin have been identified which are not present in control samples (McLean et al., 2010; Robertson et al., 2003; Xiao et al., 2008). The factor affecting peripherin expression is yet to be identified, but recent evidence from the Hafezparast lab has indicated that TDP-43 could be involved (Barri, 2015). In pooled lumbar spinal cords from a transgenic mouse line overexpressing A315T mutant TDP-43, there was an increase in soluble Per-45, and alterations in the expression of Per-56 and an unidentified isoform at 50 kDa. Interestingly, it was suggested that the increase in soluble Per-45 was an indication that TDP-43 may be involved in regulating the alternative translation of this isoform. However, the overexpression of TDP-43 in these transgenic mice means that it is unclear if TDP-43 is able to alter peripherin expression and/or alternative translation at endogenous levels, or if this was an overexpression artefact.

The aim of this work was to further investigate if TDP-43 is capable of altering the expression of peripherin isoforms and to explore its involvement in the alternative translation of Per-45. To determine if previously observed alterations are an artefact of TDP-43 overexpression, a mouse model with endogenous ENU mutagenized TDP-43, causing a F210I substitution localised to RRM2, was used. It is hypothesised that peripherin expression will be altered in these mice, and that there will be an alteration in the alternative translation of Per-45. Additionally, *in vitro* analysis was used to further investigate the role of TDP-43 in alternative translation using the overexpression of wild type, F210I and M337V mutant TDP-43 in HEK293 cells made to stably express Myc-tagged peripherin.

3.2 Results

3.2.1 Analysis of peripherin expression from the entire spinal cord of TDP-43^{F210I} mice

As discussed, aberrant peripherin expression has been found in the lumbar spinal cord of transgenic mice which overexpress A315T mutant TDP-43. To eliminate the overexpression of TDP-43 as the cause of these changes rather than the mutation, a mouse line which has endogenous TDP-43 mutated causing a F210I substitution was used. Additionally, previous experiments with the TDP-43^{A315T} mouse line were performed by pooling the lumbar spinal cords to ensure sufficient protein was obtained for analysis. However, for the following experiment the entire spinal cord was used to try and mitigate the need for this pooling. The entire spinal cord was dissected and neurofilament enrichment performed as detailed in the materials and methods.

Figure 3.1 shows a representative S1 fraction from several experiments analysed by western blotting and probing with a polyclonal peripherin antibody which detects all peripherin isoforms. Per-58 was clearly identifiable as the most abundant isoform. Interestingly, Per-61 was also present in both wild type and TDP-43$^{+/F210I}$ mice despite being previously reported as an aberrant disease associated isoform not found in wild type mice (McLean et al., 2010; Robertson et al., 2003). However, several other unidentifiable bands are present which prohibited further detailed analysis of the expression of other peripherin isoforms.

Despite the use of the entire spinal cord likely causing the detection of several unidentifiable bands which prohibited quantification, these experiments showed that Per-61 is not a neurotoxic splice variant as it was found in both wild type and TDP-43$^{+/F210I}$ mice. Importantly, Dr Muruj Barri from the Hafezparast lab used an antibody specific to the Per-61 isoform and confirmed the identity of this band as Per-61.

Figure 3.1

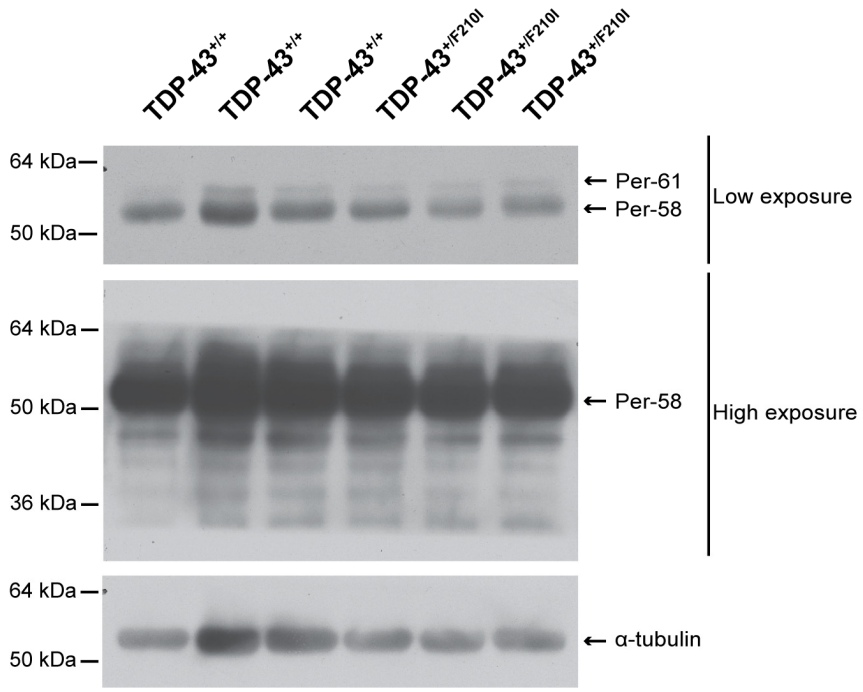

Figure 3.1 Analysis of peripherin expression in the spinal cord of both wild type and TDP-43$^{+/F210I}$ mice. The blot shows three biological repeats for each genotype. Per-58 is identifiable as the most abundant isoform and Per-61 is present in both wild type and TDP-43$^{+/F210I}$ mice. α-tubulin was used as the loading control.

3.2.2 Increased peripherin expression in the lumbar spinal cord of TDP-43^{F210I} mice

To overcome the difficulties in assessing peripherin expression in the entire spinal cord, the lumbar region was instead used. Initial results revealed that the pooling of the lumber spinal cords was not necessary as sufficiently clear bands were detected (Figure 3.2). As with the entire spinal cord, sequential homogenisation was used to analyse soluble peripherin content and peripherin in enriched intermediate filaments. Each extraction produced two soluble fractions (DPBS soluble S1 and Triton X-100 soluble S2) and an insoluble fraction (P3) consisting of the enriched neurofilaments which were disrupted with 2 % SDS. Note that while the S3 sucrose fraction was ran in the western blot analysis and so is shown in Figure 3.2, it did not undergo further analysis as it represents the product of a step designed to only remove lipids from the P3 fraction. Four biological repeats were conducted per genotype. Western blot analysis of each fraction was performed to compare peripherin expression between wild type and TDP-43$^{+/F210I}$ mice. As before, probing was performed with a polyclonal peripherin antibody which detected all peripherin isoforms.

Figure 3.3a shows the result of western blot analysis of the DPBS soluble fraction (S1) which represents non-filamentous soluble peripherin. Several peripherin isoforms were detected in this fraction, including Per-58 and Per-45. Additionally, an isoform of approximately 50 kDa was detected, which has previously been suggested to be the equivalent of a human isoform of the same size generated by alternative splicing of exon one (McLean et al., 2010). Within this fraction, this isoform appears to be the most abundant (Figure 3.3a). A further unknown isoform between Per-45 and Per-58 was also detected in both genotypes but remains unidentified. Finally, an isoform was seen above Per-58 in both wild type and TDP-43$^{+/F210I}$ mice and due to its unusual size at approximately 64 kDa its identify was checked and confirmed as corresponding to Per-61 by Dr Muruj Barri using an antibody specific for this isoform.

Figures 3.3b-e shows the densitometric quantification of the levels of peripherin isoforms. This analysis revealed no significant difference in the expression of Per-58 between genotypes (one sample t-test, $P = 0.3806$). Furthermore, a one sample t-test showed no statistically significant difference in the levels of the 50

kDa isoform (*P = 0.2274*; Figure 3.3c). Similarly, no significant difference between genotypes was seen in Per-45 and in the unknown isoform above it (one sample t-test, *P = 0.3151* and *P = 0.3719* respectively).

Figure 3.2

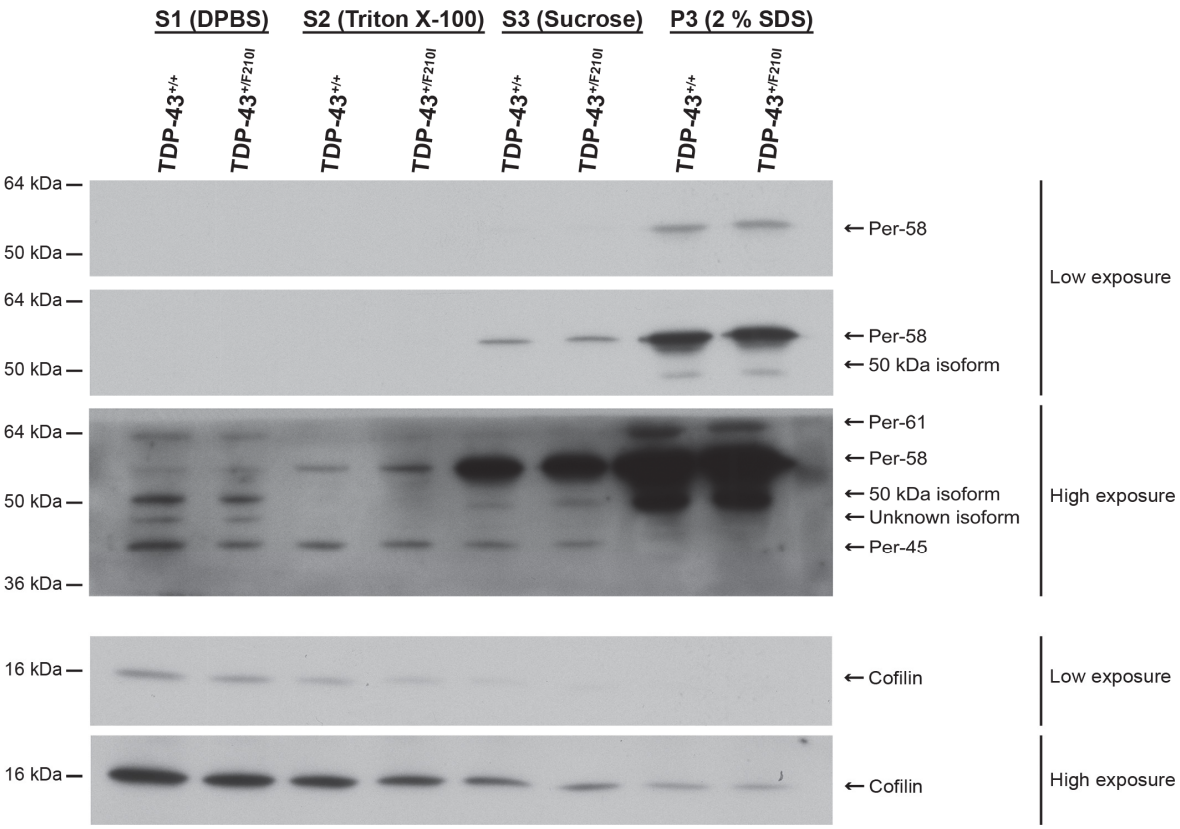

Figure 3.2 Western blot analysis of peripherin levels in the lumbar spinal cords of wild type and TDP-43$^{+/F210I}$ mice. The blot shows the expression of Per-61, Per-58, Per-45, the 50 kDa isoform and an unknown isoform between 45 kDa and 50 kDa in the fractions produced from the neurofilament extraction protocol.

Figure 3.3

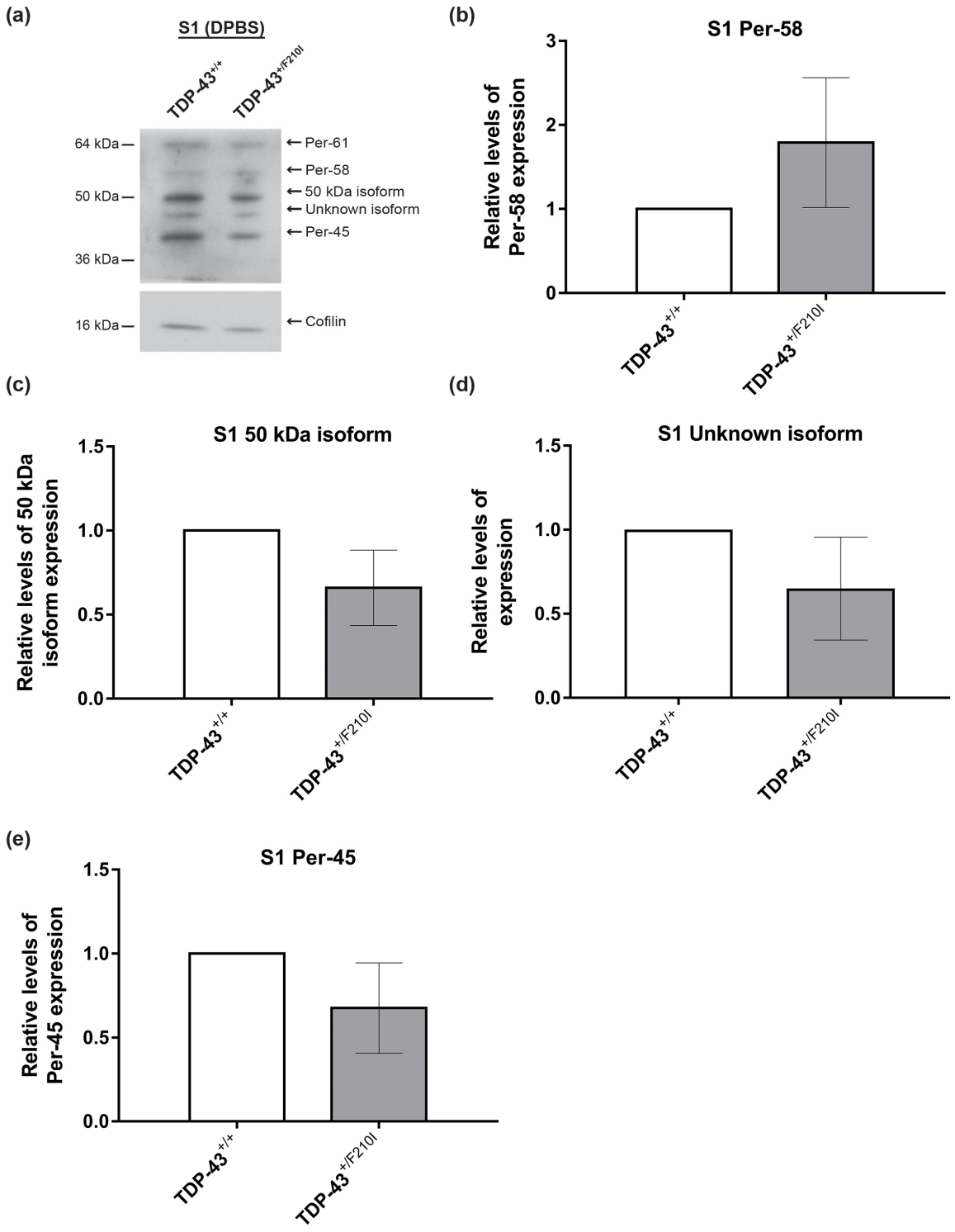
(a)
S1 (DPBS)
TDP-43+/+
TDP-43+/F210I
64 kDa
50 kDa
36 kDa
16 kDa
← Per-61
← Per-58
← 50 kDa isoform
← Unknown isoform
← Per-45
← Cofilin
(b)
S1 Per-58
Relative levels of Per-58 expression
(c)
S1 50 kDa isoform
Relative levels of 50 kDa isoform expression
(d)
S1 Unknown isoform
Relative levels of expression
(e)
S1 Per-45
Relative levels of Per-45 expression

Figure 3.3 (a) Western blot analysis of peripherin levels in the DPBS soluble S1 fraction of lumbar spinal cords of wild type and TDP-43$^{+/F210I}$ mice. The blot shows Per-61, Per-58, Per-45, the 50 kDa isoform and an unknown isoform between 45 kDa and 50 kDa. **(b)** Densitometric quantification of Per-58 levels in S1 showed an increase in TDP-43$^{+/F210I}$ mice which is not statistically significant (one sample t-test, *P = 0.3806*). **(c)** Densitometric quantification of the 50 kDa isoform and a one sample t-test showed a non-statistically significant decrease (*P = 0.2274*). **(d)** Similarly, the unknown isoform detected between Per-45 and 50 kDa showed a decrease, which a one sample t-test revealed not to be statistically significant (*P = 0.3719*). **(e)** Densitometric quantification of Per-45 showed a decrease in TDP-43$^{+/F210I}$ mice but did not reach statistical significance (one sample t-test, *P = 0.3151*). For each densitometric quantification, the levels of each peripherin isoform were normalised to the cofilin loading control and expressed as relative levels to the wild type samples. N = 4 biological repeats. Error bars represent SEM.

In the Triton X-100 soluble fraction (S2) that also constituted of non-filamentous peripherin, only Per-58 and Per-45 were consistently detected while the 50 kDa isoform was only seen in one of the four biological repeats for each genotype (Figure 3.4a). In this fraction, there was a distinguishable increase in the levels of Per-58 in TDP-43$^{+/F210I}$ mice in comparison to wild type mice, which was confirmed by densitometric quantification (Figure 3.4b). However, a one sample t-test showed this difference did not reach the significance threshold (*P = 0.1082*). Importantly, Per-45 was also increased in the TDP-43$^{+/F210I}$ mice in Figure 3.4a and this was reflected in the densitometric quantification, analysis of which with a one sample t-test showed this to be statistically significant (*P = 0.0353*; Figure 3.4c). Despite the increase in Per-58 not reaching significance, the concomitant increase in Per-58 and Per-45 suggests that the increase in Per-45 may not due to altered alternative translation of the Per-58 transcript. Therefore, to test this, the ratio of Per-45 to Per-58 was analysed between genotypes (Figure 3.4d). Unexpectedly, the results showed that the levels of Per-45 relative to Per-58 are decreased in the TDP-43$^{+/F210I}$ mice but this did not reach the threshold for statistical significance (*P = 0.1049*). Therefore, while this data is potentially

indicative of an alteration in the selection of the start codon on the Per-58 transcript towards the production of Per-58 rather than Per-45, the lack of a statistically significant change means further confirmation is required.

Finally, several isoforms were detected in the insoluble fraction (P3) consisting of enriched filamentous peripherin (Figure 3.5a). In both genotypes, the most abundant isoform detected was Per-58, followed by the isoform at 50 kDa. However, while both Per-45 and the unknown isoform are present in this figure at very low levels, this was not consistent across all repeats. Therefore, these isoforms were not quantified in this fraction.

Densitometric quantification of Per-58 levels and a one sample t-test showed no significant difference between genotypes (*P = 0.3454*). On the other hand, the 50 kDa isoform was consistently increased in TDP-43$^{+/F210I}$ mice and densitometric quantification showed an approximately 2-fold increase, as seen in Figure 3.5c. A one sample t-test confirmed a statistically significant increase in this isoform in TDP-43$^{+/F210I}$ mice (*P = 0.0241*). To determine whether the increase in the 50 kDa isoform was altering its stoichiometry relative to Per-58 within the filaments, the ratio between these two isoforms was analysed (Figure 3.5d). An unpaired t-test showed no significant change in the ratio of the 50 kDa isoform to Per-58 (*P = 0.6437*).

Overall, data presented here suggests that peripherin expression was altered within the murine lumbar spinal cord in TDP-43$^{+/F210I}$ mice. This was indicated by the significant increase in soluble Per-45 (S2) and a significant increase in filamentous peripherin isoform of 50 kDa (P3), the latter of which appears not to be altering the stoichiometry of peripherin isoforms within the filaments.

Figure 3.4

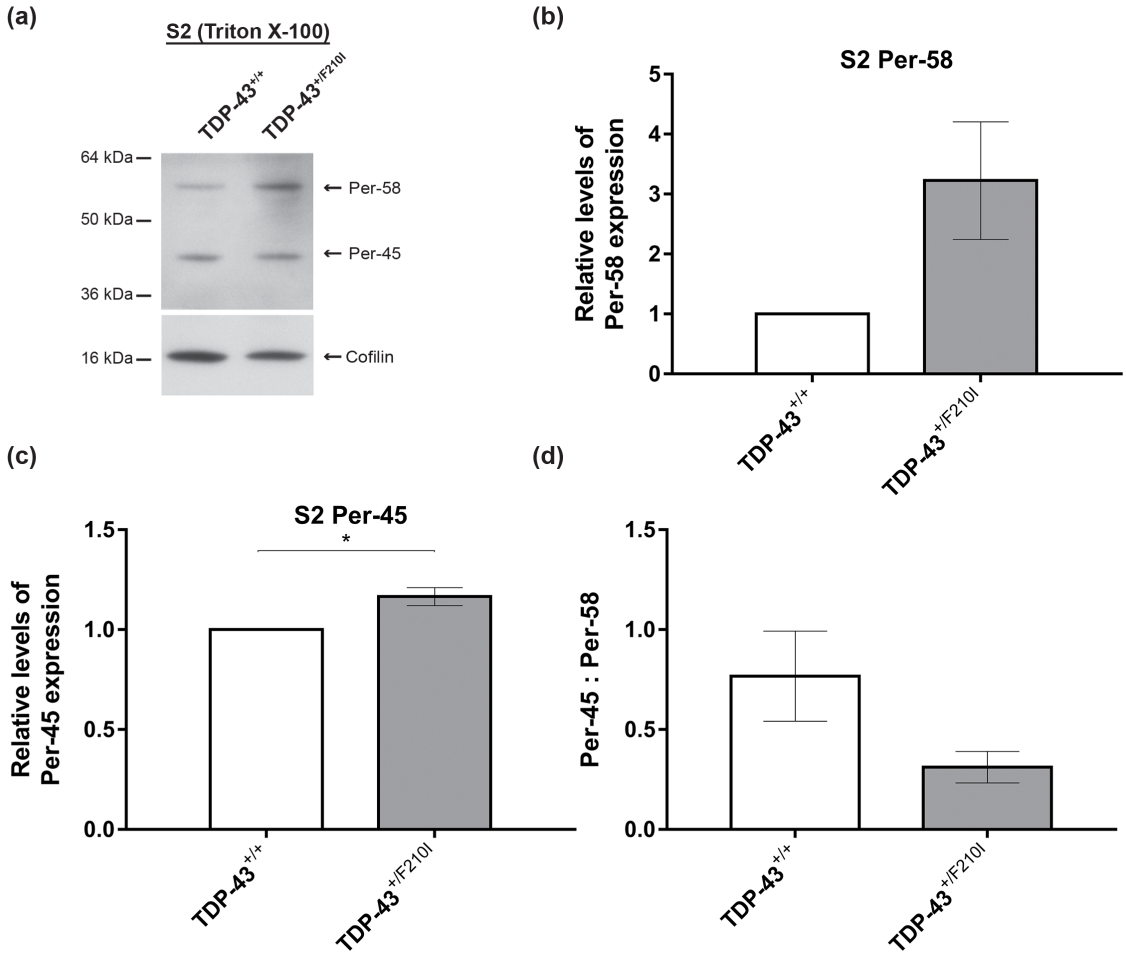

Figure 3.4 (a) Western blot analysis of the Triton X-100 soluble S2 fraction from the neurofilament extraction performed on the lumbar spinal cord of wild type and TDP-43$^{+/F210I}$ mice. Per-58 and Per-45 were detected and both are visibly increased in TDP-43$^{+/F210I}$ mice. **(b)** Densitometric quantification of Per-58 expression in S2 from wild type and TDP-43$^{+/F210I}$ mice. A one sample t-test shows no significant difference in the levels of Per-58 (*P = 0.1082*). **(c)** Densitometric quantification of Per-45 levels in S2 showing a statistically significant increase in Per-45 in TDP-43$^{+/F210I}$ mice (one sample t-test, *P = 0.0353*). **(d)** An unpaired t-test on the ratio of Per-45 to Per 58 in the S2 soluble fraction showed no significant difference in TDP-43$^{+/F210I}$ mice *(P = 0.1049)*. For each densitometric quantification the levels of each peripherin isoform were normalised to the cofilin loading control. Apart for the Per-45 to Per 58 ratio analysis, these were expressed as relative levels to the wild type samples. N = 4 biological repeats. Error bars represent SEM. (* *P < 0.05*)

Figure 3.5

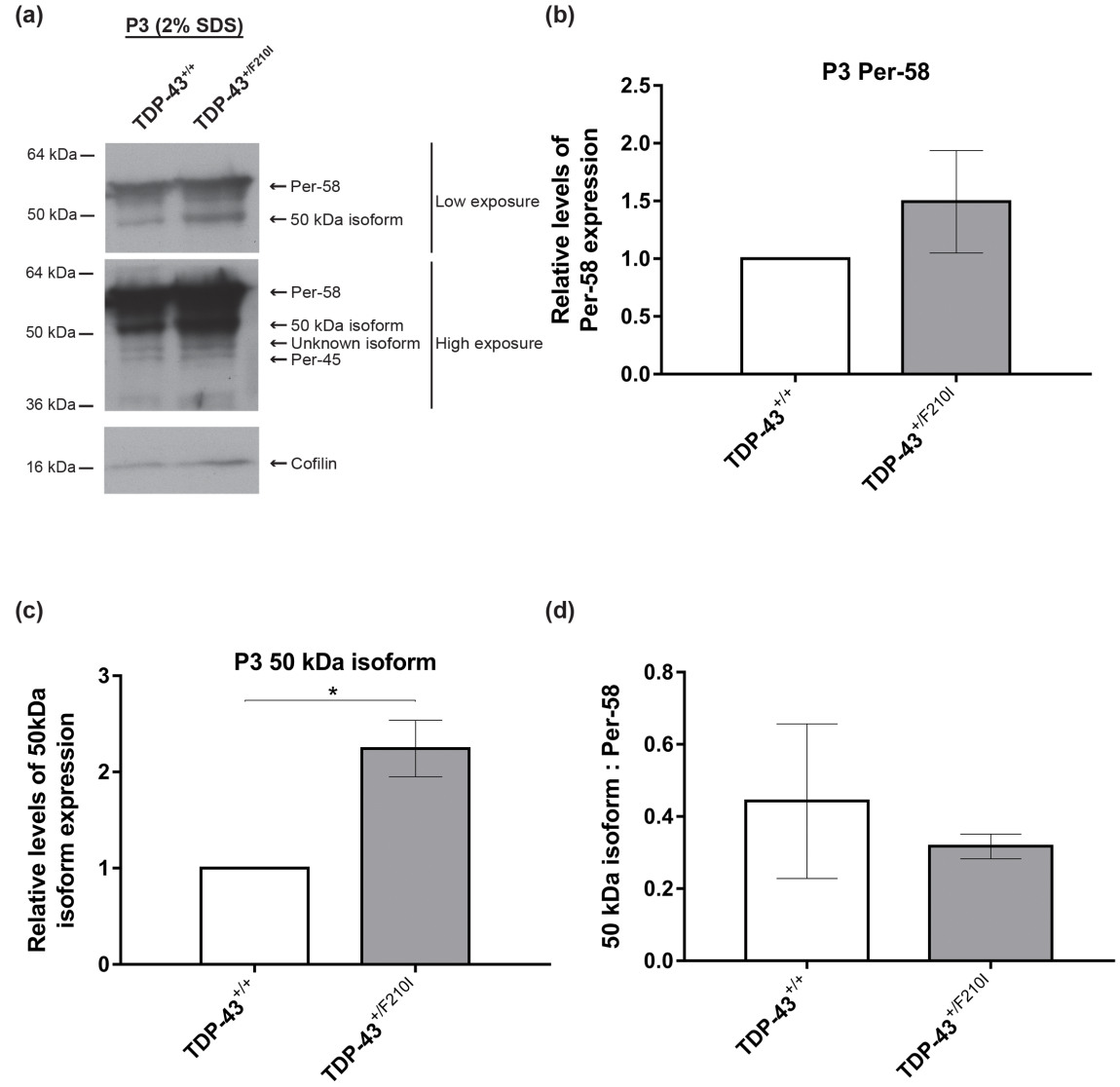
(a)
P3 (2% SDS)
TDP-43+/+
TDP-43+/F210I
64 kDa
50 kDa
← Per-58
← 50 kDa isoform
Low exposure
64 kDa
50 kDa
36 kDa
← Per-58
← 50 kDa isoform
← Unknown isoform
← Per-45
High exposure
16 kDa
← Cofilin
(b)
P3 Per-58
Relative levels of Per-58 expression
2.5
2.0
1.5
1.0
0.5
0.0
TDP-43+/+
TDP-43+/F210I
(c)
P3 50 kDa isoform
Relative levels of 50kDa isoform expression
*
3
2
1
0
TDP-43+/+
TDP-43+/F210I
(d)
50 kDa isoform : Per-58
0.8
0.6
0.4
0.2
0.0
TDP-43+/+
TDP-43+/F210I

Figure 3.5 (a) Western blot analysis of the insoluble P3 fraction of the neurofilament extraction conducted from the lumbar spinal cord of wild type and TDP-43$^{+/F210I}$ mice. Per-58 and the 50 kDa isoforms were strongly detected, whilst Per-45 and an unknown isoform between Per-45 and 50 kDa were detected inconsistently and weakly. **(b)** Densitometric quantification of Per-58 levels in fraction P3 showed an increase in TDP-43$^{+/F210I}$ mice which does not reach statistical significance (one sample t-test, $P = 0.3454$). **(c)** Densitometric quantification showed a statistically significant increase in the levels of the 50 kDa isoform in the lumbar spinal cord of TDP-43$^{+/F210I}$ mice (one sample t-test, $P = 0.0241$). **(d)** Analysis of the ratio of the 50 kDa isoform to Per-58 in the filamentous fraction. An unpaired t-test showed no significant difference between wild type and TDP-43$^{+/F210I}$ mice ($P = 0.6437$). For each densitometric quantification the levels of each peripherin isoform were normalised to the cofilin loading control. Apart for the Per-50 to Per 58 ratio analysis, these were expressed as relative levels to the wild type samples. N = 4 biological repeats. Error bars represent SEM. ($* P < 0.05$)

3.2.3 Peripherin expression in neuro2a cells overexpressing TDP-43

To further investigate whether TDP-43 is able to alter the alternative translation of Per-45, neuro2a cells which express peripherin in an undifferentiated state were transfected via electroporation with wild type TDP-43 tagged with a V5 epitope. 24 hours after transfection with 6.11 µg of wild type pCDNA3.1-V5-His TDP-43 plasmid, the cells were lysed with RIPA lysis buffer.

Western blot analysis was performed to check the transfection and to detect any changes in peripherin expression (Figure 3.6). Probing for the V5 epitope shows a high level of transfection of wild type TDP-43. Using the same polyclonal peripherin antibody previously used, a high expression of Per-58 was detected. Additionally, Per-45 and the 50 kDa isoform were also detected at very low levels. Consequently, the low levels of the expression of these isoforms made it difficult to quantify accurately and thus to overcome this difficulty a different approach was taken.

Figure 3.6

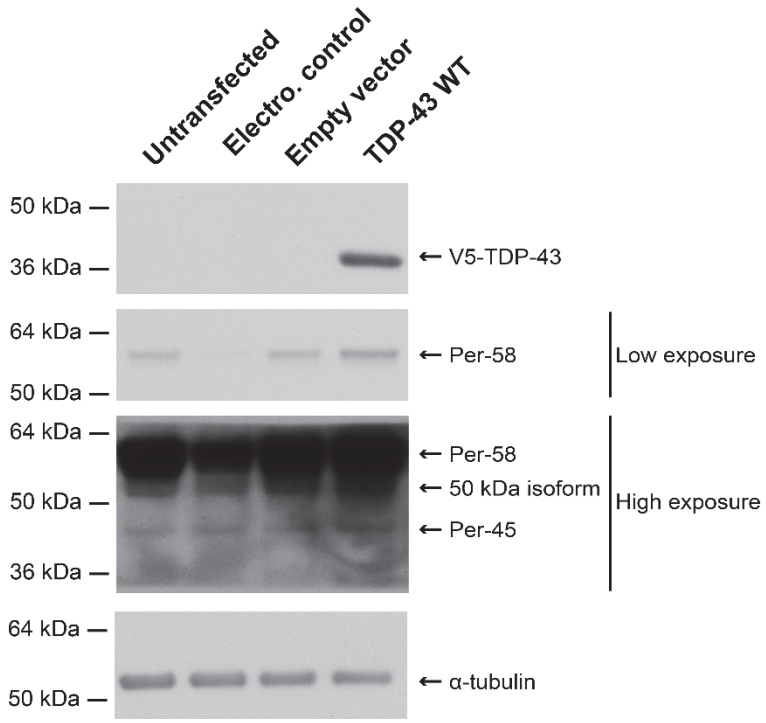

Figure 3.6 Peripherin expression in neuro2a cells following overexpression of wild type TDP-43 tagged with a V5 epitope. The electroporation control consisted of cells which underwent electroporation without the presence of a plasmid but an equivalent volume of water. The empty vector control consists of transfection with the pcDNA-V5-His vector without TDP-43. Probing for V5 shows the transfection to be successful, whilst peripherin probing produces bands corresponding to the Per-58, Per-45 and 50 kDa isoforms. However, Per-45 levels are minimal and difficult to quantify. α-tubulin was used as a loading control.

3.2.4 Overexpression of wild type and mutant TDP-43 does not alter Per-45 alternative translation in HEK293 cells stably expressing peripherin

To overcome the difficulties in investigating the role of TDP-43 in the alternative translation of Per-45 using neuro2a cells, a stable cell line was generated from HEK293 cells which expressed peripherin at higher levels. An antibiotic kill curve was performed where HEK293 cells were incubated with varying concentrations of G418 antibiotic to determine the appropriate concentration for the selection of stably transfected cells. As shown in Figure 3.7a, the concentration which caused almost complete cell death within a period of two weeks was 0.8 mg/mL. However, 0.5 mg/mL, 0.65 mg/mL and 0.8 mg/mL of G418 antibiotic were used to select for stably transfected cells to ensure the survival of these cells. HEK293 cells were transfected with lipofectamine 2000 with either 2.5 µg or 5 µg of a plasmid expressing human peripherin tagged with Myc. After maintaining the cells in G418 at the aforementioned concentrations for 7 weeks, western blot analysis was performed and a Myc antibody was used to detect tagged peripherin. As shown in Figure 3.7b, cells transfected with both 2.5 µg or 5 µg of the human peripherin clone were still expressing Myc tagged peripherin in every concentration of G418. This expression was not detected in the negative HEK293 control which did not undergo this process.

Subsequently, the HEK293 cells that were made to stably express Myc-peripherin by selection with 0.8 mg/mL of G418 were used to investigate the effect of wild type and mutant TDP-43 on the alternative translation of Per-45. These cells were transfected using lipofectamine LTX with either wild type TDP-43, TDP-43 F210I or TDP-43 M337V which were all tagged with a V5 epitope in pcDNA3.1-V5-His. Western blot analysis and probing for the V5 epitope showed a high transfection efficiency in all samples (Figure 3.8a). The peripherin expression in transfected cells were subsequently analysed by probing for the c-terminal Myc tag. As was seen previously, both Per-58 and Per-45 were detected, whilst a third band at 39 kDa was also detected (Figure 3.8b). However, this 39 kDa band was seen in the negative control in Figure 3.7b and so it was excluded from the analysis.

Densitometric quantification of Per-58 did not show a statistically significant difference between the control samples and those transfected with either wild type, F210I or M337V TDP-43 as shown by a one-way ANOVA ($P = 0.9868$, N= 3)

(Figure 3.8c). Similarly, a one-way ANOVA of the quantification of Per-45 showed no significant difference between samples transfected with wild type, F210I or M337V TDP-43 and control samples (*P = 0.6214*) (Figure 3.8d). Finally, the ratio of Per-45 to Per-58 was analysed to ensure that TDP-43 was not affecting alternative translation (Figure 3.8e). A one-way ANOVA showed no significant difference in this ratio across the samples *(P = 1.108*).

In summary, the overexpression of both wild type and mutant TDP-43 (with either the F210I or M337V substitution) did not alter alternative translation of Per-45 in HEK293 cells made to stably express peripherin. However, it may be the case that the use of a cDNA clone to induce peripherin expression lacked regulatory elements necessary for TDP-43 to affect alternative translation.

Figure 3.7

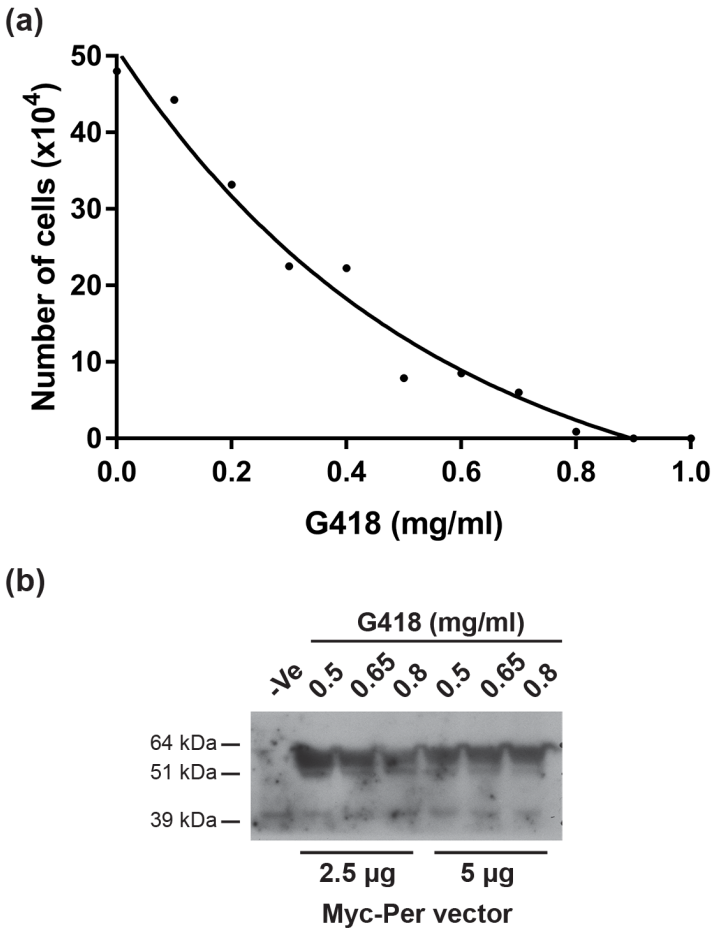

Figure 3.7 (a) G418 antibiotic kill curve for HEK293 cells. A 24 well plate was seeded with 100,000 cells and the next day, varying concentrations of G418 antibiotic were added and maintained for 2 weeks. After this period, the cells which remained alive were counted. The curve shows the optimum concentration to be 0.8 mg/mL. **(b)** Western blot analysis of stably transfected HEK293 cells maintained in varying concentrations of the G418 antibiotic after transfection with a vector expressing C-terminally Myc-tagged human peripherin that also imparts G418 resistance. Myc-peripherin expression was detected at all concentrations of G418 and in both concentrations of transfected plasmid (2.5 µg and 5 µg). Note the presence of a non-specific band at 39 kDa in both the negative control (untransfected HEK293 cells) and the stably transfected cells.

Figure 3.8

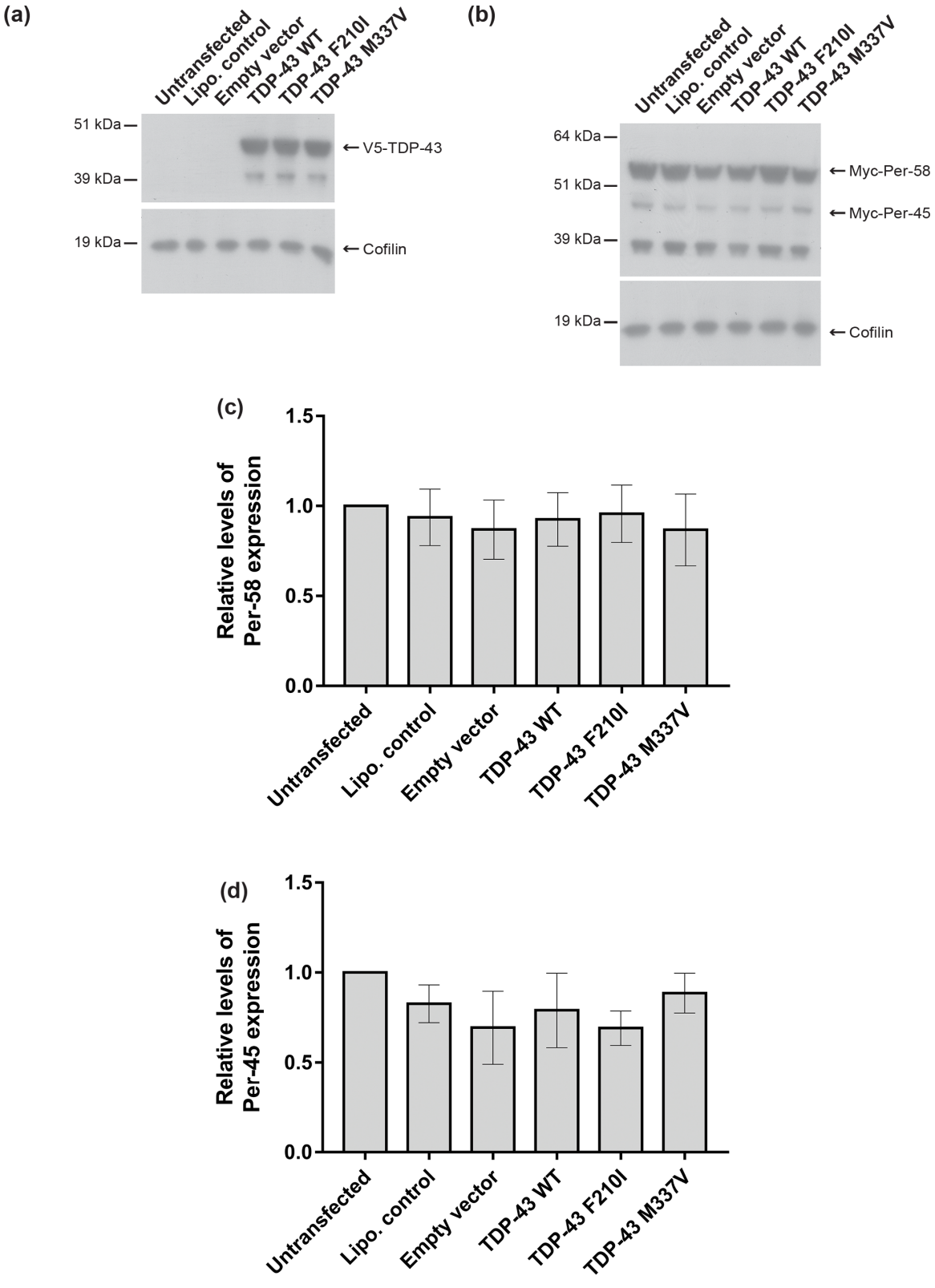
(a)
Untransfected
Lipo. control
Empty vector
TDP-43 WT
TDP-43 F210I
TDP-43 M337V
51 kDa
39 kDa
19 kDa
← V5-TDP-43
← Cofilin
(b)
Untransfected
Lipo. control
Empty vector
TDP-43 WT
TDP-43 F210I
TDP-43 M337V
64 kDa
51 kDa
39 kDa
19 kDa
← Myc-Per-58
← Myc-Per-45
← Cofilin
(c)
Relative levels of Per-58 expression
1.5
1.0
0.5
0.0
Untransfected
Lipo. control
Empty vector
TDP-43 WT
TDP-43 F210I
TDP-43 M337V
(d)
Relative levels of Per-45 expression
1.5
1.0
0.5
0.0
Untransfected
Lipo. control
Empty vector
TDP-43 WT
TDP-43 F210I
TDP-43 M337V

Figure 3.8 continued

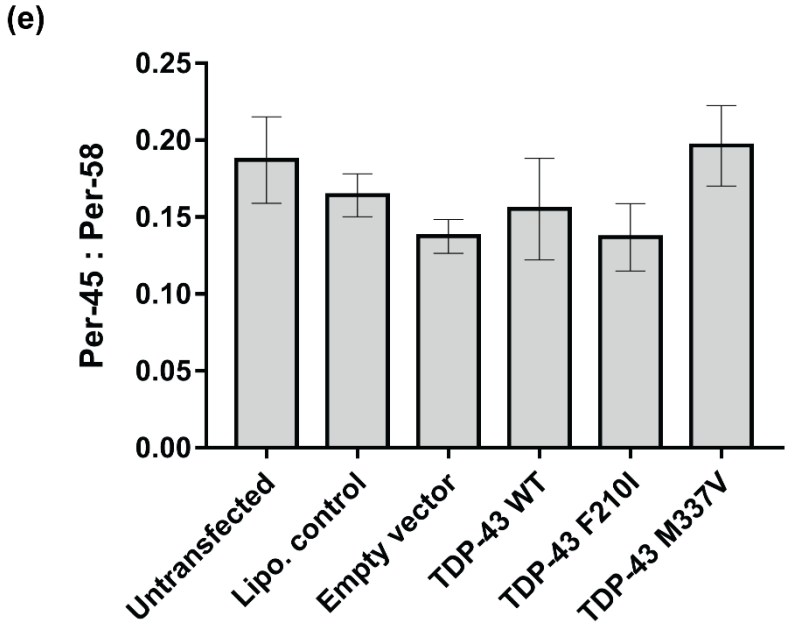

Figure 3.8 (a) Western blot to check the transfection of V5 tagged TDP-43 (wild type, F210I or M337V mutant) in HEK293 cells made to stably express Myc-tagged peripherin. Probing was performed for the V5 tag and shows successful transfection in all samples. **(b)** Western blot analysis of Myc-peripherin expression in HEK293 cells made to stably express Myc-tagged peripherin following overexpression of either V5 tagged wild type, F210I or M337V mutant TDP-43. No differences between transfected samples and controls can be seen in both Per-58 and Per-45. A non-specific band is seen at 39 kDa. **(c)** Densitometric quantification of the Per-58 isoform following overexpression of the different variants of TDP-43. A one-way ANOVA shows no significant difference across all samples (*P = 0.9868*). **(d)** Densitometric quantification of the Per-45 isoform following overexpression of the different variants of TDP-43. A one-way ANOVA shows no significant difference across all samples (*P = 0.6214*). **(e)** Analysis of the ratio of Per-45 to Per-58 after transfection with TDP-43 (wild type, F210I or M337V mutant). A one-way ANOVA shows no significant difference in this ratio across the samples *(P = 1.108*). In each densitometric quantification, the levels of each peripherin isoform were normalised to the cofilin loading control. Aside from the Per-45 : Per58 ratio, there were expressed as relative levels to the untransfected samples. N = 3. Error bars represent SEM.

3.2.5 Summary

Firstly, data presented here supports recent evidence that Per-61 is not exclusively found in disease associated tissues but is also present in wild type tissue. Further evidence, showed that the F210I mutation of TDP-43 altered the levels of several peripherin isoforms. There was significantly increased Per-45 and statistically non-significant increased Per-58 in S2. A significant increase in the 50 kDa isoform in the filamentous fraction (P3) was also observed. Interestingly, ratio analysis of Per-45 to Per-58 levels in S2 suggested that there may be a change in the alternative translation of Per-45 as despite an overall increase in peripherin, Per-45 was reduced in comparison to Per-58. However, this change did not reach statistical significance. Furthermore, ratio analysis of the 50 kDa isoform to Per-58 in the filamentous fraction showed no alterations in their stoichiometry. Overall, this suggests that in the lumber spinal cord of TDP-43$^{+/F210I}$ mice there is an increased expression of peripherin as a whole, and that there may be a change in the alternative translation of Per-45. Furthermore, the overexpression of wild type TDP-43 did not alter the alternative translation of Per-45 in HEK293 cells stably expressing peripherin. Similarly, F210I and M337V mutant TDP-43 also failed to elicit changes in Per-45 levels in these cells.

Table 3.1 shows a summary of the changes observed in the TDP-43$^{+/F210I}$ mice and what had previously been seen in the TDP-43^{A315T} transgenic mice in the Hafezparast lab (Barri, 2015).

Table 3.1

Peripherin isoform	S1 (DPBS)		S2 (Triton X-100)		P3 (SDS)	
	TDP-43$^{+/F210I}$	TDP-43^{A315T}	TDP-43$^{+/F210I}$	TDP-43^{A315T}	TDP-43$^{+/F210I}$	TDP-43^{A315T}
Per-61	Present	Present				
Per-58	Increase	Not quantified	Increase	No change	Increase	No change
Per-56						No change
Per-45	Decrease	Increase	Increase*		Not quantified	
50 kDa isoform	Decrease			Not quantified	Increase*	No change
Unidentified isoform	Decrease				Not quantified	
Per-45 : Per-58			Decrease			
50 kDa isoform : Per-58					Decrease	

Table 3.1 Changes in peripherin isoforms identified here in the TDP-43$^{+/F210I}$ mouse model in contrast with the changes previously reported in the TDP-43^{A315T} mouse model (Barri, 2015). * denotes a statistically significant change (* *P < 0.05)*

3.3 Discussion

3.3.1 Analysis of peripherin expression in the spinal cord of TDP-43^{F210I} mice

To investigate if TDP-43 is involved in regulating the alternative translation of Per-45 and if endogenous levels can affect peripherin expression, a mouse model where endogenous TDP-43 contained a F210I substitution was used. Firstly, peripherin expression was analysed using the entire spinal cord by western blot analysis using the same extraction method used previously in the Hafezparast lab which was adapted from Xiao et al. 2008. Probing with a polyclonal peripherin antibody which detects all known isoforms of peripherin showed a high level of Per-58 expression, agreeing with previous observations that it forms the most abundant isoform in the spinal cord (McLean et al., 2008). However, above Per-58 another band was detected at the expected size for Per-61, in both wild type and TDP-43$^{+/F210I}$ mice. As discussed, the identify of this band as Per-61 was later verified by Dr Muruj Barri from the Hafezparast lab using a Per-61 specific antibody. These data contradict previous observations that Per-61 is a disease associated isoform only detected in motor neurons of SOD1^{G37R} and in symptomatic SOD1^{G93A} mice (Robertson et al., 2003; McLean et al., 2010). However, it does agree with previous findings in the Hafezparast lab which also found Per-61 in wild type mice (Barri, 2015).

Further analysis was prohibited by the presence of several unidentified bands in both wild type and TDP-43$^{+/F210I}$ samples. This unexpected complication was not seen in the analysis of the lumbar spinal cord previously performed in the Hafezparast lab. This may have been caused by the use of the entire spinal cord as peripherin is differentially expressed in different regions of the spinal cord (McLean et al., 2008). To overcome this, experiments proceeded to use only the lumbar spinal cord, but it was found that unlike experiments previously conducted in the Hafezparast lab, pooling of the samples was not required.

The sequential enrichment began with the use of DPBS as the lysis buffer, giving the first soluble fraction (S1). Peripherin detected in this fraction should not have been disrupted from the filaments but represents free peripherin within the cytosol. The use of the lumbar spinal cord confirmed that the issues encountered in the previous analysis were indeed due to the use of the entire spinal cord. However, as with the previous analysis of the entire spinal cord, a band was detected above

Per-58 which as mentioned was later confirmed to represent Per-61 despite appearing a 64 kDa. Furthermore, no other peripherin isoform is found in this region (McLean et al., 2010). Conversely, while the analysis of the entire spinal cord showed Per-58 to be the most abundant isoform in the S1 fraction, data here revealed that in this fraction the 50 kDa isoform appeared at consistently higher levels than Per-58. Previously, this 50 kDa isoform has been suggested to be the mouse equivalent of a human isoform of the same molecular weight and is generated by alternative splicing of exon 1 (McLean et al., 2010). In addition to the Per-61, Per-58 and the 50 kDa isoform two further bands were detected. The lower band was identified as Per-45 as it was also present in the Triton X-100 S2 fraction as previously reported, whilst the band above this was not present in this fraction (McLean et al., 2008). Importantly, there was no significant difference in the levels of any of the peripherin isoforms detected in S1 between wild type and TDP-43$^{+/F210I}$ mice. In contrast, Per-45 was found increased in this fraction in the TDP-43^{A315T} mice in the Hafezparast lab (Barri, 2015).

In the Triton X-100 soluble fraction (S2), Triton X-100 was used to ensure complete lysis of the tissue without disrupting the filaments. In this fraction, only Per-45 and Per-58 were consistently detected. Interestingly, there was a significant increase in Per-45 in the TDP-43$^{+/F210I}$ mice. It is likely that the shift in the difference from S1 in the TDP-43^{A315T} mice to S2 in the data presented here is due to variation between experimenters in the harshness of the homogenisation of the tissue. In this fraction, densitometric quantification showed an increase in the levels of Per-58, and while this change was not statistically significant, it was a feature seen in all 4 biological repeats. The variation in the amount of the increase between the samples may have underpinned the lack of a significance. This suggests that the increase in Per-45 is accompanied by an increase in Per-58 which initially indicated that Per-45 alternative translation in not being altered by TDP-43. However, analysis of the Per-45 to Per-58 ratio shows that Per-45 decreases relative to Per-58 in the mutant. This may be indicative of a shift in the alternative translation of Per-45 towards that of Per-58. This is in contrast to observations that the alternatively translated Per-45 is increased TDP-43^{A315T} mice (Barri, 2015). However, it is important to note that the shift in the Per-45 to Per-58 in the TDP-43$^{+/F210I}$ presented here failed to reach statistical significance.

Furthermore, it may be the case that the overall increase in peripherin levels may cause a shift in the balance of the alternative translation and so this change may not represent a direct intervention by TDP-43. Finally, the increases seen in Per-45 and Per-58 might indicate a breakdown of the peripherin filaments in TDP-$43^{+/F210I}$ mice that would result in an increase in soluble peripherin.

However, analysis of the final fraction (P3), which consists of the enriched filaments disrupted with 2 % SDS, disputes this. Here the most abundant isoform detected is Per-58, showing that it is the main constituent of peripherin filaments, in agreement with previous reports (McLean et al., 2008). Importantly, there is no detectable loss of Per-58 in comparison to wild type mice in this fraction to suggest a breakdown of the filaments. Therefore, it is more likely that the increase in Per-58 and Per-45 seen in S2 are due to overall upregulation of peripherin. Interestingly, the second most abundant isoform detected in P3 was the isoform at 50 kDa, which was found to be significantly increase in TDP-$43^{+/F210I}$ mice. This could potentially indicate that the detected overexpression of peripherin is causing a change in the stoichiometric ratio of peripherin at the filaments with increased incorporation of the 50 kDa isoform. To assess this, the ratio of the 50 kDa isoform to Per-58 in the filaments was analysed, and it showed that there is no significant change. This indicates that the increase in peripherin expression is causing an overall increase in filamentous peripherin without altering the stoichiometric ratio between the 50 kDa isoform and Per-58. Only in one of the four biological repeats was Per-45 and the unknown isoform between Per-45 and 50 kDa detected. This is in agreement with previous observations that whilst Per-45 is not able to form homopolymeric filaments, it is incorporated into heteropolymeric filaments with other species of peripherin (McLean et al., 2008).

Overall, these data indicate that there is an overall upregulation of peripherin expression in TDP-$43^{+/F210I}$ mice which is potentially accompanied by a shift in the alternative translation of Per-45 towards Per-58. However, it is unclear whether the shift in alternative translation is due to the overall increase in expression or TDP-43 specifically altering alternative translation. Interestingly, others have observed peripherin upregulation in both TDP-43^{A315T} and TDP-43^{G348C} mice (Swarup et al., 2011). This indicates the peripherin isoform changes seen previously in the TDP-43^{A315T} mice in the Hafezparast lab could also be due to changes in peripherin

expression. Furthermore, the finding of increased peripherin expression in TDP-43$^{+/F210I}$ mice indicates that changes in peripherin expression seen in the TDP-43^{A315T} mice are not due to an artefact of TDP-43 overexpression. However, while it is tempting to conclude that TDP-43 is able to upregulate peripherin expression, it is important to note that peripherin expression is known to increase following sciatic nerve injury indicating that it is potentially involved in regeneration of the PNS (Beaulieu et al., 2002). It may be the case that there is neuronal injury to spinal cord neurons in TDP-43$^{+/F210I}$ mice as a consequence of altered TDP-43 function, which could underlie the increase in peripherin expression. However, histopathological analysis of older TDP-43$^{+/F210I}$ mice showed no abnormalities in the spinal cord (De Oliveira, 2014).

3.3.2 Peripherin expression in neuro2a cells overexpressing wild type TDP-43

To further test whether TDP-43 is involved in the alternative translation of Per-45, an *in vitro* system using neuro2a cells was initially used. However, the levels of peripherin expression in these cells was not sufficient to allow for detailed analysis. Despite this, it is interesting to note that as with the lumbar spinal cord analysis, the 50 kDa isoform was also observed in these cells.

3.3.3 Role of TDP-43 in Per-45 alternative translation in HEK239 cells stably expressing peripherin

To overcome the limitations encountered in the neuro2a cells, HEK293 cells were made to overexpress human peripherin tagged with Myc by the stable transfection of a cDNA clone, as described in section 3.2.4. The stable transfectants were made to overexpress wild type TDP-43, TDP-43^{F210I} and TDP-43^{M337V}. The M337V mutation of TDP-43 was selected as it is known to be an ALS causing mutation with a high pathogenicity (Xu et al., 2011; Janssens et al., 2013). Overexpressed TDP-43 was tagged with V5 to allow for confirmation of the transfection. Analysis revealed that the stable transfectants were fully capable of expressing both Per-58 and Per-45. There was also a band at approximately 39 kDa which was previously observed as a non-specific band when probing with anti-myc was performed in control HEK293 cells.

The data shows that there is no significant alteration to the levels of Per-45 or Per-58. Furthermore, analysis of the ratio of Per-45 to Per-58 levels also confirms that there are no significant changes in any of the TDP-43 transfectants. This would indicate that TDP-43 is not altering the alternative translation of Per-45 from the Per-58 transcript. However, despite the machinery required for the alternative translation of Per-45 clearly being present in these cells, it is possible that the use of a cDNA clone containing only the coding sequence for peripherin lacks the regulatory elements required by TDP-43 to affect this process. Future studies can address this by including regulatory elements such as a UG rich element downstream of the coding sequence in a similar assay as described by Lin et al. 2007. Alternatively, a BAC clone could be used to include the entire peripherin gene inclusive of all its regulatory elements. However, this method may result in low expression of peripherin and therefore cause similar problems as to those seen in the neuro2a cells.

In summary, peripherin expression is increased in TDP-43$^{+/F210I}$ mice and a shift from Per-45 translation to the translation of the Per-58 isoform was observed but was not statistically significant. In vitro experiments aimed at investigating whether TDP-43 is indeed capable of altering peripherin expression provided initial data suggesting that it does not. However, the system was limited by the lack of regulatory elements in the peripherin transcript as it was generated from a cDNA clone containing only the coding sequence. To provide conclusive proof that TDP-43 is affecting alternative translation a more sophisticated system is required as described above. Further work is also necessary to determine if the increase in peripherin is due to TDP-43 mediated upregulation or as a consequence of neuronal injury caused by the mutant TDP-43.

Chapter 4: Investigating the effect of the *Loa Dync1h1* mutation on paxillin

4.1 Introduction

Mutations in *DYNC1H1* which cause SMA-LED have previously been shown to cause malformations of cortical development (Scoto et al., 2015). Additionally, mutations in *Lis1* are known to cause the neuronal migration disorder lissencephaly (Wynshaw-Boris, 2007). Defects in neuronal migration have also been observed in the *Loa* mouse model resembling the phenotypes described in human diseases (Ori-McKenney and Vallee, 2011; Hafezparast et al., 2003). Recently, abnormalities in focal adhesions (FAs) were observed in *Loa/Loa* MEFs, in the Hafezparast lab (Barri, 2015). Specifically, FAs in spreading *Loa/Loa* MEFs were more numerous and significantly smaller. Additionally, there was a reduction in the phosphorylation of paxillin at Tyr118 ($pPax^{Y118}$) and a reduction in migration in a wound healing assay. Paxillin is a scaffolding protein within FAs which is crucial for cellular migration (López-colomé et al., 2017). The phosphorylation at Tyr118 is particularly important for regulating paxillin turnover at FAs and the overall turnover of adhesions. This site is also involved in the activation of signalling pathways to remodel the cytoskeleton for migration. These changes may contribute towards the neuronal migration defects associated with dynein dysfunction.

The aim of the work presented here was to establish how dynein can affect the phosphorylation of paxillin at Tyr118 and to investigate potential consequences on FA dynamics. Therefore, the turnover of paxillin at FAs in *Loa/Loa* MEFs was measured using FRAP, and several drugs were used to dissect the role of dynein in the regulation of paxillin. Based on results from previous data obtained in the Hafezparast lab, it was hypothesised that dynein is causing a change in $pPax^{Y118}$ which would consequently impact paxillin turnover at focal adhesions. Furthermore, it was hypothesised that dynein affects $pPax^{Y118}$ by affecting the RhoA signalling pathway and actomyosin contractility.

4.2 Results

4.2.1 Turnover of paxillin at FAs in spreading wild type and *Loa/Loa* MEFs

Paxillin phosphorylation at Tyr118 by FAK and Src promotes the disassembly of paxillin from FAs (Qin et al., 2015). As reduced $pPax^{Y118}$ has been observed in *Loa/Loa* MEFs in the Hafezparast lab, paxillin turnover at FAs may be affected. To determine if this was the case, wild type and *Loa/Loa* MEFs were transfected using lipofectamine LTX with a GFP-Paxillin expressing plasmid previously used in Rosse et al. 2012. 48 hours after transfection, cells were plated in live cell imaging chambers coated with collagen type I. After being allowed to spread for 3.5 hours the cells were imaged and FRAP performed.

Cells transfected with GFP-paxillin displayed prominent FAs at the cell edge (Figure 4.1a). During imaging, bleaching was performed for 1 millisecond at the 10 second time point and the fluorescence recovery measured for 5 minutes with an image taken every 5 seconds. As shown in Figure 4.1b, quantification of the recovery showed no significant difference in the recovery of the GFP signal between genotypes (multiple t-tests were performed with Holm-Sidak correction for multiple comparisons). In summary, this indicates that there is no alteration in the dynamics of paxillin turnover at FAs in *Loa/Loa* MEFs compared to wild type MEFs.

Figure 4.1

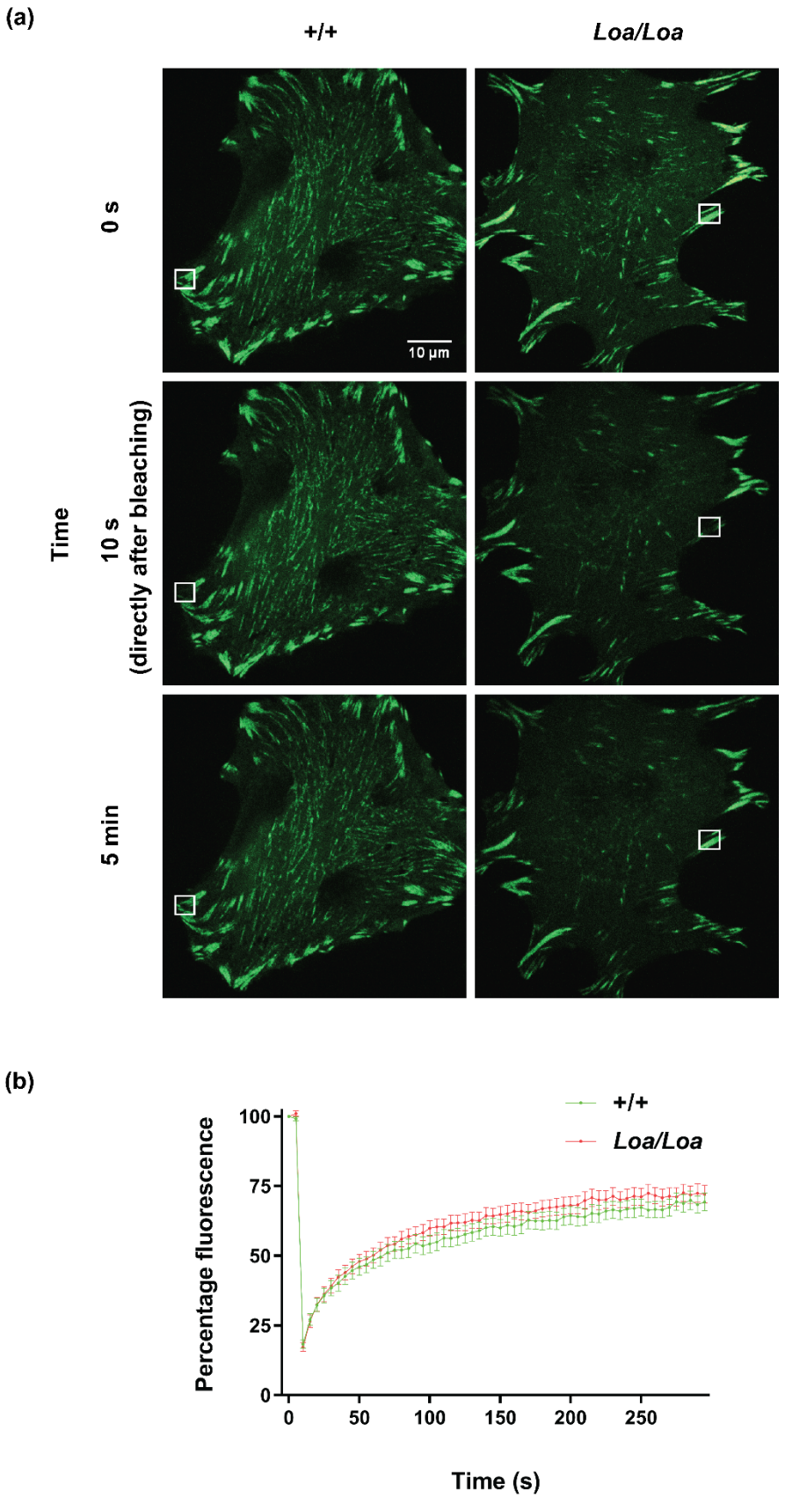
(a)
+/+
Loa/Loa
0 s
10 s
(directly after bleaching)
5 min
Time
10 µm
(b)
+/+
Loa/Loa
Percentage fluorescence
100
75
50
25
0
0
50
100
150
200
250
Time (s)

Figure 4.1 (a) FRAP analysis of paxillin turnover at FAs in *Loa/Loa* and wild type MEFs. Cells transfected with GFP-Paxillin were plated on collagen type I coated live imaging chambers and allowed to spread prior to FRAP analysis. FRAP was performed for 1 millisecond at 10 seconds and recovery measured for 5 minutes with an image taken every 5 seconds. **(b)** Quantification of fluorescence recovery following bleaching, showing percentage fluorescence relative to the 0 second time point. There is no significant difference between wild type and *Loa/Loa* as shown by multiple t-tests with Holm-Sidak correction for multiple comparisons. Wild type N = 20 and *Loa/Loa* N = 21. Error bars represent SEM.

4.2.2 Co-immunoprecipitation of the dynein IC and Lfc/GEF-H1

Tension generated by myosin II is transmitted through the actin network to sites of integrin binding to the extracellular matrix and is critical for the maturation of nascent adhesions (Pasapera et al., 2010). Myosin II driven contractility causes the elongation of actin bundles associated with FAs and induces the phosphorylation of FA proteins including that of paxillin by FAK (Pasapera et al., 2010). As previously mentioned, myosin II activity is regulated by the phosphorylation state of the myosin light chain (MLC) (Ridley, 2003). One of the proteins responsible for phosphorylating MLC is Rho Kinase (ROCK), which acts in a twofold fashion; it directly phosphorylates MLC and dephosphorylates myosin phosphatase targeting subunit (MYPT1) which inactivates myosin phosphatase activity (Kaneko-Kawano et al., 2012).

ROCK is an effector of RhoA which in turn can be activated by a microtubule-associated guanine nucleotide exchange factor (GEF) known as GEF-H1 (Meiri et al., 2012). Relevantly, it has been shown that the murine isoform of GEF-H1 (Lfc), interacts with the dynein complex through the LC Tctex-1 in a tripartite complex involving the IC (Meiri et al., 2012). This interaction serves to inhibit Lfc's nucleotide exchange activity by sequestering it to microtubules, prohibiting it from activating RhoA. Interestingly, it has been previously reported that Tctex-1 and the IC have a tighter association with the dynein complex in *Loa*/*Loa* MEFs (Deng et al., 2010). Therefore, there is the potential that this may increase the sequestration of Lfc into the inactive state, thus reducing RhoA signalling which could result in decreased myosin II activity and consequently reduced $pPax^{Y118}$.

To investigate this, immunoprecipitations were performed to determine if the interaction between Tctex-1 and Lfc/GEF-H1 is affected by the *Loa* mutation. Firstly, the IC chain was immunoprecipitated from lysates originating from both wild type and *Loa/Loa* MEFs. Subsequent analysis was performed by western blotting (Figure 4.2a). The IC chain was successfully immunoprecipitated in both genotypes as shown by the presence of a band at the expected size in both wild type and *Loa/Loa* MEFs. The pull down appears to have been more efficient in the wild type sample. As a positive control, probing was performed for RP3 (one of the dynein LCs) to check that it was co-precipitated with the IC. As is evident in Figure 4.2a, there is a strong signal in the IPs and a low signal in the post IP lysates

(protein not pulled down by the IP from the lysates), suggesting a strong co-precipitation of RP3 in both genotypes. Lfc/GEF-H1 was however, only detected in the inputs and was not present in the IPs of either genotypes. Despite multiple attempts, no interaction was detected between these proteins.

Additionally, the reverse pull-down was performed using a Lfc/GEF-H1 antibody (Figure 4.2b). There was a strong immunoprecipitation of Lfc/GEF-H1 in both genotypes, but the IC was not present in the IPs, indicating that IC was not co-precipitated with Lfc/GEF-H1. Also, RP3 was not pulled down via Lfc/GEF-H1.

In summary, the interaction of Lfc/GEF-H1 to dynein was not detected when pulling down endogenous IC or Lfc/GEF-H1, prohibiting the possibility of assessing for a potential phenotype.

Figure 4.2

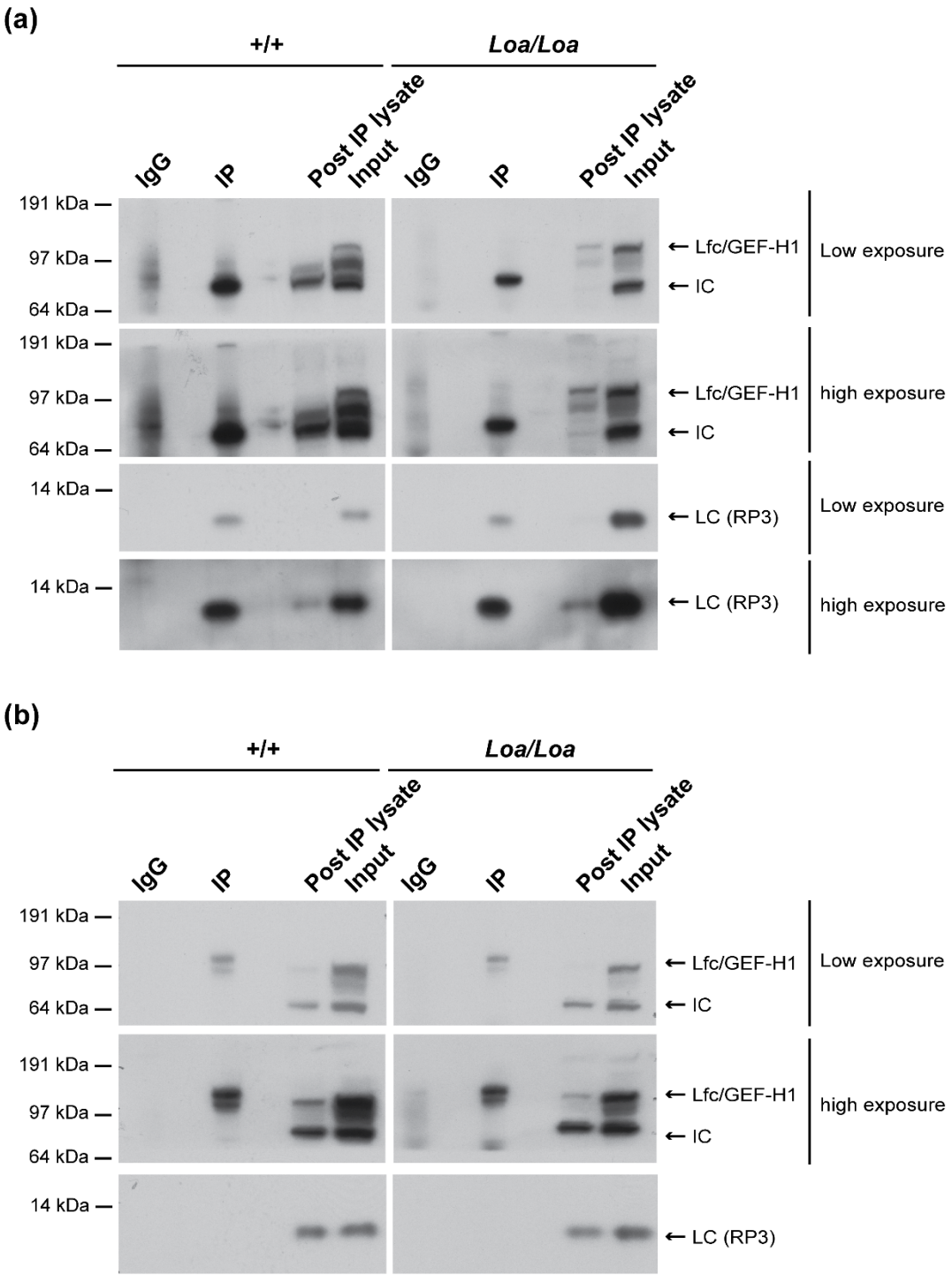

Figure 4.2 (a) Western blot analysis of the immunoprecipitation of the IC from lysate derived from wild type and *Loa/Loa* MEFs. The RP3 LC of dynein was co-precipitated with the IC whilst Lfc/GEF-H1 was unable to be detected in the IP. **(b)** Western blot analysis of the immunoprecipitation of Lfc/GEF-H1 from lysate derived from wild type and *Loa/Loa* MEFs. Lfc/GEF-H1 was successfully immunoprecipitated but neither RP3 nor IC were co-precipitated.

4.2.3 Co-immunoprecipitation of the dynein IC and cofilin

As discussed, paxillin phosphorylation is dependent on the transmission of force generated by myosin II through the actin network (Pasapera et al., 2010). Therefore, actin dynamics are important for the formation of FAs and potentially the phosphorylation of paxillin. Interestingly, an immunoprecipitation of the IC performed on an embryonic day 18 brain followed by mass spectrometry carried out in the Hafezparast lab indicated that dynein might interact with Cofilin-1. Cofilin-1 regulates actin dynamics by severing actin filaments and can also regulate actomyosin contractility by competing for actin binding with myosin II (Kanellos and Frame, 2016). In doing so, it provides a counter balance stopping excessive myosin II contractility.

To investigate any potential link between the paxillin phosphorylation phenotype and dynein interaction with cofilin, immunoprecipitations were performed by pulling down with an anti-IC or anti-cofilin antibody on lysate from wild type embryonic day 18 brain. Subsequently, the samples were analysed by western blot analysis. The IC pull down was successful as there was a strong signal in the IP that was not detected in the post IP lysate (Figure 4.3a). However, no cofilin co-precipitated with the IC. Similarly, despite a small pull down of cofilin with an anti-cofilin antibody, the IC was not co-precipitated (Figure 4.3b).

In summary, the data is unable to verify the mass spectrometry data.

Figure 4.3

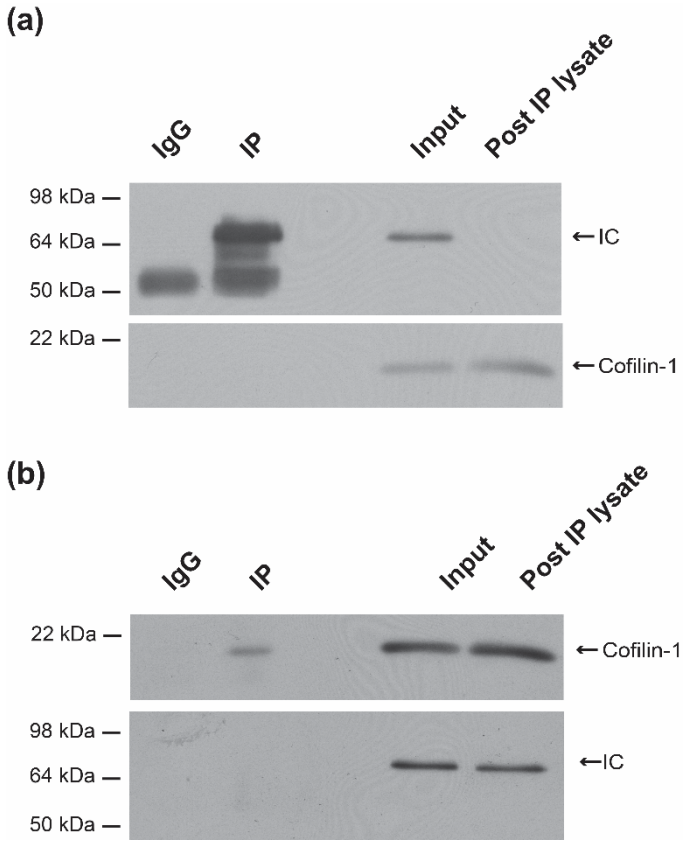

Figure 4.3 (a) Western blot analysis of an immunoprecipitation of the IC from lysate derived from wild type embryonic day 18 brain homogenate. Despite the IC being immunoprecipitated there was no cofilin co-precipitation. **(b)** Western blot analysis of the immunoprecipitation of cofilin-1 from lysate derived from wild type embryonic age 18 brain homogenate. A small amount of Cofilin-1 was successfully immunoprecipitated but the IC was not co-precipitated.

4.2.4 Role of pERK1/2 in the regulation of paxillin phosphorylation

Interestingly, it has previously been suggested that ERK1/2 inhibits the RhoA signalling pathway by the inhibition of ROCK (Sahai et al., 2001). Specifically, it was shown that treatment with the ERK1/2 inhibitor U0126 rescued actomyosin contractility as indicated by an increase in stress fibre formation (Sahai et al., 2001). ERK1/2 is activated by phosphorylation at threonine and tyrosine residues (Roskoski, 2012). Interestingly, increased pERK1/2 has been reported in *Loa/Loa* MEFs (Garrett et al., 2014). Consequently, this increase in ERK1/2 activity may underlie the reduction in $pPax^{Y118}$ due to reduced actomyosin activity.

Therefore, wild type and *Loa/Loa* MEFs were treated with the ERK1/2 inhibitor U0126 to increase the levels of active ROCK and consequently increase actomyosin contractility and rescue the levels of $pPax^{Y118}$ in *Loa/Loa* MEFs. Western blot analysis was used to assess the levels of $pPax^{Y118}$ and the levels of pERK1/2 (using an antibody which detects ERK1/2 phosphorylated at Thr202 and Tyr204). Firstly, the results appeared to confirm the previously observed phenotype of increased pERK1/2 in *Loa/Loa* MEFs in comparison to wild type MEFs (Figure 4.4a). However, densitometric quantification and statistical analysis using a one-sample t-test showed that the increase in pERK1/2 in *Loa/Loa* MEFs did not reach the threshold for statistical significance ($P = 0.1071$, N = 3), as shown in Figure 4.4b. Despite this, it was clear that the inhibition of ERK1/2 was successful in both genotypes, as pERK1/2 is absent or severely reduced in the U0126 treated cells (this made the levels of pERK1/2 unquantifiable in treated samples).

Surprisingly, the levels of $pPax^{Y118}$ in the *Loa/Loa* MEFs within the untreated conditions do not appear different from their wild type counterparts (Figure 4.4a). However, it does appear that the inhibition of ERK1/2 did cause a mild increase in $pPax^{Y118}$ in both wild type and *Loa/Loa* MEFs (Figure 4.4a). However, following densitometric quantification, a two-way ANOVA was carried out to determine the effect of the genotype and the U0126 treatment on the levels of $pPax^{Y118}$ (N = 3). The results showed that there is no significant interaction between the effect of genotype (wild type or *Loa/Loa*) and U0126 treatment on the levels of $pPax^{Y118}$ ($P = 0.4295$). Furthermore, neither the genotype ($P = 0.7872$) or the U0216 treatment ($P = 0.0654$) had a significant main effect on $pPax^{Y118}$ levels.

Overall, while the western blot appears to indicate the previously described increase in pERK1/2 in *Loa/Loa* MEFs, it did not reach statistical significance. Additionally, data shown here disputes the decrease in $pPax^{Y118}$ in *Loa/Loa* MEFs previously observed in the Hafezparast lab due to a lack of a significant main effect of the genotype on $pPax^{Y118}$ levels.

Figure 4.4

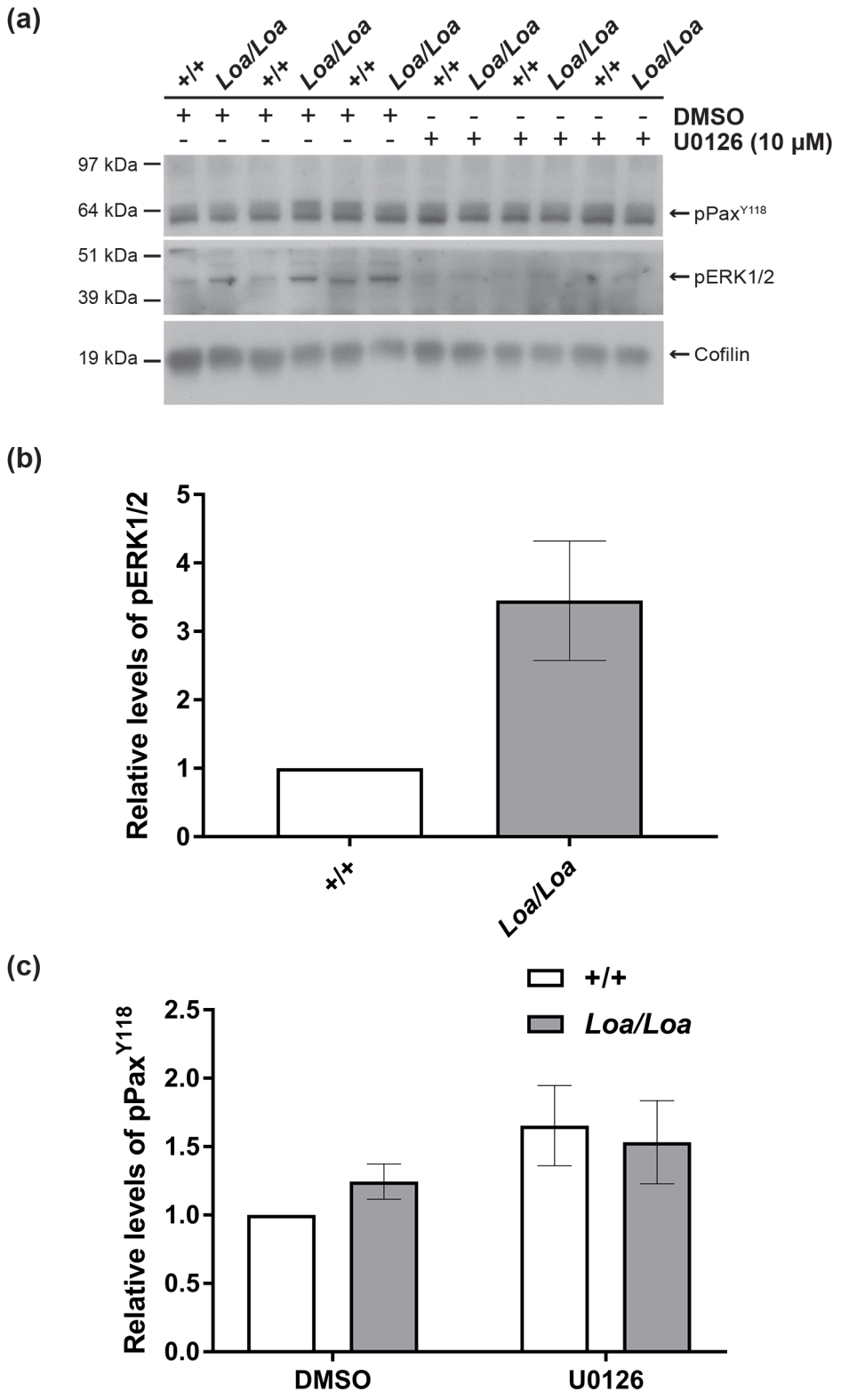
(a)
+/+
Loa/Loa
+/+
Loa/Loa
+/+
Loa/Loa
+/+
Loa/Loa
+/+
Loa/Loa
+/+
Loa/Loa
DMSO
U0126 (10 µM)
97 kDa
64 kDa
51 kDa
39 kDa
19 kDa
← pPax^{Y118}
← pERK1/2
← Cofilin
(b)
Relative levels of pERK1/2
0
1
2
3
4
5
+/+
Loa/Loa
(c)
Relative levels of pPax^{Y118}
0.0
0.5
1.0
1.5
2.0
2.5
+/+
Loa/Loa
DMSO
U0126

Figure 4.4 (a) Western blot analysis of three replicates of pPax^{y118} levels in wild type and *Loa/Loa* MEFs treated with DMSO or U0126 ERK1/2 inhibitor (10 μM for 2 hours). pERK1/2 is increased in *Loa/Loa* MEFs in comparison to wild type MEFs in the untreated condition. Treatment with U0126 drastically reduces the levels of pERK1/2 detected in both genotypes. No difference in pPax^{Y118} levels is seen between wild type and *Loa/Loa* MEFs in both the untreated and treated conditions. **(b)** Densitometric quantification of pERK1/2 levels in wild type and *Loa/Loa* MEF's in the DMSO condition. The increased levels of pERK1/2 did not reach statistical significance as shown by a one sample t-test (*P = 0.1071*, N = 3) **(c)** Densitometric quantification of pPax^{y118} levels in wild type and *Loa/Loa* MEFs treated with DMSO or U0126. A two-way ANOVA (N = 3) showed no significant interaction between genotype and U0126 treatment (*P = 0.4295*). Additionally, no significant main effects of genotype or U0126 treatment on pPax^{y118} levels were found (*P = 0.7872 and P = 0.0654* respectively). β-actin was used as the loading control and normalised values are plotted relative to DMSO wild type. Error bars represent SEM.

4.2.5 Investigating the effect of laminin on paxillin phosphorylation

The absence of an interaction between U0126 treatment and genotype and the absence of a significant main effect of genotype on pPax^{Y118} levels in the previous experiment contradicts previous findings in the Hafezparast lab. To attempt to replicate the decrease in pPax^{Y118} observed in *Loa/Loa* MEFs, stimulation of cell dynamics was attempted by treating MEFs with 25 µg/mL of the extracellular matrix protein laminin directly into culture media.

Western blot analysis was performed to determine if a difference in pPax^{Y118} between wild type and *Loa/Loa* MEFs was induced by laminin treatment (Figure 4.5a). In the untreated MEFs, there was no distinguishable decrease in pPax^{Y118} levels in *Loa/Loa* in comparison to wild type samples. In fact, there was a slight increase in the levels of pPax^{Y118}. The same pattern was visible between wild type and *Loa/Loa* MEFs in the laminin treated samples. Densitometric quantification and two-way ANOVA analysis (N = 3) revealed no significant interaction between the effect of the genotype (wild type and *Loa/Loa*) and laminin treatment on the levels of pPax^{Y118} (*P = 0.7130*). Furthermore, neither the genotype (*P = 0.6034*) or laminin treatment (*P = 0.4752*) had a significant main effect on the levels of pPax^{Y118} (Figure 4.5b). Overall, these data indicate that both the *Loa* mutation and laminin treatment do not have an effect on the levels of pPax^{Y118}. Therefore, there is a discrepancy between these findings and those previously seen in the Hafezparast lab.

Figure 4.5

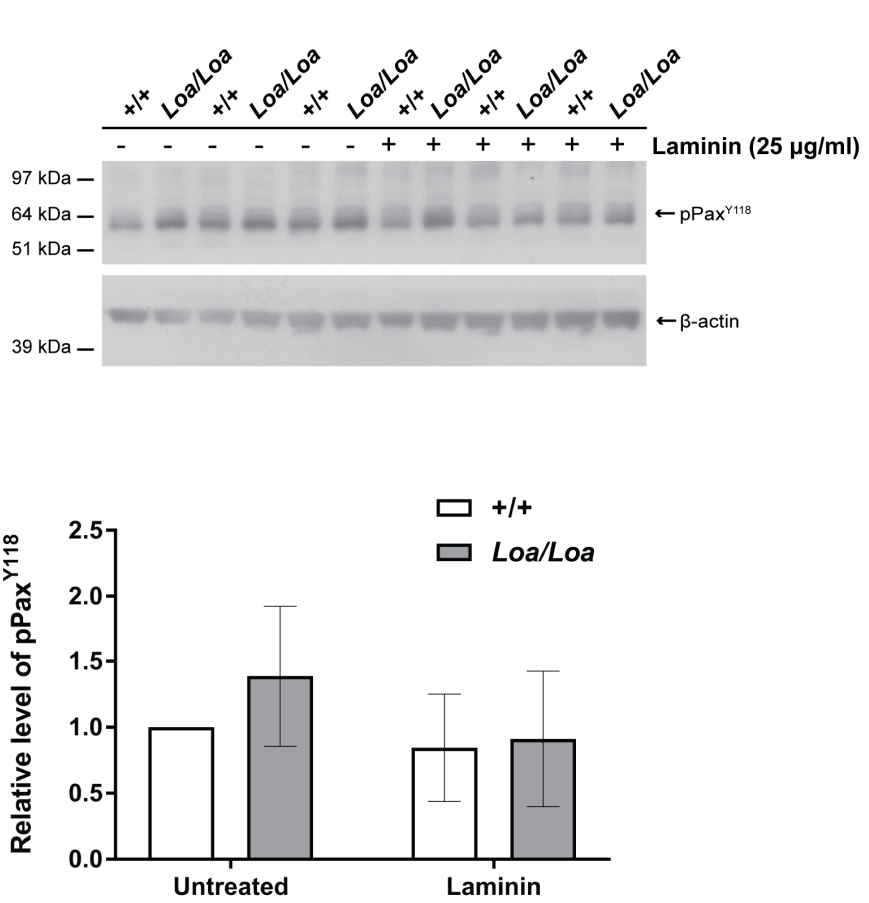

Figure 4.5 (a) Western blot analysis of three replicates of pPax^{Y118} levels in wild type and *Loa/Loa* MEFs, untreated and treated with 25 µg/mL of laminin for 4 hours. pPax^{Y118} levels are not reduced in *Loa/Loa* MEFs in both untreated and treated samples. **(b)** Densitometric quantification of pPax^{Y118} levels in wild type and *Loa/Loa* MEFs in untreated and laminin treated conditions. A two-way ANOVA showed no significant interaction between genotype and laminin treatment *(P = 0.7130*). Additionally, both genotype *(P = 0.6034*) and laminin treatment (*P = 0.4752*) failed to elicit a significant main effect on the levels of pPax^{Y118}. β-actin is used as the loading control and normalised levels are shown relative to wild type untreated. Error bars represent SEM.

4.2.6 Blebbistatin induces a paxillin phenotype in *Loa/Loa* MEFs

As discussed, paxillin phosphorylation is known to be affected by the activity of myosin II. Therefore, treatment with blebbistatin, which causes inhibition of myosin II, results in a reduction of paxillin phosphorylation at Tyr118 (Pasapera et al., 2010). As the previous attempt at inducing the previously observed pPax^{Y118} phenotype in *Loa/Loa* MEFs did not succeed, cells were treated with 20 µM blebbistatin for 1 hour and the levels of pPax^{Y118} checked by western blot analysis. Additionally, the levels of total paxillin were also examined to ascertain whether the variability in the pPax^{Y118} phenotype could be caused by changes in overall paxillin levels.

Consistent with previous observations, pPax^{Y118} levels in DMSO control samples appeared similar in wild type and *Loa/Loa* MEFs (Figure 4.6a, top panel). Treatment with blebbistatin drastically reduced the levels of pPax^{Y118} in both wild type and *Loa/Loa* MEFs. Additionally, it appears that the duplet which is seen for pPax^{Y118} in the DMSO samples becomes primarily a single band which represents the higher band of the two previously present. Following densitometric quantification, a two-way ANOVA was performed to determine the effect of the genotype and blebbistatin treatment on the levels of pPax^{Y118} (N = 3). This analysis reveals that there is no significant interaction between the effects of genotype and blebbistatin treatment on pPax^{Y118} (*P = 0.2145*), thus indicating that the effect of blebbistatin was not affected by genotype. As shown in Figure 4.6b, there are lower levels of pPax^{Y118} in *Loa/Loa* mutants in comparison to wild type levels in both untreated and treated conditions and analysis reveals that genotype has a significant main effect on pPax^{Y118} levels (*P = 0.0057*), meaning the marginal mean for wild type (0.796 ± 0.036) was significantly higher than the marginal mean of *Loa/Loa* MEFs (0.603 ± 0.036) (note that from this point forward marginal means are stated as mean ± standard error). This may be indicative of a decrease in pPax^{Y118} in *Loa/Loa* MEFs as previously reported in the Hafezparast lab. Similarly, Figure 4.6b shows that both wild type and *Loa/Loa* exhibit a decrease in the levels of pPax^{Y118} following treatment with blebbistatin. Consequently, analysis shows blebbistatin treatment to have a significant main effect on pPax^{Y118} levels (*P < 0.0001*), where the marginal mean for blebbistatin samples was significantly lower (0.461 ± 0.036) than in DMSO samples (0.938 ± 0.036).

Western blot analysis of total paxillin levels in both wild type and *Loa/Loa* MEFs indicates that there is a potential difference between the genotypes. A decrease in total paxillin levels in *Loa/Loa* MEFs in comparison to wild type MEFs is observed in all three replicates of DMSO control samples and two of the three presented blebbistatin treated samples (Figure 6a, bottom panel). Densitometric quantification confirmed a decrease in total paxillin levels in *Loa/Loa* MEFs in both control and treated conditions. Subsequently, a two-way ANOVA was performed to determine the effect of blebbistatin and genotype on the levels of total paxillin (N = 3). The results of this analysis show that there is no significant interaction between blebbistatin treatment and genotype (*P = 0.9716*). This indicates that blebbistatin is having an equal effect on both wild type and *Loa/Loa* MEFs. Furthermore, while Figure 6c shows lower levels of total paxillin in *Loa/Loa* MEFs in both DMSO and blebbistatin treated conditions, analysis showed no significant main effect with regards to genotype (*P = 0.0804*). Similarly, there was no significant main effect of blebbistatin treatment on the level of total paxillin (*P = 0.3330*).

Finally, since equal amounts of the same samples were loaded to determine pPax^{Y118} and total paxillin levels and both were normalised to the same internal control (β-actin), it is possible to work out the ratio of pPax^{Y118} to total paxillin levels (Figure 4.6d). A two-way ANOVA was performed to determine the effect of genotype and blebbistatin treatment on this ratio (N = 3). There is no significant interaction between genotype and blebbistatin treatment (*P = 0.0799*), thereby indicating that blebbistatin treatment has an equal effect irrespective of genotype. Figure 4.6d shows that within the DMSO condition there was a higher ratio of pPax^{Y118}/total paxillin in the *Loa/Loa* MEFs in comparison to wild type MEFs, while the opposite is true in the blebbistatin treatment condition. Consequently, analysis showed no significant main effect of genotype on the pPax^{Y118}/total paxillin ratio (*P = 0.6430*). Therefore, contradicting the initial indication of reduced pPax^{Y118} in *Loa/Loa* MEFs which was seen when looking only at pPax^{Y118} levels (Figure 4.6b). Additionally, Figure 4.6d shows a reduction in the pPax^{Y118}/total paxillin ratio in both wild type and *Loa/Loa* MEFs in comparison to their corresponding DMSO controls. Analysis confirms that there is a significant main effect of blebbistatin treatment on the pPax^{Y118}/total paxillin ratio (*P = 0.0099*). This means DMSO

samples had a significantly higher marginal mean (1.254 ± 0.145) than blebbistatin treated samples (0.567 ± 0.145).

Overall, data presented here shows that blebbistatin decreased the levels of pPax^{Y118} in both genotypes as seen in both the analysis of pPax^{Y118} levels and the analysis of pPax^{Y118}/total paxillin. While genotype had a significant main effect in the analysis of pPax^{Y118} levels, when total paxillin levels were considered, this effect is no longer evident. Therefore, this experiment has not produced the previously observed reduction of pPax^{Y118} in *Loa/Loa* MEFs previously reported in the Hafezparast lab.

Figure 4.6

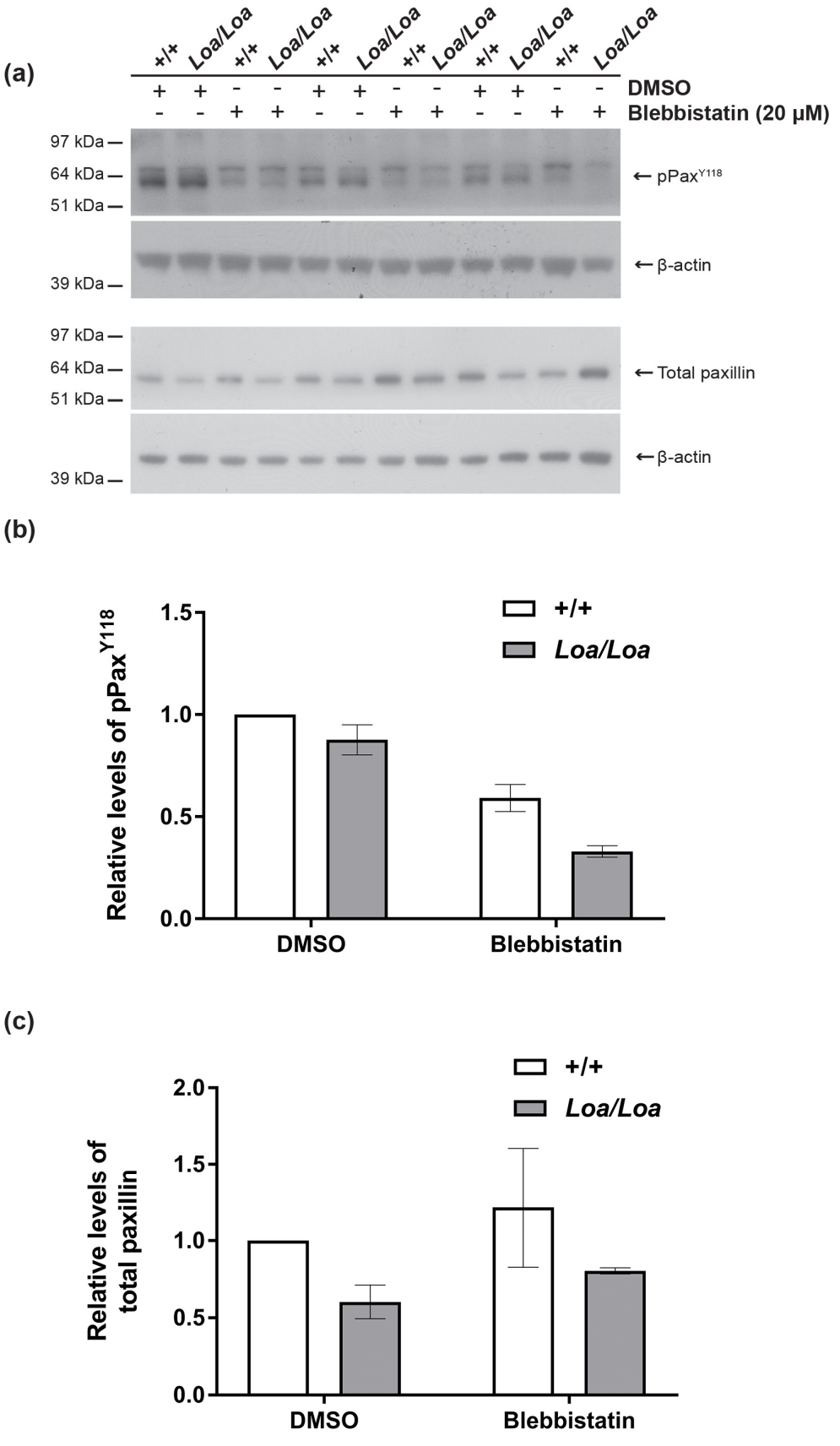
(a)
+/+
Loa/Loa
DMSO
Blebbistatin (20 μM)
97 kDa
64 kDa
51 kDa
39 kDa
← pPax^Y118
← β-actin
← Total paxillin
(b)
Relative levels of pPax^Y118
+/+
Loa/Loa
1.5
1.0
0.5
0.0
DMSO
Blebbistatin
(c)
Relative levels of total paxillin
2.0
1.5
1.0
0.5
0.0

Figure 4.6 continued

(d)

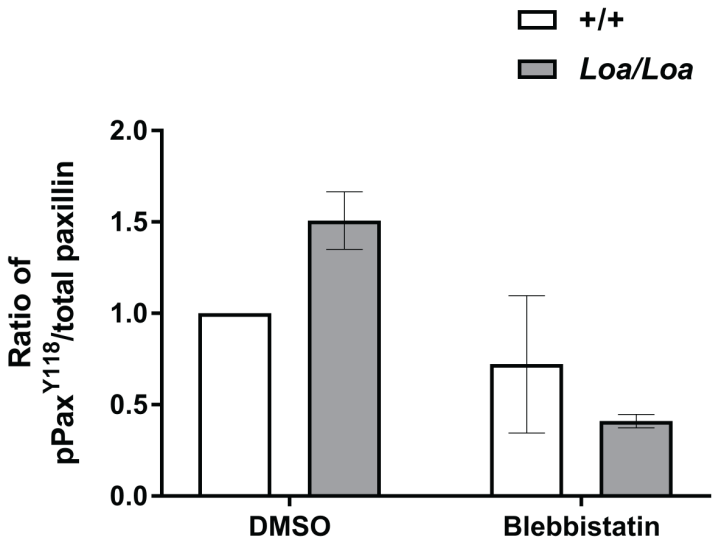

Figure 4.6 (a) Top panel: Western blot analysis of three replicates of $pPax^{Y118}$ levels in wild type and *Loa/Loa* MEFs treated with DMSO or blebbistatin (20 μM for 1 hour). Bottom panel: Western blot analysis of total paxillin levels in the same three replicates of wild type and *Loa/Loa* MEFs treated with DMSO and blebbistatin (20 μM for 1 hour). **(b)** Densitometric quantification of $pPax^{Y118}$ levels in wild type and *Loa/Loa* MEFs treated with DMSO or blebbistatin. A two-way ANOVA (N = 3) showed no significant interaction between genotype and blebbistatin treatment (*P = 0.2145*). However, there was a significant main effect on $pPax^{Y118}$ levels by both genotype (*P = 0.0057*) and blebbistatin treatment (*P < 0.0001*). **(c)** Densitometric quantification of the total paxillin western blot analysis. A two-way ANOVA (N = 3) showed no significant interaction occurred between genotype and blebbistatin treatment (*P = 0.9716*). Additionally, no significant main effect on total paxillin levels were found for both genotype (*P = 0.0804*) and blebbistatin treatment (*P = 0.3330*). **(d)** Analysis of the ratio of $pPax^{Y118}$ to total paxillin. A two-way ANOVA (N = 3) showed no significant interaction between genotype and blebbistatin treatment occurred (*P = 0.0799*). Furthermore, no significant main effect of genotype on $pPax^{Y118}$/total paxillin ratio was found (*P = 0.6430*). Conversely, there was a significant main effect of blebbistatin treatment on the $pPax^{Y118}$/total paxillin ratio (*P = 0.0099*). For both $pPax^{Y118}$ and total paxillin, β-actin was used as the loading control. In all analysis normalised values are plotted relative to DMSO wild type. Error bars represent SEM.

4.2.7 Effect of thymidine arrest on paxillin phosphorylation

Interestingly, the phosphorylation of paxillin at Tyr118 has been implicated in proliferative signalling during the cell cycle (Sastry et al., 1999). Therefore, to further investigate the absence of the previously observed pPax^{Y118} phenotype, a double thymidine block was performed to synchronise cells to the G1/S phase of the cell cycle (Harper, 2005). The aim was to eliminate potential cell to cell variation in pPax^{Y118} phosphorylation caused by their differing progression through the cell cycle.

Western blot analysis was used to analyse the levels of pPax^{Y118} and total paxillin in DMSO treated control cells and in cells which had undergone a double thymidine block. Interestingly, in the untreated samples, there appears to be a reduction in pPax^{Y118} in the *Loa/Loa* MEFs in comparison to wild type MEFs, while this difference was less apparent in the cells which underwent the double thymidine block (Figure 4.7a, top panel). Densitometric quantification was performed (Figure 4.7b), and a two-way ANOVA was used to assess the effect of thymidine treatment and genotype on the levels of pPax^{Y118} (N = 3). Analysis showed no significant interaction between thymidine treatment and genotype (*P = 0.2000*). Furthermore, there was no significant main effect of thymidine treatment on the levels of pPax^{Y118} (*P = 0.8853*). The reduction in the difference between wild type *and Loa/Loa* MEFs after thymidine treatment in comparison to the DMSO condition meant that no significant main effect of genotype on the levels of pPax^{Y118} was found (*P = 0.0761*).

Interestingly, there was a striking reduction in total paxillin in the *Loa/Loa* MEFs, which is seen both in the DMSO and thymidine block conditions (Figure 4.7a). Densitometric analysis further confirms this observation (Figure 4.7c). A two-way ANOVA was performed to ascertain the effect of thymidine treatment and genotype on the levels of total paxillin (N = 3). This analysis showed a significant interaction between genotype and thymidine treatment (*P = 0.0008*), indicating that the effect of thymidine on the total paxillin levels is dependent on the genotype. As such, analysis of the simple main effects for genotype using Bonferroni's multiple comparisons test showed that there is a statistically significant decrease in total paxillin levels between wild type and *Loa/Loa* MEFs within the DMSO condition (*P < 0.0001*). Additionally, there is also a significant decrease in total paxillin levels

between the wild type and *Loa/Loa* MEFs within the thymidine treatment condition (*P < 0.0001*). Furthermore, similar analysis of the simple main effects of the thymidine treatment shows that there is a significant decrease in total paxillin levels between the wild type DMSO and wild type thymidine treated samples (*P < 0.0001*). However, there is no significant difference in total paxillin levels between *Loa/Loa* MEFs treated with DMSO and thymidine (*P = 0.2327*).

As with the previous experiment the $pPax^{Y118}$/total paxillin ratio was quantified. Surprisingly, there appears to be an increased ratio of $pPax^{Y118}$/total paxillin in the *Loa/Loa* MEFs in comparison to wild type MEFs in both DMSO and thymidine treated conditions. Statistical analysis of the effect of genotype and thymidine treatment on the ratio of $pPax^{Y118}$/total paxillin (N = 3) shows no significant interaction between genotype and thymidine treatment (*P = 0.1800*). Furthermore, there is no significant main effect of thymidine treatment on the ratio of $pPax^{Y118}$/total paxillin (*P = 0.1060*). However, there is a significant main effect of genotype on the ratio of $pPax^{Y118}$/total paxillin (*P = 0.0042*), meaning that the marginal mean for the wild type samples (1.217 ± 0.872) was significantly lower than that of the *Loa/Loa* samples (6.088 ± 0.872). This indicates that there is an increase in the ratio of $pPax^{Y118}$/total paxillin in *Loa/Loa* MEFs in comparison to wild type MEFs.

In summary, synchronization of the cell cycle using thymidine did not reveal a difference when measuring $pPax^{Y118}$ levels between genotypes. However, there was a significant reduction in total paxillin between wild type and *Loa/Loa* MEFs in both DMSO and thymidine treatment conditions. Thymidine treatment was able to reduce the total paxillin levels in wild type samples but not in *Loa/Loa* MEFs. Finally, analysis of the ratio of $pPax^{Y118}$/total paxillin revealed a significant main effect of the genotype. However, unlike previous observations within the Hafezparast lab, there was an increase in this ratio which is not conducive with the previously reported decrease in $pPax^{Y118}$ levels in *Loa/Loa* MEFs.

Figure 4.7

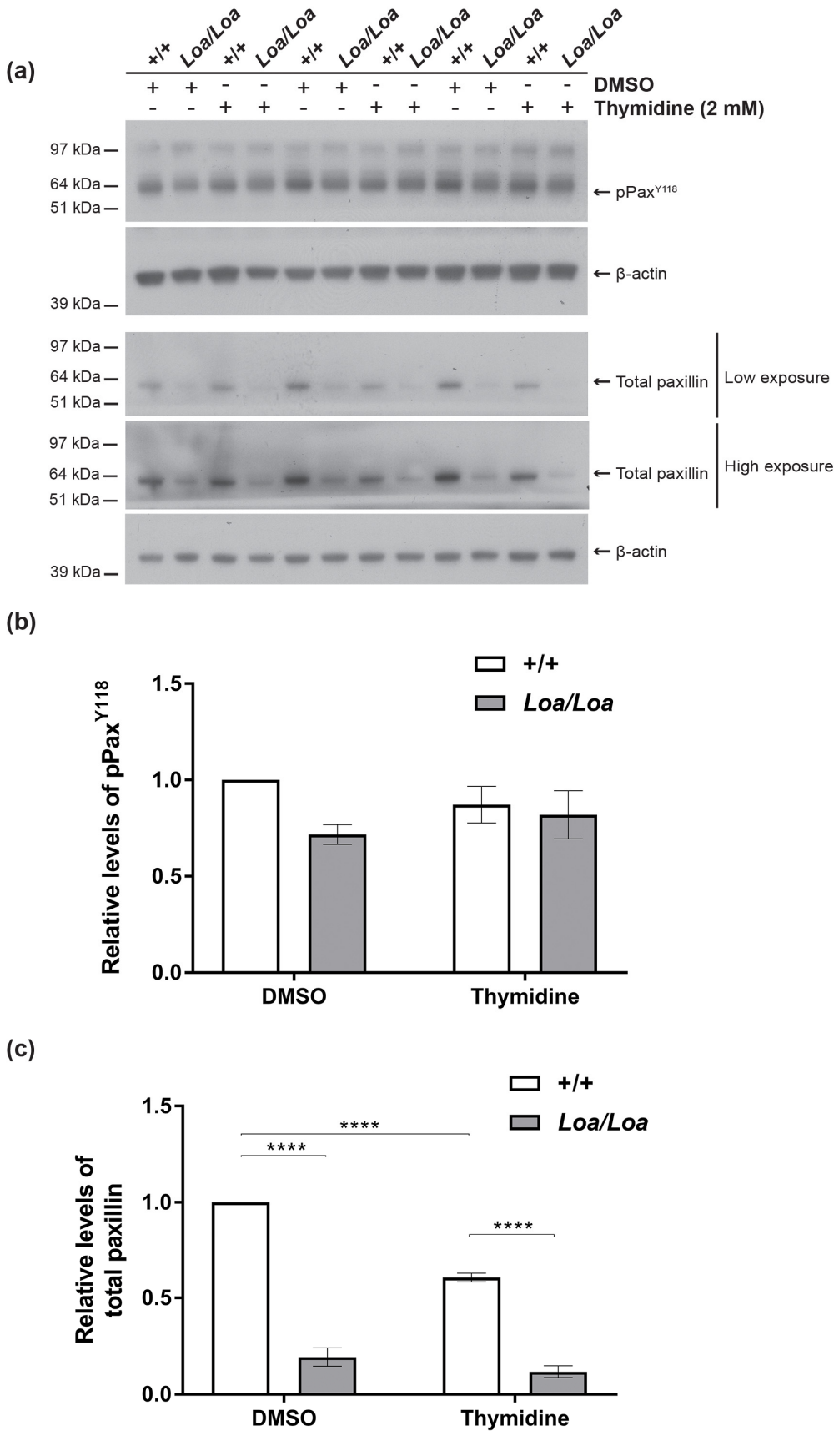
(a)
+/+
Loa/Loa
DMSO
Thymidine (2 mM)
97 kDa
64 kDa
51 kDa
39 kDa
← pPax^{Y118}
← β-actin
← Total paxillin
Low exposure
High exposure
(b)
+/+
Loa/Loa
Relative levels of pPax^{Y118}
1.5
1.0
0.5
0.0
DMSO
Thymidine
(c)
Relative levels of total paxillin
****
****
****

Figure 4.7 continued

(d)

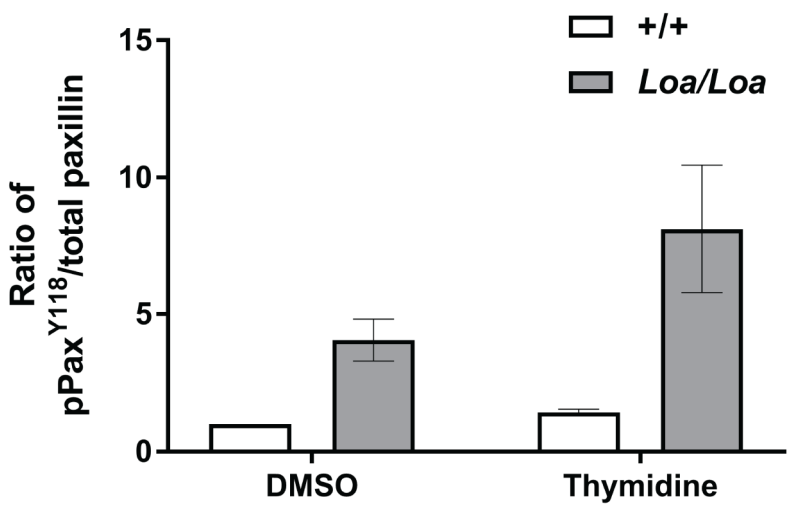

Figure 4.7 (a) Top panel: Western blot analysis of three replicates of pPax^{Y118} levels in wild type and *Loa/Loa* MEFs which underwent a double thymidine block to synchronise their cell cycle or were treated with DMSO. Bottom panel: Western blot analysis of total paxillin levels in the same three replicates of wild type and *Loa/Loa* MEFs after cell cycle synchronisation by double thymidine block or DMSO treatment. **(b)** Densitometric quantification of pPax^{Y118} levels in wild type and *Loa/Loa* MEFs in both conditions. A two-way ANOVA (N = 3) showed no significant interaction occurred between genotype and thymidine treatment (*P = 0.2000*). Additionally, no significant main effect of both genotype (*P = 0.0761*) and thymidine treatment (*P = 0.8853*) on pPax^{y118} levels was observed. **(c)** Densitometric quantification of the total paxillin western blot analysis. A two-way ANOVA (N = 3) showed that a significant interaction between genotype and thymidine occurred (*P = 0.0008*). Analysis of simple main effect of genotype using Bonferroni's multiple comparison test showed a significant reduction in total paxillin between wild type and *Loa/Loa* MEFs in both the DMSO (*P < 0.0001*) and thymidine condition (*P = 0.0001*). Additionally, analysis of the simple main effects of thymidine treatment showed a significant reduction in total paxillin between wild type DMSO and wild type thymidine treated MEFs (*P < 0.0001*) but not between DMSO and thymidine treated *Loa/Loa* MEFs (*P = 0.2327*). **(d)** Analysis of the ratio of the pPax^{Y118}/total paxillin ratio. A two-way ANOVA (N = 3) showed no significant interaction between genotype and thymidine treatment occurred (*P = 0.1800*) and no significant main effect of thymidine treatment was found (*P = 0.1060*). Conversely, a significant main effect of genotype on the pPax^{Y118}/total paxillin ratio was found (*P = 0.0042*). For both pPax^{y118} and total paxillin, β-actin was used as the loading control. Normalised values are plotted relative to the wild type in their respective treatment conditions. Error bars represent SEM. (**** *P < 0.0001*)

4.2.8 Inhibition of dynein ATPase activity reduces levels of total paxillin and pPax^{Y118}

To investigate further whether dynein activity can influence the levels of total paxillin, both wild type and *Loa/Loa* MEFs were treated with the dynein ATPase activity inhibitor Ciliobrevin D (50 µM for 1 hour). Subsequently, western blot analysis was used to assess the levels of pPax^{Y118} and total paxillin.

As shown in Figure 4.8a, there is no distinguishable difference in pPax^{Y118} levels between wild type and *Loa/Loa* MEFs within both DMSO and Ciliobrevin D treated conditions. However, the treatment with Ciliobrevin D appears to have reduced the levels of pPax^{Y118} in both wild type and *Loa/Loa* MEFs. Densitometric quantification and statistical analysis using a two-way ANOVA to analyse the effect of genotype and Ciliobrevin D treatment on the levels of pPax^{Y118} was performed (N = 3), as shown in Figure 4.8b. The results of this analysis showed that there was no significant interaction between genotype and Ciliobrevin D treatment (*P = 0.3983*), indicating that the effect of Ciliobrevin D was unaffected by genotype. As with previous experiments there was no significant main effect of genotype on the levels of pPax^{Y118} (*P = 0.5806*), which again contradicts previous data from the Hafezparast lab which showed a reduction in pPax^{Y118} in *Loa/Loa* MEFs. However, there was a significant main effect for Ciliobrevin D treatment on the levels of pPax^{Y118} (*P = 0.0028*). This means that the marginal mean for DMSO samples (1.024 ± 1.07) was significantly higher compared to samples treated with Ciliobrevin D (0.381 ± 1.07), indicating that Ciliobrevin D was able to reduce the levels of pPax^{Y118} irrespective of genotype, as shown in Figure 4.8b.

As shown in Figure 4.8a, total paxillin appears to be reduced in *Loa/Loa* MEFs in both DMSO and Ciliobrevin D treatment conditions. Importantly, as with pPax^{Y118} levels, treatment with Ciliobrevin D causes a reduction in the levels of total paxillin. However, a wild type sample in the second replicate appears to have a smaller response to Ciliobrevin D treatment regarding pPax^{Y118} and total paxillin levels. Densitometric quantification and two-way ANOVA analysis (N = 3) showed no significant interaction between genotype and Ciliobrevin D treatment with regards to total paxillin levels (*P = 0.7962*), showing the effect of Ciliobrevin D on total paxillin is independent of genotype. Further analysis reveals that there is no significant main effect of genotype on the levels of total paxillin (*P = 0.2147*).

However, there was a significant main effect for Ciliobrevin D treatment on the levels of total paxillin (*P = 0.0004*). Therefore, the marginal mean for DMSO samples (0.905 ± 0.084) were significantly higher than those for Ciliobrevin D treated samples (0.211 ± 0.084). This shows that Ciliobrevin D reduced the levels of total paxillin irrespective of genotype.

Finally, analysis of the ratio of $pPax^{Y118}$/total paxillin through a two-away ANOVA (N = 3), showed no significant interaction between genotype and Ciliobrevin D treatment (*P = 0.1537*) and no significant main effect for genotype (*P = 0.3481*). However, there was a significant main effect of Ciliobrevin D on the $pPax^{Y118}$/total paxillin ratio (*P = 0.0238*). The marginal mean of the DMSO samples (1.147 ± 0.359) was significantly lower than that of the Ciliobrevin D treated samples (2.559 ± 0.359). Therefore, this shows that Ciliobrevin D increased the proportion of total paxillin that is phosphorylated at Tyr118.

In summary, Ciliobrevin D inhibition of dynein ATPase activity strongly reduced the levels of total paxillin detected, which likely underlies the sharp decrease also observed in the levels of $pPax^{Y118}$. However, when $pPax^{Y118}$ is analysed relative to the total paxillin levels there is actually a higher proportion of the paxillin available that is found phosphorylated at Tyr118. Importantly, the lack of interaction between Ciliobrevin D treatment and genotype suggests that the effect of Ciliobrevin D occurs in both wild type and *Loa/Loa* MEFs, thereby suggesting a role for dynein activity in the regulation of total paxillin and consequently $pPax^{Y118}$.

Figure 4.8

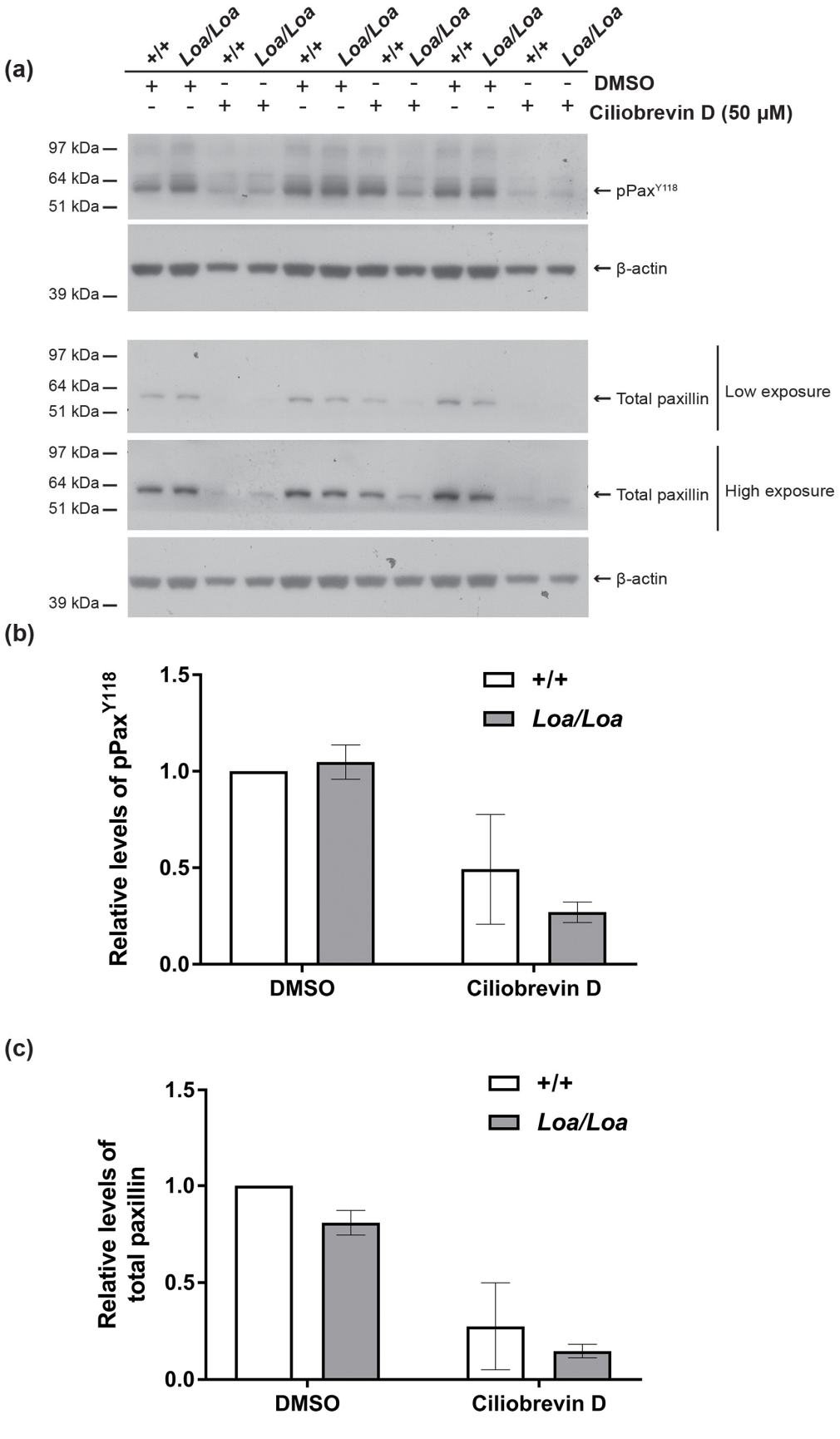
(a)
+/+
Loa/Loa
DMSO
Ciliobrevin D (50 µM)
97 kDa
64 kDa
51 kDa
39 kDa
← pPax^Y118
← β-actin
← Total paxillin
Low exposure
High exposure
(b)
Relative levels of pPax^Y118
1.5
1.0
0.5
0.0
DMSO
Ciliobrevin D
(c)
Relative levels of total paxillin

Figure 4.8 continued

(d)

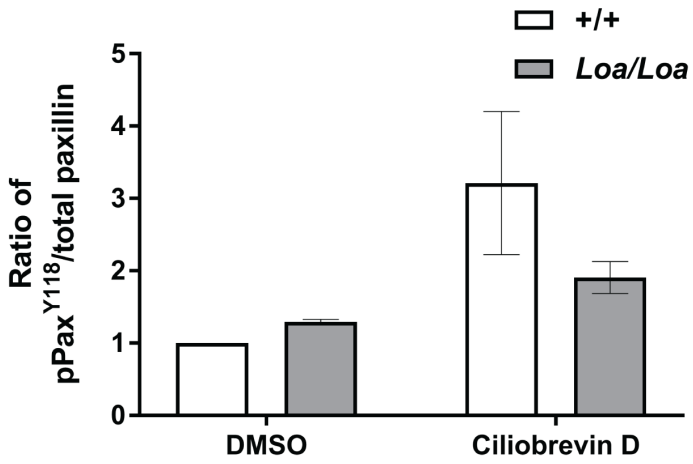

Figure 4.8 (a) Top panel: Western blot analysis of three replicates of pPax^{Y118} levels in wild type and *Loa/Loa* MEFs treated with DMSO or the dynein ATPase inhibitor Ciliobrevin D. Bottom panel: Western blot analysis of total paxillin levels in the same three replicates of wild type and *Loa/Loa* MEFs treated with DMSO or Ciliobrevin D **(b)** Densitometric quantification of pPax^{Y118} levels in wild type and *Loa/Loa* MEFs in both conditions. A two-way ANOVA (N = 3) showed no significant interaction between genotype and Ciliobrevin D treatment occurred (*P = 0.3983*). Additionally, no significant main effect of genotype on pPax^{y118} levels was found (*P = 0.5806*). Conversely, there was a significant main effect of Ciliobrevin D treatment on pPax^{y118} levels (*P = 0.0028*). **(c)** Densitometric quantification of the total paxillin western blot analysis. A two-way ANOVA (N = 3) showed that there was no significant interaction between genotype and Ciliobrevin D treatment (*P = 0.7962*). There was also no significant main effect of genotype on total paxillin levels (*P = 0.2147*). However, there was a significant main effect of Ciliobrevin D treatment on the levels of total paxillin (*P = 0.0004*). **(d)** Analysis of the ratio of pPax^{Y118} to total paxillin. A two-way ANOVA (N = 3) showed no significant interaction occurred between genotype and Ciliobrevin D treatment (*P = 0.1537*). Furthermore, no significant main effect of genotype on pPax^{Y118}/total paxillin ratio was found (*P = 0.3481*). Conversely, there was a significant main effect of Ciliobrevin D treatment on the pPax^{Y118}/total paxillin ratio (*P = 0.0238*). For both pPax^{y118} and total paxillin, β-actin was used as the loading control. Normalised values are plotted relative to DMSO wild type. Error bars represent SEM.

4.2.9 Reduced total paxillin in *Loa/Loa* MEFs

To further illustrate the reduction of total paxillin in *Loa/Loa* MEFs in comparison to wild type MEFs, statistical analysis was performed on the control samples from Figure 4.6, 4.7 and 4.8. Additionally, to provide further evidence of a lack of a difference in $pPax^{Y118}$ levels between genotypes the control samples of Figure 4.4, 4.5. 4.6, 4.7 and 4.8 were used for statistical analysis. Similarly, $pPax^{Y118}$/total paxillin ratios from the control samples in Figures 4.6, 4.7 and 4.8 also underwent combined statistical analysis.

This analysis conclusively shows that there is a statistically significant decrease, as shown by a one sample t-test, in total paxillin in *Loa/Loa* MEFs in comparison to wild type MEFs (*P = 0.0015*, N = 9), as shown in Figure 4.9a. Conversely, no significant difference in $pPax^{Y118}$ levels was found between wild type and *Loa/Loa* MEFs as confirmed by a one sample t-test (*P = 0.4836*, wild type N = 15 and *Loa/Loa* N= 14), as shown in Figure 4.9b. However, there was a statistically significant increase in the $pPax^{Y118}$/total paxillin ratio in *Loa/Loa* MEFs in comparison to wild type MEFs as shown by a one sample t-test (*P = 0.0323*, N = 9).

In summary, the Loa mutation causes a reduction in the levels of total paxillin within *Loa/Loa* MEFs in comparison to wild type MEFs, while an increase in $pPax^{Y118}$/total paxillin ratio in *Loa/Loa* MEFs is seen as cells maintain the levels of $pPax^{Y118}$.

Figure 4.9

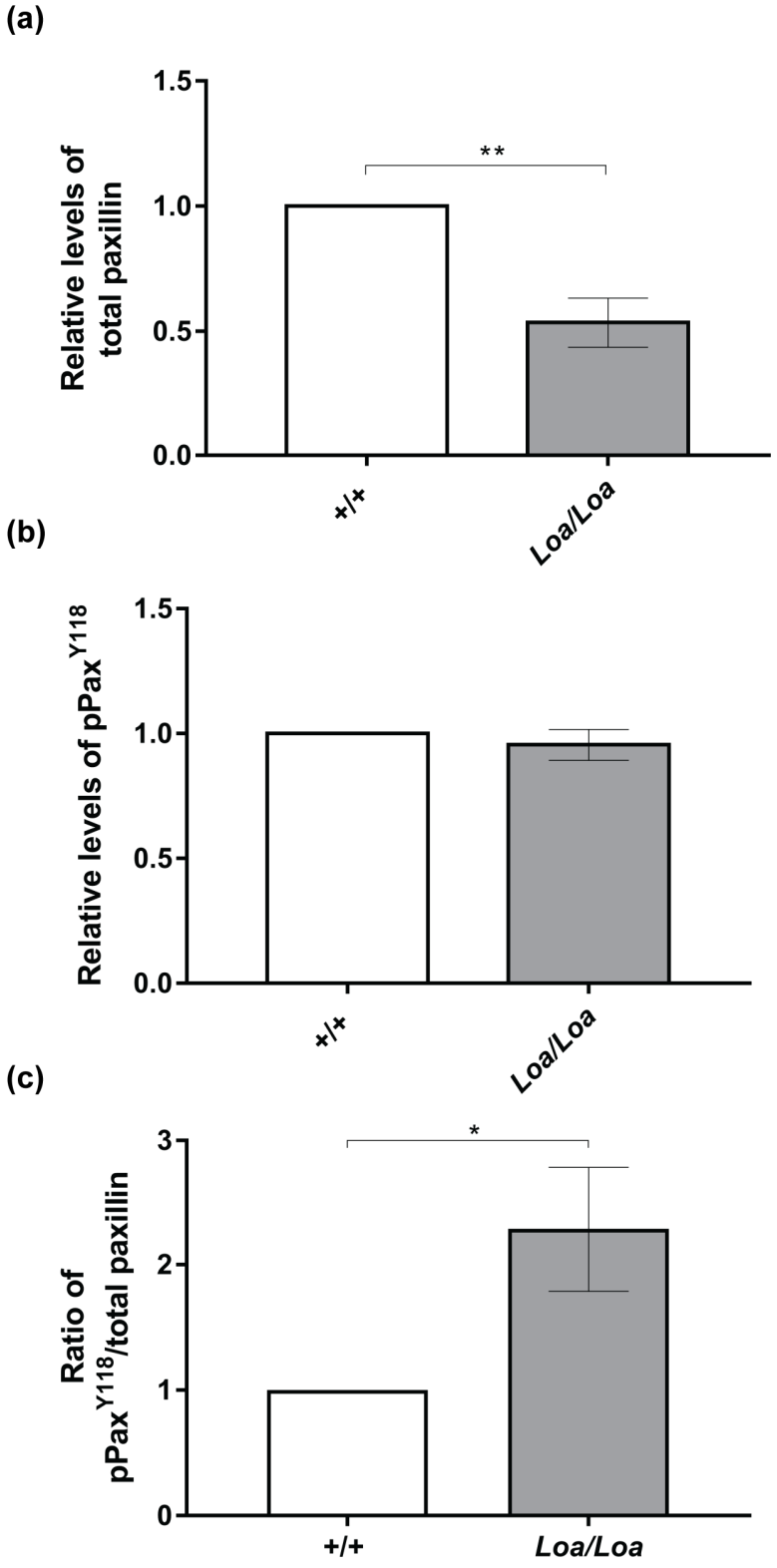
(a)
Relative levels of total paxillin
1.5
1.0
0.5
0.0
**
+/+
Loa/Loa
(b)
Relative levels of pPax Y118
1.5
1.0
0.5
0.0
+/+
Loa/Loa
(c)
Ratio of pPax Y118 /total paxillin
3
2
1
0
*
+/+
Loa/Loa

Figure 4.9 (a) Meta-analysis of total paxillin levels in wild type and *Loa/Loa* MEFs from control samples in Figures 4.6, 4.7 and 4.8. One sample t-test showed a significant reduction of total paxillin in *Loa/Loa* MEFs in comparison to wild type MEFS. (*P = 0.0015*, N = 9). **(b)** Meta-analysis of $pPax^{y118}$ in wild type and *Loa/Loa* MEFs from control samples in Figures 4.4, 4.5. 4.6, 4.7 and 4.8. One sample t-test shows no significant difference between genotypes (*P = 0.4836*, wild type N = 15 and *Loa/Loa* N= 14). **(c)** Meta-analysis of the $pPax^{Y118}$/total paxillin ratio in wild type and *Loa/Loa* MEFs from control samples in Figures 4.6, 4.7 and 4.8. One sample t-test showed a significant increase of the $pPax^{Y118}$/total paxillin ratio in *Loa/Loa* MEFs in comparison to wild type MEFS. (*P = 0.0323* N = 9). Normalised values are plotted relative to wild type samples. Error bars represent SEM. (**P < 0.05*, *** P < 0.01*)

4.2.10 Summary

Of the experiments which measured pPax^{Y118} levels, all but the blebbistatin experiment failed to show a significant effect of the genotype on pPax^{Y118} levels. Therefore, these results appear to contradict the previous observation made in the Hafezparast lab of reduced pPax^{Y118} in *Loa/Loa* MEFs. This explains why no difference in the turnover of paxillin at FAs was seen in a FRAP study. Furthermore, investigating the role of Lfc/GEF-H1, cofilin-1 and pERK1/2 in causing a pPax^{Y118} phenotype is no longer as informative. Note that the interaction of Lfc/GEF-H1 and Cofilin-1 with the IC could not be shown in this study.

Interestingly, for the first-time multiple experiments suggested that there is a reduction in the levels of total paxillin within *Loa/Loa* MEFs in comparison to wild type MEFs. This was found to be significantly different between genotypes in the cell synchronisation experiment in both untreated and thymidine treated conditions. Interestingly, this reduction in total paxillin was also observed following inhibition of dynein activity using Ciliobrevin D. Finally, a meta-analysis of controls from the previous experiments further confirmed that there is a reduction of total paxillin in *Loa/Loa* MEFs but pPax^{Y118} remains unaltered in *Loa/Loa* MEFs. This is because a greater proportion of available paxillin is phosphorylated at Tyr118 as indicated by a significant increase in pPax^{y118}/total paxillin ratio. Table 4.1 summarises the results from the various drug treatments carried out to assess the levels of pPax^{Y118}, total paxillin and pPax^{Y118}/total paxillin in *Loa/Loa* MEFs in comparison to wild type MEFs.

Table 4.1

	4.2.4 ERK1/2 inhibition (U0126)			4.2.5 Laminin treatment			4.2.6 Inhibition of myosin II (blebbistatin)			4.2.7 Cell cycle synchronisation (thymidine block)			4.2.8 Inhibition of dynein (Ciliobrevin D)				Meta-analysis of paxillin levels	Previous data from Hafezparast lab
Two-way ANOVA analysis	**Interaction**	**Genotype main effect**	**Drug main effect**	**Interaction**	**Genotype main effect**	**Drug main effect**	**Interaction**	**Genotype main effect**	**Drug main effect**	**Interaction**	**Genotype main effect**	**Drug main effect**	**Interaction**	**Genotype main effect**	**Drug main effect**			
pPax^{Y118}	No	No	No	No	No	No	No	Decrease**	Decrease****	No	No	No	No	No	Decrease**		No Change	Decrease
Total paxillin							No	No	No	Yes***¥	N/A	N/A	No	No	Decrease***		Decrease**	
pPax^{Y118} /total paxillin ratio							No	No	Decrease**	No	Increase**	No	No	No	Increase*		Increase*	

Table 4.1 Table summarising the results of the different drug treatments used to assess the levels of $pPax^{Y118}$, total paxillin and $pPax^{Y118}$/total paxillin in *Loa/Loa* MEFs in comparison to wild type MEFs. The meta-analysis performed is also contrasted to previous data obtained in the Hafezparast lab (Barri, 2015). ¥ A significant interaction meant that simple main effects were instead analysed. A significant decrease in total paxillin was seen between wild type and *Loa/Loa* MEFs in both DMSO and thymidine treated conditions. Additionally, thymidine treatment caused a significant decrease in total paxillin levels in wild type MEFs. N/A = not applicable. * denotes a significant change (* *P < 0.05, ** P < 0.01, *** P < 0.001, **** P < 0.0001*).

4.3 Discussion

4.3.1 Paxillin turnover at FAs is not affected in *Loa/Loa* MEFs.

Paxillin is found in two separate pools, a transiently immobile pool associated with FAs and a diffuse pool within the cytoplasm (Le Devedec et al., 2012). The exchange of paxillin between these two pools is measured as paxillin turnover. Paxillin phosphorylation at Tyr118 has been shown to be important for the turnover of paxillin at adhesions, as shown by the inhibition of Src family kinases with PP2, which causes a reduction in $pPax^{Y118}$ and resulted in a sharp decrease in the turnover of paxillin at pre-existing adhesions (Qin et al., 2015). This indicates that, as $pPax^{Y118}$ was shown to be decreased in *Loa/Loa* MEFs, this could have an impact on paxillin turnover at adhesions.

To determine if paxillin turnover was indeed affected in *Loa/Loa* MEFs, both wild type and *Loa/Loa* MEFs were transfected with GFP-paxillin and allowed to spread on a collagen I coated live cell imaging dish for 3.5 hours before FRAP was performed. Specifically, FRAP was targeted to the larger FAs observed at the edge of the cell. The quantification of the time required for the recovery of the GFP-paxillin signal at FAs following bleaching did not show a significant difference between wild type and *Loa/Loa* fibroblasts. Note that in both genotypes the levels of GFP-paxillin did not return to pre-bleaching levels as there is likely an immobile paxillin pool at FAs which did not turnover. Additionally, it is likely that some of this is also caused by photobleaching of the signal due to imaging over an extended period.

The phosphorylation of Tyr118 on paxillin is mediated by FAK and Src (López-colomé et al., 2017). It has been previously shown that the inhibition of Src family kinases decreases the turnover of paxillin by 14-fold in comparison to wild type MEFs. Similarly, the turnover of paxillin in $FAK^{-/-}$ cells was also reduced by 14-fold (Webb et al., 2004). Moreover, in a more targeted experiment in which $Pax^{-/-}$ cells were transfected with different paxillin variants, the expression of non-phosphorylatable Y118F mutant paxillin reduced paxillin turnover 4-fold in comparison to wild type cells. Therefore, the lack of a reduction in paxillin turnover at adhesions in *Loa/Loa* MEFs is surprising. However, subsequent data produced here shows that there is no significant difference in $pPax^{Y118}$ in *Loa/Loa* MEFs in

comparison to wild type MEFs in contrast to what was previously observed, thus explaining this lack of a difference in paxillin turnover.

Interestingly, FAs in *Loa/Loa* MEFs had been shown to be smaller in size and more numerous (Barri, 2015). Based on observations made during the microscopy performed for this experiment, it was difficult to discern a visually distinguishable difference in FA size between wild type and *Loa/Loa* MEFs. However, it may be that the overexpression of GFP-paxillin may have abrogated any differences which might have existed.

4.3.2 Lack of co-immunoprecipitation of dynein IC with either Lfc/GEF-H1 or cofilin

As previously described, myosin II activity has been shown to regulate Tyr118 paxillin phosphorylation by increasing FAK and Src activity (Pasapera et al., 2010). RhoA regulates myosin II activity through ROCK which stimulates the phosphorylation of myosin light chain, increasing contractility (Kaneko-Kawano et al., 2012). RhoA is known to be regulated by the microtubule associated guanine nucleotide exchange factor Lfc/GEF-H1 (Meiri et al., 2012). Interestingly, GEF-H1 activity is governed by its association with Tctex-1, a dynein light chain. While the original impetus for checking the Lfc/GEF-H1 interaction with dynein was based on the $pPax^{Y118}$ phenotype, which was no longer observed, it would still be interesting to test if the dynein interaction with Lfc/GEF-H1 is affected as this could have a wide-ranging impact on RhoA signalling within the cell.

First, the IC was immunoprecipitated from wild type and *Loa/Loa* lysates and probing was performed for the dynein LC RP3, Lfc/GEF-H1 and the IC. The results showed that Lfc/GEF-H1 was not co-immunoprecipitated with the IC. This was not caused in by a failure in the immunoprecipitation of the IC, as a strong IC signal is seen in the IP. In support of this, a strong RP3 signal is also seen in the IP. Similarly, the reverse experiment which immunoprecipitated Lfc/GEF-H1, did not pull down the IC and RP3. Previously, immunoprecipitations of the IC have been shown to co-precipitate with Lfc/GEF-H1(Meiri et al., 2012). However, these experiments were performed following the overexpression of Lfc/GEF-H1. Additionally, this interaction was increased following the overexpression of Tctex-1. It is possible that at endogenous levels it is not possible to pick up this

interaction as it may be transient. Further attempts should be made following the overexpression of both Lfc/GEF-H1 and Tctex-1.

Previous findings in the Hafezparast lab from immunoprecipitations on embryonic day 18 brains followed by mass-spectrometry indicated a potential interaction between dynein and cofilin-1. Therefore, immunoprecipitations were performed to validate this prediction. However, immunoprecipitations carried out by either pulling down the IC or cofilin-1 failed to show this interaction and therefore the prediction was not validated.

4.3.3 Normal pPax^{Y118} levels in the *Loa/Loa* MEFs

ERK1/2 is known to inhibit ROCK and affects actomyosin contractility (Sahai et al., 2001). Therefore, it could have consequently affected paxillin phosphorylation by downregulating the pathway above. Active ERK1/2 (pERK1/2) has been previously shown to be increased in *Loa/Loa* MEFs (Garrett et al., 2014). The aim of this experiment was to investigate if this could cause a reduction in pPax^{Y118} levels which had previously been seen in these fibroblasts (Barri, 2015).

Western blot analysis was performed following treatment with the ERK1/2 inhibitor U0126. These results supported previous observations in that *Loa/Loa* MEFs have increased pERK1/2, with levels seen more than threefold higher in *Loa/Loa* MEFs despite not reaching statistical significance due to a small sample size (Garrett et al., 2014). Additionally, the treatment with U0126 lowered pERK1/2 levels in both genotypes to almost undetectable levels. The lack of an interaction between genotype and U0126 treatment as indicated by a two-way ANOVA shows that the inhibition of ERK1/2 was unable to induce a difference between wild type and *Loa/Loa* MEFs in terms of pPax^{Y118} levels. Furthermore, despite a mild increase in pPax^{Y118} levels in both genotypes after U0126 treatment, there was no significant effect of U0216 on pPax^{Y118} levels. Therefore, inhibition of ERK1/2 does not appear to affect paxillin phosphorylation at Tyr118. Interestingly, ERK1/2 has been shown to be involved in the phosphorylation of paxillin at sites other than Tyr118, causing the phosphorylation of Ser130, 106, 231 and 290 (López-colomé et al., 2017).

Surprisingly, there was no distinguishable difference in pPax^{Y118} levels between wild type and *Loa/Loa* fibroblasts both in the DMSO control and following the

U0126 treatment. This observation was supported by a lack of a significant genotype main effect. These data are in contrast to the previously observed reduction in pPax^{Y118} levels in *Loa/Loa* MEFs (Barri, 2015). It is tempting to conclude that the differences between these data and the original observation in the Hafezparast lab are due to differences in experimental design. Potentially, the cells in this experiment might have been in a less active state, and this might have hidden any differences in pPax^{Y118} levels. However, it is important to note that both experiments were conducted on cells with similar levels of confluency and performed using the same pPax^{Y118} antibody. Also, these results support the observations made in the experiment measuring paxillin turnover at FAs which is dependent on Tyr118 phosphorylation (Qin et al., 2015).

The surprising lack of a difference in pPax^{Y118} levels in the previous experiment prompted an attempt to stimulate MEFs by adding laminin directly to the media, aiming to induce the previously observed phenotype by stimulating the cells (Barri, 2015). However, the lack of a significant interaction between genotype and laminin treatment showed that laminin failed to stimulate a difference in pPax^{Y118} between wild type and *Loa/Loa* MEFs. Additionally, analysis of main effects showed that as with the previous experiment, the genotype failed to have an impact on the levels of pPax^{Y118}. Therefore, these data are again in contradiction with the observation within the Hafezparast lab which showed reduced levels of pPax^{Y118} in the *Loa/Loa* MEFs. Additionally, analysis showed that laminin treatment also did not affect the levels of pPax^{Y118}, which suggests laminin was ineffective in stimulating the dynamics of the cell. Overall, given that the previous experiment by Dr Murj Barri in the Hafezparast lab showed the phenotype without the need for stimulation of the cells and the similarity in the methods used to those used here, it is likely that the data presented is evidence that pPax^{Y118} is not altered in *Loa/Loa* MEFs.

4.3.4 Blebbistatin treatment induces a difference between wild type and *Loa/Loa* MEFs in pPax^{Y118} levels

To sensitise the cells for exhibiting any potential difference in pPax^{Y118} levels between wild type and *Loa/Loa* MEFs, blebbistatin was used to inhibit myosin II. As discussed, myosin II activity induces the phosphorylation of paxillin Tyr118 via FAK (Pasapera et al., 2010).

Data from this experiment was analysed using a two-way ANOVA which revealed no significant interaction between the genotype and the blebbistatin treatment in relation to pPax^{Y118} levels, total paxillin levels and the pPax^{Y118}/total paxillin ratio. Therefore, it is clear that the effect of blebbistatin on the cells is not dependent on the genotype for any of these measures. Interestingly, analysis of the main effects showed that the genotype had a significant impact on the levels of pPax^{Y118}, with a reduction in *Loa/Loa* MEFs. While it would be tempting to conclude that this experiment yielded the phenotype previously observed in the Hafezparast lab further analysis provided a more intricate picture of the effect of *Loa* mutation on paxillin.

Importantly, there was a previously unreported reduction in the levels of total paxillin in *Loa/Loa* MEFs in comparison to wild type MEFs in both the DMSO and the blebbistatin condition, which should be taken into consideration despite the fact that genotype did not have a significant main effect on the levels of total paxillin within this experiment. Therefore, the ratio of pPax^{Y118} to total paxillin was analysed and revealed a suprising increase in *Loa/Loa* MEFs in the DMSO condition. This increase in the pPax^{Y118}/total paxillin ratio in *Loa/Loa* MEFs suggests that despite data indicating a potentially smaller pool of total paxillin within these cells, a greater proportion of this is found phosphorylated at Tyr118. This suggests that the limiting factor here may be the levels of total paxillin. Therefore, this would appear to support a scenario in which total paxillin levels are reduced and while the proprotion of paxillin phosphorylated at Tyr118 is actually higher to maintain pPax^{Y118} levels, the reduction in total paxillin levels prevents this from being successful. However, it is important to note that genotype did not have a significant main effect on pPax^{Y118}/total paxillin ratio. The lack of a significant main effect of genotype on total paxillin and on the pPax^{Y118}/total paxillin ratio may be underlined by the third replicate where total paxillin levels in wild type are uncharacteristically low in comparison to the other wild type samples. Therefore, further repeats should be performed to determine if this was an outlier.

Analysis also revealed that blebbistatin treatment had a significant effect on the levels of pPax^{Y118} and pPax^{Y118}/total paxillin ratio but not on the levels of total paxillin. Specficially, blebbistatin significantly reduced the levels of pPax^{Y118} and consequently the pPax^{Y118}/total paxillin ratio. Therefore, these data indicate that as

expected blebbistatin treatment does not affect the available pool of total paxillin but affects the phosphorylation of paxillin at Tyr118 by affecting the activity of myosin II. Interestingly, blebbistatin treatment appears to have a more pronounced effect on the *Loa/Loa* MEFs as evidenced by the fact that the pPax^{Y118}/total paxillin ratio went from above wild type levels in the DMSO condition to below that of the wild type samples in blebbistatin condition. This may be due to lower amounts of available total paxillin in *Loa/Loa* MEFs which could yield a more pronounced effect of blebbistatin mediated pPax^{Y118} reduction.

In summary, this experiment suggested that there may be a reduction in the levels of total paxillin in *Loa/Loa* MEFs and that within these cells a higher proportion of total paxillin is phosphorylated at Tyr118 to attempt to maintain levels of pPax^{Y118}. However, this compensation proved to be ineffective as overall levels of pPax^{Y118} appeared to be reduced, but this is likely due to the reduction in total paxillin. Alternatively, since the previous two experiments failed to show such a difference, it may be that the decrease in pPax^{Y118} is due to variability caused by a cofounding factor. One such factor may be the cell cycle which was subsequently controlled in the next experiment.

4.3.5 Effect of cell cycle synchronisation on pPax^{Y118} in wild type and *Loa/Loa* MEFs.

During mitosis, the phosphorylation of tyrosine residues on paxillin has been shown to decrease (Yamaguchi et al., 1997). Furthermore, paxillin Tyr188 phosphorylation has been implicated in proliferative signalling in myoblasts (Sastry et al., 1999). Moreover, the association between FAK and Src which is critical for paxillin Tyr118 phosphorylation is reduced during mitosis (Yamakita et al., 1999; López-colomé et al., 2017). Therefore, it is possible that variations in the cell cycle between genotypes could affect Tyr118 phosphorylation and give the appearance of a pathogenic phenotype. To eliminate the cell cycle as a potential confounding factor in the pPax^{Y118} phenotype, a double thymidine block was used to synchronise the cell cycle in each genotype to the G1/S phase (Harper, 2005).

Two-way ANOVAs were used to analyse the impact of the genotype and thymidine treatment on pPax^{Y118} levels. No significant interaction was found between genotype and thymidine treatment, indicating that the effect of the treatment did

not vary between genotypes. Importantly, in contrast to the previous experiment (discussed in section 4.3.4) but in agreement to the data from the ERK1/2 inhibition and laminin treatment experiments (discussed in section 4.3.3), there was no significant main effect of the genotype on pPax^{Y118} levels. Interestingly, while there appears to be a reduced amount of pPax^{Y118} in the *Loa/Loa* MEFs in the DMSO condition, this difference is abrogated by the thymidine treatment. This potentially indicates that as was previously discussed the reduction in pPax^{Y118} observed in the blebbistatin treatment experiment (discussed in section 4.3.4) was due to variability caused by a confounding factor, which this experiment indicates may have been the cell cycle. However, it is important to note that thymidine treatment did not have a significant main effect on pPax^{Y118} levels.

With regards to total paxillin levels, analysis using a two-way ANOVA revealed a significant interaction between the genotype and thymidine treatment. This indicates that the thymidine treatment affected total paxillin levels differently between wild type and *Loa/Loa* MEFs. To elucidate this further, simple main effects of the genotype were analysed, which revealed that there was a significant reduction in the levels of total paxillin in *Loa/Loa* MEFs in both the DMSO and thymidine condition in comparison to wild type MEFs. This is in agreement with the patterns observed in the blebbistatin experiment (discussed in section 4.3.4). Additionally, analysis of the simple main effects of thymidine treatment showed that while the treatment caused a significant reduction in total paxillin levels in wild type samples when compared to the DMSO condition, this was not seen between the DMSO *Loa/Loa* samples and thymidine treated *Loa/*Loa samples. These data suggest that synchronization of the cell cycle to G1/S causes a reduction in total paxillin levels, as exhibited in the wild type MEFs. However, as total paxillin levels were already severely depleted in *Loa/Loa* MEFs, no further reduction was seen in these cells.

Finally, two-way ANOVA analysis was performed on the ratio of pPax^{Y118} to total paxillin. Results showed that there was no significant interaction between genotype and thymidine treatment. Additionally, as expected, despite the previously discussed effect of thymidine on total paxillin levels in the wild type MEFs, the lack of an effect on total paxillin levels within *Loa/Loa* MEFs resulted in a lack of a significant main effect of the thymidine on the pPax^{Y118}/total paxillin

ratio. Importantly, there was a significant main effect of genotype on the pPax^{Y118}/total paxillin ratio. Specifically, a significant increase in the pPax^{Y118}/total paxillin ratio in *Loa/Loa* MEFs was observed. These data support the previous suggestion that in *Loa/Loa* MEFs, the decrease in total paxillin levels results in a higher proportion of paxillin being phosphorylated at Tyr118 to maintain the overall levels of pPax^{Y118}. Interestingly, while the pPax^{Y118}/total paxillin ratio appears higher in the thymidine treated *Loa/Loa* MEFs even compared to the already increased levels seen in the DMSO treated *Loa/Loa* MEFs, the wild type MEFs exhibit no change in pPax^{Y118}/total paxillin ratio in response to thymidine. This is suprising considering that as discussed previously there was a reduction in total paxillin levels in these cells following thymidine treatment. Therefore, it may have been expected that a similar increase in the proportion of total paxillin phosphorylated at Tyr118 would be observed to maintain pPax^{Y118} levels.

4.3.6 Dynein inhibition causes a decrease in both total paxillin and pPax^{Y118}

As the previous experiments indicated that dynein could affect the levels of total paxillin, dynein ATPase activity was inhibited with Ciliobrevin D and the effect on total paxillin and pPax^{Y118} was analysed using western blot analysis.

As with the previous experiments, two-way ANOVA analysis was performed which revealed no significant interaction between the genotype and the Ciliobrevin D treatment when measuring pPax^{Y118} levels, indicating that the effect of Ciliobrevin D is independent of genotype. Furthermore, analysis showed that genotype did not have a significant main effect on the levels of pPax^{Y118}. This data is in agreement with data from the ERK1/2 inhibition experiment, laminin treatment experiment and thymidine treatment experiment (discussed in sections 4.3.3 and 4.3.5). This further supports the hypothesis that the difference in pPax^{Y118} observed in the blebbistatin treatment experiment (discussed in section 4.3.4) was likely due to variability and was not representative. Interestingly, analysis showed that there was a significant main effect of Ciliobrevin D treatment, indicating significantly reduced levels of pPax^{Y118} in comparison to the DMSO condition.

Similar analysis of total paxillin levels showed no significant interaction between genotype and Ciliobrevin D treatment, indicating that Ciliobrevin D also affects both genotypes equally with regards to total paxillin levels. Interestingly,

densitometric quantification of total paxillin levels showed that there was a reduced level in *Loa/Loa* MEFs in comparison to wild type MEFs in the DMSO condition and Ciliobrevin D treated condition. This is similar to the pattern seen in the DMSO controls of the previous experiments and their respective treatment conditions. However, analysis for this experiment showed that there was no significant main effect of the genotype on the levels of total paxillin. The lack of a significant effect is likely due to a small sample number and the second wild type replicate exhibiting a smaller response to Ciliobrevin D treatment which increased the variation between the samples. Interestingly, statistical analysis revealed a significant main effect of Ciliobrevin D treatment on the levels of total paxillin. The marginal means suggested that there was a significant reduction in the levels of total paxillin in the Ciliobrevin D treatment condition in comparison to the DMSO condition. This reduction in total paxillin in response to Ciliobrevin D treatment likely underlies the significant effect of the treatment on the levels of pPax^{Y118}, as such a strong reduction in total paxillin levels reduces the available pool of paxillin available to become phosphorylated at Tyr118. Importantly, this data provides further evidence that as suggested by the previous experiments, in which total paxillin levels appeared reduced in the *Loa/Loa* MEFs (reaching statistical significance in the thymidine experiment), dynein activity may be able to affect the levels of total paxillin. At this stage, the mechanisms that could underlie the decrease in total paxillin levels following inhibition of dynein activity are unclear.

Additionally, analysis was carried out on the effect of genotype and Ciliobrevin D treatment on the pPax^{Y118}/total paxillin ratio. This also showed no significant interaction between the genotype and Ciliobrevin D treatment and no significant main effect of the genotype on the pPax^{Y118}/total paxillin ratio. As seen in previous experiments, the *Loa/Loa* MEFs showed an increase in the pPax^{Y118}/total paxillin ratio in the DMSO condition but to a lower extent. Again this may suggest that a higher proportion of total paxillin is phosphorylated to maintain pPax^{Y118} levels. This notion is supported by the fact that there is a significant main effect of Ciliobrevin D treatment on the ratio of pPax^{Y118} to total paxillin, with a significant increase seen in the Ciliobrevin D treatment condition. Therefore, this shows that following the inhibition of dynein activity there is a reduction in the levels of total paxillin (as dicussed above) and consequently the proportion of total paxillin that is

phosphorylated at Tyr118 is higher to attempt to maintain the levels of pPax^{Y118}. However, since Ciliobrevin D treatment significantly reduced pPax^{Y118} levels in these cells, it suggests that the remaining available pool of total paxillin is below what is necessary to maintain the levels of pPax^{Y118}. Note that the increase in the proportion of total paxillin phosphorylated at Tyr118 is more prominent in the wild type samples, this is likely a consequence of an already depleted pool of total paxillin in *Loa/Loa* MEFs. However, it is important to note that Ciliobrevin D treatment appears to cause a reduction in the levels of β-actin which was used as the loading control for this experiment. This unexpected consequence of the treatment may reflect an increase in apoptosis which can be tested in future experiments by measuring apoptotic markers such as cleaved Poly(ADP-ribose) polymerase 1 (PARP-1) or performing terminal deoxynucleotidyl transferase dUTP nick end labelling (TUNEL).

4.3.7 Meta-analysis of paxillin controls show a significant reduction in total paxillin levels in *Loa/Loa* MEFs

To determine if total paxillin levels are definitively altered in *Loa/Loa* fibroblasts and to confirm that pPax^{Y118} levels are not, the control samples in the experiments above were used in combined statistical analysis. The results showed that there is a significant reduction in the levels of total paxillin in *Loa/Loa* MEFs but no significant difference in the levels of pPax^{Y118} between genotypes. The latter of which is in agreement with the lack of a difference in the turnover of paxillin at FAs which is dependent on Tyr118 phosphorylation. Combined statistical analysis of the pPax^{Y118}/total paxillin ration showed a significant increase in the *Loa/Loa* MEFs, which shows that in these cells a higher proportion of total paxillin is phosphorylated at Tyr118 which consequently maintains the levels of pPax^{Y118}. Overall, these data indicate that the migration and reduced FA size phenotype might be underpinned by a reduction in total paxillin levels rather than a decrease in the levels of pPax^{Y118}. Further work is required to ascertain how dynein affects the levels of total paxillin.

Chapter 5: Molecular phenotypes of DYNC1H1$^{+/D338N}$ and BICD2$^{+/I189F}$ patient fibroblasts

5.1 Introduction

SMA-LED is a congenital or early onset autosomal dominant form of SMA which primarily targets the proximal muscles of the lower limbs (Harms et al., 2010). The neuronal loss, muscle weakness and atrophy caused by SMA-LED shows little to no progression, but it is often compounded with cognitive impairment (Harms et al., 2012; Scoto et al., 2015). The precise aetiology of this disease remains unknown but causative mutations have been identified in two genes, both of which implicate the molecular motor dynein in its pathogenesis.

Most of the disease causing mutations have thus far been identified in the gene encoding the HC of the dynein complex (*DYNC1H1*) (Harms et al., 2012; Scoto et al., 2015). The HC harbours the complex's motor domain and forms the core around which other components assemble (Schiavo et al., 2013). Mutations have also been found in the *BICD2* gene which encodes the BICD2 cargo adaptor of dynein (Neveling et al., 2013; Oates et al., 2013; Peeters et al., 2013). BICD2 is also important for the formation of a stable dynein-dynactin complex and activation of dynein processivity (Carter et al., 2016; Zhang et al., 2017b).

Dynein is a retrograde motor which is responsible for the transport of a wide diversity of cargo towards the minus end of microtubules. This cargo includes endosomes, lysosomes, organelles, cytoskeletal filaments and phagosomes, amongst others (Roberts et al., 2013). However, dynein also serves vital functions at the Golgi apparatus, including mediating vesicular transport from the ER to the Golgi (Jaarsma and Hoogenraad, 2015). Importantly, dynein is also required for the pericentrosomal positioning of the Golgi and the maintenance of its integrity. This is exemplified by the resulting Golgi fragmentation that arises when dynein function is disrupted (Burkhardt et al., 1997; Palmer et al., 2009). Coincidently, BICD2 is considered a golgin protein due to its structure, localisation to the TGN of the Golgi, and its interaction with RAB6A (Martinez-Carrera and Wirth, 2015; Matanis et al., 2002; Harada et al., 1998). Like dynein, the disruption of BICD2 also causes the fragmentation of the Golgi (Fumoto et al., 2006; Teuling et al., 2008).

Therefore it is perhaps unsurprising that Golgi pathology has been established as a feature of SMA-LED caused by both dynein and BICD2 mutations. Delayed

Golgi reassembly following nocodazole washout has been observed in patient fibroblasts harbouring SMA-LED *DYNC1H1* mutations (Fiorillo et al., 2014). Embryonic fibroblasts from the *Loa* mouse model of SMA-LED also exhibit a similar phenotype (Hafezparast et al., 2003). Additionally, Golgi fragmentation is also caused by several BICD2 mutations (Neveling et al., 2013; Peeters et al., 2013; Unger et al., 2016).

More recently, work conducted in the Hafezparast lab by Dr Ryan Green has shown that inherent fragmentation of the Golgi is present in patient fibroblasts which harbour the p.R399G DYNC1H1 substitution. Additionally, this was compounded with decreased microtubule acetylation and a reduction of dynein present at the Golgi, the combination of which was suggested as the cause of the Golgi fragmentation.

These data suggest that Golgi pathology may be a common feature of SMA-LED and could be important in its pathogenesis. To test this hypothesis, patient fibroblasts which harbour either the p.D338N DYNC1H1 substitution or the p.I189F BICD2 substitution were used to explore if they share this Golgi pathology. Additionally, these fibroblasts will be examined for alterations in the post-translational modification of microtubules to determine if this is a common feature in SMA-LED.

5.2 Results

5.2.1 Analysis of the integrity of the Golgi apparatus in patient fibroblasts

As discussed, Golgi fragmentation has been observed in patient cells harbouring the DYNC1H1^{R399G} substitution in the Hafezparast lab. Additionally, Golgi fragmentation is caused by several mutations in BICD2 (Neveling et al., 2013; Peeters et al., 2013; Unger et al., 2016). To ascertain if either DYNC1H1$^{+/D338N}$ or BICD2$^{+/I189F}$ patient fibroblasts exhibit inherent Golgi fragmentation, cells were fixed and stained for the Golgi marker giantin to allow full visualisation of the organelle. As can be seen in the right panel of Figure 5.1a, the Golgi in wild type fibroblasts were mostly seen to be an elaborate organelle with the ribbon structure clearly visible. DYNC1H1$^{+/D338N}$ fibroblasts did not appear to exhibit Golgi fragmentation as previously described for the DYNC1H1^{R399G} mutation. However, the Golgi appeared to be visually more condensed and less elaborate. Similarly, the Golgi in BICD2$^{+/I189F}$ fibroblasts also had no visually perceptible fragmentation phenotype.

To verify these observations, high-throughput quantification was performed by Dr. Constantino Carlos Reyes-Aldasoro to automatically isolate the Golgi and count the average number of Golgi fragments per cell (see Figure 5.1b). A Kruskal-Wallis test was performed on Log^{10} transformed data, which confirmed that there was no significant difference with regards to the average number of Golgi fragments between genotypes, $P = 0.2260$ (Wild type N = 76, DYNC1H1$^{+/D338N}$ N = 60, BICD2$^{+/I189F}$ N= 98). The results from this quantification are shown in Figure 5.1c.

The same algorithm also produced further metrics for the analysis of the Golgi. Firstly, the total area of the Golgi was analysed and a Welch's ANOVA with Games-Howell multiple comparison's test performed. The Welch's ANOVA showed a significant difference between genotypes ($P < 0.0001$). As shown in Figure 5.1d, Games-Howell multiple comparison test showed a significant reduction in the average area of the Golgi between wild type and BICD2$^{+/I189F}$ fibroblasts ($P = 0.0278$). Similarly, a striking significant reduction in the average area of the Golgi was seen between the wild type and DYNC1H1$^{+/D338N}$ fibroblasts ($P < 0.0001$). There was also a significant difference in Golgi area between

DYNC1H1$^{+/D338N}$ and BICD2$^{+/I189F}$ fibroblasts (*P = 0.0176*). The N number is as described for the previous quantification.

Secondly, the algorithm used allowed for a measure of the spread of the Golgi in each cell by measuring the gaps between the Golgi membranes (Figure 5.1e). A Welch's ANOVA on Log^{10} transformed data showed a significant difference between genotypes (*P = 0.0010*). To identify where these differences occurred, Games-Howell multiple comparison test was performed which showed a significantly lower average area between Golgi membranes in the DYNC1H1$^{+/D338N}$ fibroblasts in comparison to both the wild type (*P = 0.0015*) and BICD2$^{+/I189F}$ (*P = 0.0002*) fibroblasts. Therefore, the Golgi in the DYNC1H1$^{+/D338N}$ fibroblasts is less spread in comparison to the other two genotypes (Figure 5.1f).

As cell morphology may impact the morphology of the Golgi, the images taken were qualitatively assessed for potential differences. As shown in the left panel of Figure 5.1a in which the outline of the cells in a representative image have been marked, there appears to be a greater confluency in the BICD2$^{+/I189F}$ images which may have impacted cell morphology. On the other hand, wild type and DYNC1H1$^{+/D338N}$ images had similar number of cells and the morphology of the cells did not appear to be qualitatively different.

Overall, the data suggests that there is no inherent fragmentation of the Golgi in both DYNC1H1$^{+/D338N}$ and BICD2$^{+/I189F}$ fibroblasts in comparison to wild type cells. Interestingly, there appears to be a condensation of the Golgi in DYNC1H1$^{+/D338N}$ fibroblasts so that it occupies a smaller area and has less space between its membranes. However, BICD2$^{+/I189F}$ fibroblasts only exhibited a smaller area of the Golgi but did not show a reduced Golgi spread. Although, it is important to note that the confluency of the BICD2$^{+/I189F}$ fibroblasts was greater than wild type and DYNC1H1$^{+/D338N}$ fibroblasts. A factor that could have caused differences in cell morphology which may have in turn impacted the area of the Golgi.

Figure 5.1

(a)

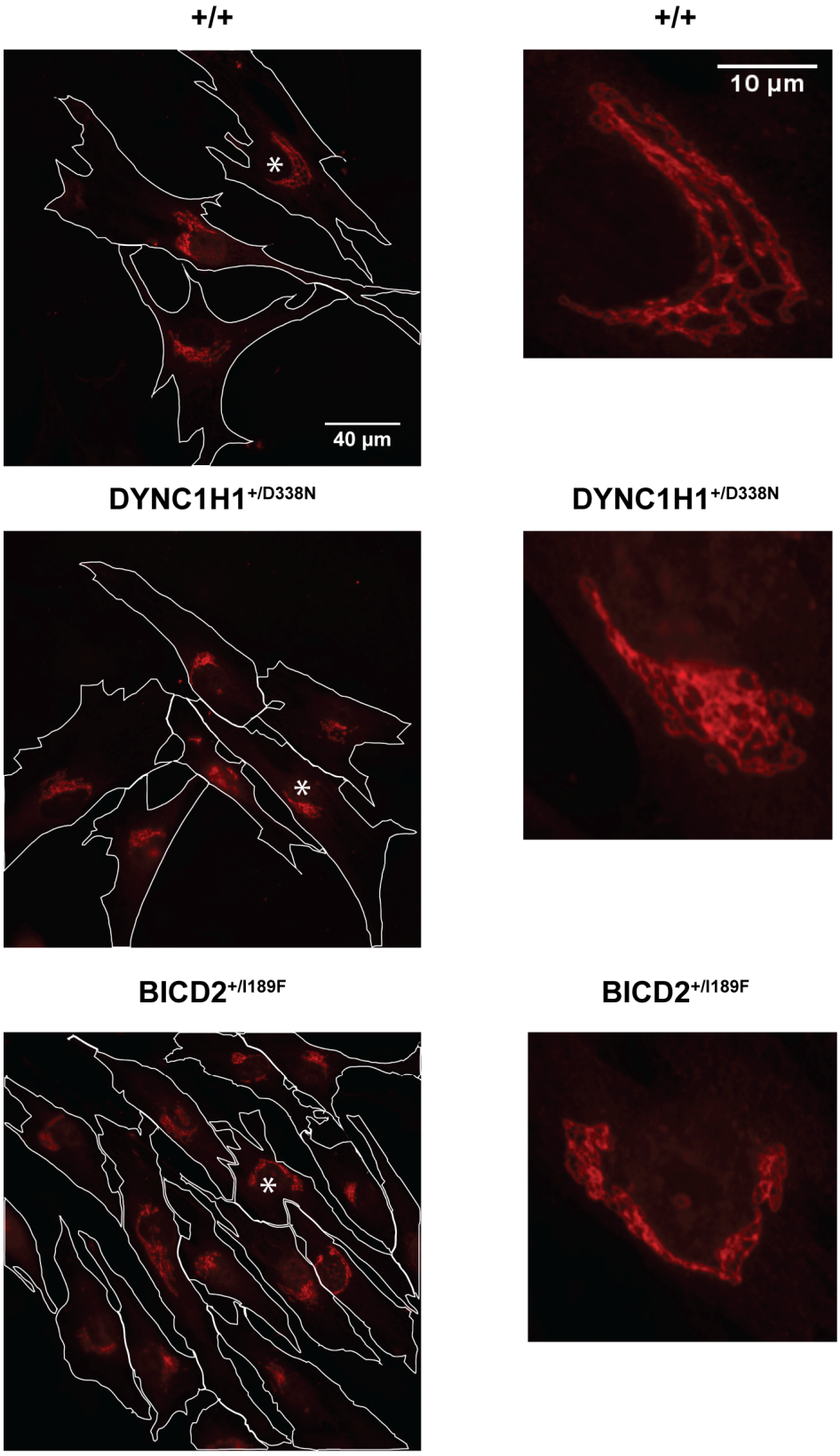
+/+
+/+
10 µm
40 µm
DYNC1H1+/D338N
DYNC1H1+/D338N
BICD2+/I189F
BICD2+/I189F

Figure 5.1 continued

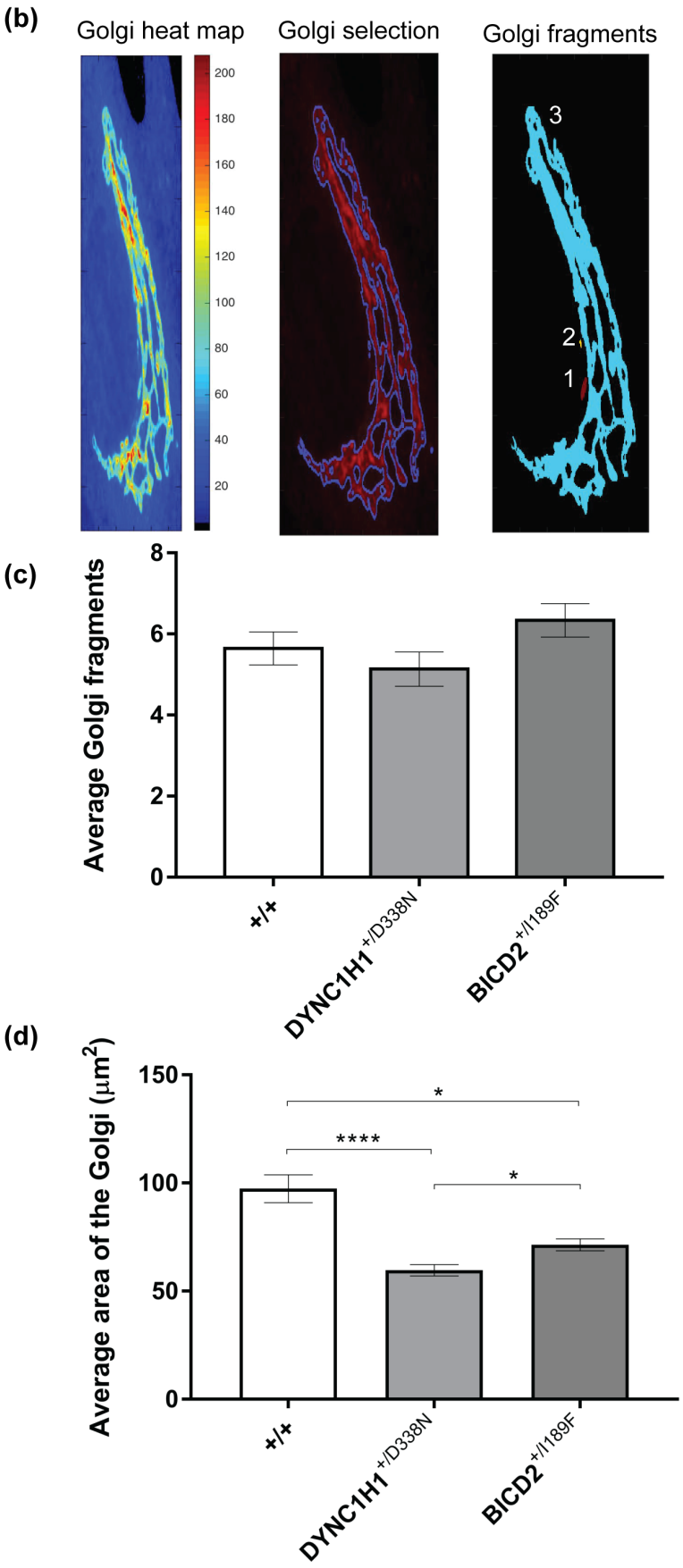

Figure 5.1 continued

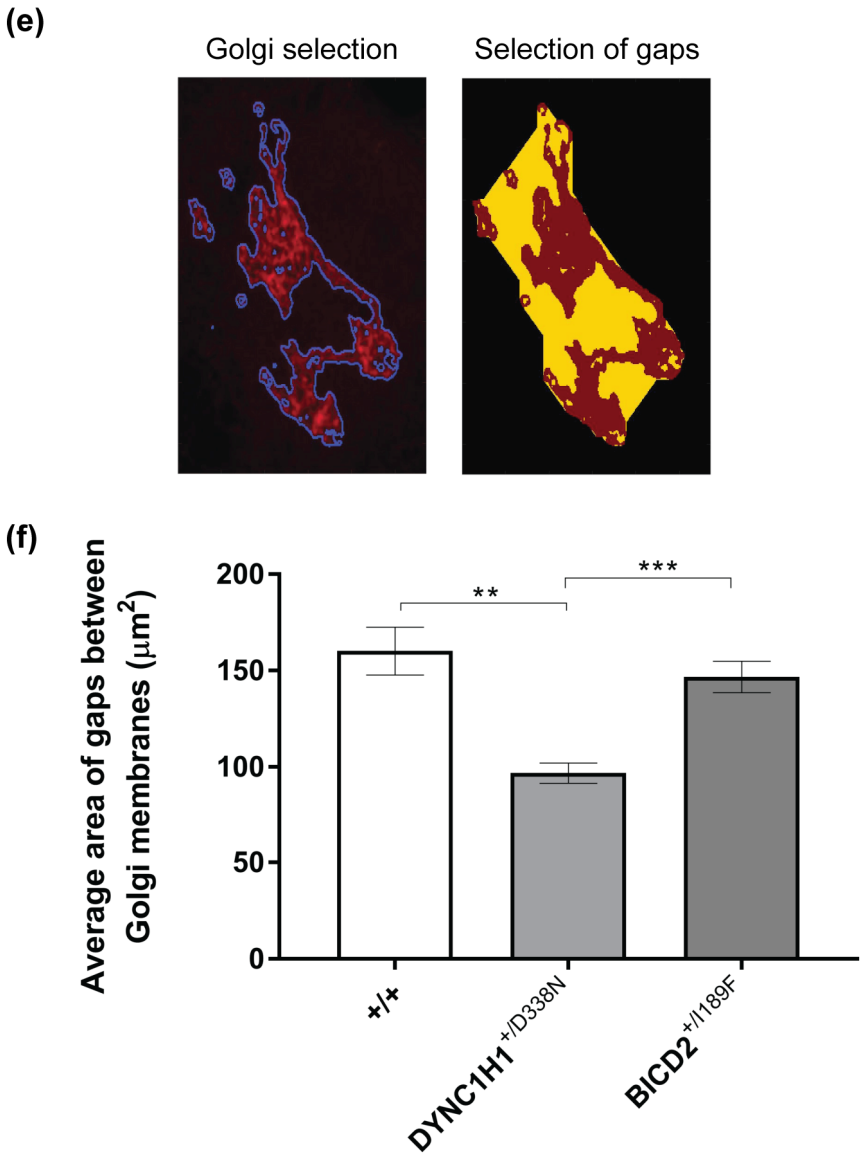

Figure 5.1 (a) Fixed cell imaging of the Golgi apparatus stained with giantin (a Golgi marker) in wild type, DYNC1H1$^{+/D338N}$ and BICD2$^{+/I189F}$ fibroblasts. Left panel: Images taken to assess Golgi morphology with cell outline marked. Right panel: shows a closer magnification of the Golgi corresponding to the Golgi marked with * in the right panel. **(b)** Example illustrating the automated high-throughput quantification of Golgi fragmentation. The first panel shows the intensity heat map used to select the Golgi, the middle panel shows the selection of the Golgi superimposed on the original image and the final panel shows the counting of the Golgi fragments (yellow, blue and red fragments). **(c)** Graph showing the average number of Golgi fragments per genotype, which showed no significant difference as indicated by a Kruskal-Wallis test performed on Log^{10} transformed data (*P = 0.2260*). **(d)** Graph showing the average area of the Golgi in each genotype. A Welch's ANOVA showed a significant difference between genotypes (*P < 0.0001*). Games-Howell multiple comparison test showed a reduction in the average area of the Golgi in both BICD2$^{+/I189F}$ fibroblasts (*P = 0.0278*) and DYNC1H1$^{+/D338N}$ fibroblasts (*P < 0.0001*) when compared to wild type fibroblasts. A significant difference was also found between DYNC1H1$^{+/D338N}$ and BICD2$^{+/I189F}$ fibroblasts (*P = 0.0176*). **(e)** Example of the quantification of the area of the gaps between the Golgi membranes to obtain a measure of Golgi spread. The first panel shows the selection of the Golgi and the second panel shows the area in between the Golgi membranes which was measured (shown in yellow) **(f)** Graph showing the average area of the gaps between Golgi membranes. A Welch's ANOVA on Log^{10} transformed data showed a significant difference between genotypes (*P = 0.0010*). Games-Howell multiple comparison test showed a significantly lower average area of gaps between Golgi membranes in the DYNC1H1$^{+/D338N}$ fibroblasts in comparison to both the wild type (*P = 0.0015*) and BICD2$^{+/I189F}$ (*P = 0.0002*) fibroblasts. Wild type N = 76, DYNC1H1$^{+/D338N}$ N = 60, BICD2$^{+/I189F}$ N= 98 for all the above quantifications. Errors bars represent SEM. (** P < 0.05, ** P < 0.01, *** P < 0.001, **** P < 0.0001*)

5.2.2 Localisation of the IC of dynein at the Golgi apparatus in patient fibroblasts

Dynein is known to be localised at the Golgi apparatus and is important for the formation and integrity of the organelle (Burkhardt et al., 1997; Palmer et al., 2009; Jaarsma and Hoogenraad, 2015). The condensation of the Golgi observed in the previous experiment might be caused by a lack of dynein at the organelle. Interestingly, data from the Hafezparast lab has shown that IC localisation at the Golgi is reduced by the DYNC1H1^{R399G} mutation. To determine if the DYNC1H1$^{+/D338N}$ fibroblasts also exhibited a lack of dynein at the Golgi, cells were fixed and stained for the IC and giantin (a Golgi marker). BICD2$^{+/I189F}$ fibroblasts were also included in this analysis as BICD2 may be involved in the recruitment of dynein to the Golgi. If this is the case, dynein may be reduced at the Golgi as the mutation resides in the IC binding domain of BICD2 (Oates et al., 2013).

Images were taken at a high resolution (2048x2048 pixels) to facilitate the assessment of the IC localisation at the Golgi. As shown in merged panel of Figure 5.2a, the IC signal appears to coat the membrane of the Golgi in the wild type and DYNC1H1$^{+/D338N}$ fibroblasts but not in the BICD2$^{+/I189F}$ fibroblasts. This can be more clearly seen in the inset panels in the same image.

Another in-house MATLAB algorithm developed by Dr Constantino Carlos Reyes-Aldasoro was used to quantify the level of the IC at the Golgi. The algorithm isolated the Golgi and identified the IC signal within the area of the organelle (Figure 5.2b). The data was quantified using two different metrics. The first used quantified the intensity of the signal at the Golgi over the area of the Golgi to obtain a measure of the amount of IC signal at the Golgi. The second method used the area of the IC at the Golgi over the total area of the Golgi to obtain a measurement of the level of Golgi which contained IC. A one-way ANOVA was performed on Log^{10} transformed data with Tukey's multiple comparison test. The one-way ANOVA for the total intensity over the area of the Golgi showed a significant difference between genotypes ($P = 0.0015$). Tukey's multiple comparison test showed a significant reduction in IC signal at the Golgi in the BICD2$^{+/I189F}$ fibroblasts when compared to both the wild type ($P= 0.0018$) and DYNC1H1$^{+/D338N}$ ($P = 0.0088$) fibroblasts, as shown in Figure 5.2c. No difference was seen between DYNC1H1$^{+/D338N}$ and wild type fibroblasts ($P = 0.8743$). A one-

way ANOVA also showed a significant difference in the Golgi localised with IC signal between genotypes (*P = 0.0004*). Tukey's multiple comparison test showed that there was a significant reduction in the area of the Golgi localised with IC between BICD2$^{+/I189F}$ and both wild type (*P =0.0006*) and DYNC1H1$^{+/D338N}$ (P = *0.002*) fibroblasts, as shown in Figure 5.2d. No significant difference was seen between wild type and DYNC1H1$^{+/D338N}$ fibroblasts (*P = 0.9402*). For all quantifications above, the wild type N = 12, DYNC1H1$^{+/D338N}$ N = 10, and BICD2$^{+/I189F}$ N = 8.

Additionally, further images were taken with Z-stacking to allow the visualisation of the IC signal at the Golgi at multiple levels (Figure 5.2e). The images were taken by finding the Golgi focal plane and then taking two slices above and below this plane with 0.32µm between each slice. A qualitative assessment indicates that these images are representative of the result obtained by the quantification of the IC at the Golgi at the Golgi focal plane.

In summary, there appears to be a reduction in the localisation of the IC at the Golgi in BICD2$^{+/I189F}$ fibroblasts which is not seen in the DYNC1H1$^{+/D338N}$ fibroblasts. Therefore, it suggests the condensed Golgi morphology observed in DYNC1H1$^{+/D338N}$ fibroblasts is not due to a lack of dynein at the Golgi. However, this data could suggest that wild type BICD2 is required for recruiting dynein to the Golgi.

Figure 5.2

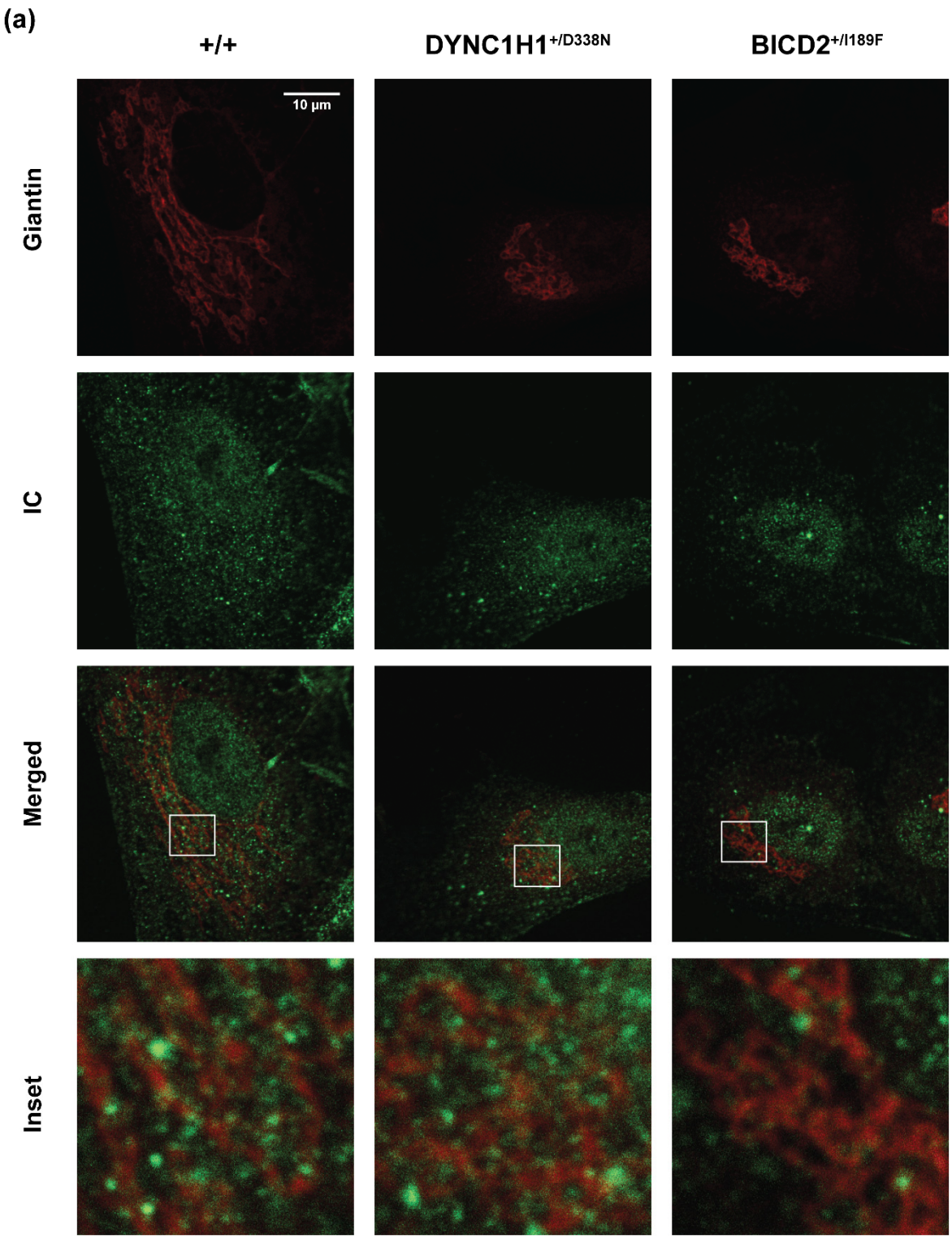

Figure 5.2 continued

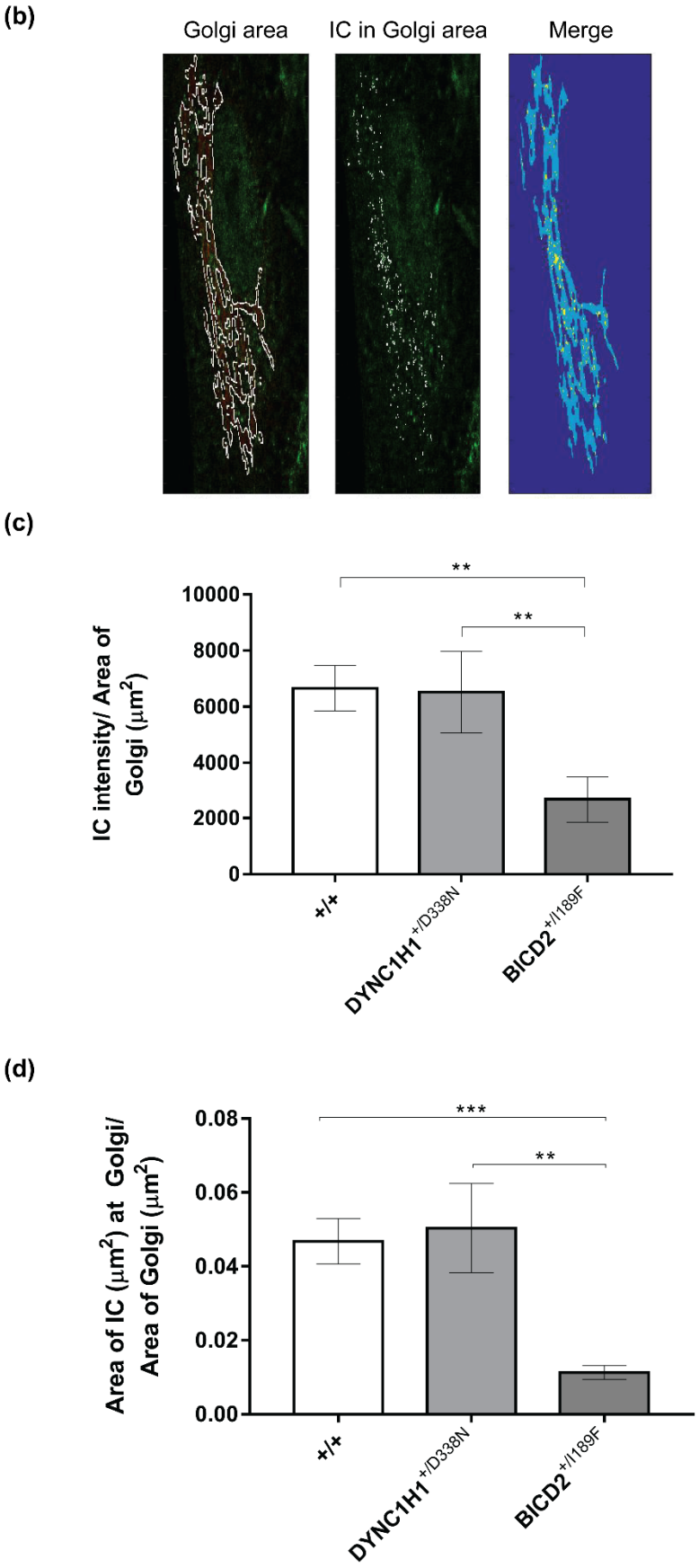

Figure 5.2 continued

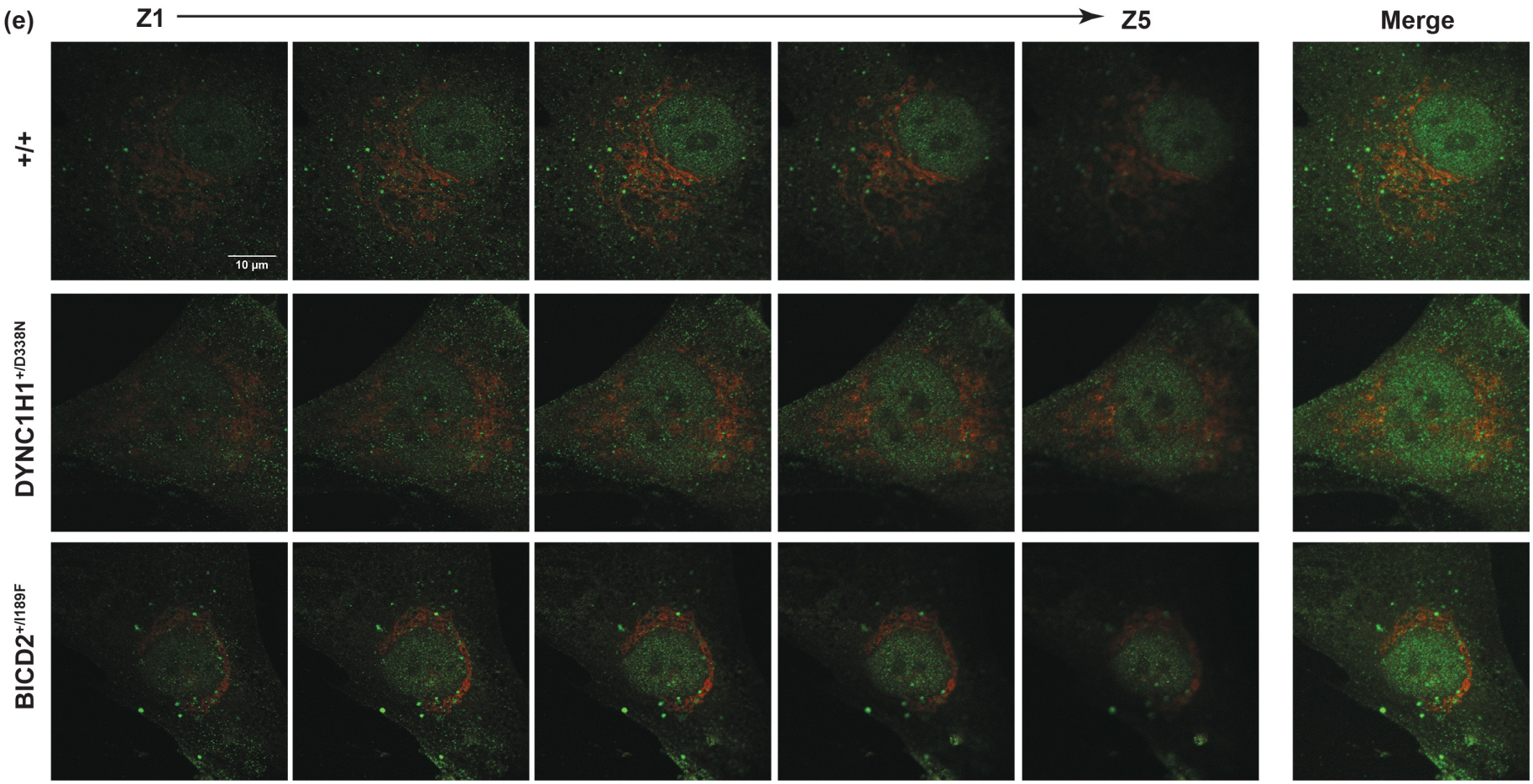

Figure 5.2 (a) Localisation of dynein IC at the Golgi visualised in fixed cells stained for IC and Giantin (a Golgi marker). There is a reduction in the levels of IC at the Golgi in the BICD2$^{+/I189F}$ fibroblasts which is not seen in DYNC1H1$^{+/D338N}$ fibroblasts when compared to wild type cells. **(b)** Example of quantification of levels of IC at the Golgi. The left panel shows the isolation of the Golgi, the middle panel shows the IC signal within the Golgi after normalisation to background and the third panel shows the overlay of the IC at the Golgi. **(c)** Graph showing the total intensity of the IC over the area of the Golgi. A one-way ANOVA on Log^{10} transformed data showed a significant difference between genotypes (*P = 0.0015*). Tukey's multiple comparisons test showed a significant reduction of the intensity of the total IC signal over the area of the Golgi in BICD2$^{+/I189F}$ fibroblasts compared to both wild type (*P = 0.0018*) and DYNC1H1$^{+/D338N}$ fibroblasts (*P = 0.0088*). No difference was seen between DYNC1H1$^{+/D338N}$ and wild type fibroblasts (*P = 0.8743*). **(d)** Graph showing the area of the IC signal over the area of the Golgi. A one-way ANOVA on Log^{10} transformed data shows a significant difference between genotypes (*P = 0.0004*) and Tukey's multiple comparisons test shows a significant decrease in this measurement in the BICD2$^{+/I189F}$ fibroblasts in comparison to both wild type (*P =0.0006*) and DYNC1H1$^{+/D338N}$ fibroblasts (P = *0.002*). No significant difference was found between DYNC1H1$^{+/D338N}$ and wild type fibroblasts (*P = 0.9402*). **(e)** Z-stacks of the localisation of the IC at the Golgi. Slices were taken 0.32 µm apart above and below the Golgi focal plane. For all of the data above the wild type N = 12, DYNC1H1$^{+/D338N}$ N = 10 and BICD2$^{+/I189F}$ N = 8. Errors bars represent SEM. (** *P < 0.01,* *** *P < 0.001*)

5.2.3 Reduced microtubule acetylation in DYNC1H1$^{+/D338N}$ mutant fibroblasts

It has been suggested that Golgi-derived microtubules are important for the formation of the Golgi ribbon (Miller et al., 2009). The condensation of the Golgi may be due to a failure in this process caused by alterations in the properties of microtubules. Interestingly, Golgi associated microtubules are found to be highly acetylated (Thyberg and Moskalewski, 1993). Since the DYNC1H1^{R399G} mutation has previously been shown to reduce microtubule acetylation in the Hafezparast lab, the levels of microtubule acetylation were checked in both DYNC1H1$^{+/D338N}$ and BICD2$^{+/I189F}$ fibroblasts.

Microtubule acetylation was assessed by western blot analysis and probing for α-tubulin acetylated at Lys40. As shown in Figure 5.3a, there is a visible decrease in the level of tubulin acetylation in DYNC1H1$^{+/D338N}$ fibroblasts in comparison to wild type fibroblasts. However, in BICD2$^{+/I189F}$ fibroblasts this does not appear to be the case. Densitometric quantification was performed to determine if the observed difference was statistically significant (Figure 5.3b). A one sample t-test was performed which showed a significant decrease in the level of acetylated tubulin in DYNC1H1$^{+/D338N}$ fibroblasts (*P = 0.0045*). However, no significant difference was seen between wild type and BICD2$^{+/I189F}$ fibroblasts using the same statistical test *P = 0.8019*). For the DYNC1H1$^{+/D338N}$ experiment, the sample number for both genotypes was 5, whilst for the BICD2$^{+/I189F}$ experiment, the sample number for both genotypes was 6.

To ensure the difference in acetylated tubulin was not simply a reflection of changes in overall tubulin levels between genotypes, western blot analysis was used to check levels of α-tubulin. As seen in Figure 5.3c, no difference in α-tubulin was found between genotypes. This was confirmed by densitometric quantification and one sample t-tests which showed no significant difference between wild type fibroblasts and both DYNC1H1$^{+/D338N}$ fibroblasts (*P = 0.6604*) and BICD2$^{+/I189F}$ fibroblasts (*P = 0.2154*).

The reduction of acetylated tubulin in the DYNC1H1$^{+/D338N}$ fibroblasts but not in the BICD2$^{+/I189F}$ fibroblasts correlates with the condensation phenotype of the Golgi in these cells.

Figure 5.3

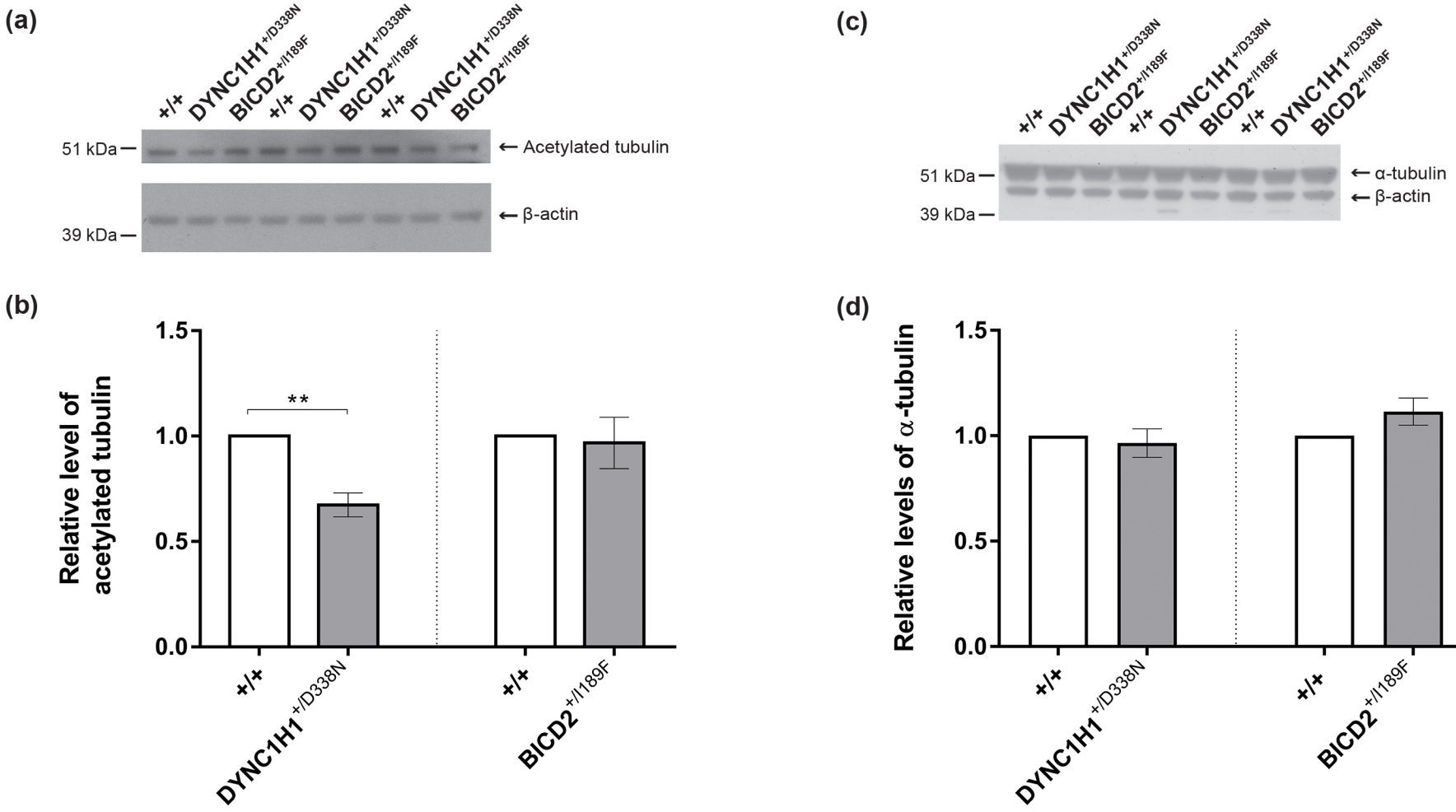
(a)
+/+
DYNC1H1+/D338N
BICD2+/I189F
51 kDa
← Acetylated tubulin
39 kDa
← β-actin
(b)
Relative level of acetylated tubulin
1.5
1.0
0.5
0.0
**
+/+
DYNC1H1+/D338N
+/+
BICD2+/I189F
(c)
51 kDa
39 kDa
← α-tubulin
← β-actin
(d)
Relative levels of α-tubulin

Figure 5.3 (a) Western blot analysis of tubulin acetylation in DYNC1H1$^{+/D338N}$ and BICD2$^{+/I189F}$ fibroblasts in comparison to wild type fibroblasts. The image represents 3 repeats for each genotype. There is an observable decrease in the amount of acetylated tubulin in DYNC1H1$^{+/D338N}$ but not in BICD2$^{+/I189F}$ fibroblasts in comparison to wild type cells. **(b)** Graph showing the densitometric quantification of acetylated tubulin levels in wild type, DYNC1H1$^{+/D338N}$ and BICD2$^{+/I189F}$ fibroblasts. A one sample t-test showed a significant reduction in the amount of acetylated tubulin in DYNC1H1$^{+/D338N}$ fibroblasts ($P = 0.0045$) but not in BICD2$^{+/I189F}$ fibroblasts ($P = 0.8019$) in comparison to wild type cells. For the DYNC1H1$^{+/D338N}$ experiment the N for both genotypes was 5, whilst for the BICD2$^{+/I189F}$ experiment N = 6. **(c)** Western blot analysis of α-tubulin in DYNC1H1$^{+/D338N}$ and BICD2$^{+/I189F}$ fibroblasts in comparison to wild type fibroblasts. There is no visible difference in the levels of α- tubulin. **(d)** Densitometric quantification of α-tubulin in DYNC1H1$^{+/D338N}$ and BICD2$^{+/I189F}$ fibroblasts in comparison to wild type fibroblasts. One sample t-tests showed no significant difference between wild type fibroblasts and both DYNC1H1$^{+/D338N}$ fibroblasts ($P = 0.6604$) and BICD2$^{+/I189F}$ fibroblasts ($P = 0.2154$). N = 3 for all genotypes. β-actin was used as the loading control for all experiments and the normalised data is presented relative to the wild type samples. Errors bars represent SEM. Note: some of repeats of the acetylated tubulin experiment used in the quantification were performed by a Masters student under my supervision (Zuzana Sedlakova). (** $P < 0.01$)

5.2.4 Reduced tubulin acetylation is a feature of the *Loa* mouse model of SMA-LED

DYNC1H1$^{+/D338N}$ fibroblasts exhibited a similar decrease in tubulin acetylation as that previously observed in the Hafezparast lab in DYNC1H1^{R399G} mutants. This potentially indicates that reduced tubulin acetylation may be a common consequence of defective dynein function caused by *DYNC1H1* mutations. To further investigate this, MEFs from the *Loa* mouse model were tested via western blot analysis for the levels of acetylated tubulin.

Figure 5.4a represents 3 repeats (of a total of 6) which all show a decrease in the levels of acetylated tubulin in *Loa* homozygous MEFs in comparison to wild type MEFs. To quantify this difference, densitometric analysis and a one sample t-test was performed, which confirmed a significant reduction in the levels of acetylated tubulin in *Loa* homozygous MEFs in comparison to wild type MEFs (*P = 0.0210*), as shown in Figure 5.4b. Furthermore, α-tubulin levels were analysed using western blot analysis, see Figure 5.4c. As shown in Figure 5.4d, densitometric quantification and a one sample t-test were performed, which showed no significant difference between genotypes (P = 0.6337, N = 3).

In summary, the *Loa* mutation is the third *DYNC1H1* mutation shown to cause reduced tubulin acetylation which may point to a common phenotype.

Figure 5.4

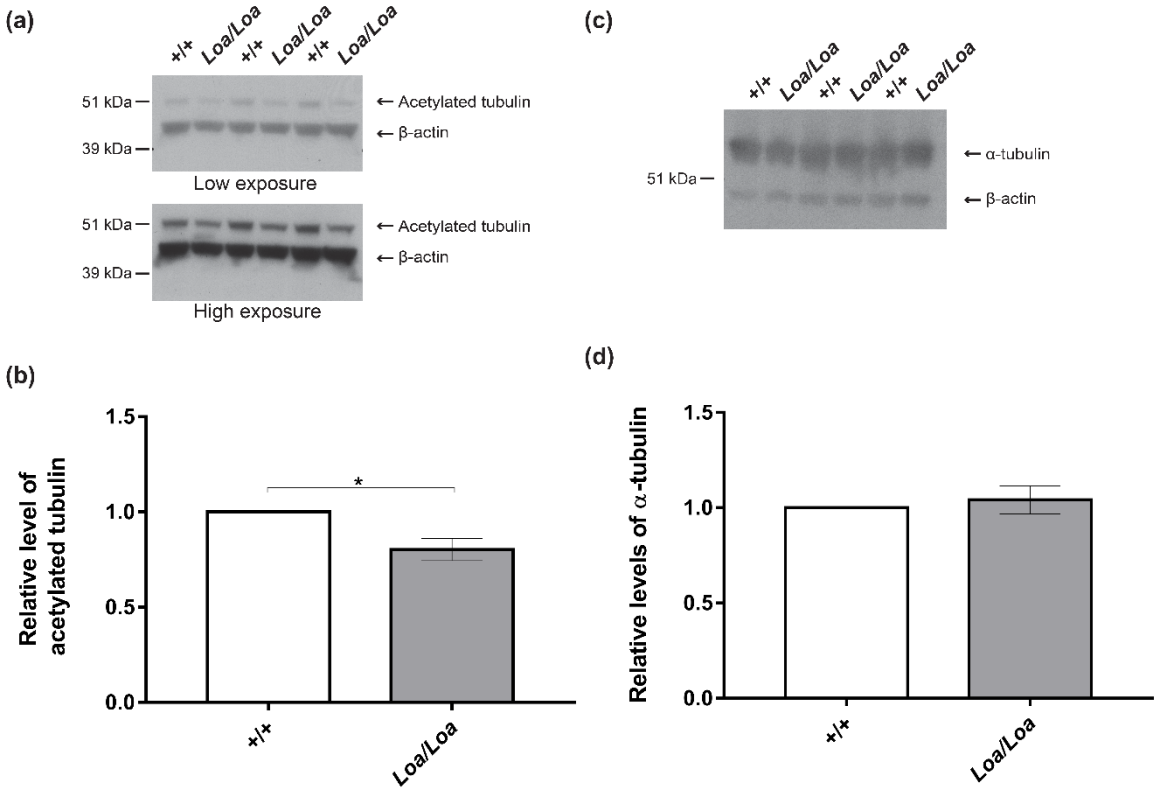

Figure 5.4 (a) Western blot analysis of tubulin acetylation in wild type and *Loa* homozygous MEFs. There is a consistent decrease in the amount of acetylated tubulin visible in *Loa* homozygous MEFs in comparison to wild type MEFs **(b)** Graph showing the densitometric quantification of acetylated tubulin levels in wild type and *Loa* homozygous MEFs. A one sample t-test showed a significant reduction in the amount of acetylated tubulin in *Loa* homozygous MEFs (*P = 0.0210*, N= 6). **(c)** Western blot analysis of α-tubulin in wild type and *Loa* homozygous MEFs. **(d)** Densitometric quantification of α-tubulin showing no significant difference between genotypes as indicated by a one sample t-test (P = 0.6337, N = 3). β-actin was used as the loading control for all experiments and the normalised data is presented relative to the wild type samples. Note: some of repeats of the acetylated tubulin experiment used in the quantification were performed by a Masters student under my supervision (Zuzana Sedlakova). Errors bars represent SEM. (* *P < 0.05)*

5.2.5 Analysis of detyrosination of tubulin in DYNC1H1$^{+/D338N}$ and BICD2$^{+/I189F}$ fibroblasts

The finding of reduced levels of tubulin acetylation in DYNC1H1$^{+/D338N}$ fibroblasts indicated a potential reduction in microtubule stability. To verify this, the levels of detyrosinated tubulin, which is also highly enriched at the Golgi was checked by western blot analysis (Skoufias et al., 1990). This analysis was performed in wild type, DYNC1H1$^{+/D338N}$ and BICD2$^{+/I189F}$ fibroblasts. Additionally, DYNC1H1$^{R399G/R399G}$ fibroblasts were also tested as they are known to exhibit decreased tubulin acetylation.

The results show that there was no detectable alteration in the levels of detyrosinated tubulin in DYNC1H1$^{+/D338N}$ or BICD2$^{+/I189F}$ fibroblasts in comparison to wild type cells, as shown in Figure 5.5a and b respectively. Similarly, DYNC1H1$^{R399G/R399G}$ fibroblasts also did not show an observable difference in detyrosinated tubulin, as shown in Figure 5.5c.

Densitometric analysis was performed to quantify the levels of detyrosinated tubulin. A one sample t-test was performed which showed no significant difference between both DYNC1H1$^{+/D338N}$ (*P = 0.4228*) and DYNC1H1$^{R399G/R399G}$ (*P = 0.2802*) fibroblasts when compared to wild type fibroblasts (Figure 5.5d). Similarly, a one sample t-test showed no significant changes in detyrosinated tubulin in BICD2$^{+/I189F}$ (*P = 0.6939*; Figure 5.5d).

In summary, unlike levels of acetylated tubulin, there was no significant change in the levels of detyrosinated tubulin (another maker of microtubule stability) in any of the *DYNC1H1* mutants tested and in the BICD2$^{+/I189F}$ fibroblasts.

Figure 5.5

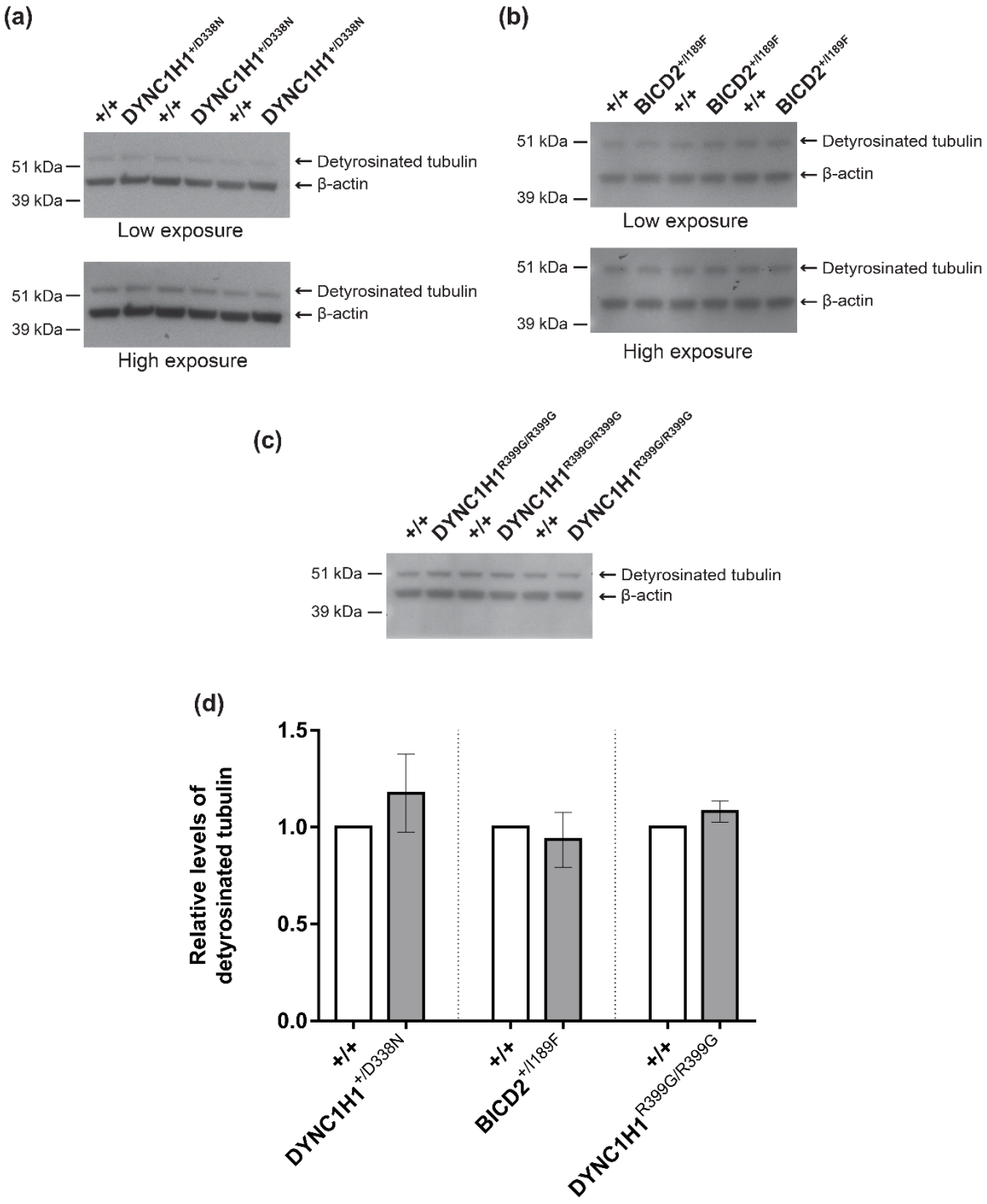
(a)
+/+
DYNC1H1+/D338N
+/+
DYNC1H1+/D338N
+/+
DYNC1H1+/D338N
51 kDa
39 kDa
← Detyrosinated tubulin
← β-actin
Low exposure
51 kDa
39 kDa
← Detyrosinated tubulin
← β-actin
High exposure
(b)
+/+
BICD2+/I189F
+/+
BICD2+/I189F
+/+
BICD2+/I189F
51 kDa
39 kDa
← Detyrosinated tubulin
← β-actin
Low exposure
51 kDa
39 kDa
← Detyrosinated tubulin
← β-actin
High exposure
(c)
+/+
DYNC1H1R399G/R399G
+/+
DYNC1H1R399G/R399G
+/+
DYNC1H1R399G/R399G
51 kDa
39 kDa
← Detyrosinated tubulin
← β-actin
(d)
Relative levels of detyrosinated tubulin
1.5
1.0
0.5
0.0
+/+
DYNC1H1+/D338N
+/+
BICD2+/I189F
+/+
DYNC1H1R399G/R399G

Figure 5.5 (a-c) Western blot analysis comparing detyrosinated tubulin in wild type fibroblasts to DYNC1H1$^{+/D338N}$, BICD2$^{+/I189F}$ and DYNC1H1$^{R399G/R399G}$ fibroblasts, respectively. There is no observable difference in the levels of detyrosinated tubulin in any of the genotypes. **(d)** Graph of the quantification of detyrosinated tubulin levels. A one sample t-test showed no significant difference in detyrosinated tubulin in DYNC1H1$^{+/D338N}$ (*P = 0.4228*, N = 6) and DYNC1H1$^{R399G/R399G}$ fibroblasts (*P = 0.2802*, N = 3). Additionally, a one sample t-test confirmed no significant difference between wild type and BICD2$^{+/I189F}$ fibroblasts (*P = 0.6939*, N = 3). β-actin was used as the loading control for all experiments and the normalised data is presented relative to the wild type samples. Note: some of repeats of the detyrosinated tubulin experiments for DYNC1H1$^{+/D338N}$ and BICD2$^{+/I189F}$ fibroblasts used in the quantification were performed by a Masters student under my supervision (Zuzana Sedlakova). Errors bars represent SEM.

5.2.6 Analysis of acetylated tubulin following HC knockdown

To further investigate the role of dynein in the regulation of microtubule acetylation, a system which allows for the knockdown of the HC of dynein using auxin-inducible degron (AID) technology was tested. The addition of the phytohormone auxin to culture media in cells expressing the F-box transport inhibitor response 1 (TIR1) protein derived from *Oryza sativa* (Os-TIR1) results in the rapid knockdown of the AID tagged protein of interest (Natsume et al., 2016). Os-TIR1 forms a SCF (Skp1-Cullin-F-box) ubiquitin ligase complex which targets the AID tag in the presence of auxin and leads to polyubiquitination of the protein of interest and rapid degradation by the proteasome. The system used here consists of human colorectal cancer HCT116 cells which have tetracycline inducible Os-TIR1 (tet-OsTIR1) and the AID cassette inserted after the last codon of DYNC1H1 (Natsume et al., 2016). Therefore, in the presence of both doxycycline (induce Os-TIR1 expression) and auxin, there is predicted to be rapid depletion of the HC of dynein.

Cells plated in 6 well plates were treated with 500 µM of indole-3-acetic-acid (a natural auxin) and 2 µg/mL of doxycycline for 4 hours, 8 hours and 24 hours. Western blot analysis was then used to ascertain if there was a knockdown of the HC (Figure 5.6a). There was an appreciable decrease in the HC which correlated with increased incubation with the drugs in comparison to the untreated control. Densitometric quantification also showed a trend of HC depletion with increasing incubation time (Figure 5.6b). However, this trend was not statistically significant as calculated using a one-way ANOVA ($P = 0.2969$, $N = 3$). Despite this, as every repeat at every time point showed a decrease in HC, the amount of acetylated tubulin was checked at each time point via western blot analysis (Figure 5.6c). Densitometric analysis and a one-way ANOVA was performed which indicated a significant difference between samples ($P = 0.003$, $N = 3$). Tukey's multiple comparison test showed a statistically significant increase between the Auxin control and the 4 hour ($P = 0.0039$) and 8 hour time points ($P = 0.0049$), as shown in Figure 5.6d. However, it is surprising that no increase was seen in acetylated tubulin at 24 hours as this represents the point with the least amount of dynein. The significance at the 4 and 8 hour time points likely arose due to an apparent decrease in acetylated tubulin in the auxin control.

Finally, a western blot for α-tubulin was performed to ensure that any changes in acetylated tubulin were not a reflection of changes in total tubulin (Figure 5.6e). Densitometric quantification and subsequent statistical analysis using a one-way ANOVA confirmed no significant difference between any of the samples ($P = 0.617$, $N = 3$).

Overall, the system used here has not produced conclusive data and requires further optimisation.

Figure 5.6

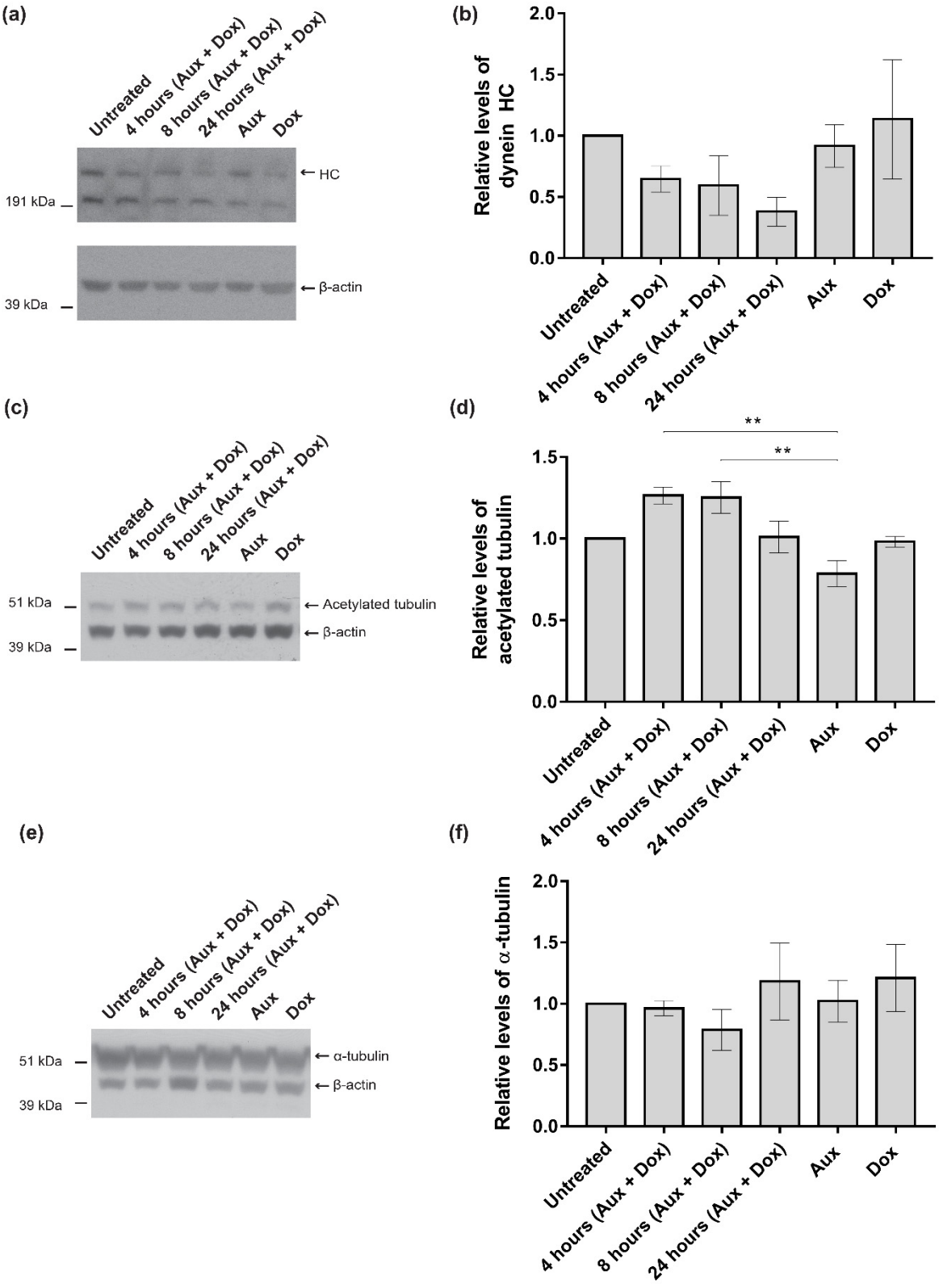
(a)
Untreated
4 hours (Aux + Dox)
8 hours (Aux + Dox)
24 hours (Aux + Dox)
Aux
Dox
191 kDa
← HC
39 kDa
← β-actin
(b)
Relative levels of dynein HC
2.0
1.5
1.0
0.5
0.0
Untreated
4 hours (Aux + Dox)
8 hours (Aux + Dox)
24 hours (Aux + Dox)
Aux
Dox
(c)
Untreated
4 hours (Aux + Dox)
8 hours (Aux + Dox)
24 hours (Aux + Dox)
Aux
Dox
51 kDa
39 kDa
← Acetylated tubulin
← β-actin
(d)
**
**
Relative levels of acetylated tubulin
1.5
1.0
0.5
0.0
Untreated
4 hours (Aux + Dox)
8 hours (Aux + Dox)
24 hours (Aux + Dox)
Aux
Dox
(e)
Untreated
4 hours (Aux + Dox)
8 hours (Aux + Dox)
24 hours (Aux + Dox)
Aux
Dox
51 kDa
39 kDa
← α-tubulin
← β-actin
(f)
Relative levels of α-tubulin
2.0
1.5
1.0
0.5
0.0
Untreated
4 hours (Aux + Dox)
8 hours (Aux + Dox)
24 hours (Aux + Dox)
Aux
Dox

Figure 5.6 (a) Western blot analysis of HC levels following the activation of the degron system in HCT116 cells using 500 μM of indole-3-acetic-acid (Aux) and 2 μg/mL of doxycycline (Dox). **(b)** Densitometric quantification of HC knockdown showing no statistically significant difference in the levels of HC between samples (one-way ANOVA, $P = 0.2969$, N= 3). **(c)** Western blot analysis of the levels of acetylated tubulin following HC knockdown. **(d)** Densitometric quantification of acetylated tubulin which showed a significant difference in the levels of acetylated tubulin between samples (one-way ANOVA, $P = 0.003$, N=3). Tukey's multiple comparison test showed a significant increase in acetylated tubulin at the 4 hour ($P = 0.0039$) and 8 hour ($P = 0.0049$) time points in comparison to the auxin control. **(e)** Western blot analysis of α-tubulin levels following HC knockdown. **(f)** Densitometric quantification of α-tubulin levels showing no significant difference between samples (one-way ANOVA, $P = 0.617$, N= 3). β-actin was used as the loading control for all experiments and the normalised data is presented relative to the wild type samples. Errors bars represent SEM. (** $P < 0.01$)

5.2.7 Analysis of paxillin in DYNC1H1$^{+/D338N}$ and BICD2$^{+/I189F}$ fibroblasts

It has been reported that the focal adhesion (FA) protein paxillin exerts an inhibitory effect on the major microtubule deacetylase enzyme, HDAC6 (Deakin and Turner, 2014). Importantly, evidence suggested that this enables paxillin to regulate the integrity of the Golgi. Interestingly, reduced paxillin phosphorylation has been noted previously in both DYNC1H1^{R399G} mutant fibroblasts (by Dr Muruj Barri in the Hafezparast lab) and in this thesis a decrease in total paxillin levels in *Loa* MEFs is reported. Therefore, to investigate whether alterations in paxillin could underlie the observed changes in microtubule acetylation in DYNC1H1$^{+/D338N}$ fibroblasts, these cells were checked for the levels of paxillin phosphorylation at Tyr188 (pPax^{Y118}) and total paxillin levels. BICD2$^{+/I189F}$ fibroblasts were also included in this analysis.

Western blot analysis showed that there was no appreciable difference in the levels of pPax^{Y118} between wild type fibroblasts and both DYNC1H1$^{+/D338N}$ and BICD2$^{+/I189F}$ fibroblasts (Figure 5.7a). Subsequently, densitometric analysis and one sample t-tests were performed which showed no significant difference between wild type fibroblasts and both DYNC1H1$^{+/D338N}$ (*P = 0.9468,* N = 6) and BICD2$^{+/I189F}$ (*P = 0.8823,* N = 3) fibroblasts. Surprisingly, analysis of the levels of total paxillin indicated an increase in both DYNC1H1$^{+/D338N}$ and BICD2$^{+/I189F}$ fibroblasts in comparison to wild type fibroblasts (Figure 5.7c). Densitometric analysis and one sample t-tests failed to show a significant increase in total paxillin in DYNC1H1$^{+/D338N}$ (*P = 0.0854*). However, the analysis did show a significant increase in BICD2$^{+/I189F}$ (*P = 0.0166*) fibroblasts in comparison to wild type fibroblasts. Unfortunately, unlike previous paxillin data the total paxillin western blot analysis was not performed using the same homogenates as those used for analysis of pPax^{Y118}, which precludes the possibility of looking at the ratio of pPax^{Y118} to total paxillin accurately.

In summary, no difference in pPax^{Y118} was found and thus it cannot underlie the reduced tubulin acetylation noted in the DYNC1H1$^{+/D338N}$ fibroblasts. However, there was a significant increase in total paxillin in the BICD2$^{+/I189F}$ fibroblasts.

Figure 5.7

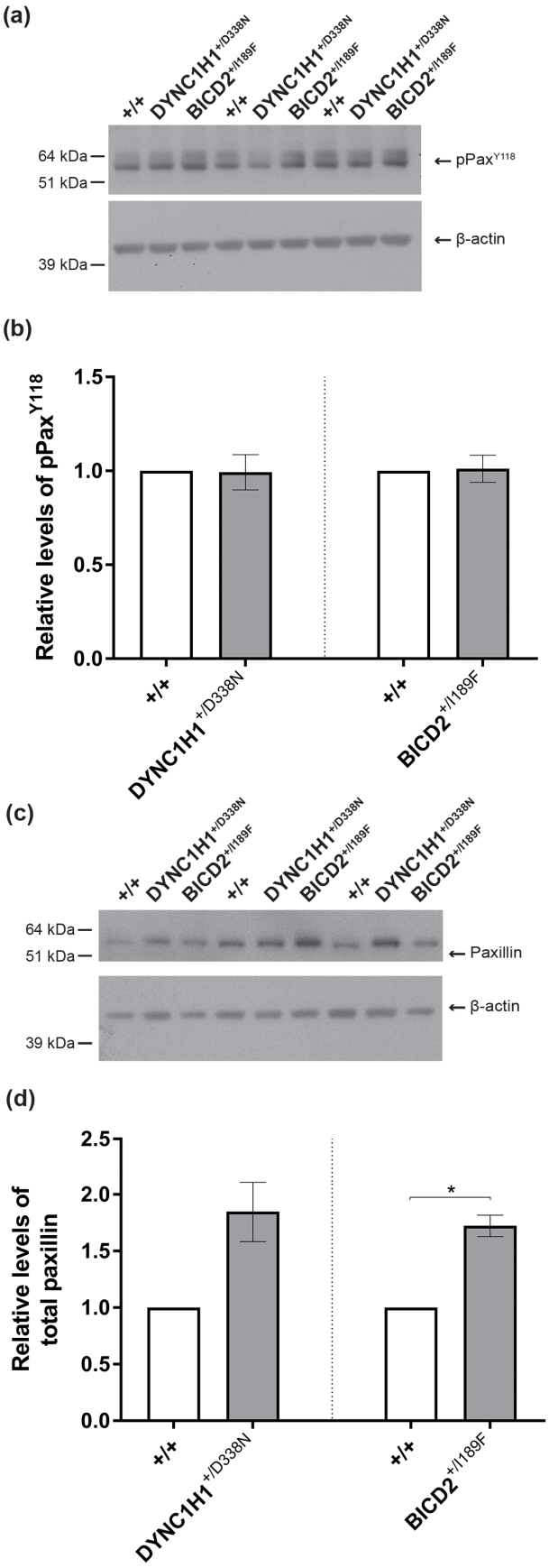
(a)
+/+
DYNC1H1+/D338N
BICD2+/I189F
64 kDa
51 kDa
39 kDa
← pPaxY118
← β-actin
(b)
Relative levels of pPaxY118
1.5
1.0
0.5
0.0
+/+
DYNC1H1+/D338N
+/+
BICD2+/I189F
(c)
← Paxillin
(d)
Relative levels of total paxillin
2.5
2.0
1.5
1.0
0.5
0.0
*

Figure 5.7 (a) Western blot analysis of pPax^{y118} in DYNC1H1$^{+/D338N}$ and BICD2$^{+/I189F}$ fibroblasts in comparison to wild type cells. There is no observable difference in the levels of pPax^{Y118} between genotypes. **(b)** Graph of the quantification of pPax^{Y118} levels. One sample t-tests confirmed that there was no significant difference between wild type fibroblasts and both DYNC1H1$^{+/D338N}$ (*P = 0.9468,* N = 6) and BICD2$^{+/I189F}$ (*P = 0.8823,* N = 3) fibroblasts. **(c)** Western blot of total paxillin in DYNC1H1$^{+/D338N}$, BICD2$^{+/I189F}$ and wild type fibroblasts. An increase in total paxillin is apparent in the mutant fibroblasts. **(d)** Densitometric quantification of total paxillin in DYNC1H1$^{+/D338N}$, BICD2$^{+/I189F}$ and wild type fibroblasts. One sample t-tests showed no significant difference between wild type and DYNC1H1$^{+/D338N}$ (*P = 0.*0854, N = 3) fibroblasts but there was a significant increase in BICD2$^{+/I189F}$ fibroblasts (*0.0166*, N = 3). β-actin was used as the loading control for all experiments and the normalised data is presented relative to the wild type samples. Note: some of repeats of the pPax^{y118} experiment used in the quantification were performed by a Masters student under my supervision (Zuzana Sedlakova). Errors bars represent SEM. (** P < 0.05)*

5.2.8 Chapter 5 summary

In this chapter, it was shown that unlike previous *DYNC1H1* mutations investigated in the Hafezparast lab, there is no inherent Golgi fragmentation evident in the DYNC1H1$^{+/D338N}$ patient fibroblasts. Similarly, there was also no Golgi fragmentation in BICD2$^{+/I189F}$ fibroblasts. However, further examination did reveal the presence of other Golgi phenotypes. Both DYNC1H1$^{+/D338N}$ and BICD2$^{+/I189F}$ fibroblasts showed a significant reduction in the area of the Golgi, a phenotype which was more pronounced in the former in comparison to the latter. In line with this, only DYNC1H1$^{+/D338N}$ fibroblasts had a significantly condensed Golgi as measured by the area of the space between Golgi membranes. Therefore, these data further support the hypothesis that *DYNC1H1* mutations affect dynein's function in the formation and maintenance of an organised Golgi organelle.

To explain the cause of these Golgi phenotypes, the localisation of dynein at the Golgi and the levels of microtubule acetylation was explored. Uniquely between these two mutants, only the BICD2$^{+/I189F}$ fibroblasts had a reduction in the level of dynein IC localised at the Golgi. Conversely, only DYNC1H1$^{+/D338N}$ mutants exhibited a decrease in the levels of microtubule acetylation. This illustrates different pathogenic mechanisms between these two mutants which converge at the Golgi with equally differing presentations. Interestingly, *Loa* homozygous fibroblasts also showed a decrease in the level of microtubule acetylation, thus making it the third *DYNC1H1* mutation to cause this phenotype. This potentially indicates a unifying phenotype in SMA-LED caused by *DYNC1H1* mutations. Furthermore, no difference was found in detyrosinated tubulin between DYNC1H1$^{+/D338N}$, DYNC1H1$^{+/D338N}$ and BICD2$^{+/I189F}$ fibroblasts in comparison to wild type fibroblasts. Unfortunately, HC knockdown by using an auxin inducible degron in HCT116 cells did not provide conclusive data. Furthermore, no difference was observed in the levels of pPax^{Y118} indicating that it does not underlie the previously observed microtubule acetylation phenotype. However, an increase in total paxillin levels was observed in both DYNC1H1$^{+/D338N}$ and BICD2$^{+/I189F}$ fibroblasts but only reached statistical significance in the latter. A summary of the results obtained from these experiments is shown in Table 5.1.

Table 5.1

	Golgi fragmentation	Golgi area	Are between Golgi membranes	IC localisation at the Golgi	Microtubule acetylation	Microtubule detyrosination	pPax^{Y118}	Total paxillin
DYNC1H1$^{+/D338N}$	No	Reduced****	Reduced**	No change	Reduced**	No change	No change	Increase
BICD2$^{+/I189F}$	No	Reduced*	No change	Reduced¥	No change	No change	No change	Increase*
DYNC1H1$^{R399G/R399G}$	Yes			Reduced	Reduced	No change	Decrease	

Table 5.1 Summary of the data acquired in this thesis on Golgi pathology, microtubule modifications and paxillin in both DYNC1H1$^{+/D338N}$ and BICD2$^{+/I189F}$ fibroblasts in comparison to wild type fibroblasts. Additionally, this is contrasted to previous data which data obtained in the Hafezparast lab for the DYNC1H1$^{R399G/R399G}$ fibroblast line. ¥ Localisation of the IC to the Golgi was assessed using two different metrics with both being significantly reduced in BICD2$^{+/I189F}$ fibroblasts. * denotes a significant change (* *P* < 0.05, ** *P* < 0.01, **** *P* < 0.0001).

5.3 Discussion

5.3.1 Golgi morphology and integrity in DYNC1H1$^{+/D338N}$ and BICD2$^{+/I189F}$ fibroblasts

Dynein is pivotal for the formation, positioning, and maintenance of the Golgi ribbon (Lowe, 2011). Therefore, it is not surprising that Golgi pathology is observed in association with SMA-LED caused by *DYNC1H1* mutations and in the *Loa* mouse model of the disease (Fiorillo et al., 2014; Hafezparast et al., 2003). Most strikingly, inherent Golgi fragmentation was recently observed in DYNC1H1^{R399G} SMA-LED patient fibroblasts in the Hafezparast lab. Similarly, inherent Golgi fragmentation has also been reported in *BICD2* mutant patient primary fibroblasts and myocytes (Neveling et al., 2013; Unger et al., 2016).

To further investigate Golgi pathology in SMA-LED, Golgi morphology and integrity in DYNC1H1$^{+/D338N}$ and BICD2$^{+/I189F}$ patient fibroblasts was assessed using fixed cell imaging and high-throughput analysis. This analysis revealed that Golgi fragmentation was not present in either patient line. The lack of fragmentation in BICD2$^{+/I189F}$ fibroblasts is particularly interesting as the phenotype had been previously observed in fibroblasts with a heterozygous asparagine to threonine substitution one residue away at position 188 (p.N188T) (Neveling et al., 2013). Similarly, both the p.D338N and p.R399G DYNC1H1 substitutions are in relatively close proximity within the tail domain of the DYNC1H1 protein (Scoto et al., 2015).

However, further analysis revealed that the Golgi area was reduced in both DYNC1H1$^{+/D338N}$ and BICD2$^{+/I189F}$ fibroblasts in comparison to wild type cells. Additionally, the Golgi in DYNC1H1$^{+/D338N}$ fibroblasts appeared to be particularly condensed into a smaller area without the same level of elaboration of the Golgi ribbon seen in wild type and BICD2$^{+/I189F}$ fibroblasts. Analysis of the area of the gaps between the Golgi membranes confirmed a condensation of the Golgi in the DYNC1H1$^{+/D338N}$ fibroblasts. Importantly, these changes could have been explained by differences in cellular morphology between genotypes. However, a qualitative analysis of the images taken to assess Golgi morphology identified no major differences in morphology between wild type and DYNC1H1$^{+/D338N}$ fibroblasts. This suggests that these mutations are indeed having a detrimental effect on Golgi morphology despite the lack of Golgi fragmentation. Further supporting this is the fact that despite the images taken for analysis of BICD2$^{+/I189F}$

Golgi morphology indicating that the cells were more confluent and consequently more compact. The Golgi condensation phenotype was not present in these cells. However, this observation could explain the reduced Golgi area in the BICD2$^{+/I189F}$ patient fibroblasts.

Similar condensation of the Golgi has previously been observed in cells where a dominant negative mutant of AKAP450 is expressed or in AKAP450 knockout cells (Hurtado et al., 2011; Wu et al., 2016). AKAP450 is recruited to the Golgi by GM130 and is itself pivotal for the recruitment of γ-TurRC to the Golgi for the nucleation of Golgi-derived microtubules (Rivero et al., 2009; Hurtado et al., 2011). In fact, the expression of the dominant negative mutant of AKAP450 inhibits microtubule nucleation at the Golgi (Hurtado et al., 2011). It is important to note that in some of the experiments where the Golgi-derived microtubule network is inhibited, the condensation of the Golgi at the centrosome is accompanied by fragmentation (Miller et al., 2009; Hurtado et al., 2011; Wu et al., 2016). However, this fragmentation was not seen in DYNC1H1$^{+/D338N}$ fibroblasts. This difference may be due to the severity of completely removing the Golgi microtubule network in these experiments in comparison to the milder consequence of the p.D338N mutation on this network.

Importantly, the p150^{Glued} subunit of the essential dynein adaptor dynactin, is known to interact with AKAP450 (Kim et al., 2007). Additionally, dynactin has been shown to be required for microtubule nucleation at the Golgi (Rivero et al., 2009). Therefore, this implicates dynein in the nucleation of microtubules at the Golgi, a function which could be impaired by p.D338N substitution in DYNC1H1 and could therefore result in a similarly condensed Golgi.

Further supporting the hypothesis that the compact Golgi morphology observed in DYNC1H1$^{+/D338N}$ fibroblasts could be attributed to defects in the Golgi associated microtubule network, is the finding that the knockout of end-binding proteins (EB1, EB2 and EB3) results in detachment of microtubules from the Golgi and consequently a more compact organelle (Yang et al., 2017). Specifically, it was found the EB proteins are able to tether microtubules to the Golgi directly, via their interaction with myomegalin (MMG) on Golgi membranes. Note that MMG is recruited to the Golgi by AKAP450 with which it forms a complex (Roubin et al.,

2013). Secondly, it was also able to affect the length of microtubule minus ends decorated with calmodulin-regulated spectrin-associated protein 2 (CAMSAP2), a protein known to be important for the tethering of microtubules to the Golgi through its interaction with MMG (Yang et al., 2017). Therefore, it is possible that the compaction of the Golgi seen in DYNC1H1$^{+/D338N}$ fibroblasts is due to an aberrant Golgi associated microtubule network. Other examples of in which molecular motors impact the size of the Golgi have been noted, such as the reduction in Golgi mass seen in immortalized fibroblasts from Snell's waltzer mice in which myosin VI is absent (Warner et al., 2003).

Finally, the reason for the discrepancy in phenotypes between the p.D338N and p.R399G DYNC1H1 mutants is unclear. Interestingly, condensation of the Golgi was also observed in DYNC1H1$^{R399G/R399G}$ fibroblasts whilst undergoing a re-orientation assay (performed in the Hafezparast lab by Dr Ryan Green). Therefore, the p.R399G cells do display a similar phenotype but this appears to be compounded by a further factor in normal resting conditions causing the Golgi to appear dispersed and fragmented.

5.3.2 IC at the Golgi is reduced in BICD2$^{+/I189F}$ but not in DYNC1H1$^{+/D338N}$ fibroblasts

In the Hafezparast lab, DYCN1H1^{R399G} fibroblasts were also observed to have a significantly reduced level of dynein present at the Golgi. To investigate whether a similar phenotype is present in DYNC1H1$^{+/D338N}$ fibroblasts and could therefore be a factor in the condensation of the Golgi seen in these cells, fixed cell analysis and high-throughput quantification was performed. Additionally, BICD2$^{+/I189F}$ fibroblasts were also analysed as the p.I189F substitution resides within the dynein IC chain binding domain of BICD2 and could impair any potential recruitment of dynein to the Golgi by BICD2 (Oates et al., 2013).

Analysis showed that in BICD2$^{+/I189F}$ cells, there was a significant reduction in the levels of the IC at the Golgi. This indicates that there is reduced recruitment of dynein to the Golgi caused by alterations in the interaction between the p.I189F mutant BICD2 and the dynein IC. Furthermore, Z-stacks were taken which qualitatively appeared to confirm the quantifications made on the single images taken at the Golgi focal plane. However, since it is not possible to definitively

assess whether dynein is absent or present on the Golgi via immunofluorescent imaging alone, further verification is required. Firstly, Golgi pull-down assays using magnetic beads and an anti-giantin antibody can be carried out to assess the level of IC that is co-precipitated with the organelle membranes, a method previously described by Yadav *et al.*, 2012. Furthermore, immunoprecipitation studies to investigate the nature of the IC interaction with BICD2^{I189F} should be carried out.

Interestingly, if verification confirms a reduction in the levels of IC at the Golgi in BICD2$^{+/I189F}$ fibroblasts, it is of note that previous studies have shown that the pathogenic p.S107L and p.R501P substitutions alter the interaction between IC and BICD2 (Peeters et al., 2013; Oates et al., 2013). Moreover, in the Hafezparast lab, an increased interaction between IC and golgin160, which is the only known adaptor shown to recruit dynein to the Golgi, is seen in DYNC1H1$^{R399G/R399G}$ fibroblasts (Yadav et al., 2012). This increase in IC-golgin160 interaction is despite a loss of dynein at the Golgi, thereby suggesting the existence of other adaptors responsible for the recruitment of dynein, which data presented here indicates could include BICD2.

Interestingly, the DYNC1H1$^{+/D338N}$ fibroblasts did not appear to have any decrease in IC at the Golgi. This difference between the DYNC1H1$^{+/D338N}$ and DYNC1H1$^{R399G/R399G}$ fibroblasts may underlie the differing Golgi phenotypes. Previously, inhibition of dynein by the overexpression of p50/dynamin or the CC1 domain of p150^{Glued} halted both the clustering of the Golgi stacks mediated by Golgi-derived microtubules and the movement of the Golgi stacks towards the centrosome, which is dependent on centrosomal microtubules (Miller et al., 2009). It is possible that the p.D338N mutation allows for the centripetal movement of the membranes to the centrosome, whilst detrimentally affecting the Golgi-derived microtubule network. This would not only affect the clustering of the Golgi stacks at the periphery but also the ribbon formation and morphology once at the centrosome, both of which are dependent on Golgi-derived microtubules (Miller et al., 2009; Yang et al., 2017). Consequently, this could result in a correctly positioned but condensed Golgi as observed in these cells. On the other hand, the p.R399G mutation experiences a more severe impact of dynein function at the Golgi, where not only may the clustering and ribbon formation be affected but the centripetal movement may also be lost. Therefore, the result would be a dispersed

Golgi away from its typical localisation at the centrosome. This could be studied using similar methods as Miller et al 2009, where nocodazole washout in combination with microscopy could be used to assess the centripetal movement of Golgi membranes in DYNC1H1$^{+/D338N}$ and DYNC1H1$^{R399G/R399G}$ fibroblasts, and the nucleation of microtubules at the Golgi membranes.

5.3.3 Reduced microtubule acetylation in DYNC1H1$^{+/D338N}$ fibroblasts is not accompanied by reduced microtubule detyrosination

Golgi-derived microtubules are particularly enriched in post-translational modifications such as acetylation at Lys40 and detyrosination (Thyberg and Moskalewski, 1993; Skoufias et al., 1990). Interestingly, Dr Ryan Green in the Hafezparast lab previously showed a decrease in microtubule acetylation in DYNC1H1$^{R399G/R399G}$ fibroblasts. This could indicate that the Golgi-derived microtubule network is less stable as acetylation is commonly seen as a marker of stability (Sadoul and Khochbin, 2016).

Therefore, the levels of acetylated tubulin were assessed in both DYNC1H1$^{+/D338N}$ and BICD2$^{+/I189F}$ fibroblasts as they could indicate alterations in the properties of Golgi-derived microtubules which are crucial for the formation of the Golgi ribbon (Miller et al., 2009). Western blot analysis showed a significant reduction in the levels of acetylated tubulin in DYNC1H1$^{+/D338N}$ but not in BICD2$^{+/I189F}$ fibroblasts. Importantly, the levels of total tubulin remained unaffected in DYNC1H1$^{+/D338N}$ fibroblasts, confirming that the reduction in acetylation was not merely a reflection of a decrease in total tubulin content. These initial results indicate that there is a change in the properties of microtubules at the Golgi which could underlie the condensation phenotype observed in DYNC1H1$^{+/D338N}$ fibroblasts. To further explore this, a second marker of microtubule stability was checked.

Detyrosinated tubulin is also highly enriched at the Golgi and is known to be enriched in stable, long lived microtubules (Skoufias et al., 1990; Song and Brady, 2015). Therefore, the levels of detyrosinated tubulin were assessed in DYNC1H1$^{+/D338N}$, BICD2$^{+/I189F}$ and DYNC1H1$^{R399G/R399G}$ fibroblasts. Detyrosinated tubulin showed no significant deficit in any of these three cell lines, indicating that the reduction in acetylation is not likely a consequence of reduced stability but perhaps a specific effect of dynein impairment. However, to confirm this,

microtubule stability would have to be directly assessed by observing microtubule dynamics. This could be achieved using EB1 tagged with mcherry and u-track, a software package to measure microtubule dynamics (Applegate et al., 2011). This method has previously been employed in the Hafezparast lab (Barri, 2015).

Interestingly, the opposite pattern is seen when Ciliobrevin D is used to inhibit dynein ATPase activity in chicken DRG neurons (Sainath and Gallo, 2014). This causes a reduction in tyrosinated tubulin indicating increased stability, concomitantly with reduced levels of tubulin acetylation which would seemingly indicate reduced stability. Therefore, alterations in dynein activity can have specific and contrasting effects on these post-translational modifications.

There is strong evidence that the acetylation state of microtubules is crucial to maintaining normal Golgi morphology. The expression of non-acetylatable tubulin results in fragmentation of the Golgi apparatus (Deakin and Turner, 2014). Similarly, the reduction of tubulin acetylation caused by paxillin depletion also results in a fragmented Golgi. However, while Golgi fragmentation is seen in DYNC1H1^{R399G} fibroblasts, this is not a feature of DYNC1H1$^{+/D338N}$ cells despite sharing a reduction in tubulin acetylation. This indicates that a reduction in acetylated tubulin is not sufficient to induce complete Golgi fragmentation in these patient fibroblasts in contrast to what was seen in the aforementioned studies. Interestingly, the expression of a dynamin 2 mutant associated with CMT causes an increase in microtubule acetylation and concomitantly induces Golgi fragmentation (Tanabe and Takei, 2009). It may be that in the DYNC1H1^{R399G} fibroblasts, the reduction in acetylation is compounded with the reduced dynein at the Golgi to cause fragmentation. On the other hand, in DYNC1H1$^{+/D338N}$ fibroblasts the reduced acetylation impairs the Golgi-derived network, which impairs normal Golgi ribbon formation causing a condensed Golgi phenotype. In support of this, the reduced dynein at the Golgi seen in BICD2$^{+/I189F}$ fibroblasts does not cause fragmentation as might be expected, it may be that since acetylation levels are normal within these cells, there is no second factor to induce Golgi fragmentation.

Alternatively, as previously mentioned the compaction of the Golgi in DYNC1H1$^{+/D338N}$ fibroblasts may indicate a similar impairment of Golgi associated

microtubules as that seen in cells in which either have EB proteins or proteins associated with microtubule nucleation at the Golgi are knocked out (Hurtado et al., 2011; Wu et al., 2016; Yang et al., 2017). Therefore, a reduction in microtubule association may be a consequence of such an impairment rather the cause.

Previously, it has been shown that HDAC6, the primary deacetylase for Lys40 (Sadoul and Khochbin, 2016), interacts with the $p150^{Glued}$ subunit of dynactin in the context of aggresome formation (Kawaguchi et al., 2003). It is unclear if this interaction may allow dynein to affect the deacetylation of microtubules. However, preliminary data from the Hafezparast lab gathered by Dr Ryan Green suggested that there may be increased deacetylation in $DYNC1H1^{R399G/R399G}$ fibroblasts using a HDAC6 inhibitor washout experiment. These experiments should be repeated in the $DYNC1H1^{+/D338N}$ fibroblasts to ascertain if there is a similar effect.

Interestingly, acetylated tubulin was also shown here to be decreased in *Loa/Loa* MEFs in comparison to wild type MEFs, thereby becoming the third *DYNC1H1* mutation known to cause reduced acetylated tubulin. Again, this change was not caused by changes in the levels of total tubulin as these levels were comparable to wild type levels. This implies that reduced tubulin acetylation is a common phenotype shared by *DYNC1H1* mutations. As all the mutations tested thus far are within tail domain of the HC it would be interesting to test the effect of mutations outside of this region to determine the involvement of other HC regions in regulating acetylation.

5.3.4 Microtubule acetylation following HC knockdown using the Auxin-inducible degron system

To further investigate the role of dynein in the regulation of microtubule acetylation a system where the HC of dynein could be easily knocked down was used. As discussed previously, this system employed the use of auxin-inducible degron (AID) technology (Natsume et al., 2016).

Here, HTC116 cells were treated with 500 μM of indole-3-acetic-acid (a natural auxin) and 2 μg/mL of doxycycline for 4 hours, 8 hours and 24 hours. After these periods cells were lysed and analysed by western blotting for levels of HC, acetylated tubulin and total tubulin. Firstly, despite not reaching statistical significance there is a clear correlation of incubation time and levels HC. The

longer the incubation with the drugs, the greater the HC knockdown observed in each of the three repeats performed. The levels of total tubulin remained unchanged at all time points. Surprisingly, the levels of acetylated tubulin at 4 and 8 hours showed a significant increase in comparison to the Auxin control (indole-3-acetic-acid on its own). This is likely due to the slight decrease in the levels of tubulin acetylation seen in this control. When compared to either the doxycycline or the untreated controls, there was no significant change in the levels of acetylated tubulin at 4 or 8 hours. In line with this, the blots also have no distinguishable differences between samples. It is unclear why the levels of acetylated tubulin decreased in the auxin control.

In summary, despite the promise of this system in its ability to test the role of dynein in the regulation of microtubule acetylation it failed to produce conclusive results.

5.3.5 Increased total paxillin in DYNC1H1$^{+/D338N}$ and BICD2$^{+/I189F}$ fibroblasts

Finally, it has previously been shown that the FA protein paxillin is able to interact and inhibit HDAC6, and therefore regulate the acetylation of microtubules and consequently affect the integrity of the Golgi apparatus (Deakin and Turner, 2014). Interestingly, Dr Muruj Barri in the Hafezparast lab has previously observed decreased paxillin phosphorylation at Tyr118 in DYNC1H1$^{R399G/R399G}$ fibroblasts. A similar phenotype was also observed in *Loa/Loa* fibroblasts but was not replicated in work presented in Chapter 4, instead a decrease in total paxillin levels was observed. Therefore, to determine if paxillin may be altered and thus potentially causing the reduction in acetylation seen in DYNC1H1$^{+/D338N}$ fibroblasts, the levels of total and pPax^{Y118} were analysed by western blot analysis. BICD2$^{+/I189F}$ fibroblasts were also included in this analysis.

In contrast to DYNC1H1^{R399G} fibroblasts, there was no difference in pPax^{Y118} in DYNC1H1$^{+/D338N}$ fibroblasts. Similarly, no difference was observed in BICD2$^{+/I189F}$ in comparison to wild type fibroblasts. Furthermore, despite analysis of total paxillin levels showing an increase in DYNC1H1$^{+/D338N}$ fibroblasts in comparison to wild type fibroblasts, this did not reach statistical significance. However, a significant increase was observed in BICD2$^{+/I189F}$ fibroblasts.

This would seemingly contradict data showing that the knockdown of paxillin increases HDAC6 activity and therefore reduces tubulin acetylation (Deakin and Turner, 2014). This is because if paxillin levels were indeed regulating the activity of HDAC6, in both DYNC1H1$^{+/D338N}$ and BICD2$^{+/I189F}$ fibroblasts we would expect increased acetylation as HDAC6 inhibition would increase. However, Deakin & Turner 2014 also observed the presence of large stress fibres when the interaction between HDAC6 and paxillin appeared most strongly. Interestingly, they postulate that this may indicate that the association of HDAC6 and paxillin is regulated by RhoA, which is responsible for inducing stress fibre formation (Deakin and Turner, 2014). RhoA induces stress fibre formation by stimulating actomyosin contractility which in turn induces the phosphorylation of FA proteins including paxillin through FAK (Pasapera et al., 2010; Bhadriraju et al., 2007; Kaneko-Kawano et al., 2012). Therefore, it is possible that RhoA induces paxillin association to HDAC6 through paxillin phosphorylation, which would allow for these changes to coincide with FA formation (López-colomé et al., 2017). Indeed, the phosphorylation of paxillin is an important step which allows for its association with a variety of effectors at FAs (López-colomé et al., 2017).

If this is the pathway responsible for paxillin regulation of microtubule acetylation, the lack of difference in pPax^{Y118} levels in DYNC1H1$^{+/D338N}$ cells would indicate that it is not responsible for the differences in acetylation in these cells. This would also align with the fact that there is no alteration in microtubule acetylation levels in BICD2$^{+/I189F}$ fibroblasts as they also lack a difference in pPax^{Y118}. Additionally, the preliminary data which showed a decrease in pPax^{Y118} in DYNC1H1^{R399G} fibroblasts requires further analysis in light of the data presented in chapter 4. Alternatively, if total paxillin is responsible for the regulation of acetylation, the results presented here would contradict the expected consequence of an increase in total paxillin levels. An increase in acetylation would be expected, but this is not seen in BICD2$^{+/I189F}$ fibroblasts, and the opposite is found in DYNC1H1$^{+/D338N}$ fibroblasts.

Overall, data presented here showed that the Golgi in DYNC1H1$^{+/D338N}$ fibroblasts exhibits a condensed phenotype which may be linked to an impaired Golgi associated microtubule network as seen by a decrease in microtubule acetylation. Conversely, while BICD2$^{+/I189F}$ fibroblasts did not exhibit a condensation

phenotype or a decrease in acetylation, they did present a reduced Golgi area (which may be attributable to a difference in cell morphology) and a striking reduction in IC at the Golgi. This potentially indicates that BICD2 is necessary for the recruitment of dynein to the Golgi. Finally, both DYNC1H1$^{+/D338N}$ and BICD2$^{+/I189F}$ fibroblasts showed an increase total paxillin but this was only statistically significant in the latter cells.

Chapter 6: General discussion and conclusions

6.1 General discussion and conclusions

Motor neuron diseases (MNDs) represent a broad and diverse collection of diseases which are clinically and pathologically linked by motor neuron degeneration. ALS is the most common adult onset MND and affects both upper and lower motor neurons (Taylor et al., 2016; Bruijn et al., 2004). In contrast, SMA-LED is a rare autosomal dominant form of SMA, with congenital or early onset which primarily affects the proximal muscles of the lower limbs (Harms et al., 2010). The pathogenesis of both diseases is not entirely understood, and patients desperately lack effective treatment.

The dysfunction of RNA metabolism in ALS pathogenesis is increasingly a central focus of research (Mackenzie et al., 2010; Polymenidou et al., 2012; Ling et al., 2013). This avenue of research began with the emerging importance of the RNA binding protein TDP-43 in ALS. It was not only discovered to be the main component of the ubiquitinated proteinaceous inclusions which characterise the disease but mutations in the TDP-43 gene (*TARDBP*) are now known to account for 4 % of fALS cases and up to 1 % of sALS cases (Neumann et al., 2006; Arai et al., 2006; Cirulli et al., 2015; Buratti, 2015). The importance of RNA metabolism in ALS was later solidified by the identification of causative mutations in *FUS*, another RNA binding protein (Vance et al., 2009; Kwiatkowski et al., 2009).

More recently, this line of research was further indorsed by the discovery of the *C9orf72* $(G_4C_2)_n$ hexanucleotide repeat expansion mutation, which is tightly associated with RNA pathology and accounts for 40 % of fALS cases and 7 % of sALS cases (Gitler and Tsuiji, 2016; Cirulli et al., 2015).

TDP-43 is involved in several steps of RNA metabolism and recently data from the Hafezparast lab showed that it may be involved in the alternative translation of peripherin (Barri, 2015; Lagier-Tourenne et al., 2010). Peripherin is also a component of the proteinaceous inclusions found in ALS and mutations in its gene (*PRPH*) are also associated with the disease (Corbo and Hays, 1992; He and Hays, 2004; Migheli et al., 1993; Wong et al., 2000; Mizuno et al., 2011; Corrado et al., 2011).

In this thesis, data acquired from a mouse line in which endogenous TDP-43 had been ENU mutagenized to induce a F210I substitution provides further evidence of

TDP-43's ability to affect peripherin expression. Specifically, data presented here showed that peripherin levels were increased in the lumbar spinal cord of TDP-43$^{+/F210I}$ mice, mirroring previous findings in patient ALS lumbar spinal cord tissue (Robertson et al., 2003; McLean et al., 2010). This is also similar to previous results in transgenic mice overexpressing mutant TDP-43 (Swarup et al., 2011). However, unlike these models, TDP-43$^{+/F210I}$ mice allowed the effect of TDP-43 mutations on peripherin expression to be investigated while TDP-43 was expressed at isogenic levels. Therefore, this thesis presents the first evidence that TDP-43 can alter peripherin expression without overexpressing the protein. Overexpression of peripherin is known to cause neuron cell death and so this mutant TDP-43 dependent increase in peripherin may contribute to neuronal loss (Beaulieu et al., 1999).

It is important to note that it is a possibility that peripherin expression is increased due to potential neuronal injury caused by the TDP-43 mutation as peripherin expression has been noted to do so in response to neuronal injury (Beaulieu et al., 2002). However, previous histopathological analysis of TDP-43$^{+/F210I}$ mice of a similar age to those tested here found no signs of abnormalities in both the brain and spinal cord (De Oliveira, 2014). Therefore, TDP-43 pathology in ALS may be responsible for misregulating peripherin expression.

Additionally, it may be the case that TDP-43 is further complicating peripherin pathology in ALS by affecting the expression of the Per-45 isoform. Evidence shows that while Per-45 is not able to assemble into homopolymers, it is necessary for normal assembly of the peripherin network (McLean et al., 2008). Data presented here showed an alteration in the ratio of Per-45 to Per-58 in the insoluble fraction. This change indicated a shift from the use of the Per-45 start codon to the codon leading to the translation of Per-58. However, this change was not statistically significant. Furthermore, since these changes were accompanied by an increase in overall peripherin expression, it is unclear if the shift in alternative translation is due to a regulatory role of TDP-43 that is affected by the F210I mutation, or if this is a consequence of the upregulation of peripherin. An in vitro system aiming to provide a more conclusive answer in which HEK293 cells were made to express peripherin using a stably transfected cDNA clone suggested that TDP-43 does not affect alternative translation. However, this

system is limited due to the lack of regulatory elements which may be necessary for TDP-43 to affect alternative translation. Therefore, a more advanced system is required whereby peripherin is expressed from a clone containing the relevant regulatory elements, perhaps achieved by using a BAC clone. However, the expression yielded from such a method may be too low for analysis as was encountered in neuro2a cells.

SMA-LED is caused by mutations in *DYNC1H1* which encodes the HC of the molecular motor dynein, and in *BICD2* which encodes a dynein adaptor protein of the same name (Harms et al., 2012; Neveling et al., 2013; Oates et al., 2013; Peeters et al., 2013). Several of these *DYNC1H1* mutations also cause malformations of cortical development leading to intellectual disability. Additionally, mutations in the dynein adaptor *Lis1* causes lissencephaly, a neuronal migration disorder. This indicates that dynein is important for normal cortical development which is highly dependent on neuronal migration (Pang et al., 2008). Interestingly, both dynein and Lis1 are not only important for neuronal migration but also for axonal outgrowth (Grabham et al., 2007). Therefore, SMA-LED might represent a neurodevelopmental disorder caused by abnormal neuronal migration and axonal innervation of muscles. In support of this, neuronal migration phenotypes have also been found in the *Loa* model of the disease (Ori-McKenney and Vallee, 2011; Hafezparast et al., 2003). Recent data from the Hafezparast lab provides further evidence that cellular migration is affected in *DYNC1H1* mutants (Barri, 2015). Abnormal focal adhesion (FA) morphology, slowed migration during a wound healing assay, and a decrease in the phosphorylation of paxillin (a key FA protein) at Tyr118 were observed in *Loa/Loa* MEFs.

Data presented in this thesis clarifies the initial findings from the Hafezparast lab. Here, it was shown that previous observations of altered $pPax^{Y118}$ levels were likely a result of variations caused by cells being at different stages of the cell cycle. However, a significant reduction in the levels of total paxillin was observed in *Loa/Loa* MEFs. Importantly, the inhibition of dynein ATPase activity appeared to recapitulate this phenotype. This loss of paxillin in *Loa/Loa* MEFs may underlie the aberrant FA morphology and slowed migration previously observed in these cells. Future experiments should aim to confirm this hypothesis by transfecting *Loa/Loa* MEFs with paxillin to rescue total paxillin levels and see if the above phenotypes

are in turn ameliorated. Interestingly, observations made during the assessment of paxillin turnover at FAs (which was unchanged in *Loa/Loa* MEFs) indicated that there were no distinguishable abnormalities in FA morphology in GFP-paxillin transfected *Loa/Loa* MEFs. However, this anecdotal preliminary observation requires further investigation and quantification. Additionally, a wound healing assay should be carried out following paxillin transfection in both wild type and *Loa/Loa* MEFs to determine if this is sufficient to rescue the migration deficit seen in the latter. If the loss of paxillin does indeed prove to be the cause of the migration deficit in these cells, it might indicate that it could also contribute to the neuronal migration defects seen in *Loa* mice. Therefore, experiments should be conducted to analyse the levels of total paxillin in cortical and motor neurons of these mice. The results of these experiments could potentially have ramifications on the understanding of the pathogenesis of SMA-LED.

Finally, Golgi pathology has been observed in response to mutations in both *DYNC1H1* and *BICD2* SMA-LED patients. Delayed re-assembly of the Golgi following nocodazole washout is seen in SMA-LED *DYNC1H1* mutations and in the *Loa* mouse model of the disease which also harbours a *Dync1h1* mutation (Hafezparast et al., 2003; Fiorillo et al., 2014). More recently, inherent Golgi fragmentation was seen in patient fibroblasts with a p.R399G DYNC1H1 substitution in the Hafezparast lab. Similarly, Golgi fragmentation has also been found in association with multiple *BICD2* mutations (Fumoto et al., 2006; Teuling et al., 2008).

Data presented here shows that in DYNC1H1$^{+/D338N}$ patient fibroblasts, the Golgi appears condensed and exhibits a smaller area. While the BICD2$^{+/I189F}$ fibroblasts exhibited a smaller area of the Golgi with no measurable condensation which may have been due to differences in cell morphology. There also appeared to be a loss of dynein at the Golgi in BICD2$^{+/I189F}$ fibroblasts, indicating that BICD2 may be necessary for the recruitment of dynein to the Golgi. Furthermore, in line with previously discussed data relating to neuronal development and migration, the Golgi apparatus is crucial for this process (Yadav and Linstedt, 2011). During neuronal migration the Golgi is reoriented towards the leading edge and towards the site of axonal outgrowth in developing neurons (Yadav and Linstedt, 2011). This allows for the directed secretion of cargo towards these areas. It is possible

that the observed Golgi pathology affects these processes. In fact, the Golgi fragmentation previously observed in the Hafezparast lab in DYNC1H1^{R399G} fibroblasts was shown to impair the projection of the Golgi towards the leading edge of migrating cells. Interestingly, when Golgi re-orientation was stimulated using a wound healing assay the Golgi re-orientated but appeared condensed in a similar fashion to what was inherently seen in DYNC1H1$^{+/D338N}$ fibroblasts. It would be interesting to perform the same experiment on DYNC1H1$^{+/D338N}$ fibroblasts to see if this would exacerbate the phenotype. Additionally, to ascertain if this may affect cellular migration, the rate of wound healing should be assessed. These experiments should also be carried out on BICD2$^{+/I189F}$ fibroblasts as dynein at the Golgi is important for its re-orientation (Yadav et al., 2012).

Furthermore, the Golgi phenotype in DYNC1H1$^{+/D338N}$ fibroblasts was accompanied by a decrease in microtubule acetylation in a similar fashion to what was previously seen in the Hafezparast lab in DYNC1H1^{R399G} fibroblasts. Interestingly, in the Hafezparast lab it was observed that the rescue of microtubule acetylation rescued the Golgi fragmentation in the DYNC1H1^{R399G} fibroblasts. It would be interesting to assess the effect of rescuing microtubule acetylation on the Golgi morphology in DYNC1H1$^{+/D338N}$ fibroblasts. If the condensation of the Golgi was ameliorated, it would be prudent to see the effect of this on both the re-orientation of the Golgi and cellular migration in DYNC1H1$^{+/D338N}$, assuming the previously suggested experiments showed an impairment in these processes. Additionally, neurons should be generated from patient fibroblasts to asses if these phenotypes translate to a neuronal context. This is especially important since in neurons Golgi outposts are found within dendrites and act as sites of acentrosomal microtubule nucleation (Wei and Seemann, 2017; Jeyifous et al., 2009; Sanders and Kaverina, 2015).

Importantly, data in this thesis also showed that microtubule acetylation in *Loa/Loa* MEFs is reduced. Therefore, this phenotype is found in association with three different *DYNC1H1* mutations. This may indicate a common pathogenic mechanism in *DYNC1H1* related SMA-LED which could be targeted by therapeutics. Finally, total paxillin levels in both DYNC1H1$^{+/D338N}$ and BICD2$^{+/I189F}$ fibroblasts appeared to be increased, but only the latter showed a statistically significant change. Therefore, while further repeats are required to confirm this

observation, it suggests a different pathology to the *Loa/Loa* MEFs which had decreased total paxillin. However, the presence of increased paxillin may also further impair migration in these cells.

Interestingly, it has been suggested that paxillin exerts an inhibitory effect on HDAC6 which is responsible for the deacetylation of microtubules at Lys40 (Deakin and Turner, 2014). It was shown that if this inhibitory effect is affected, it causes the fragmentation of the Golgi. However, since the phenotype observed in both DYNC1H1$^{+/D338N}$ and BICD2$^{+/I189F}$ fibroblasts appeared to be increased paxillin levels, it suggests that this does not underlie the changes in microtubule acetylation seen in DYNC1H1$^{+/D338N}$ fibroblasts. It may be the case that the increase in total paxillin may be an attempt to reduce HDAC6 activity to rescue the acetylation of microtubules in these cells. Conversely, in *Loa/Loa* MEFs there is indeed both a decrease in total paxillin levels and a reduction in microtubule acetylation. Therefore, in these cells it may be the case that the former is affecting the latter and thus this pathway requires further investigation within these cells.

In summary, data presented in this thesis advances our understanding of the potential role of TDP-43 in the regulation of peripherin expression, which may contribute to the pathology seen in ALS. Additionally, investigations into the role of dynein in migration through its effect on the FA protein paxillin clarified a potentially pathogenic change in paxillin expression. Finally, the molecular consequences of SMA-LED causing *DYNC1H1* and *BICD2* mutations were investigated in the context of previous observations of Golgi pathology which further exposed a pathogenic effect of mutations in both of these genes on the Golgi apparatus and associated microtubule network. A summary of the results obtained in this thesis concerning the Golgi pathology, microtubule modifications and paxillin, alongside data obtained previously in the Hafezparast lab can be seen in table 6.1.

Table 6.1

	Golgi fragmentation	Golgi area	Are between Golgi membranes	IC localisation at the Golgi	Microtubule acetylation	Microtubule detyrosination	pPax^{Y118}	Total paxillin	pPax^{Y118}/total paxillin ratio
DYNC1H1$^{+/D338N}$	No	Reduced****	Reduced**	No change	Reduced**	No change	No change	Increase	
BICD2$^{+/I189F}$	No	Reduced*	No change	Reduced¥	No change	No change	No change	Increase*	
DYNC1H1$^{R399G/R399G}$	Yes			Reduced	Reduced	No change	Decrease		
***Loa/Loa* MEFs (from this thesis)**					Reduced*	No change	No change	Decrease**	Increase *
Previous data on *Loa/Loa* MEFs from Hafezparast lab	Delayed recovery after nocodazole#						Decrease		

Table 5.1 Summary of the data acquired in this thesis on Golgi pathology, microtubule modifications and paxillin in DYNC1H1$^{+/D338N}$, BICD2$^{+/I189F}$ fibroblasts and *Loa/Loa* MEFs. Additionally, this is contrasted to previous data which data obtained in the Hafezparast lab for the DYNC1H1$^{R399G/R399G}$ fibroblast line and *Loa/Loa* MEFs. ¥ Localisation of the IC to the Golgi was assessed using two different metrics with both being significantly reduced in BICD2$^{+/I189F}$ fibroblasts. # Hafezparast *et al.*, 2003 (* $P < 0.05$, ** $P < 0.01$, **** $P < 0.0001$).

References

Abel, O., A. Shatunov, A.R. Jones, P.M. Andersen, J.F. Powell, and A. Al-Chalabi. 2013. Development of a smartphone app for a genetics website: The amyotrophic lateral sclerosis online genetics database (ALSoD). *J. Med. Internet Res.* 15:1–10.

Abhyankar, M.M., C. Urekar, and P.P. Reddi. 2007. A novel CpG-free vertebrate insulator silences the testis-specific SP-10 gene in somatic tissues: Role for TDP-43 in insulator function. *J. Biol. Chem.* 282:36143–36154.

Acevedo-Arozena, A., B. Kalmar, S. Essa, T. Ricketts, P. Joyce, R. Kent, C. Rowe, A. Parker, A. Gray, M. Hafezparast, J.R. Thorpe, L. Greensmith, and E.M.C. Fisher. 2011. A comprehensive assessment of the SOD1G93A low-copy transgenic mouse, which models human amyotrophic lateral sclerosis. *Dis. Model. Mech.* 4:686–700.

Acharya, K.K., C.K. Govind, A.N. Shore, M.H. Stoler, and P.P. Reddi. 2006. cis-Requirement for the maintenance of round spermatid-specific transcription. *Dev. Biol.* 295:781–790.

Akella, J.S., D. Wloga, J. Kim, N.G. Starostina, S. Lyons-Abbott, N.S. Morrissette, S.T. Dougan, E.T. Kipreos, and J. Gaertig. 2010. MEC-17 is an α-tubulin acetyltransferase. *Nature*. 467:218–222.

Al-Chalabi, A., F. Fang, M.F. Hanby, P.N. Leigh, C.E. Shaw, W. Ye, and F. Rijsdijk. 2010. An estimate of amyotrophic lateral sclerosis heritability using twin data. *J. Neurol. Neurosurg. Psychiatry*. 81:1324–1326.

Al-Chalabi, A., and O. Hardiman. 2013. The epidemiology of ALS: a conspiracy of genes, environment and time. *Nat. Rev. Neurol.* 9:617–28.

Al-Chalabi, A., O. Hardiman, M.C. Kiernan, A. Chiò, B. Rix-Brooks, and L.H. van den Berg. 2016. Amyotrophic lateral sclerosis: moving towards a new classification system. *Lancet Neurol.* 15:1182–1194.

Alami, N.H., R.B. Smith, M.A. Carrasco, L.A. Williams, C.S. Winborn, S.S.W. Han, E. Kiskinis, B. Winborn, B.D. Freibaum, A. Kanagaraj, A.J. Clare, N.M. Badders, B. Bilican, E. Chaum, S. Chandran, C.E. Shaw, K.C. Eggan, T. Maniatis, and J.P. Taylor. 2014. Axonal Transport of TDP-43 mRNA Granules Is Impaired by ALS-Causing Mutations. *Neuron*. 81:536–543.

Allan, V.J., H.M. Thompson, and M. a McNiven. 2002. Motoring around the Golgi. *Nat. Cell Biol.* 4:E236–E242.

Alper, J.D., F. Decker, B. Agana, and J. Howard. 2014. The motility of axonemal dynein is regulated by the tubulin code. *Biophys J*. 107:2872–2880.

Aman, P., I. Panagopoulos, C. Lassen, T. Fioretos, M. Mencinger, H. Toresson, M. Höglund, A. Forster, T.H. Rabbitts, D. Ron, N. Mandahl, and F. Mitelman. 1996. Expression patterns of the human sarcoma-associated genes FUS and EWS and the genomic structure of FUS. *Genomics*. 37:1–8.

Amos, L.A. 1989. Brain dynein crossbridges microtubules into bundles. *J. Cell Sci.* 93 (Pt 1):19–28.

Andersen, P.M. 2006. Amyotrophic lateral sclerosis associated with mutations in the CuZn superoxide dismutase gene. *Curr. Neurol. Neurosci. Rep.* 6:37–46.

Appenzeller-Herzog, C. 2006. The ER-Golgi intermediate compartment (ERGIC): in search of its identity and function. *J. Cell Sci.* 119:2173–2183.

Applegate, K.T., S. Besson, A. Matov, M.H. Bagonis, K. Jaqaman, and G. Danuser. 2011. plusTipTracker: Quantitative image analysis software for the measurement of microtubule dynamics. *J. Struct. Biol.* 176:168–84.

Arai, T., M. Hasegawa, H. Akiyama, K. Ikeda, T. Nonaka, H. Mori, D. Mann, K. Tsuchiya, M. Yoshida, Y. Hashizume, and T. Oda. 2006. TDP-43 is a component of ubiquitin-positive tau-negative inclusions in frontotemporal lobar degeneration and amyotrophic lateral sclerosis. *Biochem. Biophys. Res. Commun.* 351:602–11.

Arnold, E.S., S.-C. Ling, S.C. Huelga, C. Lagier-Tourenne, M. Polymenidou, D. Ditsworth, H.B. Kordasiewicz, M. McAlonis-Downes, O. Platoshyn, P. a Parone, S. Da Cruz, K.M. Clutario, D. Swing, L. Tessarollo, M. Marsala, C.E. Shaw, G.W. Yeo, and D.W.

Cleveland. 2013. ALS-linked TDP-43 mutations produce aberrant RNA splicing and adult-onset motor neuron disease without aggregation or loss of nuclear TDP-43. *Proc. Natl. Acad. Sci. U. S. A.* 110:E736-45.
Arnold, W.D., D. Kassar, and J.T. Kissel. 2015. Spinal muscular atrophy: Diagnosis and management in a new therapeutic era. *Muscle Nerve*. 51:157–167.
Athlan, E.S., and W.E. Mushynski. 1997. Heterodimeric associations between neuronal intermediate filament proteins. *J. Biol. Chem.* 272:31073–31078.
Ayala, Y.M., L. De Conti, S.E. Avendaño-Vázquez, A. Dhir, M. Romano, A. D'Ambrogio, J. Tollervey, J. Ule, M. Baralle, E. Buratti, and F.E. Baralle. 2011. TDP-43 regulates its mRNA levels through a negative feedback loop. *EMBO J.* 30:277–288.
Ayala, Y.M., S. Pantano, A. D'Ambrogio, E. Buratti, A. Brindisi, C. Marchetti, M. Romano, and F.E. Baralle. 2005. Human, Drosophila, and C.elegans TDP43: nucleic acid binding properties and splicing regulatory function. *J. Mol. Biol.* 348:575–88.
Ayala, Y.M., P. Zago, A. D'Ambrogio, Y.-F. Xu, L. Petrucelli, E. Buratti, and F.E. Baralle. 2008. Structural determinants of the cellular localization and shuttling of TDP-43. *J. Cell Sci.* 121:3778–85.
Baechtold, H., M. Kuroda, J. Sok, D. Ron, B.S. Lopez, and A.T. Akhmedov. 1999. Human 75-kDa DNA-pairing protein is identical to the pro-oncoprotein TLS/FUS and is able to promote D-loop formation. *J. Biol. Chem.* 274:34337–34342.
Baffet, A.D., D.J. Hu, and R.B. Vallee. 2015. Cdk1 Activates Pre-mitotic Nuclear Envelope Dynein Recruitment and Apical Nuclear Migration in Neural Stem Cells. *Dev. Cell*. 33:703–716.
Bandyopadhyay, U., M. Nagy, W.A. Fenton, and A.L. Horwich. 2014. Absence of lipofuscin in motor neurons of SOD1-linked ALS mice. *Proc. Natl. Acad. Sci.* 111:11055–11060.
Barri, M. 2015. Functional analysis of motor neuron disease-associated mutations in TAR DNA-binding protein 43 and cytoplasmic dynein heavy chain 1, PhD thesis. University of Sussex.
Batista, P.J., and H.Y. Chang. 2013. Long noncoding RNAs: Cellular address codes in development and disease. *Cell*. 152:1298–1307.
Bäumer, D., K. Talbot, and M.R. Turner. 2014. Advances in motor neurone disease. *J. R. Soc. Med.* 107:14–21.
Beaulieu, J., M.D. Nguyen, and J. Julien. 1999. Late Onset Death of Motor Neurons in Mice Overexpressing Wild-Type Peripherin. *J. Cell Biol.* 147:531–544.
Beaulieu, J.M., J. Kriz, and J.P. Julien. 2002. Induction of peripherin expression in subsets of brain neurons after lesion injury or cerebral ischemia. *Brain Res.* 946:153–161.
Bellingham, M.C. 2011. A Review of the Neural Mechanisms of Action and Clinical Efficiency of Riluzole in Treating Amyotrophic Lateral Sclerosis: What have we Learned in the Last Decade? *CNS Neurosci. Ther.* 17:4–31.
Del Bene, F., A.M. Wehman, B.A. Link, and H. Baier. 2008. Regulation of Neurogenesis by Interkinetic Nuclear Migration through an Apical-Basal Notch Gradient. *Cell*. 134:1055–1065.
Bento, C.F., M. Renna, G. Ghislat, C. Puri, A. Ashkenazi, M. Vicinanza, F.M. Menzies, and D.C. Rubinsztein. 2016. Mammalian Autophagy: How Does It Work? *Annu. Rev. Biochem.* 85:685–713.
Bertolotti, A., Y. Lutz, D.J. Heard, P. Chambon, and L. Tora. 1996. hTAF(II)68, a novel RNA/ssDNA-binding protein with homology to the pro-oncoproteins TLS/FUS and EWS is associated with both TFIID and RNA polymerase II. *EMBO J.* 15:5022–5031.
Bhabha, G., G.T. Johnson, C.M. Schroeder, and R.D. Vale. 2016. How Dynein Moves Along Microtubules. *Trends Biochem. Sci.* 41:94–105.
Bhadriraju, K., M. Yang, S. Alom Ruiz, D. Pirone, J. Tan, and C.S. Chen. 2007. Activation of ROCK by RhoA is regulated by cell adhesion, shape, and cytoskeletal tension. *Exp. Cell Res.* 313:3616–3623.
Bhuwania, R., A. Castro-Castro, and S. Linder. 2014. Microtubule acetylation regulates dynamics of KIF1C-powered vesicles and contact of microtubule plus ends with

podosomes. *Eur. J. Cell Biol.* 93:424–437.
Bieling, P., S. Kandels-Lewis, I.A. Telley, J. Van Dijk, C. Janke, and T. Surrey. 2008. CLIP-170 tracks growing microtubule ends by dynamically recognizing composite EB1/tubulinbinding sites. *J. Cell Biol.* 183:1223–1233.
Bilsland, L.G., E. Sahai, G. Kelly, M. Golding, L. Greensmith, and G. Schiavo. 2010. Deficits in axonal transport precede ALS symptoms in vivo. *Proc. Natl. Acad. Sci.* 107:20523–20528.
Blasco, H., F. Patin, C. Andres, P. Corcia, and P. Gordon. 2016. Amyotrophic Lateral Sclerosis, 2016: existing therapies and the ongoing search for neuroprotection. *Expert Opin. Pharmacother.* 17:1669–1682.
Blokhuis, A.M., E.J.N. Groen, M. Koppers, L.H. van den Berg, and R.J. Pasterkamp. 2013. Protein aggregation in amyotrophic lateral sclerosis. *Acta Neuropathol.* 125:777–94.
Bogucki, A., J. Pigonska, I. Szadkowska, and A. Gajos. 2016. Unilateral progressive muscular atrophy with fast symptoms progression. *Neurol. Neurochir. Pol.* 50:52–54.
Bonafede, R., and R. Mariotti. 2017. ALS Pathogenesis and Therapeutic Approaches: The Role of Mesenchymal Stem Cells and Extracellular Vesicles. *Front. Cell. Neurosci.* 11:1–16.
Borchelt, D.R., M.K. Lee, H.S. Slunt, M. Guarnieri, Z.S. Xu, P.C. Wong, R.H. Brown, D.L. Price, S.S. Sisodia, D.W. Cleveland, M.K. Leeo, H.S. Sluntt, M. Guarnierit, Z.S. Xu, P.C. Wong, R.H. Brown, D.L. Price, S.S. Sisodia, and D.O.N.W. Clevelandt. 1994. Superoxide dismutase 1 with mutations linked to familial amyotrophic lateral sclerosis possesses significant activity. *Proc. Natl. Acad. Sci. U. S. A.* 91:8292–8296.
Borroni, B., C. Bonvicini, A. Alberici, E. Buratti, C. Agosti, S. Archetti, A. Papetti, C. Stuani, M. Di Luca, M. Gennarelli, and A. Padovani. 2009. Mutation within TARDBP leads to frontotemporal dementia without motor neuron disease. *Hum. Mutat.* 30:E974-83.
Brandizzi, F., and C. Barlowe. 2013. Organization of the ER–Golgi interface for membrane traffic control. *Nat. Rev. Mol. Cell Biol.* 14:382–392.
Brody, B.A., C.A. Ley, and L.M. Parysek. 1989. Selective distribution of the 57 kDa neural intermediate filament protein in the rat CNS. *J Neurosci*. 9:2391–2401.
Vanden Broeck, L., P. Callaerts, and B. Dermaut. 2014. TDP-43-mediated neurodegeneration: Towards a loss-of-function hypothesis? *Trends Mol. Med.* 20:66–71.
Brown, M.C., J.A. Perrotta, and C.E. Turner. 1996. Identification of LIM3 as the principal determinant of paxillin focal adhesion localization and characterization of a novel motif on paxillin directing vinculin and focal adhesion kinase binding. *J. Cell Biol.* 135:1109–1123.
Brown, M.C., J. a Perrotta, and C.E. Turner. 1998. Serine and threonine phosphorylation of the paxillin LIM domains regulates paxillin focal adhesion localization and cell adhesion to fibronectin. *Mol. Biol. Cell*. 9:1803–1816.
Bruijn, L.I., M.W. Becher, M.K. Lee, K.L. Anderson, N.A. Jenkins, N.G. Copeland, S.S. Sisodia, J.D. Rothstein, D.R. Borchelt, D.L. Price, and D.W. Cleveland. 1997. ALS-linked SOD1 mutant G85R mediates damage to astrocytes and promotes rapidly progressive disease with SOD1-containing inclusions. *Neuron*. 18:327–338.
Bruijn, L.I., T.M. Miller, and W. Cleveland. 2004. Unraveling the Mechanisms Involved in Motor Neuron Degeneration in Als. *Annu. Rev. Neurosci*. 27:723–49.
Brzustowicz, L.M., T. Lehner, L.H. Castilla, G.K. Penchaszadeh, K.C. Wilhelmsen, R. Daniels, K.E. Davies, M. Leppert, F. Ziter, D. Wood, V. Dubowitz, K. Zerres, I. Hausmanowa-Petrusewicz, J. Ott, T.L. Munsat, and T.C. Gilliam. 1990. Genetic mapping of chronic childhood-onset spinal muscular atrophy to chromosome 5q1 1.2–13.3. *Nature*. 344:540–541.
Buratti, E. 2015. Functional Significance of TDP-43 Mutations in Disease. 91. 1-53 pp.
Buratti, E., and F.E. Baralle. 2001. Characterization and functional implications of the RNA binding properties of nuclear factor TDP-43, a novel splicing regulator of CFTR exon 9. *J. Biol. Chem.* 276:36337–43.

Buratti, E., and F.E. Baralle. 2008. Multiple roles of TDP-43 in gene expression, splicing regulation, and human disease. *Front. Biosci.* 13:867–878.
Buratti, E., A. Brindisi, M. Giombi, S. Tisminetzky, Y.M. Ayala, and F.E. Baralle. 2005. TDP-43 binds heterogeneous nuclear ribonucleoprotein A/B through its C-terminal tail: an important region for the inhibition of cystic fibrosis transmembrane conductance regulator exon 9 splicing. *J. Biol. Chem.* 280:37572–84.
Buratti, E., T. Dörk, E. Zuccato, F. Pagani, M. Romano, and F.E. Baralle. 2001. Nuclear factor TDP-43 and SR proteins promote in vitro and in vivo CFTR exon 9 skipping. *EMBO J.* 20:1774–84.
Buratti, E., M. Romano, and F.E. Baralle. 2013. TDP-43 high throughput screening analyses in neurodegeneration: Advantages and pitfalls. *Mol. Cell. Neurosci.* 56:465–474.
Burkhardt, J.K., C.J. Echeverri, T. Nilsson, and R.B. Vallee. 1997. Overexpression of the dynamitin (p50) subunit of the dynactin complex disrupts dynein-dependent maintenance of membrane organelle distribution. *J. Cell Biol.* 139:469–484.
Burnett, B.G., E. Munoz, A. Tandon, D.Y. Kwon, C.J. Sumner, and K.H. Fischbeck. 2009. Regulation of SMN Protein Stability. *Mol. Cell. Biol.* 29:1107–1115.
Caccamo, A., S. Majumder, and S. Oddo. 2012. Cognitive decline typical of frontotemporal lobar degeneration in transgenic mice expressing the 25-kDa C-terminal fragment of TDP-43. *Am. J. Pathol.* 180:293–302.
Cannon, A., B. Yang, J. Knight, I.M. Farnham, Y. Zhang, C.A. Wuertzer, S. D'Alton, W.L. Lin, M. Castanedes-Casey, L. Rousseau, B. Scott, M. Jurasic, J. Howard, X. Yu, R. Bailey, M.R. Sarkisian, D.W. Dickson, L. Petrucelli, and J. Lewis. 2012. Neuronal sensitivity to TDP-43 overexpression is dependent on timing of induction. *Acta Neuropathol.* 123:807–823.
Di Carlo, V., E. Grossi, P. Laneve, M. Morlando, S. Dini Modigliani, M. Ballarino, I. Bozzoni, and E. Caffarelli. 2013. TDP-43 regulates the microprocessor complex activity during in vitro neuronal differentiation. *Mol. Neurobiol.* 48:952–963.
Carter, A.P., C. Cho, L. Jin, and R.D. Vale. 2011. Crystal Structure of the Dynein Motor Domain. *Science*. 331:1159–1165.
Carter, A.P., A.G. Diamant, and L. Urnavicius. 2016. How dynein and dynactin transport cargos: A structural perspective. *Curr. Opin. Struct. Biol.* 37:62–70.
Casafont, I., R. Bengoechea, O. Tapia, M.T. Berciano, and M. Lafarga. 2009. TDP-43 localizes in mRNA transcription and processing sites in mammalian neurons. *J. Struct. Biol.* 167:235–41.
Case, L.B., and C.M. Waterman. 2015. Integration of actin dynamics and cell adhesion by a three-dimensional, mechanosensitive molecular clutch. *Nat Cell Biol*. 17:955–963.
Chabin-Brion, K., J. Marceiller, F. Perez, C. Settegrana, A. Drechou, G. Durand, and C. Poüs. 2001. The Golgi complex is a microtubule-organizing organelle. *Mol. Biol. Cell*. 12:2047–60.
Chang-Hong, R., M. Wada, S. Koyama, H. Kimura, S. Arawaka, T. Kawanami, K. Kurita, T. Kadoya, M. Aoki, Y. Itoyama, and T. Kato. 2005. Neuroprotective effect of oxidized galectin-1 in a transgenic mouse model of amyotrophic lateral sclerosis. *Exp. Neurol.* 194:203–211.
Che, M., R. Wang, X. Li, H.Y. Wang, and X.F.S. Zheng. 2016. Expanding roles of superoxide dismutases in cell regulation and cancer. *Drug Discov. Today*. 21:143–149.
Chen, S., P. Sayana, X. Zhang, and W. Le. 2013. Genetics of amyotrophic lateral sclerosis: an update. *Mol. Neurodegener.* 8:28.
Chen, X.-J., E.N. Levedakou, K.J. Millen, R.L. Wollmann, B. Soliven, and B. Popko. 2007. Proprioceptive sensory neuropathy in mice with a mutation in the cytoplasmic Dynein heavy chain 1 gene. *J. Neurosci.* 27:14515–14524.
Chen, Y., H. Liu, Y. Guan, Q. Wang, F. Zhou, L. Jie, J. Ju, L. Pu, H. Du, and X. Wang. 2015. The altered autophagy mediated by TFEB in animal and cell models of amyotrophic lateral sclerosis. *Am. J. Transl. Res.* 7:1574–1587.

Chen, Y., and Z.H. Sheng. 2013. Kinesin-1-syntaphilin coupling mediates activity-dependent regulation of axonal mitochondrial transport. *J. Cell Biol.* 202:351–364.
Chen, Y., Y. Xu, G. Li, N. Li, T. Yu, R. Yao, X. Wang, Y. Shen, and J. Wang. 2017. Exome Sequencing Identifies De Novo DYNC1H1 Mutations Associated With Distal Spinal Muscular Atrophy and Malformations of Cortical Development Journal. *J. Child Neurol.* 32:379–386.
Chernyatina, A.A., D. Guzenko, and S. V. Strelkov. 2015. Intermediate filament structure: The bottom-up approach. *Curr. Opin. Cell Biol.* 32:65–72.
Chew, J., T.F. Gendron, M. Prudencio, H. Sasaguri, M. Castanedes-casey, C.W. Lee, K. Jansen-west, A. Kurti, M.E. Murray, K.F. Bieniek, P.O. Bauer, E.C. Whitelaw, J.N. Stankowski, C. Stetler, L.M. Daughrity, A. Emilie, P. Desaro, A. Johnston, K. Overstreet, D. Edbauer, R. Rademakers, K.B. Boylan, D.W. Dickson, J.D. Fryer, and L. Petrucelli. 2015. C9ORF72 repeat expansions in mice cause TDP-43 pathology, neuronal loss, and behavioral deficits. *Science*. 348:1151–1154.
Chio, A., A. Calvo, C. Moglia, L. Mazzini, and G. Mora. 2011. Phenotypic heterogeneity of amyotrophic lateral sclerosis: a population based study. *J. Neurol. Neurosurg. Psychiatry*. 82:740–746.
Choi, C.K., M. Vicente-Manzanares, J. Zareno, L.A. Whitmore, A. Mogilner, and A.R. Horwitz. 2008. Actin and alpha-actinin orchestrate the assembly and maturation of nascent adhesions in a myosin II motor-independent manner. *Nat. Cell Biol.* 10:1039–50.
Chowdhury, S., S. a Ketcham, T. a Schroer, and G.C. Lander. 2015. Structural organization of the dynein–dynactin complex bound to microtubules. *Nat. Struct. Mol. Biol.* 22:345–347.
Chrzanowska-Wodnicka, M., and K. Burridge. 1996. Rho-stimulated Contractiliry Drives the Formation of Stress Fibers and Focal Adhesions. *J. Cell Biol.* 133:1403–1415.
Chung, W.-H. 2017. Unraveling new functions of superoxide dismutase using yeast model system: Beyond its conventional role in superoxide radical scavenging. *J. Microbiol.* 1–8.
Cianfrocco, M. a., M.E. DeSantis, A.E. Leschziner, and S.L. Reck-Peterson. 2015. Mechanism and Regulation of Cytoplasmic Dynein. *Annu. Rev. Cell Dev. Biol.* 31:83–108.
Cirillo, D., F. Agostini, P. Klus, D. Marchese, S. Rodriguez, B. Bolognesi, and G.G. Tartaglia. 2013. Neurodegenerative diseases : Quantitative predictions of protein – RNA interactions. *Bioinformatics*. 129–140.
Cirulli, E.T., B.N. Lasseigne, S. Petrovski, P.C. Sapp, P.A. Dion, C.S. Leblond, J. Couthouis, Y. Lu, Q. Wang, B.J. Krueger, Z. Ren, J. Keebler, Y. Han, S.E. Levy, B.E. Boone, J.R. Wimbish, L.L. Waite, A.L. Jones, J.P. Carulli, A.G. Day-williams, J.F. Staropoli, W.W. Xin, A. Chesi, A.R. Raphael, D. Mckenna-yasek, J. Cady, J.M.B.V. De Jong, K.P. Kenna, B.N. Smith, S. Topp, S. Swarup, J. Landers, F. Baas, A.S. Allen, R.S. Bedlack, J.W. Harper, A.D. Gitler, G.A. Rouleau, R. Brown, M.B. Harms, G.M. Cooper, T. Harris, R.M. Myers, and D.B. Goldstein. 2015. Exome sequencing in amyotrophic lateral sclerosis identifies risk genes and pathways. *Science*. 347:1436.
Clainche, C. Le, and M.-F.F. Carlier. 2008. Regulation of actin assembly associated with protrusion and adhesion in cell migration. *Physiol. Rev.* 88:489–513.
Colombrita, C., E. Onesto, E. Buratti, P. de la Grange, V. Gumina, F.E. Baralle, V. Silani, and A. Ratti. 2015. From transcriptomic to protein level changes in TDP-43 and FUS loss-of-function cell models. *Biochim. Biophys. Acta - Gene Regul. Mech.* 1849:1398–1410.
Colombrita, C., E. Onesto, F. Megiorni, A. Pizzuti, F.E. Baralle, E. Buratti, V. Silani, and A. Ratti. 2012. TDP-43 and FUS RNA-binding proteins bind distinct sets of cytoplasmic messenger RNAs and differently regulate their post-transcriptional fate in motoneuron-like cells. *J. Biol. Chem.* 287:15635–15647.
Colombrita, C., E. Zennaro, C. Fallini, M. Weber, A. Sommacal, E. Buratti, V. Silani, and A. Ratti. 2009. TDP-43 is recruited to stress granules in conditions of oxidative insult.

J. Neurochem. 111:1051–61.
Comley, L., I. Allodi, S. Nichterwitz, M. Nizzardo, C. Simone, S. Corti, and E. Hedlund. 2015. Motor neurons with differential vulnerability to degeneration show distinct protein signatures in health and ALS. *Neuroscience*. 291:216–229.
Corbo, M., and a P. Hays. 1992. Peripherin and neurofilament protein coexist in spinal spheroids of motor neuron disease. *J. Neuropathol. Exp. Neurol.* 51:531–7.
Corrado, L., Y. Carlomagno, L. Falasco, S. Mellone, M. Godi, E. Cova, C. Cereda, L. Testa, L. Mazzini, and S. D'Alfonso. 2011. A novel peripherin gene (PRPH) mutation identified in one sporadic amyotrophic lateral sclerosis patient. *Neurobiol. Aging*. 32:552.e1-6.
Corthésy-Theulaz, I., A. Pauloin, and S.R. Pfeffer. 1992. Cytoplasmic dynein participates in the centrosomal localization of the Golgi complex. *J. Cell Biol.* 118:1333–1345.
Courchesne, S.L., M.F. Pazyra-Murphy, D.J. Lee, and R.A. Segal. 2011. Neuromuscular junction defects in mice with mutation of dynein heavy chain 1. *PLoS One*. 6:e16753.
Cox, L.E., L. Ferraiuolo, E.F. Goodall, P.R. Heath, A. Higginbottom, H. Mortiboys, H.C. Hollinger, J.A. Hartley, A. Brockington, C.E. Burness, K.E. Morrison, S.B. Wharton, A.J. Grierson, P.G. Ince, J. Kirby, and P.J. Shaw. 2010. Mutations in CHMP2B in lower motor neuron predominant amyotrophic lateral sclerosis (ALS). *PLoS One*. 5:e9872.
Crapo, J.D., T. Oury, C. Rabouille, J.W. Slot, and L.Y. Chang. 1992. Copper,zinc superoxide dismutase is primarily a cytosolic protein in human cells. *Proc. Natl. Acad. Sci. U. S. A.* 89:10405–9.
Cronin, S., O. Hardiman, and B.J. Traynor. 2007. Ethnic variation in the incidence of ALS: A systematic review. *Neurology*. 68:1002–1007.
Cui, C., P.J. Stambrook, and L.M. Parysek. 1995. Peripherin assembles into homopolymers in SW13 cells. *J Cell Sci.* 108:3279–84.
Cushman, M., B.S. Johnson, O.D. King, A.D. Gitler, and J. Shorter. 2010. Prion-like disorders: blurring the divide between transmissibility and infectivity. *J. Cell Sci.* 123:1191–1201.
D'Alton, S., M. Altshuler, A. Cannon, D.W. Dickson, L. Petrucelli, and J. Lewis. 2014. Divergent phenotypes in mutant TDP-43 transgenic mice highlight potential confounds in TDP-43 transgenic modeling. *PLoS One*. 9:e86513.
D'amico, E., M. Pasmantier, and Y. Lee. 2013. Clinical evolution of pure upper motor neuron disease/dysfunction (PUMND). *Muscle Nerve*. 47:1–5.
Damiano, M., A.A. Starkov, S. Petri, K. Kipiani, M. Kiaei, M. Mattiazzi, M. Flint Beal, and G. Manfredi. 2006. Neural mitochondrial Ca2+ capacity impairment precedes the onset of motor symptoms in G93A Cu/Zn-superoxide dismutase mutant mice. *J. Neurochem.* 96:1349–1361.
Deakin, N.O., and C.E. Turner. 2008. Paxillin comes of age. *J. Cell Sci.* 121:2435–44.
Deakin, N.O., and C.E. Turner. 2014. Paxillin inhibits HDAC6 to regulate microtubule acetylation, Golgi structure, and polarized migration. *J. Cell Biol.* 206:395–413.
DeJesus-Hernandez, M., I.R. Mackenzie, B.F. Boeve, A.L. Boxer, M. Baker, N.J. Rutherford, A.M. Nicholson, N. a. Finch, H. Flynn, J. Adamson, N. Kouri, A. Wojtas, P. Sengdy, G.Y.R. Hsiung, A. Karydas, W.W. Seeley, K. a. Josephs, G. Coppola, D.H. Geschwind, Z.K. Wszolek, H. Feldman, D.S. Knopman, R.C. Petersen, B.L. Miller, D.W. Dickson, K.B. Boylan, N.R. Graff-Radford, and R. Rademakers. 2011. Expanded GGGGCC Hexanucleotide Repeat in Noncoding Region of C9ORF72 Causes Chromosome 9p-Linked FTD and ALS. *Neuron*. 72:245–256.
Deng, H.-X., Y. Shi, Y. Furukawa, H. Zhai, R. Fu, E. Liu, G.H. Gorrie, M.S. Khan, W.-Y. Hung, E.H. Bigio, T. Lukas, M.C. Dal Canto, T. V. O'Halloran, and T. Siddique. 2006. Conversion to the amyotrophic lateral sclerosis phenotype is associated with intermolecular linked insoluble aggregates of SOD1 in mitochondria. *Proc. Natl. Acad. Sci.* 103:7142–7147.
Deng, H., K. Gao, and J. Jankovic. 2014. The role of FUS gene variants in neurodegenerative diseases. *Nat. Rev. Neurol.* 10:337–348.

Deng, W., C. Garrett, B. Dombert, V. Soura, G. Banks, E.M.C. Fisher, M.P. Van Der Brug, and M. Hafezparast. 2010. Neurodegenerative mutation in cytoplasmic dynein alters its organization and dynein-dynactin and dynein-kinesin interactions. *J. Biol. Chem.* 285:39922–39934.

Deng, Z., K. Purtell, V. Lachance, M.S. Wold, S. Chen, and Z. Yue. 2017a. Autophagy Receptors and Neurodegenerative Diseases. *Trends Cell Biol.* 27:491–504.

Deng, Z., P. Sheehan, S. Chen, and Z. Yue. 2017b. Is amyotrophic lateral sclerosis/frontotemporal dementia an autophagy disease? *Mol. Neurodegener.* 12:1–11.

Deramaudt, T.B., D. Dujardin, F. Noulet, S. Martin, R. Vauchelles, K. Takeda, and P. Ronde. 2014. Altering FAK-paxillin interactions reduces adhesion, migration and invasion processes. *PLoS One*. 9:e92059.

Le Devedec, S.E., B. Geverts, H. de Bont, K. Yan, F.J. Verbeek, a. B. Houtsmuller, and B. van de Water. 2012. The residence time of focal adhesion kinase (FAK) and paxillin at focal adhesions in renal epithelial cells is determined by adhesion size, strength and life cycle status. *J. Cell Sci.* 125:4498–4506.

Devireddy, S., A. Liu, T. Lampe, and P.J. Hollenbeck. 2015. The Organization of Mitochondrial Quality Control and Life Cycle in the Nervous System In Vivo in the Absence of PINK1. *J. Neurosci.* 35:9391–9401.

Ding, D., Z. Chen, K. Li, Z. Long, W. Ye, Z. Tang, K. Xia, R. Qiu, B. Tang, and H. Jiang. 2016. Identification of a de novo DYNC1H1 mutation via WES according to published guidelines. *Sci. Rep.* 6:20423.

Dion, P. a, H. Daoud, and G. a Rouleau. 2009. Genetics of motor neuron disorders: new insights into pathogenic mechanisms. *Nat. Rev. Genet.* 10:769–82.

Dodding, M.P. 2014. Backseat drivers: Regulation of dynein motility. *Cell Res.* 24:1385–1386.

Dompierre, J.P., J.D. Godin, B.C. Charrin, F.P. Cordelières, S.J. King, S. Humbert, and F. Saudou. 2007. Histone deacetylase 6 inhibition compensates for the transport deficit in Huntington's disease by increasing tubulin acetylation. *J. Neurosci.* 27:3571–3583.

Dormann, D., and C. Haass. 2011. TDP-43 and FUS: a nuclear affair. *Trends Neurosci.* 34:339–48.

Dormann, D., R. Rodde, D. Edbauer, E. Bentmann, I. Fischer, A. Hruscha, M.E. Than, I.R.A. Mackenzie, A. Capell, B. Schmid, M. Neumann, and C. Haass. 2010. ALS-associated fused in sarcoma (FUS) mutations disrupt Transportin-mediated nuclear import. *EMBO J.* 29:2841–2857.

Dreser, A., J.T. Vollrath, A. Sechi, S. Johann, A. Roos, A. Yamoah, I. Katona, S. Bohlega, D. Wiemuth, Y. Tian, A. Schmidt, J. Vervoorts, M. Dohmen, C. Beyer, J. Anink, E. Aronica, D. Troost, J. Weis, and A. Goswami. 2017. The ALS-linked E102Q mutation in Sigma receptor-1 leads to ER stress-mediated defects in protein homeostasis and dysregulation of RNA-binding proteins. *Cell Death Differ.* 24:1655–1671.

Dupuis, L., A. Fergani, K.E. Braunstein, J. Eschbach, N. Holl, F. Rene, J.L. Gonzalez De Aguilar, B. Zoerner, B. Schwalenstocker, A.C. Ludolph, and J.P. Loeffler. 2009. Mice with a mutation in the dynein heavy chain 1 gene display sensory neuropathy but lack motor neuron disease. *Exp. Neurol.* 215:146–152.

Ederle, H., and D. Dormann. 2017. TDP-43 and FUS en route from the nucleus to the cytoplasm. *FEBS Lett.* 591:1489–1507.

Efimov, A., A. Kharitonov, N. Efimova, J. Loncarek, P.M. Miller, N. Andreyeva, P. Gleeson, N. Galjart, A.R.R. Maia, I.X. McLeod, J.R. Yates, H. Maiato, A. Khodjakov, A. Akhmanova, and I. Kaverina. 2007. Asymmetric CLASP-Dependent Nucleation of Noncentrosomal Microtubules at the trans-Golgi Network. *Dev. Cell*. 12:917–930.

El-Kadi, A.M., V. Bros-Facer, W. Deng, A. Philpott, E. Stoddart, G. Banks, G.S. Jackson, E.M.C. Fisher, M.R. Duchen, L. Greensmith, A.L. Moore, and M. Hafezparast. 2010. The Legs at odd angles (Loa) mutation in cytoplasmic dynein ameliorates mitochondrial function in SOD1G93A mouse model for motor neuron disease. *J. Biol. Chem.* 285:18627–18639.

Elsheikh, B., T. Prior, X. Zhang, R. Miller, S.J. Kolb, D.A.N. Moore, W. Bradley, R. Barohn, W. Bryan, D. Gelinas, S. Iannaccone, R. Leshner, J.R. Mendell, M. Mendoza, B. Russman, S. Smith, W. King, and J.T. Kissel. 2009. An analysis of disease severity based on SMN2 copy number in adults with spinal muscular atrophy. *Muscle and Nerve*. 40:652–656.

Epstein, C.J., K.B. Avraham, M. Lovett, S. Smith, O. Elroy-Stein, G. Rotman, C. Bry, and Y. Groner. 1987. Transgenic mice with increased Cu/Zn-superoxide dismutase activity: animal model of dosage effects in Down syndrome. *Proc. Natl. Acad. Sci. U. S. A.* 84:8044–8.

Eréndira Avendaño-Vázquez, S., A. Dhir, S. Bembich, E. Buratti, N. Proudfoot, and F.E. Baralle. 2012. Autoregulation of TDP-43 mRNA levels involves interplay between transcription, splicing, and alternative polyA site selection. *Genes Dev.* 26:1679–1684.

Fallini, C., G.J. Bassell, and W. Rossoll. 2012. The ALS disease protein TDP-43 is actively transported in motor neuron axons and regulates axon outgrowth. *Hum. Mol. Genet.* 21:3703–3718.

Faravelli, I., M. Nizzardo, G.P. Comi, and S. Corti. 2015. Spinal muscular atrophy—recent therapeutic advances for an old challenge. *Nat. Rev. Neurol.* 11:351–359.

Farg, M.A., V. Sundaramoorthy, J.M. Sultana, S. Yang, R.A.K. Atkinson, V. Levina, M.A. Halloran, P.A. Gleeson, I.P. Blair, K.Y. Soo, A.E. King, and J.D. Atkin. 2014. C9ORF72, implicated in amytrophic lateral sclerosis and frontotemporal dementia, regulates endosomal trafficking. *Hum. Mol. Genet.* 23:3579–3595.

Farrer, M.J., M.M. Hulihan, J.M. Kachergus, J.C. Dächsel, A.J. Stoessl, L.L. Grantier, S. Calne, D.B. Calne, B. Lechevalier, F. Chapon, Y. Tsuboi, T. Yamada, L. Gutmann, B. Elibol, K.P. Bhatia, C. Wider, C. Vilariño-Güell, O.A. Ross, L.A. Brown, M. Castanedes-Casey, D.W. Dickson, and Z.K. Wszolek. 2009. DCTN1 mutations in Perry syndrome. *Nat. Genet.* 41:163–165.

Feldkötter, M., V. Schwarzer, R. Wirth, T.F. Wienker, and B. Wirth. 2002. Quantitative Analyses of SMN1 and SMN2 Based on Real-Time LightCycler PCR: Fast and Highly Reliable Carrier Testing and Prediction of Severity of Spinal Muscular Atrophy. *Am. J. Hum. Genet.* 70:358–368.

Ferguson, T. a, and L.B. Elman. 2007. Clinical presentation and diagnosis of amyotrophic lateral sclerosis. *NeuroRehabilitation*. 22:409–16.

Fiesel, F.C., A. Voigt, S.S. Weber, C. Van den Haute, A. Waldenmaier, K. Görner, M. Walter, M.L. Anderson, J. V Kern, T.M. Rasse, T. Schmidt, W. Springer, R. Kirchner, M. Bonin, M. Neumann, V. Baekelandt, M. Alunni-Fabbroni, J.B. Schulz, and P.J. Kahle. 2010. Knockdown of transactive response DNA-binding protein (TDP-43) downregulates histone deacetylase 6. *EMBO J.* 29:209–221.

Filali, M., R. Lalonde, and S. Rivest. 2011. Sensorimotor and cognitive functions in a SOD1G37R transgenic mouse model of amyotrophic lateral sclerosis. *Behav. Brain Res.* 225:215–221.

Fiorillo, C., F. Moro, G. Brisca, A. Accogli, F. Trucco, R. Trovato, M. Pedemonte, M. Severino, M. Catala, V. Capra, F.M. Santorelli, C. Bruno, A. Rossi, and C. Minetti. 2016. Beyond spinal muscular atrophy with lower extremity dominance: Cerebellar hypoplasia associated with a novel mutation in BICD2. *Eur. J. Neurol.* 23:e19–e21.

Fiorillo, C., F. Moro, J. Yi, S. Weil, G. Brisca, G. Astrea, M. Severino, A. Romano, R. Battini, A. Rossi, C. Minetti, C. Bruno, F.M. Santorelli, and R. Vallee. 2014. Novel dynein DYNC1H1 neck and motor domain mutations link distal spinal muscular atrophy and abnormal cortical development. *Hum. Mutat.* 35:298–302.

Forscher, P., and S.J. Smith. 1988. Actions of Cytochalasins on the Organization of Actin-Filaments and Microtubules in a Neuronal Growth Cone. *J. Cell Biol.* 107:1505–1516.

Fratta, P., M. Poulter, T. Lashley, J.D. Rohrer, J.M. Polke, J. Beck, N. Ryan, D. Hensman, S. Mizielinska, A.J. Waite, M.C. Lai, T.F. Gendron, L. Petrucelli, E.M.C. Fisher, T. Revesz, J.D. Warren, J. Collinge, A.M. Isaacs, and S. Mead. 2013. Homozygosity for the C9orf72 GGGGCC repeat expansion in frontotemporal dementia. *Acta*

Neuropathol. 126:401–409.
Freibaum, B., and R. Chitta. 2010. Global analysis of TDP-43 interacting proteins reveals strong association with RNA splicing and translation machinery Brian. *J Proteome Res.* 9:1104–1120.
Freibaum, B.D., and J.P. Taylor. 2017. The Role of Dipeptide Repeats in C9ORF72-Related ALS-FTD. *Front. Mol. Neurosci.* 10:1–9.
Fu, M. meng, J.J. Nirschl, and E.L.F. Holzbaur. 2014. LC3 Binding to the scaffolding protein jip1 regulates processive dynein-driven transport of autophagosomes. *Dev. Cell*. 29:577–590.
Fujii, R., S. Okabe, T. Urushido, K. Inoue, A. Yoshimura, T. Tachibana, T. Nishikawa, G.G. Hicks, and T. Takumi. 2005. The RNA binding protein TLS is translocated to dendritic spines by mGluR5 activation and regulates spine morphology. *Curr. Biol.* 15:587–593.
Fumoto, K., C.C. Hoogenraad, and A. Kikuchi. 2006. GSK-3β-regulated interaction of BICD with dynein is involved in microtubule anchorage at centrosome. *EMBO J.* 25:5670–5682.
Gao, F., S. Almeida, and R. Lopez-Gonzalez. 2017. Dysregulated molecular pathways in amyotrophic lateral sclerosis–frontotemporal dementia spectrum disorder. *EMBO J.* 36:e201797568.
Garg, N., S.B. Park, S. Vucic, C. Yiannikas, J. Spies, J. Howells, W. Huynh, J.M. Matamala, A. V Krishnan, J.D. Pollard, D.R. Cornblath, M.M. Reilly, and M.C. Kiernan. 2016. Differentiating lower motor neuron syndromes. *J. Neurol. Neurosurg. Psychiatry*. 88:jnnp-2016-313526.
Garrett, C. a., M. Barri, A. Kuta, V. Soura, W. Deng, E.M.C. Fisher, G. Schiavo, and M. Hafezparast. 2014. DYNC1H1 mutation alters transport kinetics and ERK1/2-cFos signalling in a mouse model of distal spinal muscular atrophy. *Brain*. 137:1883–1893.
Gautier, G., A. Verschueren, A. Monnier, S. Attarian, E. Salort-Campana, and J. Pouget. 2010. ALS with respiratory onset: Clinical features and effects of non-invasive ventilation on the prognosis. *Amyotroph. Lateral Scler.* 11:379–382.
Gentil, B.J., J.R. McLean, S. Xiao, B. Zhao, H.D. Durham, and J. Robertson. 2014. A two-hybrid screen identifies an unconventional role for the intermediate filament peripherin in regulating the subcellular distribution of the SNAP25-interacting protein, SIP30. *J. Neurochem.* 131:588–601.
Gerbino, V., M.T. Carrì, M. Cozzolino, and T. Achsel. 2013. Mislocalised FUS mutants stall spliceosomal snRNPs in the cytoplasm. *Neurobiol. Dis.* 55:120–128.
Gibbons, I.R. 1963. Studies on the Protein Components of Cilia From Tetrahymena Pyriformis. *Proc. Natl. Acad. Sci. U. S. A.* 50:1002–1010.
Gibbons, I.R., and A.J. Rowe. 1965. Dynein: A Protein with Adenosine Triphosphatase Activity from Cilia. *Science*. 149:424–426.
Gitler, A.D., and J. Shorter. 2011. RNA-binding proteins with prion-like domains in ALS and FTLD-U. *Prion*. 5:179–187.
Gitler, A.D., and H. Tsuiji. 2016. There has been an awakening: Emerging mechanisms of C9orf72 mutations in FTD/ALS. *Brain Res.* 1647:19–29.
Lo Giudice, T., F. Lombardi, F.M. Santorelli, T. Kawarai, and A. Orlacchio. 2014. Hereditary spastic paraplegia: Clinical-genetic characteristics and evolving molecular mechanisms. *Exp. Neurol.* 261:518–539.
Goldstein, M.E., P. Grant, S.B. House, D.B. Henken, and H. Gainer. 1996. Developmental regulation of two distinct neuronal phenotypes in rat dorsal root ganglia. *Neuroscience*. 71:243–258.
Goldstein, M.E., S.B. House, and H. Gainer. 1991. NF-L and peripherin immunoreactivities define distinct classes of rat sensory ganglion cells. *J. Neurosci. Res.* 30:92–104.
Gomez-Suaga, P., S. Paillusson, R. Stoica, W. Noble, D.P. Hanger, and C.C.J. Miller. 2017. The ER-Mitochondria Tethering Complex VAPB-PTPIP51 Regulates Autophagy. *Curr. Biol.* 27:371–385.

Gordon, P.H., B. Cheng, I.B. Katz, M. Pinto, A.P. Hays, H. Mitsumoto, and L.P. Rowland. 2006. The natural history of primary lateral sclerosis. *Neurology*. 66:647–653.
Grabham, P.W., G.E. Seale, M. Bennecib, D.J. Goldberg, and R.B. Vallee. 2007. Cytoplasmic Dynein and LIS1 Are Required for Microtubule Advance during Growth Cone Remodeling and Fast Axonal Outgrowth. *J. Neurosci.* 27:5823–5834.
Graffmo, K.S., K. Forsberg, J. Bergh, A. Birve, P. Zetterström, P.M. Andersen, S.L. Marklund, and T. Brännström. 2013. Expression of wild-type human superoxide dismutase-1 in mice causes amyotrophic lateral sclerosis. *Hum. Mol. Genet.* 22:51–60.
Granger, E., G. McNee, V. Allan, and P. Woodman. 2014. The role of the cytoskeleton and molecular motors in endosomal dynamics. *Semin. Cell Dev. Biol.* 31:20–29.
Gregory, R.I., K. Yan, G. Amuthan, T. Chendrimada, B. Doratotaj, N. Cooch, and R. Shiekhattar. 2004. The Microprocessor complex mediates the genesis of microRNAs. *Nature*. 432:235–240.
Grigoriev, I., D. Splinter, N. Keijzer, P.S. Wulf, J. Demmers, T. Ohtsuka, M. Modesti, I. V. Maly, F. Grosveld, C.C. Hoogenraad, and A. Akhmanova. 2007. Rab6 Regulates Transport and Targeting of Exocytotic Carriers. *Dev. Cell*. 13:305–314.
Gros-Louis, F., R. Larivière, G. Gowing, S. Laurent, W. Camu, J.-P. Bouchard, V. Meininger, G. a Rouleau, and J.-P. Julien. 2004. A frameshift deletion in peripherin gene associated with amyotrophic lateral sclerosis. *J. Biol. Chem.* 279:45951–6.
Guerrero, E.N., H. Wang, J. Mitra, P.M. Hegde, S.E. Stowell, N.F. Liachko, B.C. Kraemer, R.M. Garruto, K.S. Rao, and M.L. Hegde. 2016. TDP-43/FUS in motor neuron disease: Complexity and challenges. *Prog. Neurobiol.* 145–146:78–97.
Gundersen, G.G., S. Khawaja, and J.C. Bulinski. 1987. Postpolymerization detyrosination of alpha-tubulin: a mechanism for subcellular differentiation of microtubules. *J. Cell Biol.* 105:251–264.
Gurney, M.E., H. Pu, A.Y. Chiu, M.C. Dal Canto, C.Y. Polchow, D.D. Alexander, J. Caliendo, A. Hentati, Y.W. Kwon, and H.X. Deng. 1994. Motor neuron degeneration in mice that express a human Cu,Zn superoxide dismutase mutation. *Science*. 264:1772–5.
Haase, G., and C. Rabouille. 2015. Golgi fragmentation in ALS motor neurons. New mechanisms targeting microtubules, tethers, and transport vesicles. *Front. Neurosci.* 9.
Haeusler, A.R., C.J. Donnelly, G. Periz, E.A.J. Simko, P.G. Shaw, M.-S. Kim, N.J. Maragakis, J.C. Troncoso, A. Pandey, R. Sattler, J.D. Rothstein, and J. Wang. 2014. C9orf72 nucleotide repeat structures initiate molecular cascades of disease. *Nature*. 507:195–200.
Haeusler, A.R., C.J. Donnelly, and J.D. Rothstein. 2016. The expanding biology of the C9orf72 nucleotide repeat expansion in neurodegenerative disease. *Nat. Rev. Neurosci.* 17:383–395.
Hafezparast, M., R. Klocke, C. Ruhrberg, A. Marquardt, A. Ahmad-Annuar, S. Bowen, G. Lalli, A.S. Witherden, H. Hummerich, S. Nicholson, P.J. Morgan, R. Oozageer, J. V. Priestley, S. Averill, V.R. King, S. Ball, J. Peters, T. Toda, A. Yamamoto, Y. Hiraoka, M. Augustin, D. Korthaus, S. Wattler, P. Wabnitz, C. Dickneite, S. Lampel, F. Boehme, G. Peraus, A. Popp, M. Rudelius, J. Schlegel, H. Fuchs, M.H. De Angelis, G. Schiavo, D.T. Shima, A.P. Russ, G. Stumm, J.E. Martin, and E.M.C. Fisher. 2003. Mutations in dynein link motor neuron degeneration to defects in retrograde transport. *Science*. 300:808–812.
Han-Xiang, D., J. Hujun, F. Ronggen, Z. Hong, S. Yong, L. Erdong, H. Makito, C.D.C. Mauro, and S. Teepu. 2008. Molecular dissection of ALS-associated toxicity of SOD1 in transgenic mice using an exon-fusion approach. *Hum. Mol. Genet.* 17:2310–2319.
Harada, A., Y. Takei, Y. Kanai, Y. Tanaka, S. Nonaka, and N. Hirokawa. 1998. Golgi vesiculation and lysosome dispersion in cells lacking cytoplasmic dynein. *J. Cell Biol.* 141:51–59.
Hardiman, O., L.H. van den Berg, and M.C. Kiernan. 2011. Clinical diagnosis and

management of amyotrophic lateral sclerosis. *Nat. Rev. Neurol.* 7:639–649.
Harms, M.B., P. Allred, R. Gardner, J. a Fernandes Filho, J. Florence, a Pestronk, M. Al-Lozi, and R.H. Baloh. 2010. Dominant spinal muscular atrophy with lower extremity predominance: linkage to 14q32. *Neurology*. 75:539–46.
Harms, M.B., K.M. Ori-McKenney, M. Scoto, E.P. Tuck, S. Bell, D. Ma, S. Masi, P. Allred, M. Al-Lozi, M.M. Reilly, L.J. Miller, A. Jani-Acsadi, A. Pestronk, M.E. Shy, F. Muntoni, R.B. Vallee, and R.H. Baloh. 2012. Mutations in the tail domain of DYNC1H1 cause dominant spinal muscular atrophy. *Neurology*. 78:1714–20.
Harper, J. V. 2005. Synchronization of Cell Populations in G1/S and G M Phases of the Cell Cycle. *Methods Mol. Biol.* 296:12–13.
Harrison, A.F., and J. Shorter. 2017. RNA-binding proteins with prion-like domains in health and disease. *Biochem. J.* 474:1417–1438.
Hawley, Z.C.E., D. Campos-Melo, C.A. Droppelmann, and M.J. Strong. 2017. MotomiRs: miRNAs in Motor Neuron Function and Disease. *Front. Mol. Neurosci.* 10:1–19.
He, C.Z., and A.P. Hays. 2004. Expression of peripherin in ubiquinated inclusions of amyotrophic lateral sclerosis. *J. Neurol. Sci.* 217:47–54.
Hedberg, K., and L.A.N.B.O. Chen. 1986. Absence of Intermediate Filaments in a Human Adrenal Cortex Carcinoma-derived they vary strikingly in polypeptide composition , depending on cell type [2-4]. In polypeptide of 55 kD); IFS of muscle cells , desmin (52 kD); IFS of glial cells , glial k. 163:509–517.
Hedlund, E., M. Karlsson, T. Osborn, W. Ludwig, and O. Isacson. 2010. Global gene expression profiling of somatic motor neuron populations with different vulnerability identify molecules and pathways of degeneration and protection. *Brain*. 133:2313–2330.
Helfand, B.T., M.G. Mendez, J. Pugh, C. Delsert, and R.D. Goldman. 2003. A Role for Intermediate Filaments in Determining and Maintaining the Shape of Nerve Cells. *Mol. Biol. Cell*. 14:5069–5081.
Hendrickson, B.C., C. Donohoe, V.R. Akmaev, E.A. Sugarman, P. Labrousse, L. Boguslavskiy, K. Flynn, E.M. Rohlfs, A. Walker, B. Allitto, C. Sears, and T. Scholl. 2009. Differences in SMN1 allele frequencies among ethnic groups within North America. *J. Med. Genet.* 46:641–644.
Hicks, G.G., N. Singh, a Nashabi, S. Mai, G. Bozek, L. Klewes, D. Arapovic, E.K. White, M.J. Koury, E.M. Oltz, L. Van Kaer, and H.E. Ruley. 2000. Fus deficiency in mice results in defective B-lymphocyte development and activation, high levels of chromosomal instability and perinatal death. *Nat. Genet.* 24:175–9.
Ho, C.L., S.S. Chin, K. Carnevale, and R.K. Liem. 1995. Translation initiation and assembly of peripherin in cultured cells. *Eur. J. Cell Biol.* 68:103–12.
Hoang, H.T., M.A. Schlager, A.P. Carter, and S.L. Bullock. 2017. DYNC1H1 mutations associated with neurological diseases compromise processivity of dynein–dynactin–cargo adaptor complexes. *Proc. Natl. Acad. Sci.* 114:E1597–E1606.
Hoell, J.I., E. Larsson, S. Runge, J.D. Nusbaum, S. Duggimpudi, T.A. Farazi, M. Hafner, A. Borkhardt, C. Sander, and T. Tuschl. 2011. RNA targets of wild-type and mutant FET family proteins. *Nat. Struct. Mol. Biol.* 18:1428–1431.
Hoogenraad, C.C., and A. Akhmanova. 2016. Bicaudal D Family of Motor Adaptors: Linking Dynein Motility to Cargo Binding. *Trends Cell Biol.* 26:327–340.
Hoogenraad, C.C., A. Akhmanova, S.A. Howell, B.R. Dortland, C.I. De Zeeuw, R. Willemsen, P. Visser, F. Grosveld, and N. Galjart. 2001. Mammalian golgi-associated Bicaudal-D2 functions in the dynein-dynactin pathway by interacting with these complexes. *EMBO J.* 20:4041–4054.
Hoogenraad, C.C., P. Wulf, N. Schiefermeier, T. Stepanova, N. Galjart, J.V. Small, F. Grosveld, C.I. De Zeeuw, and A. Akhmanova. 2003. Bicaudal D induces selective dynein-mediated microtubule minus end-directed transport. *EMBO J.* 22:6004–6015.
Howes, S.C., G.M. Alushin, T. Shida, M. V. Nachury, and E. Nogales. 2014. Effects of tubulin acetylation and tubulin acetyltransferase binding on microtubule structure. *Mol. Biol. Cell*. 25:257–66.

Hoyle, J.C., M.C. Isfort, J. Roggenbuck, D. Arnold, and C. Hoyle. 2015. The genetics of Charcot–Marie–Tooth disease: Current trends and future implications for diagnosis and management. *Appl Clin Genet*. 8:235–243.
Hu, D.J.K., A.D. Baffet, T. Nayak, A. Akhmanova, V. Doye, and R.B. Vallee. 2013. Dynein recruitment to nuclear pores activates apical nuclear migration and mitotic entry in brain progenitor cells. *Cell*. 154.
Hu, Y., S. Lu, K.W. Szeto, J. Sun, Y. Wang, J.C. Lasheras, and S. Chien. 2014. FAK and paxillin dynamics at focal adhesions in the protrusions of migrating cells. *Sci. Rep.* 4:6024.
Huang, X., and D. Fan. 2017. A novel mutation of BICD2 gene associated with juvenile amyotrophic lateral sclerosis. *Amyotroph. Lateral Scler. Front. Degener.* 18:1–3.
Hukema, R.K., F.W. Riemslagh, S. Melhem, H.C. van der Linde, L.-A.W.F.M. Severijnen, D. Edbauer, A. Maas, N. Charlet-Berguerand, R. Willemsen, and J.C. van Swieten. 2014. A new inducible transgenic mouse model for C9orf72-associated GGGGCC repeat expansion supports a gain-of-function mechanism in C9orf72-associated ALS and FTD. *Acta Neuropathol. Commun.* 2:166.
Hukema, R.K., F.W. Riemslagh, S. Melhem, H.C. van der Linde, L.-A.W.F.M. Severijnen, D. Edbauer, A. Maas, N. Charlet-Berguerand, R. Willemsen, and J.C. van Swieten. 2016. Retraction Note to: A new inducible transgenic mouse model for C9orf72-associated GGGGCC repeat expansion supports a gain-of-function mechanism in C9orf72-associated ALS and FTD. *Acta Neuropathol. Commun.* 4:129.
Huotari, J., and A. Helenius. 2011. Endosome maturation. *EMBO J.* 30:3481–500.
Hurtado, L., C. Caballero, M.P. Gavilan, J. Cardenas, M. Bornens, and R.M. Rios. 2011. Disconnecting the Golgi ribbon from the centrosome prevents directional cell migration and ciliogenesis. *J. Cell Biol.* 193:917–933.
Hutagalung, A.H., and P.J. Novick. 2011. Role of Rab GTPases in Membrane Traffic and Cell Physiology. *Physiol. Rev.* 91:119–149.
Huttenlocher, A. 2005. Cell polarization mechanisms during directed cell migration. *Nat. Cell Biol.* 7:336–337.
Igaz, L.M., L.K. Kwong, E.B. Lee, A. Chen-Plotkin, E. Swanson, T. Unger, J. Malunda, Y. Xu, M.J. Winton, J.Q. Trojanowski, and V.M.Y. Lee. 2011. Dysregulation of the ALS-associated gene TDP-43 leads to neuronal death and degeneration in mice. *J. Clin. Invest.* 121:726–738.
Iguchi, Y., M. Katsuno, J.I. Niwa, S. Takagi, S. Ishigaki, K. Ikenaka, K. Kawai, H. Watanabe, K. Yamanaka, R. Takahashi, H. Misawa, S. Sasaki, F. Tanaka, and G. Sobue. 2013. Loss of TDP-43 causes age-dependent progressive motor neuron degeneration. *Brain*. 136:1371–1382.
Ilić, D., Y. Furuta, S. Kanazawa, N. Takeda, K. Sobue, N. Nakatsuji, S. Nomura, J. Fujimoto, M. Okada, and T. Yamamoto. 1995. Reduced cell motility and enhanced focal adhesion contact formation in cells from FAK-deficient mice. *Nature*. 377:539–544.
Ilieva, H.S., K. Yamanaka, S. Malkmus, O. Kakinohana, T. Yaksh, M. Marsala, and D.W. Cleveland. 2008. Mutant dynein (Loa) triggers proprioceptive axon loss that extends survival only in the SOD1 ALS model with highest motor neuron death. *Proc. Natl. Acad. Sci.* 105:12599–12604.
Ince, P.G., J. Evans, M. Knopp, G. Forster, H.H.M. Hamdalla, S.B. Wharton, and P.J. Shaw. 2003. Corticospinal tract degeneration in the progressive muscular atrophy variant of ALS. *Neurology*. 60:1252–1258.
Ishigaki, S., A. Masuda, Y. Fujioka, Y. Iguchi, M. Katsuno, A. Shibata, F. Urano, G. Sobue, and K. Ohno. 2012. Position-dependent FUS-RNA interactions regulate alternative splicing events and transcriptions. *Sci. Rep.* 2:1–8.
Ishikawa, H., and W.F. Marshall. 2011. Ciliogenesis: building the cell's antenna. *Nat. Rev. Mol. Cell Biol.* 12:222–234.
Islam, M.T. 2017. Oxidative stress and mitochondrial dysfunction-linked neurodegenerative disorders. *Neurol. Res.* 39:73–82.

Jaarsma, D., E.D. Haasdijk, J.A.C. Grashorn, R. Hawkins, W. van Duijn, H.W. Verspaget, J. London, and J.C. Holstege. 2000. Human Cu/Zn Superoxide Dismutase (SOD1) Overexpression in Mice Causes Mitochondrial Vacuolization, Axonal Degeneration, and Premature Motoneuron Death and Accelerates Motoneuron Disease in Mice Expressing a Familial Amyotrophic Lateral Sclerosis Mutant SO. *Neurobiol. Dis.* 7:623–643.

Jaarsma, D., and C.C. Hoogenraad. 2015. Cytoplasmic dynein and its regulatory proteins in Golgi pathology in nervous system disorders. *Front. Neurosci.* 9:397.

Jaarsma, D., E. Teuling, E.D. Haasdijk, C.I. De Zeeuw, and C.C. Hoogenraad. 2008. Neuron-Specific Expression of Mutant Superoxide Dismutase Is Sufficient to Induce Amyotrophic Lateral Sclerosis in Transgenic Mice. *J. Neurosci.* 28:2075–2088.

Janke, C., and J. Chloë Bulinski. 2011. Post-translational regulation of the microtubule cytoskeleton: mechanisms and functions. *Nat. Rev. Mol. Cell Biol.* 12:773–786.

Jansen, K.A., P. Atherton, and C. Ballestrem. 2017. Mechanotransduction at the Cell-Matrix Interface. *Semin. Cell Dev. Biol.*

Janssens, J., H. Wils, G. Kleinberger, G. Joris, I. Cuijt, C. Ceuterick-De Groote, C. Van Broeckhoven, and S. Kumar-Singh. 2013. Overexpression of ALS-associated p.M337V human TDP-43 in mice worsens disease features compared to wild-type human TDP-43 mice. *Mol. Neurobiol.* 48:22–35.

Jeyifous, O., C.L. Waites, C.G. Specht, S. Fujisawa, M. Schubert, E.I. Lin, J. Marshall, C. Aoki, T. de Silva, J.M. Montgomery, C.C. Garner, W.N. Green, T. De Silva, and M. Johanna. 2009. SAP97 and CASK mediate sorting of N-Methyl-D-Aspartate Receptors through a novel secretory pathway. *Nature*. 12:1011–1019.

Jiang, J., Q. Zhu, T.F. Gendron, S. Saberi, M. McAlonis-Downes, A. Seelman, J.E. Stauffer, P. Jafar-nejad, K. Drenner, D. Schulte, S. Chun, S. Sun, S.C. Ling, B. Myers, J. Engelhardt, M. Katz, M. Baughn, O. Platoshyn, M. Marsala, A. Watt, C.J. Heyser, M.C. Ard, L. De Muynck, L.M. Daughrity, D.A. Swing, L. Tessarollo, C.J. Jung, A. Delpoux, D.T. Utzschneider, S.M. Hedrick, P.J. de Jong, D. Edbauer, P. Van Damme, L. Petrucelli, C.E. Shaw, C.F. Bennett, S. Da Cruz, J. Ravits, F. Rigo, D.W. Cleveland, and C. Lagier-Tourenne. 2016. Gain of Toxicity from ALS/FTD-Linked Repeat Expansions in C9ORF72 Is Alleviated by Antisense Oligonucleotides Targeting GGGGCC-Containing RNAs. *Neuron*. 90:535–550.

Jonsson, P.A., K. Ernhill, P.M. Andersen, D. Bergemalm, T. Brännström, O. Gredal, P. Nilsson, and S.L. Marklund. 2004. Minute quantities of misfolded mutant superoxide dismutase-1 cause amyotrophic lateral sclerosis. *Brain*. 127:73–88.

Jonsson, P.A., K.S. Graffmo, T. Brännström, P. Nilsson, P.M. Andersen, and S.L. Marklund. 2006. Motor neuron disease in mice expressing the wild type-like D90A mutant superoxide dismutase-1. *J. Neuropathol. Exp. Neurol.* 65:1126–1136.

Joyce, P.I., P. Fratta, E.M.C. Fisher, and A. Acevedo-Arozena. 2011. SOD1 and TDP-43 animal models of amyotrophic lateral sclerosis: Recent advances in understanding disease toward the development of clinical treatments. *Mamm. Genome*. 22:420–448.

Joyce, P.I., P. Mcgoldrick, R.A. Saccon, W. Weber, P. Fratta, S.J. West, N. Zhu, S. Carter, V. Phatak, M. Stewart, M. Simon, S. Kumar, I. Heise, V. Bros-Facer, J. Dick, S. Corrochano, M.J. Stanford, T.V. Luong, P.M. Nolan, T. Meyer, S. Brandner, D.L.H. Bennett, P. Hande Ozdinler, L. Greensmith, E.M.C. Fisher, and A. Acevedo-Arozena. 2014. A novel SOD1-ALS mutation separates central and peripheral effects of mutant SOD1 toxicity. *Hum. Mol. Genet.* 24:1883–1897.

Juntas Morales, R., N. Pageot, G. Taieb, and W. Camu. 2016. Adult-onset spinal muscular atrophy: An update. *Rev. Neurol. (Paris).* 173:1–12.

Kabashi, E., P.N. Valdmanis, P. Dion, D. Spiegelman, B.J. McConkey, C. Vande Velde, J.-P. Bouchard, L. Lacomblez, K. Pochigaeva, F. Salachas, P.-F. Pradat, W. Camu, V. Meininger, N. Dupre, and G. a Rouleau. 2008. TARDBP mutations in individuals with sporadic and familial amyotrophic lateral sclerosis. *Nat. Genet.* 40:572–4.

Kalebic, N., C. Martinez, E. Perlas, P. Hublitz, D. Bilbao-Cortes, K. Fiedorczuk, A.

Andolfo, and P.A. Heppenstall. 2013. Tubulin Acetyltransferase TAT1 Destabilizes Microtubules Independently of Its Acetylation Activity. *Mol. Cell. Biol.* 33:1114–1123.
Kandel, E.R., J.H. Schwartz, T.M. Jessel, S.A. Siegelbaum, and A.J. Hudspeth. 2013. Principles of neural science. McGraw-Hill, New York.
Kaneko-Kawano, T., F. Takasu, H. Naoki, Y. Sakumura, S. Ishii, T. Ueba, A. Eiyama, A. Okada, Y. Kawano, and K. Suzuki. 2012. Dynamic regulation of myosin light chain phosphorylation by Rho-kinase. *PLoS One*. 7:1–10.
Kanellos, G., and M.C. Frame. 2016. Cellular functions of the ADF/cofilin family at a glance. *J. Cell Sci.* 129:3211–8.
Kang, J.S., J.H. Tian, P.Y. Pan, P. Zald, C. Li, C. Deng, and Z.H. Sheng. 2008. Docking of Axonal Mitochondria by Syntaphilin Controls Their Mobility and Affects Short-Term Facilitation. *Cell*. 132:137–148.
Kapeli, K., F.J. Martinez, and G.W. Yeo. 2017. Genetic mutations in RNA-binding proteins and their roles in ALS. *Hum. Genet.* 1–22.
Karch, C.M., and D.R. Borchelt. 2010. An examination of αb-crystallin as a modifier of SOD1 aggregate pathology and toxicity in models of familial amyotrophic lateral sclerosis. *J. Neurochem.* 113:1092–1100.
Kato, S., M. Takikawa, K. Nakashima, A. Hirano, D.W. Cleveland, H. Kusaka, N. Shibata, M. Kato, I. Nakano, and E. Ohama. 2000. New consensus research on neuropathological aspects of familial amyotrophic lateral sclerosis with superoxide dismutase 1 (SOD1) gene mutations: inclusions containing SOD1 in neurons and astrocytes. *Amyotroph. Lateral Scler. Other Motor Neuron Disord.* 1:163–184.
Kaur, S.J., S.R. McKeown, and S. Rashid. 2016. Mutant SOD1 mediated pathogenesis of Amyotrophic Lateral Sclerosis. *Gene*. 577:109–118.
Kawaguchi, Y., J.J. Kovacs, A. McLaurin, J.M. Vance, A. Ito, and T.-P. Yao. 2003. The Deacetylase HDAC6 Regulates Aggresome Formation and Cell Viability in Response to Misfolded Protein Stress. *Cell*. 115:727–738.
Kawahara, Y., and A.A. Mieda-Sato. 2012. TDP-43 promotes microRNA biogenesis as a component of the Drosha and Dicer complexes. *Proc. Natl. Acad. Sci. U. S. A.* 109:3347–3352.
Kieran, D., M. Hafezparast, S. Bohnert, J.R.T. Dick, J. Martin, G. Schiavo, E.M.C. Fisher, and L. Greensmith. 2005. A mutation in dynein rescues axonal transport defects and extends the life span of ALS mice. *J. Cell Biol.* 169:561–567.
Kim, H.S., M. Takahashi, K. Matsuo, and Y. Ono. 2007. Recruitment of CG-NAP to the Golgi apparatus through interaction with dynein-dynactin complex. *Genes to Cells*. 12:421–434.
Kimura, S., T. Noda, and T. Yoshimori. 2008. Dynein-dependent movement of autophagosomes mediates efficient encounters with lysosomes. *Cell Struct. Funct.* 33:109–122.
Kino, Y., C. Washizu, M. Kurosawa, M. Yamada, H. Miyazaki, T. Akagi, T. Hashikawa, H. Doi, T. Takumi, G.G. Hicks, N. Hattori, T. Shimogori, and N. Nukina. 2015. FUS/TLS deficiency causes behavioral and pathological abnormalities distinct from amyotrophic lateral sclerosis. *Acta Neuropathol. Commun.* 3:24.
Kon, T., T. Oyama, R. Shimo-Kon, K. Imamula, T. Shima, K. Sutoh, and G. Kurisu. 2012. The 2.8 Å crystal structure of the dynein motor domain. *Nature*. 484:345–350.
Kon, T., K. Sutoh, and G. Kurisu. 2011. X-ray structure of a functional full-length dynein motor domain. *Nat. Struct. Mol. Biol.* 18:638–642.
Kornreich, M., R. Avinery, E. Malka-Gibor, A. Laser-Azogui, and R. Beck. 2015. Order and disorder in intermediate filament proteins. *FEBS Lett.* 589:2464–2476.
Kost, S.A., K. Chacko, and M.M. Oblinger. 1992. Developmental patterns of intermediate filament gene expression in the normal hamster brain. *Brain Res.* 595:270–280.
Kovacs, G.G., J.R. Murrell, S. Horvath, L. Haraszti, K. Majtenyi, M.J. Molnar, H. Budka, B. Ghetti, and S. Spina. 2009. TARDBP variation associated with frontotemporal dementia, supranuclear gaze palsy, and chorea. *Mov. Disord.* 24:1842–1847.
Kraemer, B.C., T. Schuck, J.M. Wheeler, L.C. Robinson, J.Q. Trojanowski, V.M.Y. Lee,

and G.D. Schellenberg. 2010. Loss of Murine TDP-43 disrupts motor function and plays an essential role in embryogenesis. *Acta Neuropathol.* 119:409–419.
Krause, M., and A. Gautreau. 2014. Steering cell migration: lamellipodium dynamics and the regulation of directional persistence. *Nat. Rev. Mol. Cell Biol.* 15:577–590.
Kumar, N., and M. Flavin. 1981. Preferential action of a brain detyrosinolating carboxypeptidase on polymerized tubulin. *J. Biol. Chem.* 256:7678–7686.
Kuo, P.-H., L.G. Doudeva, Y.-T. Wang, C.-K.J. Shen, and H.S. Yuan. 2009. Structural insights into TDP-43 in nucleic-acid binding and domain interactions. *Nucleic Acids Res.* 37:1799–808.
Kwiatkowski, T.J., D.A. Bosco, A.L. LeClerc, E. Tamrazian, C.R. Vanderburg, C. Russ, A. Davis, J. Gilchrist, E.J. Kasarkis, T. Munsat, P. Valdmanis, C.R. Rouleau, B.A. Hosler, P. Cortelli, P.J. de Jong, Y. Yoshinaga, J.L. Haines, M.A. Pericak-Vance, J. Yan, N. Ticozzi, T. Siddique, D. McKenna-Yasek, P.C. Sapp, H.R. Horvitz, J.E. Landers, and R.H. Brown. 2009. Mutations in the FUS/TLS gene on chromosome 16 cause familial amyotrophic lateral sclerosis. *Science*. 323:1205–1208.
Lagier-Tourenne, C., M. Polymenidou, and D.W. Cleveland. 2010. TDP-43 and FUS/TLS: emerging roles in RNA processing and neurodegeneration. *Hum. Mol. Genet.* 19:R46-64.
Lagier-Tourenne, C., M. Polymenidou, K.R. Hutt, A.Q. Vu, M. Baughn, S.C. Huelga, K.M. Clutario, S.-C. Ling, T.Y. Liang, C. Mazur, E. Wancewicz, A.S. Kim, A. Watt, S. Freier, G.G. Hicks, J.P. Donohue, L. Shiue, C.F. Bennett, J. Ravits, D.W. Cleveland, and G.W. Yeo. 2012. Divergent roles of ALS-linked proteins FUS/TLS and TDP-43 intersect in processing long pre-mRNAs. *Nat. Neurosci.* 15:1488–1497.
Laird, F.M., M.H. Farah, S. Ackerley, A. Hoke, N. Maragakis, J.D. Rothstein, J. Griffin, D.L. Price, L.J. Martin, and P.C. Wong. 2008. Motor Neuron Disease Occurring in a Mutant Dynactin Mouse Model Is Characterized by Defects in Vesicular Trafficking. *J. Neurosci.* 28:1997–2005.
Lalmansingh, A.S., C.J. Urekar, and P.P. Reddi. 2011. TDP-43 is a transcriptional repressor: The testis-specific mouse acrv1 gene is a TDP-43 target in vivo. *J. Biol. Chem.* 286:10970–10982.
Lam, C., M.A.S. Vergnolle, L. Thorpe, P.G. Woodman, and V.J. Allan. 2010. Functional interplay between LIS1, NDE1 and NDEL1 in dynein-dependent organelle positioning. *J. Cell Sci.* 123:202–212.
Landers, J.E., J. Melki, V. Meininger, J.D. Glass, L.H. van den Berg, M.A. van Es, P.C. Sapp, P.W.J. van Vught, D.M. McKenna-Yasek, H.M. Blauw, T.-J. Cho, M. Polak, L. Shi, A.-M. Wills, W.J. Broom, N. Ticozzi, V. Silani, A. Ozoguz, I. Rodriguez-Leyva, J.H. Veldink, A.J. Ivinson, C.G.J. Saris, B.A. Hosler, A. Barnes-Nessa, N. Couture, J.H.J. Wokke, T.J. Kwiatkowski, R.A. Ophoff, S. Cronin, O. Hardiman, F.P. Diekstra, P.N. Leigh, C.E. Shaw, C.L. Simpson, V.K. Hansen, J.F. Powell, P. Corcia, F. Salachas, S. Heath, P. Galan, F. Georges, H.R. Horvitz, M. Lathrop, S. Purcell, A. Al-Chalabi, and R.H. Brown. 2009. Reduced expression of the Kinesin-Associated Protein 3 (KIFAP3) gene increases survival in sporadic amyotrophic lateral sclerosis. *Proc. Natl. Acad. Sci. U. S. A.* 106:9004–9.
Landon, F., M. Lemonnier, R. Benarous, C. Huc, M. Fiszman, F. Gros, and M.M. Portier. 1989. Multiple mRNAs encode peripherin, a neuronal intermediate filament protein. *EMBO J.* 8:1719–26.
Landon, F., A. Wolff, and B. De Néchaud. 2000. Mouse peripherin isoforms. *Biol. Cell*. 92:397–407.
Van Langenhove, T., J. van der Zee, and C. Van Broeckhoven. 2012. The molecular basis of the frontotemporal lobar degeneration-amyotrophic lateral sclerosis spectrum. *Ann. Med.* 44:817–28.
Lariviere, R.C., and J.-P. Julien. 2004. Functions of intermediate filaments in neuronal development and disease. *J. Neurobiol.* 58:131–48.
Larivière, R.C., M.D. Nguyen, A. Ribeiro-Da-Silva, and J.P. Julien. 2002. Reduced number of unmyelinated sensory axons in peripherin null mice. *J. Neurochem.*

81:525–532.
Lawson, C., S.T. Lim, S. Uryu, X.L. Chen, D.A. Calderwood, and D.D. Schlaepfer. 2012. FAK promotes recruitment of talin to nascent adhesions to control cell motility. *J. Cell Biol.* 196:223–232.
Lawson, V.H., and W.D. Arnold. 2014. Multifocal motor neuropathy: A review of pathogenesis, diagnosis, and treatment. *Neuropsychiatr. Dis. Treat.* 10:567–576.
Lee, E.B., V.M.-Y. Lee, and J.Q. Trojanowski. 2012. Gains or losses: molecular mechanisms of TDP43-mediated neurodegeneration. *Nat. Rev. Neurosci.* 13:38–50.
Lee, J.K., J.H. Shin, J.E. Lee, and E.J. Choi. 2015. Role of autophagy in the pathogenesis of amyotrophic lateral sclerosis. *Biochim. Biophys. Acta - Mol. Basis Dis.* 1852:2517–2524.
Lefebvre, S., L. Burglen, S. Reboullet, O. Clermont, P. Burlet, L. Viollet, B. Benichou, C. Cruaud, P. Millasseau, M. Zeviani, D. Le Paslier, J. Frezal, D. Cohen, J. Weissenbach, A. Munnich, and J. Melki. 1995. Identification and characterization of a spinal muscular atrophy-determining gene. *Cell*. 80:155–165.
Leijnse, N., L.B. Oddershede, and P.M. Bendix. 2015. An updated look at actin dynamics in filopodia. *Cytoskeleton*. 72:71–79.
Leonard, D.G.B., J.D. Gorham, P. Cole, L.A. Greene, and E.B. Ziff. 1988. A nerve growth factor-regulated messenger RNA encodes a new intermediate filament protein. *J. Cell Biol.* 106:181–193.
Lépinoux-Chambaud, C., and J. Eyer. 2013. Review on intermediate filaments of the nervous system and their pathological alterations. *Histochem. Cell Biol.* 140:13–22.
Lerga, A., M. Hallier, L. Delva, C. Orvain, I. Gallais, J. Marie, and F. Moreau-Gachelin. 2001. Identification of an RNA Binding Specificity for the Potential Splicing Factor TLS. *J. Biol. Chem.* 276:6807–6816.
Leung, C.L., C.Z. He, P. Kaufmann, S.S. Chin, A. Naini, R.K.H. Liem, H. Mitsumoto, and A.P. Hays. 2004. A pathogenic peripherin gene mutation in a patient with amyotrophic lateral sclerosis. *Brain Pathol.* 14:290–6.
Levine, T.P., R.D. Daniels, A.T. Gatta, L.H. Wong, and M.J. Hayes. 2013. The product of C9orf72, a gene strongly implicated in neurodegeneration, is structurally related to DENN Rab-GEFs. *Bioinformatics*. 29:499–503.
Lim, J., M.L. Lachenmayer, S. Wu, W. Liu, M. Kundu, R. Wang, M. Komatsu, Y.J. Oh, Y. Zhao, and Z. Yue. 2015. Proteotoxic stress induces phosphorylation of p62/SQSTM1 by ULK1 to regulate selective autophagic clearance of protein aggregates. *PLoS Genet.* 11:e1004987.
Lin, C.H., and P. Forscher. 1995. Growth cone advance is inversely proportional to retrograde F-actin flow. *Neuron*. 14:763–771.
Lin, J.-C., M. Hsu, and W.-Y. Tarn. 2007. Cell stress modulates the function of splicing regulatory protein RBM4 in translation control. *Proc. Natl. Acad. Sci. U. S. A.* 104:2235–40.
Lin, M.Y., X.T. Cheng, Y. Xie, Q. Cai, and Z.H. Sheng. 2017. Releasing Syntaphilin Removes Stressed Mitochondria from Axons Independent of Mitophagy under Pathophysiological Conditions. *Neuron*. 94:595–610.
Ling, J.P., O. Pletnikova, J.C. Troncoso, and P.C. Wong. 2015. TDP-43 repression of nonconserved cryptic exons is compromised in ALS-FTD. *Science*. 349:650–655.
Ling, S.-C., C.P. Albuquerque, J.S. Han, C. Lagier-Tourenne, S. Tokunaga, H. Zhou, and D.W. Cleveland. 2010. ALS-associated mutations in TDP-43 increase its stability and promote TDP-43 complexes with FUS/TLS. *Proc. Natl. Acad. Sci. U. S. A.* 107:13318–23.
Ling, S.-C., M. Polymenidou, and D.W. Cleveland. 2013. Converging mechanisms in ALS and FTD: disrupted RNA and protein homeostasis. *Neuron*. 79:416–38.
Lipka, J., M. Kuijpers, J. Jaworski, and C.C. Hoogenraad. 2013. Mutations in cytoplasmic dynein and its regulators cause malformations of cortical development and neurodegenerative diseases. *Biochem. Soc. Trans.* 41:1605–12.
Liu, Y., A. Pattamatta, T. Zu, T. Reid, O. Bardhi, D.R. Borchelt, A.T. Yachnis, and L.P.W.

Ranum. 2016a. C9orf72 BAC Mouse Model with Motor Deficits and Neurodegenerative Features of ALS/FTD. *Neuron*. 90:521–534.
Liu, Y., H.K. Salter, A.N. Holding, C.M. Johnson, E. Stephens, P.J. Lukavsky, J. Walshaw, and S.L. Bullock. 2013. Bicaudal-D uses a parallel, homodimericcoiled coil with heterotypic registry tocoordinate recruitment of cargos to dynein. *Genes Dev.* 27:1233–1246.
Liu, Z.D., S. Zhang, J.J. Hao, T.R. Xie, and J.S. Kang. 2016b. Cellular model of neuronal atrophy induced by DYNC1I1 deficiency reveals protective roles of RAS-RAF-MEK signaling. *Protein Cell*. 7:638–650.
Logroscino, G., B.J. Traynor, O. Hardiman, A. Chiò, D. Mitchell, R.J. Swingler, A. Millul, E. Benn, and E. Beghi. 2010. Incidence of amyotrophic lateral sclerosis in Europe. *J. Neurol. Neurosurg. Psychiatry*. 81:385–90.
López-colomé, A.M., I. Lee-Rivera, R. Benavides-hidalgo, and E. López. 2017. Paxillin: a crossroad in pathological cell migration. *J. Hematol. Oncol.* 10:50.
Lorson, C.L., E. Hahnen, E.J. Androphy, and B. Wirth. 1999. A single nucleotide in the SMN gene regulates splicing and is responsible for spinal muscular atrophy. *Proc. Natl. Acad. Sci.* 96:6307–6311.
Lourenco, G.F., M. Janitz, Y. Huang, and G.M. Halliday. 2015. Long noncoding RNAs in TDP-43 and FUS/TLS-related frontotemporal lobar degeneration (FTLD). *Neurobiol. Dis.* 82:445–454.
Lowe, M. 2011. Structural organization of the Golgi apparatus. *Curr. Opin. Cell Biol.* 23:85–93.
Mach, J.M., and R. Lehmann. 1997. An egalitarian-BicaudalD complex is essential for oocyte specification and axis determination in Drosophila. *Genes Dev.* 11:423–435.
Mackenzie, I.R.A., E.H. Bigio, P.G. Ince, F. Geser, M. Neumann, N.J. Cairns, L.K. Kwong, M.S. Forman, J. Ravits, H. Stewart, A. Eisen, L. McClusky, H.A. Kretzschmar, C.M. Monoranu, J.R. Highley, J. Kirby, T. Siddique, P.J. Shaw, V.M.Y. Lee, and J.Q. Trojanowski. 2007. Pathological TDP-43 distinguishes sporadic amyotrophic lateral sclerosis from amyotrophic lateral sclerosis with SOD1 mutations. *Ann. Neurol.* 61:427–434.
Mackenzie, I.R., R. Rademakers, and M. Neumann. 2010. TDP-43 and FUS in amyotrophic lateral sclerosis and frontotemporal dementia. *Lancet Neurol.* 9:995–1007.
Maday, S. 2016. Mechanisms of neuronal homeostasis: Autophagy in the axon. *Brain Res.* 1649:143–150.
Maday, S., A.E. Twelvetrees, A.J. Moughamian, and E.L.F. Holzbaur. 2014. Axonal Transport: Cargo-Specific Mechanisms of Motility and Regulation. *Neuron*. 84:292–309.
Maday, S., K.E. Wallace, and E.L.F. Holzbaur. 2012. Autophagosomes initiate distally and mature during transport toward the cell soma in primary neurons. *J. Cell Biol.* 196:407–417.
Maekawa, S., P.N. Leigh, A. King, E. Jones, J.C. Steele, I. Bodi, C.E. Shaw, T. Hortobagyi, and S. Al-Sarraj. 2009. TDP-43 is consistently co-localized with ubiquitinated inclusions in sporadic and Guam amyotrophic lateral sclerosis but not in familial amyotrophic lateral sclerosis with and without SOD1 mutations. *Neuropathology*. 29:672–683.
Magrané, J., C. Cortez, W.B. Gan, and G. Manfredi. 2014. Abnormal mitochondrial transport and morphology are common pathological denominators in SOD1 and TDP43 ALS mouse models. *Hum. Mol. Genet.* 23:1413–1424.
Majounie, E., A.E. Renton, K. Mok, E.G.P. Dopper, A. Waite, S. Rollinson, A. Chio, G. Restagno, N. Nicolaou, J. Simon-Sanchez, J.C. van Swieten, Y. Abramzon, J.O. Johnson, M. Sendtner, R. Pamphlett, R.W. Orrell, S. Mead, K.C. Sidle, H. Houlden, J.D. Rohrer, K.E. Morrison, H. Pall, K. Talbot, O. Ansorge, D.G. Hernandez, S. Arepalli, M. Sabatelli, G. Mora, M. Corbo, F. Giannini, A. Calvo, E. Englund, G. Borghero, G.L. Floris, A.M. Remes, H. Laaksovirta, L. McCluskey, J.Q. Trojanowski,

V.M. Van Deerlin, G.D. Schellenberg, M.A. Nalls, V.E. Drory, C.S. Lu, T.H. Yeh, H. Ishiura, Y. Takahashi, S. Tsuji, I. Le Ber, A. Brice, C. Drepper, N. Williams, J. Kirby, P. Shaw, J. Hardy, P.J. Tienari, P. Heutink, H.R. Morris, S. Pickering-Brown, and B.J. Traynor. 2012. Frequency of the C9orf72 hexanucleotide repeat expansion in patients with amyotrophic lateral sclerosis and frontotemporal dementia: A cross-sectional study. *Lancet Neurol.* 11:323–330.

Marangi, G., and B.J. Traynor. 2015. Genetic causes of amyotrophic lateral sclerosis: New genetic analysis methodologies entailing new opportunities and challenges. *Brain Res.* 1607:75–93.

Martin, S., A. Al Khleifat, and A. Al-Chalabi. 2017. What causes amyotrophic lateral sclerosis? *F1000Research*. 6:371.

Martinez-Carrera, L.A., and B. Wirth. 2015. Dominant spinal muscular atrophy is caused by mutations in BICD2, an important golgin protein. *Front. Neurosci.* 9:401.

Martinez, A., M. del V. Palomo Ruiz, D.I. Perez, and C. Gil. 2017. Drugs in clinical development for the treatment of amyotrophic lateral sclerosis. *Expert Opin. Investig. Drugs*. 26:403–414.

Matanis, T., A. Akhmanova, P. Wulf, E. Del Nery, T. Weide, T. Stepanova, N. Galjart, F. Grosveld, B. Goud, C.I. De Zeeuw, A. Barnekow, and C.C. Hoogenraad. 2002. Bicaudal-D regulates COPI-independent Golgi–ER transport by recruiting the dynein–dynactin motor complex. *Nat. Cell Biol.* 4:986–992.

Matsumoto, G., T. Shimogori, N. Hattori, and N. Nukina. 2015. TBK1 controls autophagosomal engulfment of polyubiquitinated mitochondria through p62/SQSTM1 phosphorylation. *Hum. Mol. Genet.* 24:4429–4442.

Mattiazzi, M., M. D'Aurelio, C.D. Gajewski, K. Martushova, M. Kiaei, M. Flint Beal, and G. Manfredi. 2002. Mutated human SOD1 causes dysfunction of oxidative phosphorylation in mitochondria of transgenic mice. *J. Biol. Chem.* 277:29626–29633.

Mayor, R., and S. Etienne-Manneville. 2016. The front and rear of collective cell migration. *Nat. Rev. Mol. Cell Biol.* 17:97–109.

Mazaki, Y., H. Uchida, O. Hino, S. Hashimoto, and H. Sabe. 1998. Paxillin Isoforms in Mouse. *J. Biol. Chem.* 273:22435–22441.

McCord, J.M., and I. Fridovich. 1969. Superoxide dismutase. An enzymic function for erythrocuprein (hemocuprein). *J. Biol. Chem.* 244:6049–6055.

McDermott, C.J., and P.J. Shaw. 2008. Diagnosis and management of motor neurone disease. *BMJ*. 336:658–62.

McGoldrick, P., P.I. Joyce, E.M.C. Fisher, and L. Greensmith. 2013. Rodent models of amyotrophic lateral sclerosis. *Biochim. Biophys. Acta - Mol. Basis Dis.* 1832:1421–1436.

McKenney, R.J., W. Huynh, M.E. Tanenbaum, G. Bhabha, and R.D. Vale. 2014. Activation of cytoplasmic dynein motility by dynactin-cargo adapter complexes. *Science*. 345:337–341.

McKenney, R.J., W. Huynh, R.D. Vale, and M. Sirajuddin. 2016. Tyrosination of α-tubulin controls the initiation of processive dynein-dynactin motility. *EMBO J.* 35:e201593071.

McLean, J., H.N. Liu, D. Miletic, Y.C. Weng, E. Rogaeva, L. Zinman, J. Kriz, and J. Robertson. 2010. Distinct biochemical signatures characterize peripherin isoform expression in both traumatic neuronal injury and motor neuron disease. *J. Neurochem.* 114:1177–1192.

McLean, J., S. Xiao, K. Miyazaki, and J. Robertson. 2008. A novel peripherin isoform generated by alternative translation is required for normal filament network formation. *J. Neurochem.* 104:1663–73.

Meiri, D., C.B. Marshall, M.A. Greeve, B. Kim, M. Balan, F. Suarez, C. Bakal, C. Wu, J. LaRose, N. Fine, M. Ikura, and R. Rottapel. 2012. Mechanistic Insight into the Microtubule and Actin Cytoskeleton Coupling through Dynein-Dependent RhoGEF Inhibition. *Mol. Cell*. 45:642–655.

Menzies, F.M., M.R. Cookson, R.W. Taylor, D.M. Turnbull, Z.M.A. Chrzanowska-Lightowlers, L. Dong, D.A. Figlewicz, and P.J. Shaw. 2002. Mitochondrial dysfunction in a cell culture model of familial amyotrophic lateral sclerosis. *Brain*. 125:1522–1533.
Migheli, A., T. Pezzulo, A. Attanasio, and D. Schiffer. 1993. Peripherin immunoreactive structures in amyotrophic lateral sclerosis. *Lab. Invest.* 68:185–91.
Miller, P.M., A.W. Folkmann, A.R.R. Maia, N. Efimova, A. Efimov, and I. Kaverina. 2009. Golgi-derived CLASP-dependent microtubules control Golgi organization and polarized trafficking in motile cells. *Nat. Cell Biol.* 11:1069–1080.
Mitchell, J.C., R. Constable, E. So, C. Vance, E. Scotter, L. Glover, T. Hortobagyi, E.S. Arnold, S.-C. Ling, M. McAlonis, S. Da Cruz, M. Polymenidou, L. Tessarolo, D.W. Cleveland, and C.E. Shaw. 2015. Wild type human TDP-43 potentiates ALS-linked mutant TDP-43 driven progressive motor and cortical neuron degeneration with pathological features of ALS. *Acta Neuropathol. Commun.* 3:36.
Mitchell, J.C., P. McGoldrick, C. Vance, T. Hortobagyi, J. Sreedharan, B. Rogelj, E.L. Tudor, B.N. Smith, C. Klasen, C.C.J. Miller, J.D. Cooper, L. Greensmith, and C.E. Shaw. 2013. Overexpression of human wild-type FUS causes progressive motor neuron degeneration in an age- and dose-dependent fashion. *Acta Neuropathol.* 125:273–288.
Mizielinska, S., T. Lashley, F.E. Norona, E.L. Clayton, C.E. Ridler, P. Fratta, and A.M. Isaacs. 2013. C9orf72 frontotemporal lobar degeneration is characterised by frequent neuronal sense and antisense RNA foci. *Acta Neuropathol.* 126:845–857.
Mizuno, Y., Y. Fujita, M. Takatama, and K. Okamoto. 2011. Peripherin partially localizes in Bunina bodies in amyotrophic lateral sclerosis. *J. Neurol. Sci.* 302:14–8.
Moens, T.G., L. Partridge, and A.M. Isaacs. 2017. Genetic models of C9orf72: what is toxic? *Curr. Opin. Genet. Dev.* 44:92–101.
Mohler, J., and E.F. Wieschaus. 1986. Dominant maternal-effect mutations of Drosophila melanogaster causing the production of double-abdomen embryos. *Genetics*. 112:803–822.
Monani, U.R., C.L. Lorson, D.W. Parsons, T.W. Prior, E.J. Androphy, A.H.M. Burghes, and J.D. McPherson. 1999. A single nucleotide difference that alters splicing patterns distinguishes the SMA gene SMN1 from the copy gene SMN2. *Hum. Mol. Genet.* 8:1177–1183.
Mondola, P., S. Damiano, A. Sasso, and M. Santillo. 2016. The Cu, Zn superoxide dismutase: Not only a dismutase enzyme. *Front. Physiol.* 7:1–8.
Mondola, P., G. Ruggiero, R. Serù, S. Damiano, S. Grimaldi, C. Garbi, M. Monda, D. Greco, and M. Santillo. 2003. The Cu,Zn superoxide dismutase in neuroblastoma SK-N-BE cells is exported by a microvesicles dependent pathway. *Mol. Brain Res.* 110:45–51.
Morimoto, N., M. Nagai, Y. Ohta, K. Miyazaki, T. Kurata, M. Morimoto, T. Murakami, Y. Takehisa, Y. Ikeda, T. Kamiya, and K. Abe. 2007. Increased autophagy in transgenic mice with a G93A mutant SOD1 gene. *Brain Res.* 1167:112–117.
Morlando, M., S. Dini Modigliani, G. Torrelli, A. Rosa, V. Di Carlo, E. Caffarelli, and I. Bozzoni. 2012. FUS stimulates microRNA biogenesis by facilitating co-transcriptional Drosha recruitment. *EMBO J.* 31:4502–4510.
Munch, C., R. Sedlmeier, T. Meyer, V. Homberg, A.D. Sperfeld, A. Kurt, J. Prudlo, G. Peraus, C.O. Hanemann, G. Stumm, and A.C. Ludolph. 2004. Point mutations of the p150 subunit of dynactin (DCTN1) gene in ALS. *Neurology*. 63:724–726.
Muresan, V., and Z.L. Muresan. 2016. Shared molecular mechanisms in Alzheimer's disease and amyotrophic lateral sclerosis: Neurofilament-dependent transport of sAPP, FUS, TDP-43 and SOD1, with endoplasmic reticulum-like tubules. *Neurodegener. Dis.* 16:55–61.
N'Diaye, E.N., K.K. Kajihara, I. Hsieh, H. Morisaki, J. Debnath, and E.J. Brown. 2009. PLIC proteins or ubiquilins regulate autophagy-dependent cell survival during nutrient starvation. *EMBO Rep.* 10:173–179.
Nakamura, N., J.H. Wei, and J. Seemann. 2012. Modular organization of the mammalian

Golgi apparatus. *Curr. Opin. Cell Biol.* 24:467–474.
Narayanan, R.K., M. Mangelsdorf, A. Panwar, T.J. Butler, P.G. Noakes, and R.H. Wallace. 2013. Identification of RNA bound to the TDP-43 ribonucleoprotein complex in the adult mouse brain. *Amyotroph. Lateral Scler. Front. Degener.* 14:252–260.
Narendra, D., A. Tanaka, D.F. Suen, and R.J. Youle. 2008. Parkin is recruited selectively to impaired mitochondria and promotes their autophagy. *J. Cell Biol.* 183:795–803.
Nassif, M., V. Valenzuela, D. Rojas-Rivera, R. Vidal, S. Matus, K. Castillo, Y. Fuentealba, G. Kroemer, B. Levine, and C. Hetz. 2014. Pathogenic role of BECN1/Beclin 1 in the development of amyotrophic lateral sclerosis. *Autophagy*. 10:1256–1271.
Natsume, T., T. Kiyomitsu, Y. Saga, and M.T. Kanemaki. 2016. Rapid Protein Depletion in Human Cells by Auxin-Inducible Degron Tagging with Short Homology Donors. *Cell Rep.* 15:210–218.
Neumann, M., D.M. Sampathu, L.K. Kwong, A.C. Truax, M.C. Micsenyi, T.T. Chou, J. Bruce, T. Schuck, M. Grossman, C.M. Clark, L.F. McCluskey, B.L. Miller, E. Masliah, I.R. Mackenzie, H. Feldman, W. Feiden, H. a Kretzschmar, J.Q. Trojanowski, and V.M.-Y. Lee. 2006. Ubiquitinated TDP-43 in frontotemporal lobar degeneration and amyotrophic lateral sclerosis. *Science*. 314:130–3.
Neveling, K., L.A. Martinez-Carrera, I. Hölker, A. Heister, A. Verrips, S.M. Hosseini-Barkooie, C. Gilissen, S. Vermeer, M. Pennings, R. Meijer, M. Te Riele, C.J.M. Frijns, O. Suchowersky, L. Maclaren, S. Rudnik-Schöneborn, R.J. Sinke, K. Zerres, R.B. Lowry, H.H. Lemmink, L. Garbes, J.A. Veltman, H.J. Schelhaas, H. Scheffer, and B. Wirth. 2013. Mutations in BICD2, which encodes a golgin and important motor adaptor, cause congenital autosomal-dominant spinal muscular atrophy. *Am. J. Hum. Genet.* 92:946–954.
Nirschl, J.J., M.M. Magiera, J.E. Lazarus, C. Janke, and E.L.F. Holzbaur. 2016. α-Tubulin Tyrosination and CLIP-170 Phosphorylation Regulate the Initiation of Dynein-Driven Transport in Neurons. *Cell Rep.* 14:2637–2652.
Nishimoto, Y., S. Nakagawa, T. Hirose, H. Okano, M. Takao, S. Shibata, S. Suyama, K. Kuwako, T. Imai, S. Murayama, N. Suzuki, and H. Okano. 2013. The long non-coding RNA nuclear-enriched abundant transcript 1_2 induces paraspeckle formation in the motor neuron during the early phase of amyotrophic lateral sclerosis. *Mol. Brain*. 6:31.
Nishimura, A.L., M. Mitne-Neto, H.C.A. Silva, A. Richieri-Costa, S. Middleton, D. Cascio, F. Kok, J.R.M. Oliveira, T. Gillingwater, J. Webb, P. Skehel, and M. Zatz. 2004. A Mutation in the Vesicle-Trafficking Protein VAPB Causes Late-Onset Spinal Muscular Atrophy and Amyotrophic Lateral Sclerosis. *Am. J. Hum. Genet.* 75:822–831.
Niu, Q., X. Wang, M. Shi, and Q. Jin. 2015. A novel DYNC1H1 mutation causing spinal muscular atrophy with lower extremity predominance. *Neurol. Genet.* 1:e20–e20.
Nolan, M., K. Talbot, and O. Ansorge. 2016. Pathogenesis of FUS-associated ALS and FTD: insights from rodent models. *Acta Neuropathol. Commun.* 4:99.
O'Rourke, J.G., L. Bogdanik, A.K.M.G. Muhammad, T.F. Gendron, K.J. Kim, A. Austin, J. Cady, E.Y. Liu, J. Zarrow, S. Grant, R. Ho, S. Bell, S. Carmona, M. Simpkinson, D. Lall, K. Wu, L. Daughrity, D.W. Dickson, M.B. Harms, L. Petrucelli, E.B. Lee, C.M. Lutz, and R.H. Baloh. 2015. C9orf72 BAC Transgenic Mice Display Typical Pathologic Features of ALS/FTD. *Neuron*. 88:892–901.
Oates, E.C., A.M. Rossor, M. Hafezparast, M. Gonzalez, F. Speziani, D.G. Macarthur, M. Lek, E. Cottenie, M. Scoto, a. R. Foley, M. Hurles, H. Houlden, L. Greensmith, M. Auer-Grumbach, T.R. Pieber, T.M. Strom, R. Schule, D.N. Herrmann, J.E. Sowden, G. Acsadi, M.P. Menezes, N.F. Clarke, S. Zuchner, F. Muntoni, K.N. North, and M.M. Reilly. 2013. Mutations in BICD2 cause dominant congenital spinal muscular atrophy and hereditary spastic paraplegia. *Am. J. Hum. Genet.* 92:965–973.
Ogino, S., D.G.B. Leonard, H. Rennert, W.J. Ewens, and R.B. Wilson. 2002. Genetic risk assessment in carrier testing for spinal muscular atrophy. *Am. J. Med. Genet.* 110:301–307.
Olenick, M.A., M. Tokito, M. Boczkowska, R. Dominguez, and E.L.F. Holzbaur. 2016.

Hook adaptors induce unidirectional processive motility by enhancing the Dynein-Dynactin interaction. *J. Biol. Chem.* 291:18239–18251.
De Oliveira, H.D.S.J.M. 2014. Investigating TDP43 biological dysfunction through the characterisation of Tardbp ENU mouse mutants : Implications for Neurodegeneration, PhD thesis. Univeristy of Oxford. 1-297 pp.
Ori-McKenney, K.M., L.Y. Jan, and Y.N. Jan. 2012. Golgi Outposts Shape Dendrite Morphology by Functioning as Sites of Acentrosomal Microtubule Nucleation in Neurons. *Neuron*. 76:921–930.
Ori-McKenney, K.M., and R.B. Vallee. 2011. Neuronal migration defects in the Loa dynein mutant mouse. *Neural Dev.* 6:26.
Ori-McKenney, K.M., J. Xu, S.P. Gross, and R.B. Vallee. 2010. A cytoplasmic dynein tail mutation impairs motor processivity. *Nat. Cell Biol.* 12:1228–1234.
Otomo, A., R. Kunita, K. Suzuki-Utsunomiya, J.E. Ikeda, and S. Hadano. 2011. Defective relocalization of ALS2/alsin missense mutants to Rac1-induced macropinosomes accounts for loss of their cellular function and leads to disturbed amphisome formation. *FEBS Lett.* 585:730–736.
Otsu, N. 1979. A threshold selection method from gray-level histograms. *IEEE Trans. Syst. Man. Cybern.* 9:62–66.
Ou, S.H., F. Wu, D. Harrich, L.F. García-Martínez, and R.B. Gaynor. 1995. Cloning and characterization of a novel cellular protein, TDP-43, that binds to human immunodeficiency virus type 1 TAR DNA sequence motifs. *J. Virol.* 69:3584–96.
Palmer, K.J., H. Hughes, and D.J. Stephens. 2009. Specificity of cytoplasmic dynein subunits in discrete membrane-trafficking steps. *Mol. Biol. Cell*. 20:2885–99.
Pang, T., R. Atefy, and V. Sheen. 2008. Malformations of cortical development. *Neurologist*. 14:181–91.
Papadopoulos, C., P. Kirchner, M. Bug, D. Grum, L. Koerver, N. Schulze, R. Poehler, A. Dressler, S. Fengler, K. Arhzaouy, V. Lux, M. Ehrmann, C.C. Weihl, and H. Meyer. 2017. VCP/p97 cooperates with YOD1, UBXD1 and PLAA to drive clearance of ruptured lysosomes by autophagy. *EMBO J.* 36:135–150.
Papoulas, O., T.S. Hays, and J.C. Sisson. 2005. The golgin Lava lamp mediates dynein-based Golgi movements during Drosophila cellularization. *Nat. Cell Biol.* 7:612–618.
Pardo, C.A., Z. Xu, D.R. Borchelt, D.L. Price, S.S. Sisodia, and D.W. Cleveland. 1995. Superoxide dismutase is an abundant component in cell bodies, dendrites, and axons of motor neurons and in a subset of other neurons. *Proc. Natl. Acad. Sci.* 92:954–958.
Parysek, L.M., and R.D. Goldman. 1988. Distribution of a novel 57 kDa intermediate filament (IF) protein in the nervous system. *J. Neurosci.* 8:555–563.
Parysek, L.M., M.A. McReynolds, R.D. Goldman, and C.A. Ley. 1991. Some neural intermediate filaments contain both peripherin and the neurofilament proteins. *J. Neurosci. Res.* 30:80–91.
Pasapera, A.M., I.C. Schneider, E. Rericha, D.D. Schlaepfer, and C.M. Waterman. 2010. Myosin II activity regulates vinculin recruitment to focal adhesions through FAK-mediated paxillin phosphorylation. *J. Cell Biol.* 188:877–890.
Paschal, B.M., H.S. Shpetner, and R.B. Vallee. 1987. MAP 1C is a microtubule-activated ATPase which translocates microtubules in vitro and has dynein-like properties. *J. Cell Biol.* 105:1273–1282.
Paschal, B.M., and R.B. Vallee. 1987. Retrograde transport by the microtubule-associated protein MAP 1C. *Nature*. 330:181–183.
Pasinelli, P., M.K. Houseweart, R.H. Brown, and D.W. Cleveland. 2000. Caspase-1 and -3 are sequentially activated in motor neuron death in Cu,Zn superoxide dismutase-mediated familial amyotrophic lateral sclerosis. *Proc. Natl. Acad. Sci.* 97:13901–13906.
Peeters, K., S. Bervoets, T. Chamova, I. Litvinenko, E. De Vriendt, S. Bichev, D. Kancheva, V. Mitev, M. Kennerson, V. Timmerman, P. De Jonghe, I. Tournev, J. MacMillan, and A. Jordanova. 2015. Novel Mutations in the DYNC1H1 Tail Domain

Refine the Genetic and Clinical Spectrum of Dyneinopathies. *Hum. Mutat.* 36:287–291.
Peeters, K., I. Litvinenko, B. Asselbergh, L. Almeida-Souza, T. Chamova, T. Geuens, E. Ydens, M. Zimon, J. Irobi, E. De Vriendt, V. De Winter, T. Ooms, V. Timmerman, I. Tournev, and A. Jordanova. 2013. Molecular defects in the motor adaptor BICD2 cause proximal spinal muscular atrophy with autosomal-dominant inheritance. *Am. J. Hum. Genet.* 92:955–964.
Peris, L., M. Thery, J. Fauré, Y. Saoudi, L. Lafanechère, J.K. Chilton, P. Gordon-Weeks, N. Galjart, M. Bornens, L. Wordeman, J. Wehland, A. Andrieux, and D. Job. 2006. Tubulin tyrosination is a major factor affecting the recruitment of CAP-Gly proteins at microtubule plus ends. *J. Cell Biol.* 174:839–849.
Peters, O.M., G.T. Cabrera, H. Tran, T.F. Gendron, J.E. McKeon, J. Metterville, A. Weiss, N. Wightman, J. Salameh, J. Kim, H. Sun, K.B. Boylan, D. Dickson, Z. Kennedy, Z. Lin, Y.J. Zhang, L. Daughrity, C. Jung, F.B. Gao, P.C. Sapp, H.R. Horvitz, D.A. Bosco, S.P. Brown, P. de Jong, L. Petrucelli, C. Mueller, and R.H. Brown. 2015. Human C9ORF72 Hexanucleotide Expansion Reproduces RNA Foci and Dipeptide Repeat Proteins but Not Neurodegeneration in BAC Transgenic Mice. *Neuron*. 88:902–909.
Petrov, D., C. Mansfield, A. Moussy, and O. Hermine. 2017. ALS clinical trials review: 20 years of failure. Are we any closer to registering a new treatment? *Front. Aging Neurosci.* 9:1–11.
Pfister, K.K., P.R. Shah, H. Hummerich, A. Russ, J. Cotton, A.A. Annuar, S.M. King, and E.M.C. Fisher. 2006. Genetic analysis of the cytoplasmic dynein subunit families. *PLoS Genet.* 2:11–26.
Philips, T., and J.D. Rothstein. 2015. Rodent models of amyotrophic lateral sclerosis. *Curr. Protoc. Pharmacol.* 2015:5.67.1-5.67.21.
Picher-Martel, V., P.N. Valdmanis, P. V. Gould, J.-P. Julien, and N. Dupré. 2016. From animal models to human disease: a genetic approach for personalized medicine in ALS. *Acta Neuropathol. Commun.* 4:70.
Pilli, M., J. Arko-Mensah, M. Ponpuak, E. Roberts, S. Master, M.A. Mandell, N. Dupont, W. Ornatowski, S. Jiang, S.B. Bradfute, J.A. Bruun, T.E. Hansen, T. Johansen, and V. Deretic. 2012. TBK-1 Promotes Autophagy-Mediated Antimicrobial Defense by Controlling Autophagosome Maturation. *Immunity*. 37:223–234.
Pollard, T.D., and J.A. Cooper. 2009. Actin, a central player in cell shape and movement. *Science*. 326:1208–12.
Polymenidou, M., C. Lagier-Tourenne, K.R. Hutt, C.F. Bennett, D.W. Cleveland, and G.W. Yeo. 2012. Misregulated RNA processing in amyotrophic lateral sclerosis. *Brain Res.* 1462:3–15.
Polymenidou, M., C. Lagier-Tourenne, K.R. Hutt, S.C. Huelga, J. Moran, T.Y. Liang, S.-C. Ling, E. Sun, E. Wancewicz, C. Mazur, H. Kordasiewicz, Y. Sedaghat, J.P. Donohue, L. Shiue, C.F. Bennett, G.W. Yeo, and D.W. Cleveland. 2011. Long pre-mRNA depletion and RNA missplicing contribute to neuronal vulnerability from loss of TDP-43. *Nat. Neurosci.* 14:459–68.
Portier, M.M., B. de Nechaud, and F. Gros. 1983. Peripherin, a new member of the intermediate filament protein family. *Dev. Neurosci.* 6:335–344.
Portran, D., L. Schaedel, Z. Xu, M. Théry, and M.V. Nachury. 2017. Tubulin acetylation protects long-lived microtubules against mechanical ageing. *Nat. Cell Biol.* 19:391–398.
Puls, I., C. Jonnakuty, B.H. LaMonte, E.L.F. Holzbaur, M. Tokito, E. Mann, M.K. Floeter, K. Bidus, D. Drayna, S.J. Oh, R.H. Brown, C.L. Ludlow, and K.H. Fischbeck. 2003. Mutant dynactin in motor neuron disease. *Nat. Genet.* 33:455–456.
Punetha, J., S. Monges, M.E. Franchi, E.P. Hoffman, S. Cirak, and C. Tesi-Rocha. 2015. Exome Sequencing Identifies DYNC1H1 Variant Associated With Vertebral Abnormality and Spinal Muscular Atrophy With Lower Extremity Predominance. *Pediatr. Neurol.* 52:239–244.

Purves, D., G.J. Augustine, D. Fitzpatrick, W.C. Hall, A.-S. LaMantia, J.O. Mcnamara, and L.E. White. 2008. Neuroscience. Fourth edi. Sinauer Associates, Inc, U.S.A.
Qin, R., H. Schmid, C. Münzberg, U. Maass, D. Krndija, G. Adler, T. Seufferlein, A. Liedert, A. Ignatius, F. Oswald, T. Eiseler, and G. von Wichert. 2015. Phosphorylation and turnover of paxillin in focal contacts is controlled by force and defines the dynamic state of the adhesion site. *Cytoskeleton*. 72:101–112.
Quarta, E., R. Bravi, I. Scambi, R. Mariotti, and D. Minciacchi. 2015. Increased anxiety-like behavior and selective learning impairments are concomitant to loss of hippocampal interneurons in the presymptomatic SOD1(G93A) ALS mouse model. *J. Comp. Neurol.* 523:1622–1638.
Rakhit, R., and A. Chakrabartty. 2006. Structure, folding, and misfolding of Cu,Zn superoxide dismutase in amyotrophic lateral sclerosis. *Biochim. Biophys. Acta - Mol. Basis Dis.* 1762:1025–1037.
Ramesh, N., and U.B. Pandey. 2017. Autophagy Dysregulation in ALS: When Protein Aggregates Get Out of Hand. *Front. Mol. Neurosci.* 10:1–18.
Ratti, A., and E. Buratti. 2016. Physiological functions and pathobiology of TDP-43 and FUS/TLS proteins. *J. Neurochem.* 138:95–111.
Ravits, J.M., and A.R. La Spada. 2009. ALS motor phenotype heterogeneity, focality, and spread: deconstructing motor neuron degeneration. *Neurology*. 73:805–811.
Reaume, A.G., J.L. Elliott, E.K. Hoffman, N.W. Kowall, R.J. Ferrante, D.R. Siwek, H.M. Wilcox, D.G. Flood, M.F. Beal, R.H. Brown, R.W. Scott, and W.D. Snider. 1996. Motor neurons in Cu/Zn superoxide dismutase-deficient mice develop normally but exhibit enhanced cell death after axonal injury. *Nat. Genet.* 13:43–47.
Renton, A.E., A. Chiò, and B.J. Traynor. 2014. State of play in amyotrophic lateral sclerosis genetics. *Nat. Neurosci.* 17:17–23.
Renton, A.E., E. Majounie, A. Waite, J. Simon-Sanchez, S. Rollinson, J.R. Gibbs, J.C. Schymick, H. Laaksovirta, J.C. van Swieten, L. Myllykangas, H. Kalimo, A. Paetau, Y. Abramzon, A.M. Remes, A. Kaganovich, S.W. Scholz, J. Duckworth, J. Ding, D.W. Harmer, D.G. Hernandez, J.O. Johnson, K. Mok, M. Ryten, D. Trabzuni, R.J. Guerreiro, R.W. Orrell, J. Neal, A. Murray, J. Pearson, I.E. Jansen, D. Sondervan, H. Seelaar, D. Blake, K. Young, N. Halliwell, J.B. Callister, G. Toulson, A. Richardson, A. Gerhard, J. Snowden, D. Mann, D. Neary, M.A. Nalls, T. Peuralinna, L. Jansson, V.M. Isoviita, A.L. Kaivorinne, M. Holtta-Vuori, E. Ikonen, R. Sulkava, M. Benatar, J. Wuu, A. Chio, G. Restagno, G. Borghero, M. Sabatelli, D. Heckerman, E. Rogaeva, L. Zinman, J.D. Rothstein, M. Sendtner, C. Drepper, E.E. Eichler, C. Alkan, Z. Abdullaev, S.D. Pack, A. Dutra, E. Pak, J. Hardy, A. Singleton, N.M. Williams, P. Heutink, S. Pickering-Brown, H.R. Morris, P.J. Tienari, and B.J. Traynor. 2011. A hexanucleotide repeat expansion in C9ORF72 is the cause of chromosome 9p21-linked ALS-FTD. *Neuron*. 72:257–268.
Richter, B., D.A. Sliter, L. Herhaus, A. Stolz, C. Wang, P. Beli, G. Zaffagnini, P. Wild, S. Martens, S.A. Wagner, R.J. Youle, and I. Dikic. 2016. Phosphorylation of OPTN by TBK1 enhances its binding to Ub chains and promotes selective autophagy of damaged mitochondria. *Proc. Natl. Acad. Sci.* 113:4039–4044.
Ricketts, T. 2012. Assessment of an allelic series of mouse TDP43 mutations, PhD thesis. University College London.
Ridley, A.J. 2003. Cell Migration: Integrating Signals from Front to Back. *Science*. 302:1704–1709.
Rinchetti, P., M. Rizzuti, I. Faravelli, and S. Corti. 2017. MicroRNA Metabolism and Dysregulation in Amyotrophic Lateral Sclerosis. *Mol. Neurobiol.* 1–14.
Ringholz, G.M., S.H. Appel, M. Bradshaw, N.A. Cooke, D.M. Mosnik, and P.E. Schulz. 2005. Prevalence and patterns of cognitive impairment in sporadic ALS. *Neurology*. 65:586–590.
Rios, R.M. 2014. The centrosome-Golgi apparatus nexus. *Philos. Trans. R. Soc. Lond. B. Biol. Sci.* 369:1–10.
Ripps, M.E., G.W. Huntley, P.R. Hof, J.H. Morrison, and J.W. Gordon. 1995. Transgenic

mice expressing an altered murine superoxide dismutase gene provide an animal model of amyotrophic lateral sclerosis. *Proc. Natl. Acad. Sci. U. S. A.* 92:689–693.
Rivero, S., J. Cardenas, M. Bornens, and R.M. Rios. 2009. Microtubule nucleation at the cis-side of the Golgi apparatus requires AKAP450 and GM130. *EMBO J.* 28:1016–1028.
Robberecht, W., and T. Philips. 2013. The changing scene of amyotrophic lateral sclerosis. *Nat. Rev. Neurosci.* 14:248–64.
Roberts, A.J., T. Kon, P.J. Knight, K. Sutoh, and S. a Burgess. 2013. Functions and mechanics of dynein motor proteins. *Nat. Rev. Mol. Cell Biol.* 14:713–26.
Robertson, J., J.M. Beaulieu, M.M. Doroudchi, H.D. Durham, J.P. Julien, and W.E. Mushynski. 2001. Apoptotic death of neurons exhibiting peripherin aggregates is mediated by the proinflammatory cytokine tumor necrosis factor-α. *J. Cell Biol.* 155:217–226.
Robertson, J., M.M. Doroudchi, M.D. Nguyen, H.D. Durham, M.J. Strong, G. Shaw, J.-P. Julien, and W.E. Mushynski. 2003. A neurotoxic peripherin splice variant in a mouse model of ALS. *J. Cell Biol.* 160:939–49.
Rogelj, B., L.E. Easton, G.K. Bogu, L.W. Stanton, G. Rot, T. Curk, B. Zupan, Y. Sugimoto, M. Modic, N. Haberman, J. Tollervey, R. Fujii, T. Takumi, C.E. Shaw, and J. Ule. 2012. Widespread binding of FUS along nascent RNA regulates alternative splicing in the brain. *Sci. Rep.* 2:1–10.
Rogers, D.C., J. Peters, J.E. Martin, S. Ball, S.J. Nicholson, A.S. Witherden, M. Hafezparast, J. Latcham, T.L. Robinson, C.A. Quilter, and E.M.C. Fisher. 2001. SHIRPA, a protocol for behavioral assessment: Validation for longitudinal study of neurological dysfunction in mice. *Neurosci. Lett.* 306:89–92.
Roossien, D.H., K.E. Miller, and G. Gallo. 2015. Ciliobrevins as tools for studying dynein motor function. *Front. Cell. Neurosci.* 9:1–10.
Rosen, D.R., T. Siddique, D. Patterson, D.A. Figlewicz, P. Sapp, A. Hentati, D. Donaldson, J. Goto, J.P. O'Regan, and H.X. Deng. 1993. Mutations in Cu/Zn superoxide dismutase gene are associated with familial amyotrophic lateral sclerosis. *Nature*. 362:59–62.
Roskoski, R. 2012. ERK1/2 MAP kinases: Structure, function, and regulation. *Pharmacol. Res.* 66:105–143.
Ross, C.A., and M.A. Poirier. 2004. Protein aggregation and neurodegenerative disease. *Nat. Med.* 10:S10–S17.
Rosse, C., K. Boeckeler, M. Linch, S. Radtke, D. Frith, K. Barnouin, A.S. Morsi, M. Hafezparast, M. Howell, and P.J. Parker. 2012. Binding of dynein intermediate chain 2 to paxillin controls focal adhesion dynamics and migration. *J. Cell Sci.* 125:3733–8.
Rossor, A.M., E.C. Oates, H.K. Salter, Y. Liu, S.M. Murphy, R. Schule, M.A. Gonzalez, M. Scoto, R. Phadke, C.A. Sewry, H. Houlden, A. Jordanova, I. Tournev, T. Chamova, I. Litvinenko, S. Zuchner, D.N. Herrmann, J. Blake, J.E. Sowden, G. Acsadi, M.L. Rodriguez, M.P. Menezes, N.F. Clarke, M.A. Grumbach, S.L. Bullock, F. Muntoni, M.M. Reilly, K.N. North, M. Auer Grumbach, S.L. Bullock, F. Muntoni, M.M. Reilly, and K.N. North. 2015. Phenotypic and molecular insights into spinal muscular atrophy due to mutations in BICD2. *Brain*. 138:293–310.
Rothenberg, C., D. Srinivasan, L. Mah, S. Kaushik, C.M. Peterhoff, J. Ugolino, S. Fang, A.M. Cuervo, R.A. Nixon, and M.J. Monteiro. 2010. Ubiquilin functions in autophagy and is degraded by chaperone-mediated autophagy. *Hum. Mol. Genet.* 19:3219–3232.
Roubin, R., C. Acquaviva, V. Chevrier, F. Sedjai, D. Zyss, D. Birnbaum, and O. Rosnet. 2013. Myomegalin is necessary for the formation of centrosomal and Golgi-derived microtubules. *Biol. Open*. 2:238–250.
Rowland, L.P. 2001. How amyotrophic lateral sclerosis got its name: the clinical-pathologic genius of Jean-Martin Charcot. *Arch. Neurol.* 58:512–515.
Rowland, L.P. 2010. Progressive muscular atrophy and other lower motor neuron syndromes of adults. *Muscle Nerve*. 41:161–165.

Rudnik-Schöneborn, S., S. ONEBORN, F. Deden, K. Eggermann, T. Eggermann, D. Wieczorek, B. Sellhaus, A. Yamoah, A. Goswami, K.G. Claeys, J. Weis, and K. Zerres. 2016. Autosomal dominant spinal muscular atrophy with lower extremity predominance: A recognizable phenotype of BICD2 mutations. *Muscle and Nerve*. 54:496–500.

Rulten, S.L., A. Rotheray, R.L. Green, G.J. Grundy, D.A.Q. Moore, F. Gomez-Herreros, M. Hafezparast, and K.W. Caldecott. 2014. PARP-1 dependent recruitment of the amyotrophic lateral sclerosis-associated protein FUS/TLS to sites of oxidative DNA damage. *Nucleic Acids Res.* 42:307–314.

Sadoul, K., and S. Khochbin. 2016. The growing landscape of tubulin acetylation: lysine 40 and many more. *Biochem. J.* 473:1859–1868.

Sahai, E., M.F. Olson, and C.J. Marshall. 2001. Cross-talk between Ras and Rho signalling pathways in transformation favours proliferation and increased motility. *EMBO J.* 20:755–766.

Sainath, R., and G. Gallo. 2014. The dynein inhibitor Ciliobrevin D inhibits the bidirectional transport of organelles along sensory axons and impairs NGF-mediated regulation of growth cones and axon branches. *Dev. Neurobiol.* 7:757–77.

Sajic, M., V. Mastrolia, C.Y. Lee, D. Trigo, M. Sadeghian, A.J. Mosley, N.A. Gregson, M.R. Duchen, and K.J. Smith. 2013. Impulse Conduction Increases Mitochondrial Transport in Adult Mammalian Peripheral Nerves In Vivo. *PLoS Biol.* 11.

Salcedo-Sicilia, L., S. Granell, M. Jovic, A. Sicart, E. Mato, L. Johannes, T. Balla, and G. Egea. 2013. βIII spectrin regulates the structural integrity and the secretory protein transport of the golgi complex. *J. Biol. Chem.* 288:2157–2166.

Sanders, A. a W.M., and I. Kaverina. 2015. Nucleation and dynamics of Golgi-derived microtubules. *Front. Neurosci.* 9:1–7.

Sangwan, S., and D.S. Eisenberg. 2016. Perspective on SOD1 mediated toxicity in Amyotrophic Lateral Sclerosis. *Postepy Biochem.* 1:362–369.

Sassone, J., M. Taiana, R. Lombardi, C. Porretta-Serapiglia, M. Freschi, S. Bonanno, S. Marcuzzo, F. Caravello, C. Bendotti, and G. Lauria. 2016. ALS mouse model SOD1G93A displays early pathology of sensory small fibers associated to accumulation of a neurotoxic splice variant of peripherin. *Hum. Mol. Genet.* 25:1588–1599.

Sastry, S.K., M. Lakonishok, S. Wu, T.Q. Truong, A. Huttenlocher, C.E. Turner, and A.F. Horwitz. 1999. Quantitative changes in integrin and focal adhesion signaling regulate myoblast cell cycle withdrawal. *J. Cell Biol.* 144:1295–1309.

Scekic-Zahirovic, J., O. Sendscheid, H. El Oussini, M. Jambeau, Y. Sun, S. Mersmann, M. Wagner, S. Dieterlé, J. Sinniger, S. Dirrig-Grosch, K. Drenner, M.-C. Birling, J. Qiu, Y. Zhou, H. Li, X.-D. Fu, C. Rouaux, T. Shelkovnikova, A. Witting, A.C. Ludolph, F. Kiefer, E. Storkebaum, C. Lagier-Tourenne, and L. Dupuis. 2016. Toxic gain of function from mutant FUS protein is crucial to trigger cell autonomous motor neuron loss. *EMBO J.* 35:e201592559.

Schaller, M.D. 2001. Paxillin: a focal adhesion-associated adaptor protein. *Oncogene*. 20:6459–6472.

Schiavo, G., L. Greensmith, M. Hafezparast, and E.M.C. Fisher. 2013. Cytoplasmic dynein heavy chain: the servant of many masters. *Trends Neurosci.* 36:641–51.

Schlager, M.A., H.T. Hoang, L. Urnavicius, S.L. Bullock, and A.P. Carter. 2014. *In vitro* reconstitution of a highly processive recombinant human dynein complex. *EMBO J.* 33:1855–1868.

Schlager, M.A., L.C. Kapitein, I. Grigoriev, G.M. Burzynski, P.S. Wulf, N. Keijzer, E. de Graaff, M. Fukuda, I.T. Shepherd, A. Akhmanova, and C.C. Hoogenraad. 2010. Pericentrosomal targeting of Rab6 secretory vesicles by Bicaudal-D-related protein 1 (BICDR-1) regulates neuritogenesis. *EMBO J.* 29:1637–1651.

Schoen, M., J.M. Reichel, M. Demestre, S. Putz, D. Deshpande, C. Proepper, S. Liebau, M.J. Schmeisser, A.C. Ludolph, J. Michaelis, and T.M. Boeckers. 2016. Super-Resolution Microscopy Reveals Presynaptic Localization of the ALS/FTD Related

Protein FUS in Hippocampal Neurons. *Front. Cell. Neurosci.* 9:1–16.
Schroeder, C.M., and R.D. Vale. 2016. Assembly and activation of dynein-dynactin by the cargo adaptor protein Hook3. *J. Cell Biol.* 214:309–318.
Schroer, T.A., E.R. Steuer, and M.P. Sheetz. 1989. Cytoplasmic dynein is a minus end-directed motor for membranous organelles. *Cell*. 56:937–946.
Schwartz, J.C., C.C. Ebmeier, E.R. Podell, J. Heimiller, D.J. Taatjes, and T.R. Cech. 2012. FUS binds the CTD of RNA polymerase II and regulates its phosphorylation at Ser2. *Genes Dev.* 26:2690–2695.
Scoto, M., A.M. Rossor, M.B. Harms, S. Cirak, M. Calissano, S. Robb, A.Y. Manzur, A.M. Arroyo, A.R. Sanz, S. Mansour, P. Fallon, I. Hadjikoumi, A. Klein, M. Yang, M. De Visser, W.C.G.T. Overweg-Plandsoen, F. Baas, J.P. Taylor, M. Benatar, A.M. Connolly, M.T. Al-Lozi, J. Nixon, C.G.E.L. De Goede, A.R. Foley, C. McWilliam, M. Pitt, C. Sewry, R. Phadke, M. Hafezparast, W.K.K. Chong, E. Mercuri, R.H. Baloh, M.M. Reilly, and F. Muntoni. 2015. Novel mutations expand the clinical spectrum of DYNC1H1-associated spinal muscular atrophy. *Neurology*. 84:668–679.
Scotter, E.L., H.J. Chen, and C.E. Shaw. 2015. TDP-43 Proteinopathy and ALS: Insights into Disease Mechanisms and Therapeutic Targets. *Neurotherapeutics*. 12:352–363.
Sephton, C.F., S.K. Good, S. Atkin, C.M. Dewey, P. Mayer, J. Herz, and G. Yu. 2010. TDP-43 is a developmentally regulated protein essential for early embryonic development. *J. Biol. Chem.* 285:6826–34.
Sephton, C.F., A.A. Tang, A. Kulkarni, J. West, M. Brooks, J.J. Stubblefield, Y. Liu, M.Q. Zhang, C.B. Green, K.M. Huber, E.J. Huang, J. Herz, and G. Yu. 2014. Activity-dependent FUS dysregulation disrupts synaptic homeostasis. *Proc. Natl. Acad. Sci.* 111:E4769–E4778.
Shan, X., P.-M. Chiang, D.L. Price, and P.C. Wong. 2010. Altered distributions of Gemini of coiled bodies and mitochondria in motor neurons of TDP-43 transgenic mice. *Proc. Natl. Acad. Sci.* 107:16325–16330.
Shaw, B.F., and J.S. Valentine. 2007. How do ALS-associated mutations in superoxide dismutase 1 promote aggregation of the protein? *Trends Biochem. Sci.* 32:78–85.
Shi, P., A.L. Ström, J. Gal, and H. Zhu. 2010. Effects of ALS-related SOD1 mutants on dynein- and KIF5-mediated retrograde and anterograde axonal transport. *Biochim. Biophys. Acta - Mol. Basis Dis.* 1802:707–716.
Shida, T., J.G. Cueva, Z. Xu, M.B. Goodman, and M. V. Nachury. 2010. The major -tubulin K40 acetyltransferase TAT1 promotes rapid ciliogenesis and efficient mechanosensation. *Proc. Natl. Acad. Sci.* 107:21517–21522.
Siddique, T., D.A. Figlewigz, M.A. Pericak-Vance, J.L. Haines, G. Rouleau, A.J. Jeffers, P. Sapp, W.-Y. Hung, J. Bebout, D. McKenna-Yasek, G. Deng, H.R. Horvitz, J.F. Gusella, R.H. Brown, and A.D. Roses. 1991. Linkage of a Gene Causing Familial Amyotrophic Lateral Sclerosis to Chromosome 21 and Evidence of Genetic-Locus Heterogeneity. *N. Engl. J. Med.* 324:1381–1384.
Skoufias, D.A., T.L. Burgess, and L. Wilson. 1990. Spatial and temporal colocalization of the Golgi apparatus and microtubules rich in detyrosinated tubulin. *J. Cell Biol.* 111:1929–1937.
Song, Y., and S.T. Brady. 2015. Post-translational modifications of tubulin: Pathways to functional diversity of microtubules. *Trends Cell Biol.* 25:125–136.
Soo, K.Y., J. Sultana, A. King, R. Atkinson, S.T. Warraich, V. Sundaramoorthy, I. Blair, M.A. Farg, and J.D. Atkin. 2015. ALS-associated mutant FUS inhibits macroautophagy which is restored by overexpression of Rab1. *Cell Death Discov.* 1:15030.
Sorkin, A., and M. von Zastrow. 2009. Endocytosis and signalling: intertwining molecular networks. *Nat. Rev. Mol. Cell Biol.* 10:609–22.
Splinter, D., D.S. Razafsky, M.A. Schlager, A. Serra-Marques, I. Grigoriev, J. Demmers, N. Keijzer, K. Jiang, I. Poser, A.A. Hyman, C.C. Hoogenraad, S.J. King, and A. Akhmanova. 2012. BICD2, dynactin, and LIS1 cooperate in regulating dynein recruitment to cellular structures. *Mol. Biol. Cell*. 23:4226–4241.

Splinter, D., M.E. Tanenbaum, A. Lindqvist, D. Jaarsma, A. Flotho, K. Lou Yu, I. Grigoriev, D. Engelsma, E.D. Haasdijk, N. Keijzer, J. Demmers, M. Fornerod, F. Melchior, C.C. Hoogenraad, R.H. Medema, and A. Akhmanova. 2010. Bicaudal D2, dynein, and kinesin-1 associate with nuclear pore complexes and regulate centrosome and nuclear positioning during mitotic entry. *PLoS Biol.* 8.

Sreedharan, J., I.P. Blair, V.B. Tripathi, X. Hu, C. Vance, B. Rogelj, S. Ackerley, J.C. Durnall, K.L. Williams, E. Buratti, F. Baralle, J. de Belleroche, J.D. Mitchell, P.N. Leigh, A. Al-Chalabi, C.C. Miller, G. Nicholson, and C.E. Shaw. 2008. TDP-43 mutations in familial and sporadic amyotrophic lateral sclerosis. *Science*. 319:1668–72.

Stallings, N.R., K. Puttaparthi, C.M. Luther, D.K. Burns, and J.L. Elliott. 2010. Progressive motor weakness in transgenic mice expressing human TDP-43. *Neurobiol. Dis.* 40:404–414.

Statland, J.M., R.J. Barohn, M.M. Dimachkie, M.K. Floeter, and H. Mitsumoto. 2015. Primary Lateral Sclerosis. *Neurol. Clin.* 33:749–760.

Stehbens, S.J., and T. Wittmann. 2014. Analysis of focal adhesion turnover. A quantitative live-cell imaging example. *Methods Cell Biol.* 123:335–346.

Stribl, C., A. Samara, D. Trumbach, R. Peis, M. Neumann, H. Fuchs, V. Gailus-Durner, M.H. De Angelis, B. Rathkolb, E. Wolf, J. Beckers, M. Horsch, F. Neff, E. Kremmer, S. Koob, A.S. Reichert, W. Hans, J. Rozman, M. Klingenspor, M. Aichler, A. Karl Walch, L. Becker, T. Klopstock, L. Glasl, S.M. Hlter, W. Wurst, and T. Floss. 2014. Mitochondrial dysfunction and decrease in body weight of a transgenic knock-in mouse model for TDP-43. *J. Biol. Chem.* 289:10769–10784.

Strickland, A. V., M. Schabhüttl, H. Offenbacher, M. Synofzik, N.S. Hauser, M. Brunner-Krainz, U. Gruber-Sedlmayr, S.A. Moore, R. Windhager, B. Bender, M. Harms, S. Klebe, P. Young, M. Kennerson, A.S.M. Garcia, M.A. Gonzalez, S. Züchner, R. Schule, M.E. Shy, and M. Auer-Grumbach. 2015. Mutation screen reveals novel variants and expands the phenotypes associated with DYNC1H1. *J. Neurol.* 262:2124–2134.

Ström, A.L., P. Shi, F. Zhang, J. Gal, R. Kilty, L.J. Hayward, and H. Zhu. 2008. Interaction of amyotrophic lateral sclerosis (ALS)-related mutant copper-zinc superoxide dismutase with the dynein-dynactin complex contributes to inclusion formation. *J. Biol. Chem.* 283:22795–22805.

Strong, M.J. 2010. The evidence for altered RNA metabolism in amyotrophic lateral sclerosis (ALS). *J. Neurol. Sci.* 288:1–12.

Strong, M.J., C. Leystra-Lantz, and W.-W. Ge. 2004. Intermediate filament steady-state mRNA levels in amyotrophic lateral sclerosis. *Biochem. Biophys. Res. Commun.* 316:317–22.

Strong, M.J., K. Volkening, R. Hammond, W. Yang, W. Strong, C. Leystra-Lantz, and C. Shoesmith. 2007. TDP43 is a human low molecular weight neurofilament (hNFL) mRNA-binding protein. *Mol. Cell. Neurosci.* 35:320–327.

Sturtz, L.A., K. Diekert, L.T. Jensen, R. Lill, and V.C. Culotta. 2001. A fraction of yeast Cu,Zn-superoxide dismutase and its metallochaperone, CCS, localize to the intermembrane space of mitochondria. A physiological role for SOD1 in guarding against mitochondrial oxidative damage. *J. Biol. Chem.* 276:38084–38089.

Sugarman, E.A., N. Nagan, H. Zhu, V.R. Akmaev, Z. Zhou, E.M. Rohlfs, K. Flynn, B.C. Hendrickson, T. Scholl, D.A. Sirko-Osadsa, and B.A. Allitto. 2012. Pan-ethnic carrier screening and prenatal diagnosis for spinal muscular atrophy: clinical laboratory analysis of >72,400 specimens. *Eur. J. Hum. Genet.* 20:27–32.

Sullivan, P.M., X. Zhou, A.M. Robins, D.H. Paushter, D. Kim, M.B. Smolka, and F. Hu. 2016. The ALS/FTLD associated protein C9orf72 associates with SMCR8 and WDR41 to regulate the autophagy-lysosome pathway. *Acta Neuropathol. Commun.* 4:51.

Sun, S., S.-C. Ling, J. Qiu, C.P. Albuquerque, Y. Zhou, S. Tokunaga, H. Li, H. Qiu, A. Bui, G.W. Yeo, E.J. Huang, K. Eggan, H. Zhou, X.-D. Fu, C. Lagier-Tourenne, and D.W.

Cleveland. 2015. ALS-causative mutations in FUS/TLS confer gain and loss of function by altered association with SMN and U1-snRNP. *Nat. Commun.* 6:6171.
Sun, Z., A. Lambacher, and R. Fässler. 2014. Nascent adhesions: From fluctuations to a hierarchical organization. *Curr. Biol.* 24:R801–R803.
Sundaramoorthy, V., J.M. Sultana, and J.D. Atkin. 2015. Golgi fragmentation in amyotrophic lateral sclerosis, an overview of possible triggers and consequences. *Front. Neurosci.* 9:1–11.
Sung, H., L.C. Tandarich, K. Nguyen, and P.J. Hollenbeck. 2016. Compartmentalized Regulation of Parkin-Mediated Mitochondrial Quality Control in the Drosophila Nervous System In Vivo. *J. Neurosci.* 36:7375–7391.
Suter, B., L.M. Romberg, and R. Steward. 1989. Bicaudal-D, a Drosophila gene involved in developmental asymmetry: Localized transcript accumulation in ovaries and sequence similarity to myosin heavy chain tail domains. *Genes Dev.* 3:1957–1968.
Suter, B., and R. Steward. 1991. Requirement for phosphorylation and localization of the Bicaudal-D protein in Drosophila oocyte differentiation. *Cell*. 67:917–926.
Suter, K.J. 2008. Advances in neurobiology: CYTOSKELETON OF THE NERVOUS SYSTEM Textbook. 48. 547 pp.
Svetoni, F., P. Frisone, and M.P. Paronetto. 2016. Role of FET proteins in neurodegenerative disorders. *RNA Biol.* 13:1089–1102.
Swan, A., T. Nguyen, and B. Suter. 1999. Drosophila Lissencephaly-1 functions with Bic-D and dynein in oocyte determination and nuclear positioning. *Nat. Cell Biol.* 1:444–449.
Swan, A., and B. Suter. 1996. Role of Bicaudal-D in patterning the Drosophila egg chamber in mid-oogenesis. *Development*. 122:3577–3586.
Swarup, V., D. Phaneuf, C. Bareil, J. Robertson, G.A. Rouleau, J. Kriz, and J.-P.P. Julien. 2011. Pathological hallmarks of amyotrophic lateral sclerosis/frontotemporal lobar degeneration in transgenic mice produced with TDP-43 genomic fragments. *Brain*. 134:2610–26.
Swinnen, B., and W. Robberecht. 2014. The phenotypic variability of amyotrophic lateral sclerosis. *Nat. Rev. Neurol.* 10:661–670.
Synofzik, M., L.A. Martinez-Carrera, T. Lindig, L. Schöls, B. Wirth, L. Schols, and B. Wirth. 2014. Dominant spinal muscular atrophy due to BICD2: a novel mutation refines the phenotype. *J. Neurol. Neurosurg. Psychiatry*. 85:590–592.
Szaro, B.G., and M.J. Strong. 2010. Post-transcriptional control of neurofilaments: New roles in development, regeneration and neurodegenerative disease. *Trends Neurosci.* 33:27–37.
Szeverenyi, I., A.J. Cassidy, W.C. Cheuk, B.T.K. Lee, J.E.A. Common, S.C. Ogg, H. Chen, Y.S. Shu, W.L.P. Goh, W.N. Kee, J.A. Simpson, L.C. Li, H.E. Goi, B. Li, D.P. Lunny, D. Chuon, A. Venkatesh, H.K. Kian, W.H.I. McLean, P.L. Yun, and E.B. Lane. 2008. The human intermediate filament database: Comprehensive information on a gene family involved in many human diseases. *Hum. Mutat.* 29:351–360.
Tafuri, F., D. Ronchi, F. Magri, G.P. Comi, and S. Corti. 2015. SOD1 misplacing and mitochondrial dysfunction in amyotrophic lateral sclerosis pathogenesis. *Front. Cell. Neurosci.* 9:1–12.
Tan, Q., H.K. Yalamanchili, J. Park, A. De Maio, H.C. Lu, Y.W. Wan, J.J. White, V. V. Bondar, L.S. Sayegh, X. Liu, Y. Gao, R. V. Sillitoe, H.T. Orr, Z. Liu, and H.Y. Zoghbi. 2016. Extensive cryptic splicing upon loss of RBM17 and TDP43 in neurodegeneration models. *Hum. Mol. Genet.* 25:5083–5093.
Tanabe, K., and K. Takei. 2009. Dynamic instability of microtubules requires dynamin 2 and is impaired in a Charcot-Marie-Tooth mutant. *J. Cell Biol.* 185:939–948.
Tang, B.L. 2016. C9orf72's Interaction with Rab GTPases—Modulation of Membrane Traffic and Autophagy. *Front. Cell. Neurosci.* 10:1–8.
Taylor, J.P., R.H. Brown, and D.W. Cleveland. 2016. Decoding ALS: from genes to mechanism. *Nature*. 539:197–206.
Teuchert, M., D. Fischer, B. Schwalenstoecker, H.J. Habisch, T.M. Böckers, and A.C.

Ludolph. 2006. A dynein mutation attenuates motor neuron degeneration in SOD1G93Amice. *Exp. Neurol.* 198:271–274.
Teuling, E., V. van Dis, P.S. Wulf, E.D. Haasdijk, A. Akhmanova, C.C. Hoogenraad, and D. Jaarsma. 2008. A novel mouse model with impaired dynein/dynactin function develops amyotrophic lateral sclerosis (ALS)-like features in motor neurons and improves lifespan in SOD1-ALS mice. *Hum. Mol. Genet.* 17:2849–2862.
Thyberg, J., and S. Moskalewski. 1993. Relationship between the Golgi complex and microtubules enriched in detyrosinated or acetylated alpha-tubulin: studies on cells recovering from nocodazole and cells in the terminal phase of cytokinesis. *Cell Tissue Res.* 273:457–466.
Tian, T., C. Huang, J. Tong, M. Yang, H. Zhou, and X.G. Xia. 2011. TDP-43 potentiates alpha-synuclein toxicity to dopaminergic neurons in transgenic mice. *Int. J. Biol. Sci.* 7:234–243.
Timme, W. 1917. Progressive muscular dystrophy as an endocrine disease. *Arch. Intern. Med.* XIX:79–104.
Tobisawa, S., Y. Hozumi, S. Arawaka, S. Koyama, M. Wada, M. Nagai, M. Aoki, Y. Itoyama, K. Goto, and T. Kato. 2003. Mutant SOD1 linked to familial amyotrophic lateral sclerosis, but not wild-type SOD1, induces ER stress in COS7 cells and transgenic mice. *Biochem. Biophys. Res. Commun.* 303:496–503.
Todd, T.W., and L. Petrucelli. 2016. Insights into the pathogenic mechanisms of Chromosome 9 open reading frame 72 (C9orf72) repeat expansions. *J. Neurochem.* 138:145–162.
Tollervey, J.R., T. Curk, B. Rogelj, M. Briese, M. Cereda, M. Kayikci, J. König, T. Hortobágyi, A.L. Nishimura, V. Zupunski, R. Patani, S. Chandran, G. Rot, B. Zupan, C.E. Shaw, and J. Ule. 2011. Characterizing the RNA targets and position-dependent splicing regulation by TDP-43. *Nat. Neurosci.* 14:452–8.
Torisawa, T., M. Ichikawa, A. Furuta, K. Saito, K. Oiwa, H. Kojima, Y.Y. Toyoshima, and K.K. Furuta. 2014. Autoinhibition and cooperative activation mechanisms of cytoplasmic dynein. *Nat. Cell Biol.* 16:1118–1124.
Troy, C.M., K. Brown, L.A. Greene, and M.L. Shelanski. 1990a. Ontogeny of the neuronal intermediate filament protein, peripherin, in the mouse embryo. *Neuroscience*. 36:217–237.
Troy, C.M., L.A. Greene, and M.L. Shelanski. 1992. Neurite outgrowth in peripherin-depleted PC12 cells. *J. Cell Biol.* 117:1085–1092.
Troy, C.M., N.A. Muma, L.A. Greene, D.L. Price, and M.L. Shelanski. 1990b. Regulation of peripherin and neurofilament expression in regenerating rat motor neurons. *Brain Res.* 529:232–238.
Tsai, J.W., W.N. Lian, S. Kemal, A.R. Kriegstein, and R.B. Vallee. 2010a. Kinesin 3 and cytoplasmic dynein mediate interkinetic nuclear migration in neural stem cells. *Nat. Neurosci.* 13:1463–1472.
Tsai, K.-J., C.-H. Yang, Y.-H. Fang, K.-H. Cho, W.-L. Chien, W.-T. Wang, T.-W. Wu, C.-P. Lin, W.-M. Fu, and C.-K.J. Shen. 2010b. Elevated expression of TDP-43 in the forebrain of mice is sufficient to cause neurological and pathological phenotypes mimicking FTLD-U. *J. Exp. Med.* 207:1661–1673.
Tsang, C.K., Y. Liu, J. Thomas, Y. Zhang, and X.F.S. Zheng. 2014. Superoxide dismutase 1 acts as a nuclear transcription factor to regulate oxidative stress resistance. *Nat. Commun.* 5:3446.
Tsurusaki, Y., S. Saitoh, K. Tomizawa, A. Sudo, N. Asahina, H. Shiraishi, J.I. Ito, H. Tanaka, H. Doi, H. Saitsu, N. Miyake, and N. Matsumoto. 2012. A DYNC1H1 mutation causes a dominant spinal muscular atrophy with lower extremity predominance. *Neurogenetics*. 13:327–332.
Tu, P.H., P. Raju, K.A. Robinson, M.E. Gurney, J.Q. Trojanowski, and V.M. Lee. 1996. Transgenic mice carrying a human mutant superoxide dismutase transgene develop neuronal cytoskeletal pathology resembling human amyotrophic lateral sclerosis lesions. *Proc. Natl. Acad. Sci. U. S. A.* 93:3155–60.

Tumbarello, D. a, M.C. Brown, S.E. Hetey, and C.E. Turner. 2005. Regulation of paxillin family members during epithelial-mesenchymal transformation: a putative role for paxillin delta. *J. Cell Sci.* 118:4849–63.
Turner, B.J. 2005. Impaired Extracellular Secretion of Mutant Superoxide Dismutase 1 Associates with Neurotoxicity in Familial Amyotrophic Lateral Sclerosis. *J. Neurosci.* 25:108–117.
Turner, C.E. 2000. Paxillin and focal adhesion signalling. *Nat. Cell Biol.* 2:E231–E236.
Tynan, S.H., M.A. Gee, and R.B. Vallee. 2000. Distinct but overlapping sites within the cytoplasmic dynein heavy chain for dimerization and for intermediate chain and light intermediate chain binding. *J. Biol. Chem.* 275:32769–32774.
Unger, A., G. Dekomien, A. Guttsches, T. Dreps, R. Kley, M. Tegenthoff, A. Ferbert, J. Weis, C. Heyer, W.A. Linke, L. Martinez-Carrera, M. Storbeck, B. Wirth, S. Hoffjan, and M. Vorgerd. 2016. Expanding the phenotype of BICD2 mutations toward skeletal muscle involvement. *Neurology*. 87:2235–2243.
Urnavicius, L., K. Zhang, A.G. Diamant, C. Motz, M. a. Schlager, M. Yu, N. a. Patel, C. V. Robinson, and A.P. Carter. 2015. The structure of the dynactin complex and its interaction with dynein. *Science*. 347:1441–1446.
Urushitani, M., S.A. Ezzi, A. Matsuo, I. Tooyama, and J.-P. Julien. 2008. The endoplasmic reticulum-Golgi pathway is a target for translocation and aggregation of mutant superoxide dismutase linked to ALS. *FASEB J.* 22:2476–2487.
Valko, M., D. Leibfritz, J. Moncol, M.T.D. Cronin, M. Mazur, and J. Telser. 2007. Free radicals and antioxidants in normal physiological functions and human disease. *Int. J. Biochem. Cell Biol.* 39:44–84.
Vallee, R.B., R.J. McKenney, and K.M. Ori-McKenney. 2012. Multiple modes of cytoplasmic dynein regulation. *Nat. Cell Biol.* 14:224–230.
Vallee, R.B., G.E. Seale, and J.W. Tsai. 2009. Emerging roles for myosin II and cytoplasmic dynein in migrating neurons and growth cones. *Trends Cell Biol.* 19:347–355.
Vance, C., B. Rogelj, T. Hortobagyi, K.J. De Vos, A.L. Nishimura, J. Sreedharan, X. Hu, B. Smith, D. Ruddy, P. Wright, J. Ganesalingam, K.L. Williams, V. Tripathi, S. Al-Saraj, A. Al-Chalabi, P.N. Leigh, I.P. Blair, G. Nicholson, J. de Belleroche, J.-M. Gallo, C.C. Miller, and C.E. Shaw. 2009. Mutations in FUS, an RNA Processing Protein, Cause Familial Amyotrophic Lateral Sclerosis Type 6. *Science*. 323:1208–1211.
Vande Velde, C., K.K. McDonald, Y. Boukhedimi, M. McAlonis-Downes, C.S. Lobsiger, S.B. Hadj, A. Zandona, J.P. Julien, S.B. Shah, and D.W. Cleveland. 2011. Misfolded SOD1 associated with motor neuron mitochondria alters mitochondrial shape and distribution prior to clinical onset. *PLoS One*. 6:1–11.
Verbeeck, C., Q. Deng, M. DeJesus-Hernandez, G. Taylor, C. Ceballos-Diaz, J. Kocerha, T. Golde, P. Das, R. Rademakers, D.W. Dickson, and T. Kukar. 2012. Expression of Fused in sarcoma mutations in mice recapitulates the neuropathology of FUS proteinopathies and provides insight into disease pathogenesis. *Mol. Neurodegener.* 7:53.
Volberg, T., L. Romer, E. Zamir, and B. Geiger. 2001. Pp60(C-Src) and Related Tyrosine Kinases: a Role in the Assembly and Reorganization of Matrix Adhesions. *J. Cell Sci.* 114:2279–89.
Vollrath, J.T., A. Sechi, A. Dreser, I. Katona, D. Wiemuth, J. Vervoorts, M. Dohmen, A. Chandrasekar, J. Prause, E. Brauers, C.M. Jesse, J. Weis, and A. Goswami. 2014. Loss of function of the ALS protein SigR1 leads to ER pathology associated with defective autophagy and lipid raft disturbances. *Cell Death Dis.* 5:e1290-13.
De vos, K.J., A.L. Chapman, M.E. Tennant, C. Manser, E.L. Tudor, K.F. Lau, J. Brownlees, S. Ackerley, P.J. Shaw, D.M. Mcloughlin, C.E. Shaw, P.N. Leigh, C.C.J. Miller, and A.J. Grierson. 2007. Familial amyotrophic lateral sclerosis-linked SOD1 mutants perturb fast axonal transport to reduce axonal mitochondria content. *Hum. Mol. Genet.* 16:2720–2728.
De Vos, K.J., and M. Hafezparast. 2017. Neurobiology of axonal transport defects in

motor neuron diseases: Opportunities for translational research? *Neurobiol. Dis.* 105:283–299.
Wang, H.-Y., I.-F. Wang, J. Bose, and C.-K.J. Shen. 2004. Structural diversity and functional implications of the eukaryotic TDP gene family. *Genomics*. 83:130–139.
Wang, I.-F., L.-S. Wu, H.-Y. Chang, and C.-K.J. Shen. 2008. TDP-43, the signature protein of FTLD-U, is a neuronal activity-responsive factor. *J. Neurochem.* 105:797–806.
Wang, J., H. Slunt, V. Gonzales, D. Fromholt, M. Coonfield, N.G. Copeland, N.A. Jenkins, and D.R. Borchelt. 2003. Copper-binding-site-null SOD1 causes ALS in transgenic mice: Aggregates of non-native SOD1 delineate a common feature. *Hum. Mol. Genet.* 12:2753–2764.
Wang, J., G. Xu, V. Gonzales, M. Coonfield, D. Fromholt, N.G. Copeland, N.A. Jenkins, and D.R. Borchelt. 2002. Fibrillar Inclusions and Motor Neuron Degeneration in Transgenic Mice Expressing Superoxide Dismutase 1 with a Disrupted Copper-Binding Site. *Neurobiol. Dis.* 10:128–138.
Wang, J., G. Xu, H. Li, V. Gonzales, D. Fromholt, C. Karch, N.G. Copeland, N.A. Jenkins, and D.R. Borchelt. 2005. Somatodendritic accumulation of misfolded SOD1-L126Z in motor neurons mediates degeneration: αB-crystallin modulates aggregation. *Hum. Mol. Genet.* 14:2335–2347.
Wang, L., H.X. Deng, G. Grisotti, H. Zhai, T. Siddique, and R.P. Roos. 2009. Wild-type SOD1 overexpression accelerates disease onset of a G85R SOD1 mouse. *Hum. Mol. Genet.* 18:1642–1651.
Wang, W., L. Li, W.L. Lin, D.W. Dickson, L. Petrucelli, T. Zhang, and X. Wang. 2013. The ALS disease-associated mutant TDP-43 impairs mitochondrial dynamics and function in motor neurons. *Hum. Mol. Genet.* 22:4706–4719.
Warner, C.L., A. Stewart, J.P. Luzio, K.P. Steel, R.T. Libby, J. Kendrick-Jones, and F. Buss. 2003. Loss of myosin VI reduces secretion and the size of the Golgi in fibroblasts from Snell's waltzer mice. *EMBO J.* 22:569–579.
Warraich, S.T., S. Yang, G. a Nicholson, and I.P. Blair. 2010. TDP-43: a DNA and RNA binding protein with roles in neurodegenerative diseases. *Int. J. Biochem. Cell Biol.* 42:1606–9.
Watanabe, Y., K. Yasui, T. Nakano, K. Doi, Y. Fukada, M. Kitayama, M. Ishimoto, S. Kurihara, M. Kawashima, H. Fukuda, Y. Adachi, T. Inoue, and K. Nakashima. 2005. Mouse motor neuron disease caused by truncated SOD1 with or without C-terminal modification. *Mol. Brain Res.* 135:12–20.
Webb, D.J., K. Donais, L.A. Whitmore, S.M. Thomas, C.E. Turner, J.T. Parsons, and A.F. Horwitz. 2004. FAK–Src signalling through paxillin, ERK and MLCK regulates adhesion disassembly. *Nat. Cell Biol.* 6:154–161.
Webster, C.P., E.F. Smith, C.S. Bauer, A. Moller, M. Guillaume, L. Ferraiuolo, M.A. Myszczynska, A. Higginbottom, M.J. Walsh, J. Whitworth, B.K. Kaspar, K. Meyer, P.J. Shaw, A.J. Grierson, K.J. De Vos, and C.P. Webster. 2016. The C9orf72 protein interacts with Rab 1 a and the ULK 1 complex to regulate initiation of autophagy. *EMBO J.* 35:1656–1676.
Webster, C.P., E.F. Smith, P.J. Shaw, and K.J. De Vos. 2017. Protein Homeostasis in Amyotrophic Lateral Sclerosis: Therapeutic Opportunities? *Front. Mol. Neurosci.* 10:1–22.
Wegorzewska, I., S. Bell, N.J. Cairns, T.M. Miller, and R.H. Baloh. 2009. TDP-43 mutant transgenic mice develop features of ALS and frontotemporal lobar degeneration. *Proc. Natl. Acad. Sci. U. S. A.* 106:18809–14.
Wei, J.H., and J. Seemann. 2017. Golgi ribbon disassembly during mitosis, differentiation and disease progression. *Curr. Opin. Cell Biol.* 47:43–51.
Wen, X., T. Westergard, P. Pasinelli, and D. Trotti. 2017. Pathogenic determinants and mechanisms of ALS/FTD linked to hexanucleotide repeat expansions in the C9orf72 gene. *Neurosci. Lett.* 636:16–26.
Wharton, R.P., and G. Struhl. 1989. Structure of the Drosophila BicaudalD protein and its

role in localizing the posterior determinant nanos. *Cell*. 59:881–892.
Wheaton, M.W., A.R. Salamone, D.M. Mosnik, R.O. McDonald, S.H. Appel, H.I. Schmolck, G.M. Ringholz, and P.E. Schulz. 2007. Cognitive impairment in familial ALS. *Neurology*. 69:1411–7.
White, M.A., and J. Sreedharan. 2016. Amyotrophic lateral sclerosis: recent genetic highlights. *Curr. Opin. Neurol.* 29:557–564.
Von Wichert, G., B. Haimovich, G.S. Feng, and M.P. Sheetz. 2003. Force-dependent integrin-cytoskeleton linkage formation requires downregulation of focal complex dynamics by Shp2. *EMBO J.* 22:5023–5035.
Wiggins, L.M., A. Kuta, J.C. Stevens, E.M.C. Fisher, and C.S. Von Bartheld. 2012. A novel phenotype for the dynein heavy chain mutation Loa: Altered dendritic morphology, organelle density, and reduced numbers of trigeminal motoneurons. *J. Comp. Neurol.* 520:2757–2773.
Wijesekera, L.C., and P.N. Leigh. 2009. Amyotrophic lateral sclerosis. *Orphanet J. Rare Dis.* 4:3.
Wijesekera, L.C., S. Mathers, P. Talman, C. Galtrey, M.H. Parkinson, J. Ganesalingam, E. Willey, M.A. Ampong, C.M. Ellis, C.E. Shaw, A. Al-Chalabi, and P.N. Leigh. 2009. Natural history and clinical features of the flail arm and flail leg ALS variants. *Neurology*. 72:1087–1094.
Wild, P., H. Farhan, D.G. McEwan, S. Wagner, V. V. Rogov, N.R. Brady, B. Richter, J. Korac, O. Waidmann, C. Choudhary, V. Dötsch, D. Bumann, and I. Dikic. 2011. Phosphorylation of the autophagy receptor optineurin restricts Salmonella growth. *Science*. 333:228–233.
Wils, H., G. Kleinberger, J. Janssens, S. Pereson, G. Joris, I. Cuijt, V. Smits, C. Ceuterick-de Groote, C. Van Broeckhoven, and S. Kumar-Singh. 2010. TDP-43 transgenic mice develop spastic paralysis and neuronal inclusions characteristic of ALS and frontotemporal lobar degeneration. *Proc. Natl. Acad. Sci.* 107:3858–3863.
Wilson, C., R. Venditti, L.R. Rega, A. Colanzi, G. D'Angelo, and M.A. De Matteis. 2011. The Golgi apparatus: an organelle with multiple complex functions. *Biochem. J.* 433:1–9.
Wingo, T.S., D.J. Cutler, N. Yarab, C.M. Kelly, and J.D. Glass. 2011. The heritability of amyotrophic lateral sclerosis in a clinically ascertained United States research registry. *PLoS One*. 6:6–10.
Winton, M.J., L.M. Igaz, M.M. Wong, L.K. Kwong, J.Q. Trojanowski, and V.M.Y. Lee. 2008. Disturbance of nuclear and cytoplasmic TAR DNA-binding protein (TDP-43) induces disease-like redistribution, sequestration, and aggregate formation. *J. Biol. Chem.* 283:13302–13309.
Witherden, A.S., M. Hafezparast, S.J. Nicholson, A. Ahmad-Annuar, N. Bermingham, D. Arac, J. Rankin, M. Iravani, S. Ball, J. Peters, J.E. Martin, D. Huntley, H. Hummerich, M. Sergot, and E.M.C. Fisher. 2002. An integrated genetic, radiation hybrid, physical and transcription map of a region of distal mouse chromosome 12, including an imprinted locus and the "Legs at odd angles" (Loa) mutation. *Gene*. 283:71–82.
Witkos, T.M., and M. Lowe. 2016. The Golgin Family of Coiled-Coil Tethering Proteins. *Front. Cell Dev. Biol.* 3:1–9.
Witkos, T.M., and M. Lowe. 2017. Recognition and tethering of transport vesicles at the Golgi apparatus. *Curr. Opin. Cell Biol.* 47:16–23.
Wong, N.K., B.P. He, and M.J. Strong. 2000. Characterization of neuronal intermediate filament protein expression in cervical spinal motor neurons in sporadic amyotrophic lateral sclerosis (ALS). *J. Neuropathol. Exp. Neurol.* 59:972–982.
Wong, P.C., C.A. Pardo, D.R. Borchelt, M.K. Lee, N.G. Copeland, N.A. Jenkins, S.S. Sisodia, D.W. Cleveland, and D.L. Price. 1995. An adverse property of a familial ALS-linked SOD1 mutation causes motor neuron disease characterized by vacuolar degeneration of mitochondria. *Neuron*. 14:1105–1116.
Wong, Y.C., and E.L.F. Holzbaur. 2014. The Regulation of Autophagosome Dynamics by Huntingtin and HAP1 Is Disrupted by Expression of Mutant Huntingtin, Leading to

Defective Cargo Degradation. *J. Neurosci.* 34:1293–1305.
Wood, J.D., T.P. Beaujeux, and P.J. Shaw. 2003. Protein aggregation in motor neurone disorders. *Neuropathol. Appl. Neurobiol.* 29:529–545.
Wu, J., C. de Heus, Q. Liu, B.P. Bouchet, I. Noordstra, K. Jiang, S. Hua, M. Martin, C. Yang, I. Grigoriev, E.A. Katrukha, A.F.M. Altelaar, C.C. Hoogenraad, R.Z. Qi, J. Klumperman, and A. Akhmanova. 2016. Molecular Pathway of Microtubule Organization at the Golgi Apparatus. *Dev. Cell*. 39:44–60.
Wu, L.S., W.C. Cheng, and C.K.J. Shen. 2012. Targeted depletion of TDP-43 expression in the spinal cord motor neurons leads to the development of amyotrophic lateral sclerosis-like phenotypes in mice. *J. Biol. Chem.* 287:27335–27344.
Wynshaw-Boris, A., and M.J. Gambello. 2001. LIS1 and dynein motor function in neuronal migration and development. *Genes Dev.* 15:639–651.
Wynshaw-Boris, a. 2007. Lissencephaly and LIS1: insights into the molecular mechanisms of neuronal migration and development. *Clin. Genet.* 72:296–304.
Xia, Q., H. Wang, Z. Hao, C. Fu, Q. Hu, F. Gao, H. Ren, D. Chen, J. Han, Z. Ying, and G. Wang. 2016. TDP-43 loss of function increases TFEB activity and blocks autophagosome-lysosome fusion. *EMBO J.* 35:121–142.
Xiao, S., L. MacNair, P. McGoldrick, P.M. McKeever, J.R. McLean, M. Zhang, J. Keith, L. Zinman, E. Rogaeva, and J. Robertson. 2015a. Isoform-specific antibodies reveal distinct subcellular localizations of C9orf72 in amyotrophic lateral sclerosis. *Ann. Neurol.* 78:568–583.
Xiao, S., J. McLean, and J. Robertson. 2006. Neuronal intermediate filaments and ALS: a new look at an old question. *Biochim. Biophys. Acta*. 1762:1001–12.
Xiao, S., T. Sanelli, H. Chiang, Y. Sun, A. Chakrabartty, J. Keith, E. Rogaeva, L. Zinman, and J. Robertson. 2015b. Low molecular weight species of TDP-43 generated by abnormal splicing form inclusions in amyotrophic lateral sclerosis and result in motor neuron death. *Acta Neuropathol.* 130:49–61.
Xiao, S., T. Sanelli, S. Dib, D. Sheps, J. Findlater, J. Bilbao, J. Keith, L. Zinman, E. Rogaeva, and J. Robertson. 2011. RNA targets of TDP-43 identified by UV-CLIP are deregulated in ALS. *Mol. Cell. Neurosci.* 47:167–80.
Xiao, S., S. Tjostheim, T. Sanelli, J.R. McLean, P. Horne, Y. Fan, J. Ravits, M.J. Strong, and J. Robertson. 2008. An aggregate-inducing peripherin isoform generated through intron retention is upregulated in amyotrophic lateral sclerosis and associated with disease pathology. *J. Neurosci.* 28:1833–40.
Xie, Y., B. Zhou, M.Y. Lin, S. Wang, K.D. Foust, and Z.H. Sheng. 2015. Endolysosomal Deficits Augment Mitochondria Pathology in Spinal Motor Neurons of Asymptomatic fALS Mice. *Neuron*. 87:355–371.
Xu, Y.-F., T.F. Gendron, Y.-J. Zhang, W.-L. Lin, S. D'Alton, H. Sheng, M.C. Casey, J. Tong, J. Knight, X. Yu, R. Rademakers, K. Boylan, M. Hutton, E. McGowan, D.W. Dickson, J. Lewis, and L. Petrucelli. 2010. Wild-Type Human TDP-43 Expression Causes TDP-43 Phosphorylation, Mitochondrial Aggregation, Motor Deficits, and Early Mortality in Transgenic Mice. *J. Neurosci.* 30:10851–10859.
Xu, Y.-F., Y.-J. Zhang, W.-L. Lin, X. Cao, C. Stetler, D.W. Dickson, J. Lewis, and L. Petrucelli. 2011. Expression of mutant TDP-43 induces neuronal dysfunction in transgenic mice. *Mol. Neurodegener.* 6:73.
Xu, Z., L. Schaedel, D. Portran, A. Aguilar, J. Gaillard, M.P. Marinkovich, M. Thery, and M. V Nachury. 2017. Microtubules acquire resistance from mechanical breakage through intralumenal acetylation. *Science*. 356:328–332.
Yadav, S., and A.D. Linstedt. 2011. Golgi positioning. *Cold Spring Harb. Perspect. Biol.* 3:1–17.
Yadav, S., M. a. Puthenveedu, and A.D. Linstedt. 2012. Golgin160 Recruits the Dynein Motor to Position the Golgi Apparatus. *Dev. Cell*. 23:153–165.
Yamaguchi, R., Y. Mazaki, K. Hirota, S. Hashimoto, and H. Sabe. 1997. Mitosis specific serine phosphorylation and downregulation of one of the focal adhesion protein, paxillin. *Oncogene*. 15:1753–1761.

Yamakita, Y., G. Totsukawa, S. Yamashiro, D. Fry, X. Zhang, S.K. Hanks, and F. Matsumura. 1999. Dissociation of FAK/p130(CAS)/c-SRC complex during mitosis: Role of mitosis-specific serine phosphorylation of FAK. *J. Cell Biol.* 144:315–324.
Yamazaki, T., S. Chen, Y. Yu, B. Yan, T.C. Haertlein, M.A. Carrasco, J.C. Tapia, B. Zhai, R. Das, M. Lalancette-Hebert, A. Sharma, S. Chandran, G. Sullivan, A.L. Nishimura, C.E. Shaw, S.P. Gygi, N.A. Shneider, T. Maniatis, and R. Reed. 2012. FUS-SMN Protein Interactions Link the Motor Neuron Diseases ALS and SMA. *Cell Rep.* 2:799–806.
Yang, C., H. Wang, T. Qiao, B. Yang, L. Aliaga, L. Qiu, W. Tan, J. Salameh, D.M. McKenna-Yasek, T. Smith, L. Peng, M.J. Moore, R.H. Brown, H. Cai, and Z. Xu. 2014. Partial loss of TDP-43 function causes phenotypes of amyotrophic lateral sclerosis. *Proc. Natl. Acad. Sci.* 111:E1121–E1129.
Yang, C., J. Wu, C. de Heus, I. Grigoriev, N. Liv, Y. Yao, I. Smal, E. Meijering, J. Klumperman, R.Z. Qi, and A. Akhmanova. 2017. EB1 and EB3 regulate microtubule minus end organization and Golgi morphology. *J. Cell Biol.* 216:3179–3198.
Yang, M., C. Liang, K. Swaminathan, S. Herrlinger, F. Lai, R. Shiekhattar, and J.-F. Chen. 2016. A C9ORF72/SMCR8-containing complex regulates ULK1 and plays a dual role in autophagy. *Sci. Adv.* 2:e1601167–e1601167.
Yoo, S.D., H.S. Kim, D.H. Yun, D.H. Kim, J. Chon, S.A. Lee, S.Y. Lee, and Y.J. Han. 2015. Monomelic amyotrophy (Hirayama disease) with upper motor neuron signs: A case report. *Ann. Rehabil. Med.* 39:122–127.
Yuan, A., M. V. Rao, Veeranna, and R.A. Nixon. 2017. Neurofilaments and neurofilament proteins in health and disease. *Cold Spring Harb. Perspect. Biol.* 9:a018309.
Yuan, A., T. Sasaki, A. Kumar, C.M. Peterhoff, M. V. Rao, R.K. Liem, J.-P. Julien, and R.A. Nixon. 2012. Peripherin Is a Subunit of Peripheral Nerve Neurofilaments: Implications for Differential Vulnerability of CNS and Peripheral Nervous System Axons. *J. Neurosci.* 32:8501–8508.
Zaidel-Bar, R., C. Ballestrem, Z. Kam, and B. Geiger. 2003. Early molecular events in the assembly of matrix adhesions at the leading edge of migrating cells. *J. Cell Sci.* 116:4605–4613.
Zaidel-Bar, R., R. Milo, Z. Kam, and B. Geiger. 2007. A paxillin tyrosine phosphorylation switch regulates the assembly and form of cell-matrix adhesions. *J. Cell Sci.* 120:137–148.
Zhang, D., L.M. Iyer, F. He, and L. Aravind. 2012. Discovery of novel DENN proteins: Implications for the evolution of eukaryotic intracellular membrane structures and human disease. *Front. Genet.* 3:1–10.
Zhang, F., A.L. Strom, K. Fukada, S. Lee, L.J. Hayward, and H. Zhu. 2007. Interaction between familial Amyotrophic Lateral Sclerosis (ALS)-linked SOD1 mutants and the dynein complex. *J. Biol. Chem.* 282:16691–16699.
Zhang, H.-G., L. Chen, L. Tang, N. Zhang, and D.-S. Fan. 2017a. Clinical Features of Isolated Bulbar Palsy of Amyotrophic Lateral Sclerosis in Chinese Population. *Chin. Med. J. (Engl).* 130:1768.
Zhang, K., H.E. Foster, A. Rondelet, S.E. Lacey, N. Bahi-buisson, A.W. Bird, A.P. Carter, K. Zhang, H.E. Foster, A. Rondelet, S.E. Lacey, N. Bahi-buisson, A.W. Bird, and A.P. Carter. 2017b. Cryo-EM Reveals How Human Cytoplasmic Dynein Is Auto-inhibited and Activated. *Cell*. 169:1–12.
Zhang, Y., S. Kwon, T. Yamaguchi, F. Cubizolles, S. Rousseaux, M. Kneissel, C. Cao, N. Li, H.-L. Cheng, K. Chua, D. Lombard, A. Mizeracki, G. Matthias, F.W. Alt, S. Khochbin, and P. Matthias. 2008. Mice Lacking Histone Deacetylase 6 Have Hyperacetylated Tubulin but Are Viable and Develop Normally. *Mol. Cell. Biol.* 28:1688–1701.
Zhao, J., and R.K.H.H. Liem. 2016. α-Internexin and Peripherin: Expression, Assembly, Functions, and Roles in Disease. 568. 1st ed. Elsevier Inc. 477-507 pp.
Zhao, J., Y. Wang, H. Xu, Y. Fu, T. Qian, D. Bo, Y.-X. Lu, Y. Xiong, J. Wan, X. Zhang, Q. Dong, and X.-J. Chen. 2016. Dync1h1 Mutation Causes Proprioceptive Sensory

Neuron Loss and Impaired Retrograde Axonal Transport of Dorsal Root Ganglion Neurons. *CNS Neurosci. Ther.* 22:1–9.
Zheng, Y., J. Wildonger, B. Ye, Y. Zhang, A. Kita, S.H. Younger, S. Zimmerman, L.Y. Jan, and Y.N. Jan. 2008. Dynein is required for polarized dendritic transport and uniform microtubule orientation in axons. *Nat. Cell Biol.* 10:1172–1180.
Zinszner, H., J. Sok, D. Immanuel, Y. Yin, and D. Ron. 1997. TLS (FUS) binds RNA in vivo and engages in nucleo-cytoplasmic shuttling. *J. Cell Sci.* 110:1741–1750.
Zufiría, M., F.J. Gil-Bea, R. Fernández-Torrón, J.J. Poza, J.L. Muñoz-Blanco, R. Rojas-García, J. Riancho, and A.L. de Munain. 2016. ALS: A bucket of genes, environment, metabolism and unknown ingredients. *Prog. Neurobiol.* 142:104–129.